# Aeroelastic Modelling and Design of Aeroelastically Tailored and Morphing Wings

Werter, Noud

**DOI**
10.4233/uuid:74925f40-1efc-469f-88ee-e871c720047e

**Publication date**
2017

**Document Version**
Final published version

**Citation (APA)**
Werter, N. (2017). *Aeroelastic Modelling and Design of Aeroelastically Tailored and Morphing Wings*. [Dissertation (TU Delft), Delft University of Technology]. https://doi.org/10.4233/uuid:74925f40-1efc-469f-88ee-e871c720047e

# Aeroelastic Modelling and Design of Aeroelastically Tailored and Morphing Wings

# Aeroelastic Modelling and Design of Aeroelastically Tailored and Morphing Wings

## Proefschrift

ter verkrijging van de graad van doctor
aan de Technische Universiteit Delft,
op gezag van de Rector Magnificus prof. ir. K. C. A. M. Luyben,
voorzitter van het College voor Promoties,
in het openbaar te verdedigen op dinsdag 26 september 2017 om 10.00 uur

door

**Noud Philip Maria WERTER**

Ingenieur Luchtvaart en Ruimtevaart
Technische Universiteit Delft
geboren te Hengelo (O), Nederland.

This dissertation has been approved by the

promotor: Prof. dr. C. Bisagni
copromotor: Dr. R. De Breuker

Composition of the doctoral committee:

| | | |
|---|---|---|
| Rector Magnificus, | chairperson | |
| Prof. dr. C. Bisagni, | promotor | Delft University of Technology |
| Dr. R. De Breuker, | copromotor | Delft University of Technology |

Independent members:

| | |
|---|---|
| Prof. dr. L.L.M. Veldhuis | Delft University of Technology |
| Prof. dr. M. Karpel | Technion - Israel Institute of Technology |
| Prof. dr. J.E. Cooper | University of Bristol |
| dr. A. Wildschek | Airbus Innovations |
| Prof. dr. W.A. Groen | Delft University of Technology, reserve member |

Other members:

| | |
|---|---|
| Prof. dr. M.I. Friswell | Swansea University |

*This research work was supported by Delft University of Technology and the CHANGE project, part of the European Union Seventh Framework Program.*



*CHANGE Project Partners:*


*Keywords:* Aeroelasticity, Morphing, Aeroelastic Tailoring, Unsteady Aerodynamics

*Printed by:* Ridderprint BV, Ridderkerk, The Netherlands

*Front & Back:* Design by Noud Werter



ISBN 978-94-6299-700-4

An electronic version of this dissertation is available at
http://repository.tudelft.nl/.

# PREFACE

This dissertation is the results of four years of PhD research and marks the end of a rewarding and enriching journey. A wise man once told me that the result of a PhD is not only a dissertation, but more importantly the growth of a person. Pursuing a PhD has, at times, brought a lot of frustration, but most of all has brought me great pleasure. Of course, this dissertation would not have existed without the help and support of my friends, family, and colleagues.

Many thanks go to my copromotor, dr. Roeland De Breuker. Thank you for offering me the opportunity to pursue a PhD and for your efforts in persuading me to actually embark on this journey, but, more importantly, thank you for all your help, support, wisdom, and the many interesting academic and non-academic discussions we had during this journey. Without you, this dissertation would not have been what it is today and I would not have been where I am today.

I would also like to thank Prof. dr. Chiara Bisagni, my promotor, for her support in the final stages of this PhD and for keeping me sharp and providing the necessary critical note that always pushed me to go just a bit further and dig just a bit deeper. I would also like to thank the chairperson, Prof. dr. Leo Veldhuis, Prof. dr. Moti Karpel, Prof. dr. Jonathan Cooper, dr. Andreas Wildschek, Prof. dr. Michael Friswell, and Prof. dr. Pim Groen for taking the time to read my dissertation, provide feedback, and take part in the doctoral ceremony.

My gratitude also extends to the other staff members of Aerospace Structures and Computational Mechanics. I enjoyed the many conversations we had at the coffee machine and would like to thank you for always taking the time to provide your perspective and share your knowledge, and the many insights this has brought me. A special thanks, of course, goes to Laura. The way you manage to keep all of us in check is simply impressive.

Of course, my PhD would not have been the same without my fellow PhDs and post-docs. Thank you for making my PhD an enjoyable and unforgettable time. I am grateful to call many of you my friends. I will not mention all of you by name, because I am sure this would result in me forgotting someone (sorry!), but I would like to especially thank (in alphabetical order) Daniel, Darwin, Erik, Jurij, Kristofer, Lars, and Paul, for your collaboration and feedback, for accompanying me to conferences and the roadtrips we planned around these conferences, and,

most importantly, for your friendship. This journey would not have been the same without you.

There is, of course, more to life than work and I am grateful to my study friends, the *Delftsche Denkers*, my friends from fencing, and my other friends for providing me with some much needed relieve from time to time. Even though I haven't seen all of you as much as I would have liked to, I've enjoyed every single time.

Where would one be without one's family? I would like to thank my in-laws for their support and for always making me feel at home. And, of course, my two little brothers, thank you for always being there for me and for never taking it easy on me. A special thanks is, of course, due to my parents. Thank you mom and dad for supporting me to go to Delft and for always believing in me. None of this would have been possible without you. Finally, of course, my grandmother, *dank je wel oma. Ze zeggen wel eens wijsheid komt met de jaren en jij bent hier het levende voorbeeld van. Hopelijk ben je nog lang in ons midden.*

Last, but certainly not least, I would like to thank my girlfriend, Hilde, whom I love with all my heart and without whom this dissertation would probably not have existed. Thank you for your never-ending love and support.

I hope you enjoy reading this dissertation as much as I enjoyed working on it.

*Noud*
*Delft, 26 September 2017*

# SUMMARY


## Aeroelastic Modelling and Design of Aeroelastically Tailored and Morphing Wings

In order to accommodate the growth in air traffic whilst reducing the impact on the environment, the European Union set a number of goals for air traffic in 2050. As a result, operational efficiency is becoming more and more important in the design of the aircraft of the future. A possible approach to increase the operational efficiency of aircraft wings is the use of (i) aeroelastic tailoring, by taking advantage of the directional stiffness properties of composite materials to control the aeroelastic deformations of the wing in a beneficial way, (ii) morphing, by actively changing the wing shape in flight to optimise performance across a range of flight conditions, or (iii) a combination of both.

In order to investigate the benefits of aeroelastic tailoring and morphing, this dissertation presents a dynamic aeroelastic analysis and optimisation framework suitable for the design of aeroelastically tailored and morphing wings that is, on the one hand, sufficiently efficient to explore the design space, but, on the other hand, sufficiently comprehensive to account for all factors relevant in the design of aircraft wings. First, the wing is discretised in several spanwise sections, where each section has a number of laminates throughout the cross-section, each having their own stiffness and thickness, to allow for aeroelastic tailoring. The laminates are described using lamination parameters, which are continuous, rather than a stacking sequence, which is inherently discrete, to allow for the use of a gradient-based optimiser. The three-dimensional wing structure is condensed into a one-dimensional beam model by means of a cross-sectional modeller to obtain a computationally efficient discretisation suitable for optimisation.

Next, the framework consists of a geometrically nonlinear static aeroelastic model and a dynamic aeroelastic model that is linearised around the static aeroelastic equilibrium solution. The static aeroelastic model is based on the work by De Breuker and has been extended with a two-dimensional vortex lattice aerodynamic model to account for the effects of wing camber, and with eccentric follower and non-follower forces to account for the effects of, for example, engine thrust or gravity on the wing designs. The dynamic aeroelastic model couples a dynamic

structural model, including the effects of non-structural masses and based on Timoshenko beam elements, to an unsteady aerodynamic model based on the unsteady vortex lattice method to obtain a monolithic system of continuous-time state-space equations describing the dynamic aeroelastic response of the wing.

By assuming small perturbations with respect to the steady solution and a fixed wake shape, a novel continuous-time state-space formulation of the unsteady vortex lattice method has been introduced. Compressibility is accounted for by introducing the Prandtl-Glauert transformation, making the model suitable for analyses up to high subsonic Mach numbers for reduced frequencies up to 1. The presented results show the benefits of the present approach over conventional discrete-time models by varying the timestep independent of the spatial discretisation and introducing a non-constant wake discretisation.

Morphing has been introduced in the framework by a novel two-step approach for the modelling of morphing aircraft wings. The first step is concept-specific and is used to identify the different morphing mechanisms on the wing and their feasibility constraints. The second step is a generic morphing optimisation framework used to identify the optimal set of morphing parameters within the concept-specific bounds and to assess whether a feasible morphing solution can be found. The main advantage of this approach is that the morphing optimisation framework is suitable for any morphing wing design, while concept-specific limitations can still be accounted for. In order to assess the feasibility of the final optimised morphing wing design, the required actuation forces and actuation energy are determined. If necessary, the feasibility constraints derived in the first step are updated and a new optimisation is run until a feasible wing design has been found.

The optimised wing designs are obtained using a gradient-based optimiser for computational efficiency where the sensitivities of the aeroelastic responses with respect to the design variables are computed analytically. In order to include a comprehensive set of constraints, aileron effectiveness, aeroelastic stability, structural strength, and panel buckling are assessed.

In order to validate the model, a combination of structural and wind tunnel tests has been carried out on a quasi-isotropic wing and an aeroelastically tailored wing. Comparison of the experimental data to the numerical results showed good agreement for both wings with errors between 0.5% and 10%, both in terms of wing deformations and in terms of predicted aeroelastic loads. Only in case of the aeroelastically tailored wing some discrepancies were observed in wing deflection with errors up to 22%, which can probably be attributed to slight variations in material properties or wing geometry, or slight flexibility in the clamping mechanism.

In order to illustrate the advantages of the framework, it has been applied to two design studies: (i) the optimisation of a morphing wing equipped with 7 morphing mechanisms designed for a 25 kg UAV and (ii) the optimisation of the

NASA Common Research Model (CRM), a contemporary transonic supercritical wing with a semispan of 29.38 m.

The optimised morphing wing shows an increase in range in the high speed flight phase of 23% over an equivalent fixed wing design, while maintaining endurance in loiter, thereby illustrating the benefits of integrating morphing mechanisms on a UAV and showing the benefits of the presented two-step morphing design approach. The corresponding wing designs were used to investigate the influence of the sequence in which different morphing manoeuvres are carried out and the flight condition at which morphing is carried out on the actuation requirements for morphing, showing changes of up to an order of magnitude. The results show that a trade-off on a systems level is required to obtain the optimal morphing flight condition and sequence for a given morphing configuration change, illustrating that the challenge of designing a morphing aircraft does not stop with designing morphing mechanisms, but requires a systems level approach where flight condition and morphing sequence are an integral part of the design process.

The optimised wing designs for the CRM clearly show the benefits of aeroelastic tailoring over conventional composite wing design approaches, resulting in more efficient wing designs with significant structural weight reductions of up to 37% within the assumptions of the present framework, although further research is required before definitive conclusions can be drawn. Aileron effectiveness, aeroelastic stability, wing stall, panel buckling, and the Tsai-Wu failure criterion have been introduced as constraints in the optimisation. By constraining the cruise twist distribution and introducing the jig twist distribution as additional design variables, aerodynamic performance in cruise is maintained, while taking advantage of aeroelastic tailoring in off-cruise conditions. In order to make a preliminary assessment of the influence of discrete gust loads and in order to show the integration of dynamic loadcases in the optimisations, several wings have been optimised under a combination of manoeuvre and gust loads. Although further research, including the effects of the flight dynamic response on the discrete gust loads acting on the wing, is required before definitive conclusions can be drawn, the results clearly show that the increased flexibility of aeroelastically tailored wings makes them more susceptible to dynamic loads.

Furthermore, the optimisation results show that the jig shape of the wings is one of the key parameters in the design of wing structures, not only to ensure optimal aircraft performance in cruise conditions, but, more importantly, to obtain the correct design loads. Moreover, the increased design freedom of aeroelastic tailoring results in wing designs that are specifically tailored to the loadcases and constraints that are included in the design. As a consequence, aeroelastically tailored wing designs have reduced design margins in off-design conditions and, therefore, a correct selection of loadcases and constraints becomes increasingly important.

Finally, in order to investigate the benefits of combined aeroelastic tailoring and

morphing, trailing edge camber morphing mechanisms have been installed on the CRM. The resulting wing designs are optimally designed across a range of flight conditions, resulting in weight reductions of up to 34% over the tailored wing designs without trailing edge camber morphing, thereby clearly showing the potential of combined aeroelastic tailoring and morphing for improved aircraft performance, although further research is required before definitive conclusions can be drawn.

In conclusion, both aeroelastic tailoring and morphing have been successfully applied to the structural design of aircraft wings, resulting in wing designs that take advantage of the aeroelastic response of the wing, ensuring optimal performance at cruise flight conditions, while showing significant improvements at off-cruise conditions.

# SAMENVATTING

## Aeroëlastisch Modelleren en Ontwerpen van *Aeroelastically Tailored* en *Morphing* Vleugels

Om zowel ruimte te bieden voor de groei van het luchtverkeer, als de belasting op het milieu te verminderen, heeft de Europese Unie een aantal doelen gesteld voor het luchtverkeer in 2050. Hierdoor wordt de operationele efficiëntie van een vliegtuig steeds bepalender in het ontwerp van een vliegtuig. Deze efficiëntie kan bijvoorbeeld worden verhoogd door het gebruik van (i) *aeroelastic tailoring*, door de richtingsafhankelijke stijfheidseigenschappen van composieten materialen te gebruiken om de aeroëlastische vervormingen van vleugels te beïnvloeden, (ii) *morphing*, door de vorm van de vleugel actief te beïnvloeden tijdens de vlucht om zo de prestaties te optimaliseren over een reeks vliegcondities of (iii) een combinatie van beiden.

Om de mogelijke voordelen van *aeroelastic tailoring* en *morphing* te onderzoeken, presenteert dit proefschrift een dynamische aeroëlastische analyse en optimalisatie raamwerk voor het ontwerp van *aeroelastically tailored* en *morphing* vleugels dat zowel efficiënt genoeg is om de ontwerpruimte te verkennen, als voldoende uitgebreid is om alle relevante parameters in het ontwerp van vliegtuigvleugels mee te nemen. Eerst wordt de vleugel langs zijn spanwijdte gediscretiseerd in een aantal secties. Verdeeld over zijn doorsnede, bestaat iedere sectie uit een aantal composieten laminaten met elk een eigen dikte en stijfheid om *aeroelastic tailoring* mogelijk te maken. De laminaten worden beschreven door middel van laminatieparameters in plaats van de laminaatopbouw, omdat laminatieparameters continue zijn, zodat een optimalisatiealgoritme gebruikt kan worden dat naast de functiewaarde ook de gradiënt gebruikt. Vervolgens wordt de driedimensionale vleugelconstructie geconcentreerd tot een eendimensionaal balkmodel door het discretiseren en concentreren van de doorsnede van elke sectie om zo een efficiënte discretisatie van de vleugel te krijgen die geschikt is voor optimalisatie.

Vervolgens bestaat het raamwerk uit een geometrisch niet-lineair statisch aeroëlastisch model en een dynamisch aeroëlastisch model dat gelineariseerd is rond de niet-lineaire statische evenwichtsoplossing. Het statische aeroëlastische model is gebaseerd op het werk van De Breuker en is uitgebreid met een tweedimensionaal

*vortex lattice* aerodynamisch model om de effecten van vleugelkromming mee te nemen en met excentrische volgende en niet-volgende krachten om de effecten van bijvoorbeeld de stuwkracht of zwaartekracht mee te nemen. Het dynamische aeroëlastische model koppelt een dynamisch structureel model, gebaseerd op Timoshenko balkelementen inclusief de effecten van niet-structurele massa's, aan een niet-stationair aerodynamisch model gebaseerd op de niet-stationaire vortex lattice methode tot een monolithisch systeem van tijd-continue state-space vergelijkingen die het dynamische aeroëlastische gedrag van een vleugel beschrijven.

Een nieuwe tijd-continue state-space formulering voor de niet-stationaire vortex lattice methode is geïntroduceerd onder de aanname van kleine verstoringen ten opzichte van de stationaire oplossing en een vaste vorm van het zog. Compressibiliteit is meegenomen door de Prandtl-Glauert transformatie te introduceren, waardoor het model geschikt is voor analyses tot en met hoog-subsonische Mach-getallen en gereduceerde frequenties kleiner dan 1. Door de tijdstap onafhankelijk van de ruimtelijke discretisatie te variëren en door een niet-constante discretisatie van het zog te introduceren tonen de gepresenteerde resultaten de voordelen van de huidige methode ten opzichte van conventionele tijd-discrete formuleringen.

*Morphing* is toegevoegd in het raamwerk door een nieuwe twee-staps methode om *morphing* vleugels te modelleren. De eerste stap is concept-afhankelijk en dient voor het identificeren van de verschillende *morphing* mechanismes op de vleugel en hun randvoorwaarden. De tweede stap is een generieke *morphing* optimalisatiestap om de optimale set *morphing* parameters binnen de concept-afhankelijke randvoorwaarden te vinden en te bepalen of een haalbare *morphing* oplossing gevonden kan worden. Het grote voordeel van deze benadering is dat het *morphing* optimalisatie raamwerk generiek is, terwijl concept-afhankelijke randvoorwaarden toch meegenomen worden. Tot slot worden de benodigde aandrijfkrachten en -energie bepaald om de haalbaarheid van de uiteindelijke *morphing* oplossing te toetsen. Waar nodig kunnen de randvoorwaarden, die bepaald zijn in de eerste stap, bijgewerkt worden en kan een nieuwe *morphing* optimalisatie gestart worden, totdat een haalbaar vleugelontwerp gevonden is.

Om de geoptimaliseerde vleugel ontwerpen te vinden wordt een optimalisatiealgoritme gebruikt dat naast de functiewaarde ook de analytische gradiënt gebruikt. Rolroereffectiviteit, aeroëlastische stabiliteit, structurele sterkte en paneelknik worden meegenomen als randvoorwaarden.

Om het model te valideren is een serie structurele en windtunneltesten uitgevoerd op een quasi-isotrope en *aeroelastically tailored* vleugel. Hierbij laten de experimentele en numerieke resultaten goede overeenkomst zien met afwijkingen tussen de 0.5% en 10% voor beide vleugels voor zowel de aeroëlastische vervormingen als de aeroëlastische belastingen. Alleen in het geval van de *aeroelastically tailored* vleugel zijn een aantal afwijkingen geobserveerd in de doorbuiging van de vleugel met afwijkingen tot 22%, waarschijnlijk veroorzaakt door kleine variaties in

materiaaleigenschappen en de vleugelgeometrie of door lichte flexibiliteit in de inklemming van de vleugel tijdens de experimenten.

Om de voordelen van het gepresenteerde raamwerk te illustreren, zijn twee ontwerpstudies uitgevoerd: (i) het optimaliseren van een *morphing* vleugel uitgerust met 7 *morphing* mechanismes, ontworpen voor een onbemand vliegtuig (UAV) van 25 kg, en (ii) het optimaliseren van het *NASA Common Research Model (CRM)*, een hedendaagse transsonische superkritische vleugel met een spanwijdte van 58.76 m.

De geoptimaliseerde *morphing* vleugel heeft een 23% groter bereik op hoge snelheid ten opzichte van het equivalente vaste vleugel ontwerp, terwijl dezelfde maximale vliegduur behaald wordt op lage snelheid, wat de voordelen illustreert van het integreren van *morphing* mechanismen op een UAV en daarnaast de voordelen laat zien van de gepresenteerde twee-staps *morphing* ontwerpmethode. Daarnaast zijn de bijbehorende vleugelontwerpen gebruikt om de invloed van de volgorde waarin verschillende *morphing* manoeuvres uitgevoerd worden en de vliegcondities waarop deze manoeuvres uitgevoerd worden op de aandrijfvereisten voor *morphing* te bepalen. Hierbij zijn verschillen tot één ordegrootte gevonden. De resultaten laten zien dat er een afweging gemaakt moet worden op systeemniveau om de optimale *morphing* vliegconditie en volgorde te vinden voor een gegeven verandering van configuratie. Dit illustreert dat de uitdaging van het ontwerpen van een *morphing* vliegtuig niet stopt bij het ontwerpen van de *morphing* mechanismen en dat een benadering op systeemniveau noodzakelijk is, waarbij de vliegconditie en *morphing* volgorde een integraal onderdeel zijn van het ontwerpproces.

De geoptimaliseerde vleugelontwerpen voor de CRM laten duidelijk het voordeel van *aeroelastic tailoring* zien ten opzichte van conventionele composieten vleugelontwerpmethodieken met als resultaat efficiëntere vleugelontwerpen met gewichtsverminderingen tot 37% binnen de randvoorwaarden van het gepresenteerde raamwerk. Verder onderzoek is echter noodzakelijk voordat definitieve conclusies getrokken kunnen worden. Rolroereffectiviteit, aeroëlastische stabiliteit, overtrekken van de vleugel, paneelknik en het Tsai-Wu bezwijkcriterium zijn geïntroduceerd als randvoorwaarden in de optimalisaties. Daarnaast blijven de aerodynamische prestaties in kruisvlucht behouden door randvoorwaarden te zetten op de twistverdeling in kruisvlucht en de maltwistverdeling te introduceren als ontwerpparameter, terwijl gebruik gemaakt wordt van *aeroelastic tailoring* buiten de kruisvluchtcondities.

Om een eerste inschatting te maken van de invloed van discrete windstoten en de integratie van dynamische belastinggevallen in de optimalisaties te demonstreren, zijn een aantal vleugels geoptimaliseerd onder een combinatie van manoeuvre- en windstootbelastingen. Hoewel verder onderzoek, waarin de invloed van de vliegdynamica op de windstootbelastingen wordt meegenomen, noodzakelijk is voordat definitieve conclusies getrokken kunnen worden, tonen de resultaten wel

aan dat de extra flexibiliteit van *aeroelastically tailored* vleugels ze gevoeliger maakt voor dynamische belastingen.

Verder tonen de optimalisaties aan dat de malvorm van de vleugels een van de belangrijkste parameters in het ontwerp van vleugelconstructies is; niet alleen voor optimale prestaties in kruisvlucht, maar, belangrijker, om de juiste ontwerpbelastingen te bepalen. Daarnaast leidt de toegenomen ontwerpvrijheid door *aeroelastic tailoring* ertoe dat de vleugels specifiek ontworpen worden voor de belastinggevallen en randvoorwaarden die meegenomen worden in het ontwerpproces. Hierdoor hebben *aeroelastically tailored* vleugelontwerpen lagere ontwerpmarges buiten de ontwerpcondities en wordt het selecteren van de juiste belastinggevallen en randvoorwaarden nog belangrijker.

Tot slot zijn *morphing* kleppen geïntroduceerd aan de achterrand van de CRM om de voordelen van het combineren van *aeroelastic tailoring* en *morphing* te onderzoeken. De bijbehorende geoptimaliseerde vleugelontwerpen zijn optimaal over een reeks vliegcondities waardoor gewichtsbesparingen tot 34% worden behaald ten opzichte van de geoptimaliseerde vleugelontwerpen zonder *morphing* kleppen. Dit laat duidelijk het potentieel zien van het combineren van *aeroelastic tailoring* en *morphing* om de prestaties van vliegtuigen te verhogen, hoewel verder onderzoek noodzakelijk is voordat definitieve conclusies getrokken kunnen worden.

Concluderend, zowel *aeroelastic tailoring* en *morphing* zijn succesvol toegepast op het ontwerp van de constructie van vliegtuigvleugels wat heeft geleid tot vleugelontwerpen die gebruik maken van het aeroëlastische gedrag van de vleugel met optimale prestaties in de kruisvlucht en significante verbeteringen buiten de kruisvlucht.

# ACADEMIC CONTRIBUTION OF THIS DISSERTATION

This dissertation presents a dynamic aeroelastic analysis and optimisation framework suitable for the design of aeroelastically tailored and morphing wings that is, on the one hand, sufficiently efficient to explore the design space, but, on the other hand, sufficiently comprehensive to account for all factors relevant in the structural design of aircraft wings. It allows for a quick assessment of the potential benefits of either aeroelastic tailoring or morphing, or a combination of both. The contributions of this dissertation can be split in three categories: modelling, experimental validation, and design.

## AEROELASTIC ANALYSIS AND OPTIMISATION FRAMEWORK

- A dynamic aeroelastic analysis and optimisation framework for the design of aeroelastically tailored and morphing wings has been introduced. The model extends the state-of-the-art by (i) including a comprehensive set of constraints (i.e. aileron effectiveness, static and dynamic aeroelastic stability, structural strength based on the Tsai-Wu failure criterion, panel buckling, and cruise performance), (ii) including the effect of non-structural masses and non-aerodynamic external forces, (iii) including the jig twist distribution as a design variable, and (iv) including a combination of static and dynamic loadcases. The optimised wing designs are obtained using a gradient-based optimiser for computational efficiency where the sensitivities of the aeroelastic responses with respect to the design variables are computed analytically.

- A novel continuous-time state-space formulation of the unsteady vortex lattice method has been introduced under the assumption of small perturbations with respect to the steady solution and a fixed wake shape. A continuous-time system is obtained by only discretising the governing advection equation for the transport of vorticity in the wake in space, while making no assumptions regarding the time derivatives.

- Morphing wings are optimised by a novel two-step approach for the modelling of morphing aircraft wings. The first step is concept-specific and is used to identify the different morphing mechanisms installed on the wing and their feasibility constraints. The second step is a generic morphing optimisation framework used to identify the optimal set of morphing parameters within the concept-specific bounds and to assess whether a feasible morphing solution can be found. The main advantage of this approach is that the morphing optimisation framework is suitable for any morphing wing design, while concept-specific limitations can still be accounted for.

### Experimental validation

- A series of structural tests and wind tunnel tests have been carried out on a quasi-isotropic wing and an aeroelastically tailored wing to provide validation data for aeroelastically tailored wings. Aerodynamic forces and moments and wing deformation have been measured.

### Application to wing structural design

- A next step in the optimisation of morphing wings by a system level optimisation of a morphing wing with a range of different morphing mechanisms including an assessment of the corresponding actuation and energy requirements.
- Investigation of the influence of the morphing flight condition and morphing sequence on the actuation requirements of a morphing manoeuvre, identifying both as key parameters in the design of morphing aircraft.
- A next step in the optimisation of aeroelastically tailored wings by optimising both the stiffness and thickness distribution of the wing including dynamic loadcases, relevant structural, aerodynamic, and aeroelastic constraints, and all relevant non-structural masses and non-aerodynamic forces. Furthermore, by matching a predefined cruise twist distribution and introducing the jig twist distribution as an additional design variable, aerodynamic performance in cruise is maintained, while taking advantage of aeroelastic tailoring in off-cruise conditions.
- Concurrent optimisation of the stiffness and thickness distribution of an aeroelastically tailored wing combined with morphing mechanisms, showing the potential benefits of combining passive and active aeroelastic solutions to optimise the performance of aircraft wings.

# NOMENCLATURE

## ROMAN SYMBOLS

| | | |
|---|---|---|
| $a$ | Speed of sound | m/s |
| $\mathbf{a}$ | Mode shape | |
| $A_{ij}$ | Aerodynamic influence coefficient | $\mathrm{N/m^2}$ |
| $\mathbf{A}$ | Laminate in-plane stiffness matrix | N/m |
| $\mathbf{A_{ss}}$ | State matrix | |
| $b$ | Reference half-chord | m |
| $\mathbf{B}$ | Laminate coupling stiffness matrix | N |
| $\mathbf{B_{ss}}$ | Input matrix | |
| $c$ | Chord | m |
| $\mathbf{c_0}$ | Chord vector | m |
| $C_D$ | Drag coefficient | - |
| $C_f$ | Skin friction coefficient | - |
| $C_l$ | Section lift coefficient | - |
| $C_L$ | Lift coefficient | - |
| $C_{L_\alpha}$ | Lift curve slope | 1/rad |
| $C_m$ | Section moment coefficient | - |
| $C_M$ | Moment coefficient | - |
| $C_p$ | Pressure coefficient | - |
| $\mathbf{C}$ | Timoshenko cross-sectional stiffness matrix | |
| $\mathbf{C_{ss}}$ | Output matrix | |
| $D$ | Diameter | m |
| $D$ | Drag | N |
| $\mathbf{D}$ | Laminate out-of-plane stiffness matrix | N m |
| $\mathbf{D_{ss}}$ | Feedthrough matrix | |
| $e$ | Shear centre location | - |
| $\mathbf{e_\Gamma}$ | Vector defining a vortex segment | m |
| $E$ | Morphing energy | N m |
| $E$ | Young's modulus | $\mathrm{N/m^2}$ |

| | | |
|---|---|---|
| $EA$ | Extensional stiffness | N |
| $EI$ | Bending stiffness | $\mathrm{N\,m^2}$ |
| $F$ | Force | N |
| $F_g$ | Flight profile alleviation factor | - |
| $\mathbf{F}$ | Force and moment vector | N, N m |
| $G$ | Shear stiffness | $\mathrm{N/m^2}$ |
| $GA_s$ | Shear resistance | N m |
| $GJ$ | Torsional stiffness | $\mathrm{N\,m^2}$ |
| $GJ_t$ | Torsional resistance | N m |
| $h$ | Plunge deformation | m |
| $h$ | Thickness | mm |
| $h_0$ | Plunge amplitude | m |
| $H$ | Half gust length | m |
| $I$ | Mass moment of inertia | $\mathrm{kg\,m^2}$ |
| $\mathbf{I}$ | Identity matrix | |
| $\mathbf{J}$ | Jacobian | |
| $k$ | Reduced frequency | - |
| $K$ | Bend-twist coupling | $\mathrm{N\,m^2}$ |
| $K$ | Form factor | - |
| $\mathbf{K}$ | Stiffness matrix | |
| $\mathbf{K_B}$ | Stiffness contribution of the numerical flux | |
| $L$ | Length | m |
| $L$ | Lift | N |
| $mA$ | Mass per unit length | kg/m |
| $\mathbf{mI}$ | Mass inertia tensor per unit length | $\mathrm{kg\,m^2/m}$ |
| $\mathbf{mQ}$ | Tensor of first mass moments per unit length | kg m/m |
| $M$ | Mach number | - |
| $M$ | Moment resultant | N m/m |
| $M$ | Moment | N m |
| $\mathbf{M}$ | Mass matrix | |
| $\mathbf{n}$ | Normal vector | |
| $N$ | Stress resultant | N/m |
| $\mathbf{N}$ | Force vector | N |
| $\mathbf{N_B}$ | Stiffness contribution of the numerical flux | |
| $p$ | Pressure | $\mathrm{N/m^2}$ |
| $p_{roll}$ | Roll rate | rad/s |
| $\mathbf{p}$ | Structural degrees of freedom | m, rad |
| $q_i$ | Internal beam degrees of freedom $\{i = 1, .., 8\}$ | m, rad |

| | | |
|---|---|---|
| $\mathbf{Q}$ | Reduced laminate stiffness matrix | $\mathrm{N/m^2}$ |
| $r$ | Inverse buckling factor | - |
| $\mathbf{r}$ | Camber morphing displacement | m |
| $\mathbf{r}$ | Position vector | m |
| $Re$ | Reynolds number | - |
| $\mathbf{R}$ | Residual | |
| $\mathbf{R}$ | Rotation matrix | - |
| $\mathbf{R}$ | Transformation matrix | - |
| $s$ | Distance | m |
| $s$ | Wing semispan | m |
| $S$ | Shear strength | $\mathrm{N/m^2}$ |
| $S$ | Surface area | $\mathrm{m^2}$ |
| $S$ | Surface description | |
| $t$ | Thickness | mm |
| $t$ | Time | s |
| $\mathbf{t}$ | Tangent vector | |
| $\mathcal{T}$ | Kinetic energy | N m |
| $\mathbf{T}$ | Transformation matrix | - |
| $\mathbf{T_s}$ | Transformation between the angular variations and the rotational pseudovector | - |
| $u$ | Elongation | m |
| $\mathbf{u}$ | Displacement vector | m |
| $\mathbf{u}$ | Input vector | |
| $\mathcal{U}$ | Strain energy | N m |
| $U_i$ | Material invariants | $\mathrm{N/m^2}$ |
| $v$ | Deflection | m |
| $\mathbf{v}$ | Velocity vector | m/s |
| $\mathcal{V}$ | Potential energy | N m |
| $\mathcal{V}$ | Virtual work | N m |
| $V$ | Velocity | m/s |
| $V$ | Volume | $\mathrm{m^3}$ |
| $V_f$ | Fibre volume fraction | - |
| $V_{i_\mathbf{A}}$ | Lamination parameters related to the in-plane stiffness | - |
| $V_{i_\mathbf{B}}$ | Lamination parameters related to the coupling stiffness | - |
| $V_{i_\mathbf{D}}$ | Lamination parameters related to the out-of-plane stiffness | - |
| $\mathbf{V}$ | Velocity vector | m/s |
| $w$ | Deflection | m |
| $w$ | Downwash | m/s |

| | | |
|---|---|---|
| $w$ | Test function | - |
| $W$ | Weight | N |
| $x$ | $x$-coordinate | m |
| $x$ | Distance | m |
| $\mathbf{x}$ | Position vector | m |
| $\mathbf{x}$ | State vector | |
| $X_c$ | Longitudinal compressive strength | $N/m^2$ |
| $X_t$ | Longitudinal tensile strength | $N/m^2$ |
| $y$ | $y$-coordinate | m |
| $\mathbf{y}$ | Output vector | |
| $Y_c$ | Transverse compressive strength | $N/m^2$ |
| $Y_t$ | Transverse tensile strength | $N/m^2$ |
| $z$ | $z$-coordinate | m |
| $Z_{mo}$ | Maximum operating altitude | m |

## Greek Symbols

| | | |
|---|---|---|
| $\alpha$ | Angle of attack | rad |
| $\gamma$ | Shear strain | - |
| $\gamma_{max}$ | Maximum principal shear strain | - |
| $\Gamma$ | Vortex strength | $m^2/s$ |
| $\mathbf{\Gamma_i}$ | Material invariant matrices | $N/m^2$ |
| $\epsilon$ | Direct strain | - |
| $\epsilon_{x_{max}}$ | Maximum principal strain | - |
| $\delta$ | Aileron deflection | rad |
| $\delta$ | Displacement | m |
| $\eta$ | Non-dimensional plate coordinate | - |
| $\eta_{ail}$ | Aileron effectiveness | - |
| $\vartheta$ | Spatial angular variations | rad |
| $\theta$ | Angle of attack induced by structural rotations | rad |
| $\theta$ | Beam bending angle | rad |
| $\theta$ | Ply angle | deg |
| $\theta_f$ | Fold morphing angle | rad |
| $\boldsymbol{\theta}$ | Total rotational pseudovector | rad |
| $\kappa$ | Curvature | 1/m |
| $\lambda$ | Morphing manoeuvre parameter | - |
| $\lambda$ | Taper ratio | - |
| $\Lambda$ | Sweep angle | deg |

| | | |
|---|---|---|
| $\nu$ | Poisson's ratio | - |
| $\xi$ | Non-dimensional beam coordinate | - |
| $\xi$ | Non-dimensional plate coordinate | - |
| $\rho$ | Density | $kg/m^3$ |
| $\sigma$ | Direct stress | $N/m^2$ |
| $\tau$ | Shear stress | $N/m^2$ |
| $\phi$ | Beam twist angle | rad |
| $\phi$ | Shape function | - |
| $\phi$ | Small disturbance velocity potential | $m^2/s$ |
| $\phi_t$ | Twist morphing angle | rad |
| $\psi$ | Beam bending angle | rad |
| $\psi$ | Shape function | - |
| $\psi_s$ | Shear morphing angle | rad |
| $\omega$ | Frequency | rad/s |
| $\Omega$ | Domain | |
| $\partial\Omega$ | Boundary of the domain | |

## SUB/SUPERSCRIPTS

| | |
|---|---|
| $\infty$ | Free stream conditions |
| 0 | Midplane |
| 0 | Undeformed |
| 1 | Aligned with the beam axis |
| 1 | Aligned with the fibre direction |
| 2 | Perpendicular to the beam axis |
| 2 | Perpendicular to the fibre direction |
| 3 | Perpendicular to the beam axis |
| $\delta$ | Aileron deflection |
| $\theta_f$ | Fold |
| $\phi_t$ | Twist |
| $\psi_s$ | Shear |
| a | Aerodynamic |
| ail | Aileron |
| asym | Anti-symmetric |
| AS | Aerodynamic to structural |
| b | Wing surface |
| c | Camber |
| c | Collocation point |

| | |
|---|---|
| ds | Design gust |
| e | Eccentric |
| e | Element |
| ec | Eccentric |
| el | Elastic |
| exp | Exposed |
| ext | External |
| f | Flexural |
| g | Defined in the global coordinate system |
| g | Gust |
| h | Interpolation function |
| i | At the internal nodes of an element |
| i | Induced |
| ini | Initial |
| l | At the end nodes of an element |
| l | Defined in the local coordinate system |
| m | Membrane |
| mac | Mean aerodynamic chord |
| p | Parasitic |
| p | Roll rate |
| ref | Reference |
| s | Structural |
| st | Steady |
| sym | Symmetric |
| unst | Unsteady |
| w | Wake |
| $w_0$ | First row of wake elements |
| wet | Wetted |
| x | Along the $x$-direction |
| y | Along the $y$-direction |
| z | Along the $z$-direction |

## Abbreviations

| | |
|---|---|
| AICs | Aerodynamic influence coefficients |
| CFD | Computational fluid dynamics |
| CLT | Classical lamination theory |
| CRM | Common Research Model |

| | |
|---|---|
| DIC | Digital image correlation |
| DLM | Doublet lattice method |
| EPP | Expanded polypropylene |
| EU | European Union |
| FEM | Finite element method |
| FP7 | Seventh framework programme |
| HALE | High altitude, long endurance |
| LC | Loadcase |
| LE | Leading edge |
| OMTS | Optical marker tracking system |
| QI | Quasi-isotropic |
| RFA | Rational function approximation |
| TE | Trailing edge |
| UAV | Unmanned aerial vehicle |
| UD | Uni-directional |
| UVLM | Unsteady vortex lattice method |

# CONTENTS

*Dimidium facti, qui coepit, habet; sapere aude, incipe.*
*He who has begun is half done; dare to know; begin.*
**Quintus Horatius Flaccus, 20 BC**

# 1 INTRODUCTION

Over the past century, air traffic has shown consistent growth and there are no signs that this growth will decay any time soon. In Flightpath 2050 (European Commission, 2011), the European Union, for example, set out a vision in which they predict an annual growth of 4% to 5%, doubling air traffic in the coming 20 years. If aircraft remain unchanged, this growth in air traffic will be accompanied by an equivalent increased impact on the environment, e.g. increased emissions or noise pollution. With increasing environmental awareness and global warming, in present day society, an increased environmental impact is undesired; however, the increasing air traffic will still have to be accommodated.

In order to accommodate this growth, whilst reducing the impact on the environment, air traffic, and more specifically aircraft, will have to become more efficient and air traffic in 2050 will look very different than that of today. In line with the predicted growth and the desired reduction of the environmental impact of aircraft, the European Union therefore set a number of goals for air traffic in 2050: a 75% reduction in CO2 emissions per passenger kilometer, a 90% reduction in NOx emissions, and a reduction in perceived noise of 65% with respect to typical new aircraft in 2000. In order to achieve these goals, new technologies and procedures will have to be developed for the aircraft of the future.

As a result of the targets set for the aircraft of the future, operational efficiency is becoming more and more important in the design of aircraft. Over the years, researchers have focused on different areas of aircraft design in order to increase

the operational efficiency of aircraft in an attempt to meet the targets. One of the aims of this research is to increase operational efficiency by designing new aircraft wings that incorporate novel technologies.

A possible approach to increase the operational efficiency of aircraft wings is the use of either passive or active aeroelastic solutions to improve aerodynamic performance and decrease wing weight. Both aim at improving efficiency by taking advantage of the interaction between aerodynamic flow around the wing and the structural deformations of the wing to, for example, reduce the loads on the structure or decrease the aerodynamic drag. Passive aeroelastic solutions typically use the bend-twist coupling of the wing to obtain a favourable twist distribution under aerodynamic loads, while active aeroelastic solutions actively change the wing shape to affect the aerodynamic loads.

## 1.1 AEROELASTIC TAILORING AND MORPHING

One of the promising passive aeroelastic solutions is the use of the directional stiffness properties of composite materials in a wing structural design to control the aeroelastic deformations of the wing in a beneficial way, the so-called aeroelastic tailoring. In contrast to metals, composite materials allow for different stiffness properties in different directions, due to their anisotropic material properties. This property can be used to tailor the bend-twist coupling of wings, thus allowing for a favourable, tailored load distribution over the wing, which can both improve the aerodynamic performance of the wing and lead to a lighter wing design.

Aeroelastic tailoring was first introduced by Munk (1949) in a patent that proposes a propeller design using the anisotropic material properties of wood to tailor the aeroelastic deformations of the propeller. Following the patent by Munk, over the past decades, substantial research has been carried out in the field of aeroelastic tailoring and aeroelastic tailoring has been applied to aircraft wings in various forms. However, new modelling approaches are required that: (i) include tailoring of the complete wingbox structure, (ii) include both static and dynamic stability effects and load cases, (iii) include variable stiffness and variable thickness, (iv) include all relevant non-structural masses and non-aerodynamic (follower) forces, and (v) allow for a variable jig shape, such that aeroelastic tailoring can be applied to realistic aircraft wings.

A possible solution for active aeroelastic tailoring is the use of morphing mechanisms, such that the wing can be optimised for several different flight phases with conflicting requirements by changing its shape when transitioning from one phase to another. Current aircraft wings are typically designed having discrete high lift devices as a compromise for the missions they fly, performing sub-optimally at

most individual flight phases. In contrast to conventional flaps and slats, morphing structures typically aim for a smooth aerodynamic surface for optimal aerodynamic performance in cruise, while still allowing for significant shape changes during flight to accommodate other flight phases. Therefore, these mechanisms can be used to optimise a wing such that it performs optimally in all flight conditions.



Morphing aircraft have existed since the very dawn of powered flight in 1903 with the Wright Flyer that used a twisting wing for roll control. The increasing demand for extra payload and higher cruise speeds led to a demand for a stiffer wing structure, making it difficult to morph the wing depending on the mission profile. Over the years, many different morphing concepts have been proposed to implement morphing on present aircraft, while the aeroelastic modelling and optimising of generic morphing wings has received little attention. Therefore, as stated by De Breuker et al. (2011),

> *there seems to be a lack of a transparent way to discretize the morphing aircraft for shape optimization in a way that results in a sufficient low amount of design variables for quick sizing, while not constraining the design space a priori.*

Even though the work by De Breuker et al. (2011) provides a first step to a generic design framework for morphing aircraft wings, their work only investigated global morphing using sweep, fold, and twist. In order to make the framework suitable for the analysis of any generic morphing aircraft wing, improvements are required that include camber and span morphing to incorporate all common morphing mechanisms.

## 1.2 Research question

In order to take full advantage of aeroelastic tailoring and morphing, modelling approaches for both technologies should be combined and extended to realistic aircraft wings, such that the potential benefits of aeroelastic tailoring and morphing can be assessed. Therefore, the main research question that provides the basis for this dissertation is:

> *Can advanced composite and morphing technologies be used in the design of aircraft to minimise structural weight and improve aerodynamic performance, making use of the aeroelastic characteristics of the wing?*

In order to answer this question, this dissertation presents a modelling framework focusing on the preliminary design of aircraft wings that is suitable for design

optimisation and allows for a quick assessment of the potential benefits of either one of these technologies or a combination of both. Novel modelling approaches to the design of aircraft wings are introduced such that composite and morphing technologies can be used to improve their operational efficiency by making use of the aeroelastic characteristics of the wing.



## 1.3 METHODOLOGY AND DISSERTATION OUTLINE

The contributions of this dissertation can be split in three categories: modelling, experimental validation, and design. Reflecting these three categories, this dissertation is split in three parts, each consisting of several chapters. An overview of this outline is given in Figure 1.1.

Before discussing the contributions of this dissertation, Chapter 2 gives an overview of the literature on aeroelastic tailoring and morphing, illustrating the evolution to the state of the art and the resulting choices that have been made for this dissertation to advance the state of the art.

Part I extends the state of the art by introducing an aeroelastic analysis and optimisation framework that incorporates both aeroelastic tailoring and morphing. Since the framework should be suitable for preliminary design, one of the key requirements of the framework is computational efficiency. Introducing morphing and aeroelastic tailoring expands the design space of aircraft wings, so in order to explore this design space efficiently, the analysis framework is embedded in an optimisation loop that uses a gradient-based optimiser for efficiency.

Chapter 3 discusses the structural model where, for this purpose, the three-dimensional wing geometry is split in several spanwise sections, each having its own composite laminate distribution throughout the cross-section to allow for variable stiffness aeroelastic tailoring. A geometrically nonlinear beam model is obtained by embedding linear Timoshenko beam elements in a co-rotational formulation. The nonlinear structural stiffness matrix, obtained from the static analysis, is linearised and together with the structural mass matrix, the dynamic structural equations of motion are obtained.

The aerodynamic model is discussed in Chapter 4 and consists of a separate steady and unsteady aerodynamic model that are both based on small disturbance potential flow theory. Both models use a thin wing approximation, where the three-dimensional wing geometry is modelled using its two-dimensional camber surface. The steady aerodynamic model uses the vortex lattice method. The unsteady aerodynamic model is a novel continuous-time state-space implementation of the unsteady vortex lattice method that is directly written in time domain and allows for easy integration with a structural or flight dynamic model.

To conclude Part I, Chapter 5 discusses the aeroelastic coupling of the structural and aerodynamic models and the implementation of morphing in the aeroelastic solution. The static aeroelastic model is closely coupled and the geometrically nonlinear static aeroelastic equilibrium is obtained using a Newton-Raphson iteration scheme. In order to obtain the dynamic aeroelastic solution, for efficiency, a linearised simulation is carried out around the nonlinear static equilibrium solution. The structural and aerodynamic models are monolithically coupled in a single continuous-time state-space system that allows for aeroelastic stability analysis and time domain simulations of e.g. gusts. Morphing is integrated in both the static and dynamic aeroelastic model and, in order to assess the potential benefits of morphing, the actuation forces and energy required for morphing are estimated by computing the quasi-steady loads acting on the wing and the corresponding work done by these loads during a morphing manoeuvre.



Part II presents a set of experiments used for experimental validation of the aeroelastic tailoring framework. Three wings have been manufactured: a quasi-isotropic wing to act as a reference wing and two aeroelastically tailored wings for validation. Structural tests and steady wind tunnel tests were carried out for each of the wings, providing aerodynamic loads and structural deformations for experimental validation of the aeroelastic framework, as presented in Chapter 6.

Finally, the aeroelastic analysis and optimisation framework is applied to several wing design studies in Part III. Chapter 7 presents an example of the optimisation of a morphing wing, where several morphing mechanisms are integrated into a single UAV wing to illustrate the potential benefits of morphing over conventional wing designs. Furthermore, the influence of the flight condition and the sequence of morphing manoeuvres on the required actuation forces and moments for morphing are investigated.

In order to illustrate the potential benefits of aeroelastic tailoring, Chapter 8 presents the optimisation of the wing structure of the NASA Common Research Model under a combination of static and dynamic load cases, including structural, aerodynamic, and aeroelastic constraints. As a final design study, aeroelastic tailoring and morphing are combined in a single wing design to provide a preliminary assessment of the potential benefits of combining both technologies.

In conclusion, Chapter 9 presents a summary of the conclusions drawn throughout the dissertation and presents a list of recommendations for future research and further development of the aeroelastic framework.

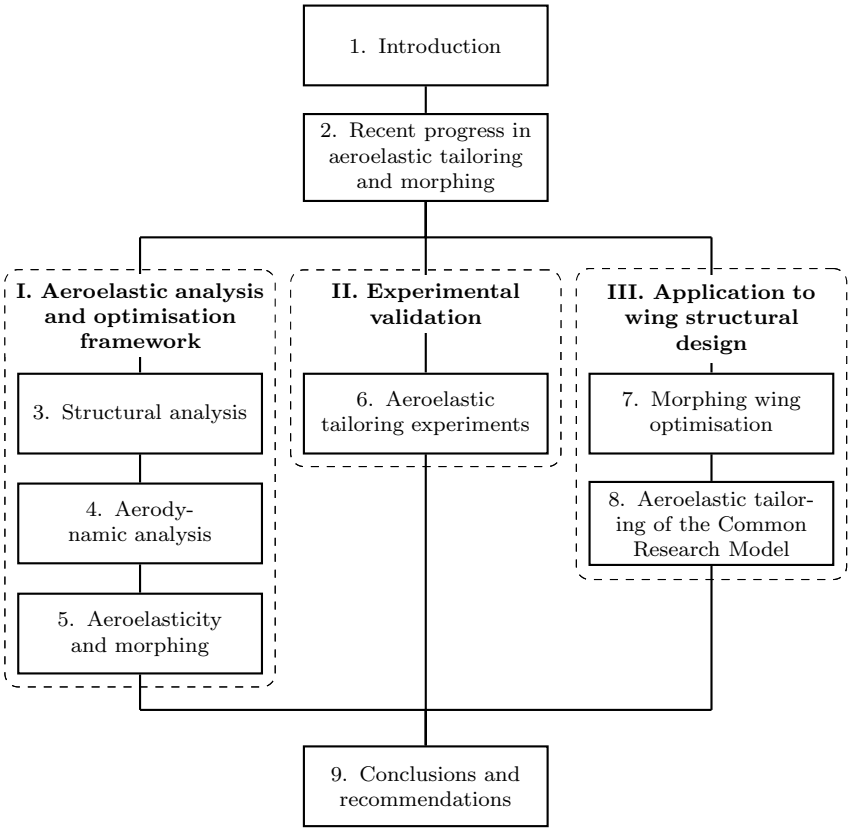


**Figure 1.1:** Dissertation outline.

*Those who cannot remember the past are condemned to repeat it.*
**George Santayana, 1905**

# 2

# Recent progress in aeroelastic tailoring and morphing

Motivated by the potential benefits of aeroelastic tailoring and morphing outlined in the introduction in Chapter 1, substantial research has been carried out in the field of both aeroelastic tailoring and morphing. This chapter provides an overview of the evolution of this research to the state of the art, identifies any shortcomings, and presents the choices made for this dissertation to mitigate some of these.

This chapter is divided into four sections. First, an overview of the research in aeroelastic tailoring and morphing is given in Sections 2.1 and 2.2, respectively. Following this overview of aeroelastic tailoring and morphing separately, Section 2.3 discusses possibilities for combined benefits of both technologies, followed by a synopsis in Section 2.4.

## 2.1 Aeroelastic tailoring

Driven by a need to improve the efficiency of aircraft and reduce the fuel consumption, composite materials are applied extensively in the design of aircraft. In addition to a high specific strength and stiffness, they also offer the designer the freedom to tailor the stiffness in desirable directions. One of the potential applications of this directional stiffness is aeroelastic tailoring, defined by Shirk

et al. (1986) as:

> *the embodiment of directional stiffness into an aircraft structural design to control aeroelastic deformation, static or dynamic, in such a fashion as to affect the aerodynamic and structural performance of that aircraft in a beneficial way.*



It should be noted that, although the focus of this dissertation is on the use of composite materials for aeroelastic tailoring because of their excellent structural properties, aeroelastic tailoring is not limited to the use of composite materials and can, for example, also be achieved by varying the stringer orientation, varying the rib orientation, using functionally graded materials, or using non-conventional structural layouts. For more information on the use of these mechanisms for aeroelastic tailoring, the reader is referred to Jutte and Stanford (2014), who give an excellent overview of recent research in the field of aeroelastic tailoring.

This section is spit in two parts: first an overview of the state of the art in aeroelastic tailoring will be given, followed by the choices made for this dissertation based on the state of the art.

### 2.1.1 LITERATURE OVERVIEW

Aeroelastic tailoring was first used by Munk (1949) in a patent describing the use of the directional stiffness properties of wood for a fixed pitch propeller to tailor the twist distribution of the propeller favorably as the thrust changes. With the introduction of fibre reinforced materials, aeroelastic tailoring gained more popularity in the 1970s and 1980s, resulting in several research programs in the USA investigating the potential benefits of aeroelastic tailoring. Hertz et al. (1981), Shirk et al. (1986), and Weisshaar (1987) provide extensive summaries of this early research into aeroelastic tailoring that resulted in the identification of a range of potential benefits of aeroelastic tailoring, as summarised in Figure 2.1.

As can be seen, typically a distinction is made between wash-in and wash-out aeroelastic tailoring. In case of wash-in, the bend-twist coupling of the wing is tailored such that upon bending the wing upwards a nose-up twist is induced, thus increasing the angle of attack, while, in case of wash-out, the bend-twist coupling of the wing is tailored such that a nose-down twist is induced, thus decreasing the angle of attack. Figure 2.1 also shows that a trade-off needs to be made between wash-in and wash-out aeroelastic tailoring depending on the critical design drivers for the wing design considered. A divergence critical wing would, for example, benefit from wash-out aeroelastic tailoring, while a flutter critical wing would benefit from wash-in aeroelastic tailoring. An important conclusion that can be drawn from this is that, as already recognised by Weisshaar (1987):

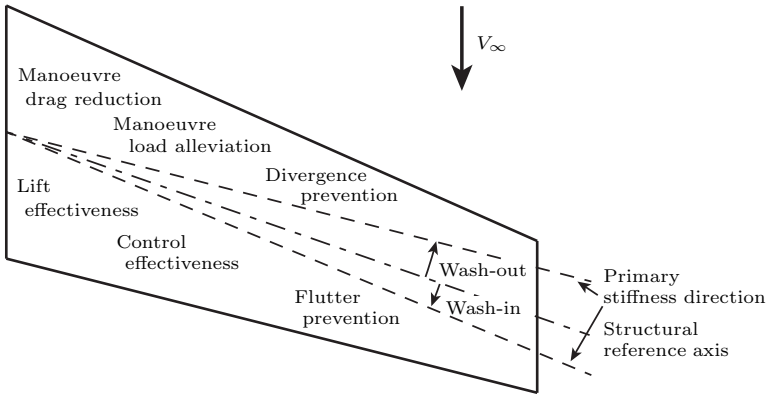


**Figure 2.1:** Potential benefits of aeroelastic tailoring. (Adapted from: Weisshaar (1987))



> *tailoring is not a "fix" for a problem, but instead is effective only when used in the preliminary design phase.*

Another important parameter to consider, which tends to be forgotten in present research, is the jig shape[1] of the wing and its influence on the potential benefits of aeroelastic tailoring, as already identified by Gimmestad (1979). Without considering the jig shape in the design of aeroelastically tailored wings, the full potential of aeroelastic tailoring cannot be harvested, while simultaneously ensuring optimal aircraft performance under normal operating conditions by maintaining an optimised 1g cruise shape. Furthermore, changing the initial wing twist changes the spanwise lift distribution, so starting from an incorrect jig shape will result in incorrect design loads.

More recently, Librescu and his co-workers (Gern and Librescu, 2000; Librescu and Khdeir, 1988; Librescu and Simovich, 1988; Librescu and Song, 1992; Librescu and Thangjitham, 1991; Qin et al., 2002) focused on the development of thin-walled aeroelastic beam models for composite wings to investigate the importance of non-classical effects, namely the warping restraint at the wing root and the effect of transverse shear effects, on the aeroelastic response of swept and unswept wings, with and without external stores. They concluded that depending on the ply angle and aspect ratio of the wing, both transverse shear effects and the warping restraint at the wing root can have a significant influence on the aeroelastic response of the wing and are effects that should be included in the aeroelastic analysis of composite wings. Furthermore, they concluded that the presence of external stores on a wing significantly influences the effect of aeroelastic tailoring on the flutter speed of a wing, and should, therefore, be included in the aeroelastic analysis of aeroelastically tailored wings. Cesnik et al. (1996) were the first to

[1] undeformed wing shape

investigate the effect of geometric nonlinearity on the aeroelastic response of composite wings by comparing the aeroelastic response obtained using a geometrically exact nonlinear beam model to a linear beam model, showing significant changes in wing lift and divergence speed as the velocity, and thus the wing deflection, increases.

Starting from the late 1990s, research into aeroelastic tailoring started to focus on laminates with different fibre angles through the thickness instead of investigating the potential of aeroelastic tailoring using a single fibre angle. When looking at the parametrisation of laminates for aeroelastic tailoring, a distinction can be made between (i) laminates with a fixed thickness, but varying fibre angles, (ii) laminates with a fixed set of discrete ply angles, but potentially varying thickness, and (iii) laminates with both varying fibre angles and varying thickness.



Starting with the first parametrisation, substantial research has been done using laminates with a fixed thickness and a fixed number of plies, but varying the ply angles, to investigate the use of aeroelastic tailoring to maximise the aeroelastic stability speed by means of evolutionary algorithms (Georgiou et al., 2014; Manan et al., 2010) or gradient-based optimisers (Guo, 2007; Guo et al., 2003, 2006). A similar form of aeroelastic tailoring has also been applied outside aerospace by Thuwis et al. (2009) to optimise the rear wing of a Formula 1 car for minimum induced drag, while maintaining sufficient downforce in the turns. The stiffness distribution of the laminates in the rear wing is modelled using the in-plane lamination parameters and the wing is optimised using Design Explorer as an optimiser.

More recently, Haddadpour and Zamani (2012), Stodieck et al. (2013), and Stanford et al. (2014) investigated the effect of fibre steering on the flutter and divergence speed of composite plate wings (Stodieck et al. (2013) and Stanford et al. (2014)) and wings with a closed thin-walled cross-section (Haddadpour and Zamani (2012)) by allowing for a varying fibre angle across the span of the wing. Both studies show significant improvements in flutter and divergence speed of steered fibre wings compared to straight fibre wings, clearly illustrating the benefits of varying the wing stiffness along the span of the wing by means of aeroelastic tailoring.

Secondly, substantial research has been done on laminates with a fixed set of discrete ply angles[2] in order to comply with certification requirements and reduce the number of design variables: (i) to minimise the laminate thickness along the chord and span of the wing under strength, buckling, and aileron effectiveness constraints for various orientations of the 0 deg axis, while varying the percentages of the different ply angles in the final stacking sequence (Eastep et al., 1999), (ii) to maximise the bending stiffness of a wing for a fixed number of plies by selecting the ply angles of each ply from a fixed set of ply angles in order to improve the

[2] 0 deg, 45 deg, −45 deg, and 90 deg

gust response of the wing (Kim and Hwang, 2005), (iii) to minimise the thickness of each ply angle separately under divergence and flutter constraints to investigate the performance of different optimisers (Tian et al., 2016), and (iv) to minimise the weight of a forward swept wing under divergence, stall, and strength constraints by finding the optimum number of plies in each discrete ply direction (Bach et al., 2017).

Within this second category using laminates with a fixed set of discrete ply angles, substantial research has also been done by the group of dr. Martins at the University of Michigan. In contrast to other works on aeroelastic tailoring that use strip theory or panel methods as their aerodynamic models, Martins focuses on high-fidelity aeroelastic analysis and optimisation using a gradient-based optimiser by coupling shell-based finite element models to CFD aerodynamics. Most of their work (Kennedy and Martins, 2014; Kenway et al., 2014; Kenway and Martins, 2014; Lambe and Martins, 2015; Liem et al., 2015) focuses on the material thickness and aerodynamic shape optimisation of isotropic wings under stress and buckling constraints to minimise the fuel burn of an aircraft during operation, while including manoeuvre load conditions for structural sizing. The results show significant reductions in fuel consumption and aircraft weight through combined aerodynamic and structural optimisation. Another conclusion that can be drawn from Kenway et al. (2014) is that for flexible aeroelastically optimised wings, the critical design loads are not necessarily governed by the manoeuvre load conditions, but also by discrete gust conditions resulting in a violation of both stress and buckling constraints for the manoeuvre load optimised wings. In their recent work, Brooks et al. (2016) investigated the use of fibre steered composites to minimise the fuel burn of a passenger aircraft by rotating a laminate, containing a fixed percentage of 0 deg, $\pm 45$ deg, and 90 deg plies, along the wing span and optimise its thickness distribution. Their results show a further decrease in fuel burn of 1% and a reduction in weight of 13% compared to an equivalently optimised wing with straight fibres, also clearly showing the benefits of varying the stiffness along the span of the wing for aeroelastic tailoring.

Similar conclusions are drawn by Stanford and Jutte (Jutte et al., 2014; Stanford and Jutte, 2016; Stanford et al., 2016) who investigated several different technologies for aeroelastic tailoring[3] to minimise the wing structural weight under strength, buckling, aileron effectiveness, and flutter constraints.

Finally, several studies have also been done on aeroelastic tailoring, where both the ply angles and thicknesses are allowed to vary freely. De Leon et al. (2012) investigated the effect of varying the fibre angle both in chordwise and spanwise direction of a four-ply symmetric flat plate wing to maximise the flutter speed of the wing, followed by a topology optimisation of the outer plies to minimise the

[3]isotropic thickness variation, functionally graded materials, balanced and unbalanced straight fibre laminates, balanced and unbalanced steered fibre laminates, curved stringers, and distributed control surfaces

mass of the wing under a flutter constraint.

In contrast to working with ply angles directly, other studies on variable ply angles and thickness have focused on the use of lamination parameters to set up the aeroelastic optimisation. Lamination parameters provide a continuous description of any composite laminate with a fixed number of design variables making them especially suitable for gradient-based optimisation. Kameyama and Fukunaga (2007) were the first to use lamination parameters for aeroelastic tailoring to optimise both the thickness and stiffness distribution of the laminates using a genetic algorithm. They investigated the optimum lamination parameter and thickness distribution for a flat plate wing with varying sweep angles for minimum weight under flutter and divergence constraints, clearly showing the effectiveness of aeroelastic tailoring to optimise the aeroelastic response. A similar approach is used by Jin et al. (2016) to minimise the weight of a composite sandwich panel plate wing, where the faces are modelled using lamination parameters and the thickness of the core is introduced as additional design variable.



Dillinger et al. (2013) were the first to extend the use of lamination parameters to the design of a wingbox structure and use a gradient-based optimiser to find the optimum thickness and lamination parameter distribution. They used a series of constant stiffness chordwise and spanwise patches to minimise the weight of the wing or maximise the aileron effectiveness of the wing under strength, buckling, and divergence speed constraints by optimising the stiffness and thickness in each of the patches.

The framework described in this dissertation also falls in this third category, where both the ply angles and the thickness distribution of the laminates in the wing are varied freely. It has also been used by Macquart et al. (2017) to investigate the effect of introducing blending constraints in the lamination parameter domain on the stacking sequence retrieval process once the optimum lamination parameter distribution and thickness distribution have been found. Their results show that for a straight fibre wing design, the use blending constraints greatly improves the matching quality between the optimised lamination parameters and the corresponding stacking sequences, resulting in an improved match in the corresponding aeroelastic response.

To conclude this literature overview of aeroelastic tailoring using composites, it should be noted that aeroelastic tailoring is not unique to aircraft and is also gaining popularity in wind turbines to improve the performance of wind turbine blades and alleviate loads (see, for example, Hayat and Ha (2015), Capuzzi et al. (2015), and Scott et al. (2016)).

### 2.1.2 CHOICES FOR THIS DISSERTATION

As can be concluded from the literature overview, substantial research in various aspects of aeroelastic tailoring has been done. However, as also concluded by Jutte and Stanford (2014), there is a need for models that can design a high performance, light weight wing that account for all relevant factors encountered in flight. Many of the present studies either simplify the problem significantly (e.g. by modelling the wing as a plate or with a simplified rectangular or elliptic wingbox structure) or ignore important constraints (e.g. control effectiveness, aeroelastic stability, strength, or buckling) that can have a significant impact on the resulting wing designs. In order to progress the state of the art in the field of aeroelastic tailoring, this dissertation describes an aeroelastic analysis and optimisation framework that can be seen as a next step towards a model that can incorporate all relevant factors encountered in flight in the preliminary design of aeroelastic tailored wings and provide insights in the potential benefits that can be achieved by aeroelastic tailoring for the structural design of wings. Therefore, based on the literature overview, the following requirements were selected for the aeroelastic analysis and optimisation framework:



- The jig twist of the wing should be included in the optimisation in order to ensure aircraft performance in cruise conditions, while still taking advantage of the benefits of aeroelastic tailoring. It is interesting to note that, except for the work by dr. Martins, who combines structural optimisation with aerodynamic shape optimisation, all studies described in the literature overview start from a predefined jig twist and therefore sacrifice performance in cruise conditions to take full advantage of the potential of aeroelastic tailoring. Furthermore, as also identified by Gimmestad (1979), changing the initial jig twist changes the spanwise lift distribution, so starting from an incorrect jig shape will result in incorrect design loads.
- All laminates should have free fibre angles and thickness and the stiffness of the wing should be allowed to vary in both chordwise and spanwise direction to fully harvest the potential benefits of aeroelastic tailoring and not limit the design space a priori.
- All relevant constraints should be included: (i) aeroelastic stability, (ii) strength, (iii) buckling, and (iv) aileron effectiveness.
- If necessary for the specific wing considered, the framework should be able to optimise the wing for both manoeuvre loads and gust loads.
- The complete wingbox structure including stringers and spars should be modelled.
- All relevant non-structural masses, such as the engine, main landing gear, leading edge and trailing edge masses, or fuel should be included.

- All relevant non-aerodynamic external forces, such as gravity and thrust, should be included.

## 2.2 MORPHING

The main advantage of morphing wings is that the wing can be optimised for several different flight phases with conflicting requirements by changing its shape when transitioning from one phase to another. The concept of morphing wings is not new and has been applied since the early ages of aviation. The Wright Flyer, the first heavier than air aircraft with an engine, enabled roll control by changing the twist of its wing using cables actuated directly by the pilot (Barbarino et al., 2011). The increasing demand for extra payload and higher cruise speeds led to a demand for a stiffer wing structure, making it difficult to morph the wing depending on the mission profile. Current aircraft wings are therefore designed as a compromise for the missions they fly, performing sub-optimal at most individual flight stages.



This section is spit in two parts: first an overview of the state of the art in modelling of morphing aircraft is given, followed by the choices made for this dissertation based on the state of the art.

### 2.2.1 LITERATURE OVERVIEW

Substantial research has been done on morphing aircraft in the past decades, as can also be concluded from the large amount of review papers on the topic (Barbarino et al., 2011, 2014; Dayyani et al., 2015; Gomez and Garcia, 2011; Kuder et al., 2013; Sun et al., 2016). In the 1980s, NASA launched two research programs dedicated to morphing structures with the Active Flexible Wing program (Perry et al., 1995) and its Mission Adaptive Wing program (Bonnema and Lokos, 1989). This research effort was followed by several research programs in the 1990s and 2000s in the USA, the Smart Materials and Structures Demonstration program (Sanders et al., 2004), the Aircraft Morphing program (McGowan et al., 2002), the Active Aeroelastic Wing program (Pendleton et al., 2000), and the Morphing Aircraft Structures program (Bowman et al., 2007; Weisshaar, 2006).

Parallel to the research done in the USA, the European Union (EU) has also funded several research programs since 2002, including the Active Aeroelastic Aircraft Structures (3AS) project (Schweiger et al., 2002), the Smart Aircraft Morphing Technologies (SMorph) project (Miller et al., 2010), the Smart Intelligent Aircraft Structures (SARISTU) project (Wölcken and Papadopoulos, 2016), the Novel Air Vehicle Configurations (NOVEMOR) project (Afonso et al., 2014; Cardoso et al., 2013; De Gaspari and Ricci, 2014, 2015) and the CHANGE project

(Ciarella et al., 2015).

Outside these major projects, several researchers have investigated modelling of morphing aircraft, focusing on the aeroelastic modelling of morphing aircraft or on the influence of morphing on the flight dynamics of an aircraft, showing that morphing is a truly multidisciplinary field.

Gern et al. (2002) developed a model for the aeroelastic analysis of camber and twist morphing wings coupling an equivalent plate structural model to a vortex lattice method aerodynamic model. They show that by incorporating twist and camber morphing instead of conventional, hinged control surfaces, the roll performance of an aircraft can be significantly improved. Webb and Subbarao (2006) developed a model for the analysis of a morphing wing with a variable airfoil geometry and telescopic span extension mechanism to investigate the influence of the cross-sectional geometry and varying wing span on the flutter speed of an aircraft using a typical section aeroelastic model. Selitrennik et al. (2012) used a structural model consisting of a superposition of large rigid-body motions and small elastic deformations coupled to a Euler/Navier-Stokes flow solver to analyse the aeroelastic response of a morphing vehicle that can rapidly change its span from zero span to full span.



A different approach is taken by Samareh et al. (2007) by developing a framework for the aeroelastic analysis of morphing aircraft that loosely couples existing analysis models instead of developing their own analysis models. Their goal is to reduce the setup time of these models for the analysis of morphing aircraft and allow for easier multidisciplinary analysis using medium- to high-fidelity models.

When looking at the effect of morphing on the flight dynamics of aircraft, several researchers have investigated the effect of morphing on the flight dynamic response of an aircraft, focusing on the different morphing configurations achieved in flight (Bowman et al., 2006; Niksch et al., 2009; Obradovic and Subbarao, 2011c; Reich et al., 2006). Furthermore, Shi and Peng (2015) focused on the effect of a transient morphing manoeuvre on the flight dynamic response of the aircraft comparing different control strategies during the morphing manoeuvre. Several studies have investigated the use of morphing for roll control of aircraft by means of antisymmetric span morphing (Beaverstock et al., 2014) or antisymmetric fold (dihedral) morphing (Cuji and Garcia, 2008) in contrast to conventional trailing edge mechanisms. Finally, Seigler et al. (2007) provide an overview of different flight control strategies tailored to morphing aircraft.

Next to the analysis of morphing aircraft, several researchers have also investigated the optimisation of morphing aircraft, which can be split in two main categories: (i) the optimisation of specific morphing concepts or mechanisms, constraining the design space a priori to reduce the number of design variables, and (ii) the generic optimisation of morphing aircraft without considering specific concepts.

In the first category, Gamboa et al. (2009) investigated the optimisation of the aerodynamic performance of morphing wings using a morphing concept capable of modifying the wing span, taper, and airfoil shape showing improved performance over a fixed wing design. Similar conclusions are drawn by Vale et al. (2011) for variable span with conformal camber morphing and by Körpe and Özgen (in press 2016) for combined planform and camber optimisation. Within the EU FP7 CHANGE project, a morphing framework (Ciarella et al., 2015) has been developed to find the optimum span and camber morphing configurations for the CHANGE wing in different flight conditions by means of design space exploration of the different morphing parameters.



Within this first category, substantial research has also been carried out in the field of leading edge and trailing edge morphing. This will, however, be treated separately in Section 2.3. Several studies have shown that similar to the previously mentioned morphing optimisations, leading edge and trailing edge morphing are also highly suitable to optimise the aerodynamic performance of aircraft.

In the second category of optimisation of morphing aircraft, special attention should be given to the work by Prof. Crossley and his co-workers (Crossley et al., 2011; Skillen and Crossley, 2007, 2008). Starting with Martin and Crossley (2002) and Roth and Crossley (2003), they developed a morphing optimisation framework that parametrises the baseline aircraft wing using the thrust-to-weight ratio, $T/W$, the wing surface area, $S$, the aspect ratio, $AR$, the thickness-to-chord ratio, $t/c$, the sweep angle, $\Lambda$, and the taper ratio, $\lambda$, while introducing morphing for each flight condition through an update of the wing span, $\Delta b$, the wing chord, $\Delta c$, and the wing sweep angle, $\Delta\Lambda$. More recently, the framework has been expanded with a parametric equation for wing weight estimation based on structural optimisation (Skillen and Crossley, 2008) and has been applied to the optimisation of morphing aircraft flying in formation (Frommer and Crossley, 2005, 2006). While the optimisation framework provides insights into the optimum wing shape for different flight conditions and gives some estimate of the resulting wing weight, the question remains whether a feasible wing structure can be found that can actually achieve these morphing shapes.

As can be concluded from the literature overview, substantial research into modelling and optimisation of morphing aircraft has been done, focusing on the development of morphing concepts for a specific aircraft or a specific mission, on the multidisciplinary, detailed analysis and optimisation of one specific concept or one specific type of morphing, or on the generic optimisation of morphing aircraft. However, as identified by De Breuker et al. (2011):

> *there seems to be a lack of a transparent way to discretize morphing aircraft for shape optimization in a way that results in a sufficiently low amount of design variables for quick sizing, while not constraining the design space a priori.*

For this reason, De Breuker et al. (2011) introduced a framework for the discretisation and optimisation of morphing aircraft with varying fold, shear, and twist morphing. The morphing analysis and optimisation framework described in this dissertation presents an extension of their work and introduces a two-step approach to the optimisation of morphing aircraft, which incorporates concept specific limitations in a generic morphing analysis and optimisation framework.

To conclude this literature overview on modelling of morphing aircraft, one important aspect of morphing aircraft which received little attention in the literature remains to be addressed: the actuation loads and energy required for morphing originating not only from the actual morphing mechanisms, but also from the external loads applied on the morphing aircraft. Studies that incorporate the actuation loads and energy required for morphing to a limited extend are: (i) Obradovic and Subbarao (2011a,b), who investigated the use of fold morphing during flight dynamic manoeuvres of a gull-wing aircraft, while imposing a constraint on the actuator moment and actuator power, (ii) Namgoong et al. (2007, 2012), who obtained a pareto front between potential drag reduction due to camber morphing and the required camber morphing energy, and (iii) De Breuker et al. (2011) and Werter et al. (2013), who investigated the actuation forces and energy requirements of morphing aircraft with varying fold, shear, and twist morphing, clearly illustrating the importance of actuation loads and energy for the design of morphing aircraft. Recently, De Breuker and Werter (2016) used the morphing analysis and optimisation framework described in this dissertation to further investigate the actuation loads and energy requirements of morphing aircraft by illustrating the importance of the flight condition and sequence of morphing manoeuvres on the actuation loads and energy.



### 2.2.2 Choices for this dissertation

As can be concluded from the literature overview, substantial research in various aspects of morphing aircraft modelling has been done. However, some important shortcomings in current models for morphing aircraft have been identified. In order to progress the state of the art in the field of morphing aircraft, this dissertation describes a morphing analysis and optimisation framework that can be seen as a first step towards a framework that incorporates all relevant morphing mechanisms, accounts for actuation forces and energy, while still maintaining a framework that is suitable for quick sizing without constraining the design space a priori. Therefore, based on the literature overview, the following requirements were selected for the morphing analysis and optimisation framework:

- All relevant morphing concepts should be incorporated: (i) shear/sweep morphing, (ii) twist morphing, (iii) fold morphing, (iv) camber morphing, and (v) span morphing.

- Actuation forces and actuation energy should be obtained.
- The framework should be suitable for morphing aircraft optimisation, incorporating concept specific limitations, while still being applicable to generic morphing aircraft.

Finally, using the work described in this dissertation, De Breuker and Werter (2016) illustrated the importance of the flight condition and the sequence in which different parts of the wing are morphed on the required actuation force and energy, which is something that, to the best of the author's knowledge, had not been addressed yet, while it is driving for the sizing of the actuation mechanism and ultimately the performance of the morphing mechanism.



## 2.3 COMBINED MORPHING AND AEROELASTIC TAILORING

As can be concluded from the previous sections, both aeroelastic tailoring and morphing potentially provide significant benefits to improve aircraft, which raises the question: can both benefits be combined in a single wing design? With recent advances of morphing technology, three promising morphing technologies have emerged with potential application to wings with a conventional wingbox structure[4]: (i) morphing leading edges to postpone stall during high-lift situations and improve the flow over the airfoil by removing gaps, (ii) morphing trailing edges for improved cruise performance and manoeuvre load alleviation, and (iii) morphing winglets for load alleviation and roll control. Given the limitations of the framework presented in this dissertation to straight, level flight without sideslip, which is one of the sizing loadcases of winglets, and to linear aerodynamics without stall, it was decided for this dissertation to combine aeroelastic tailoring with morphing trailing edge devices and investigate potential combined manoeuvre load alleviation benefits.

This section is spit into two parts: first an overview of the state of the art on the use of morphing trailing edge devices will be given, followed by the choices made for this dissertation based on the state of the art.

### 2.3.1 LITERATURE OVERVIEW

Szodruch and Hilbig (1988) and Bolonkin and Gilyard (1999) provide an initial overview of some of the benefits of variable wing camber[5], showing clear aerody-

[4] in order to maintain structural integrity, provide mounting locations for, for example, the engine and main landing gear, and provide space for fuel tanks.

[5] as introduced by, for example, leading edge or trailing edge devices.

namic benefits with respect to a fixed camber design. In order to take advantage of these benefits, the Airbus A350XWB already uses its trailing edge flaps to optimise the lift distribution during cruise flight and, furthermore, for load alleviation during manoeuvre conditions, which resulted in wing weight reduction of several hundred kilograms (Reckzeh, 2014). Recently, instead of using discrete trailing edge flaps, FlexSys (Kota, 1999, 2002; Kota and Hetrick, 2008) have developed a compliant trailing edge mechanism that has been mounted on a Gulfstream III to demonstrate the feasibility of compliant mechanisms on aircraft. Both examples show that, with current technology, the use of trailing edge flaps for optimised cruise performance and manoeuvre load alleviation is feasible.



When looking at the performance benefits of a morphing trailing edge, several researchers have investigated their aerodynamic benefits for: improved roll control (Sanders et al., 2003), fuel burn reduction (Burdette et al., 2016a; Diodati et al., 2013; Lyu and Martins, 2015; Wakayama and White, 2015), and improved off-design performance (Rodriguez et al., 2016). In order to take advantage of these benefits, NASA and Boeing introduced a joint research program focussing on the development of a Variable Camber Continuous Trailing Edge Flap (VCCTEF) (Urnes et al., 2013). Several studies were carried out to investigate the aerodynamic benefits of the VCCTEF in a high-lift configuration (Urnes et al., 2013), for improved roll control (Urnes et al., 2013), for reduced drag (Ferrier et al., 2016; Kaul and Nguyen, 2014; Urnes et al., 2013), and for load alleviation (Lebofsky et al., 2015), showing the potential of the VCCTEF. Similar conclusions have been drawn in the EU FP7 SARISTU project, in which several aspects of an adaptive trailing edge flap were investigated, tailored to the application on a regional jet: aerodynamic benefits (Carossa et al., 2016), actuation and control (Dimino et al., 2016), structural design (Pecora et al., 2016), and manufacturing and testing (Essa et al., 2016).

Special attention should be given to the work by Dr. Ricci and co-workers at the Politecnico di Milano. De Gaspari and Ricci (2011) developed a two-step approach for the optimum design of morphing compliant leading edges and trailing edges. The first step finds the optimum airfoil shape for both the leading edge and trailing edge and is followed by a second step to find the optimum internal compliant structure to meet these shapes. Following this initial work, the framework has been extended to 3D geometries (De Gaspari and Ricci, 2015), has been linked up to the aircraft conceptual design software, NeoCASS, also developed in Milan (Cavagna et al., 2013), and has been applied to a regional aircraft within the EU project NOVEMOR (De Gaspari and Ricci, 2014; De Gaspari et al., 2014, 2015). In contrast to this sequential approach, Molinari et al. (2011) investigated the combined aerostructural optimisation of a compliant trailing edge, showing further improved performance over a sequential aerodynamic-structural optimisation process.

Recently, morphing trailing edge devices have also gained interest in the field of

aerostructural optimisation of wingbox structures to optimise not only the wing aerodynamics, but also reduce the wing weight. Dr. Martins and co-workers (Burdette et al., 2015, 2016b) have shown in a number of studies significant weight reductions by using an adaptive morphing trailing edge for manoeuvre load alleviation. Similar conclusions have been drawn by Stanford et al. (2016), who used the VCCTEF for manoeuvre load alleviation in an aerostructural optimisation.

### 2.3.2 CHOICES FOR THIS DISSERTATION



As can be concluded from the literature overview, morphing trailing edge devices provide great potential for improved aircraft performance. The application on the A350XWB, the work by dr. Martins and co-workers, and the work by Stanford et al. (2016) have shown the potential of morphing trailing edge devices to reduce the weight of aircraft wings by means of manoeuvre load alleviation. However, to the best of the author's knowledge, no studies have been conducted yet on the potential combined benefits of aeroelastic tailoring and morphing trailing edge devices. Therefore, this dissertation aims to further progress the state of the art by combining the aeroelastic analysis and optimisation framework and the morphing framework to investigate the use of morphing trailing edge devices on an aeroelastically tailored wing and investigate potential combined benefits for manoeuvre load alleviation and consequently weight reduction.

## 2.4 SYNOPSIS

In this chapter, an overview of the state of the art in the fields of aeroelastic tailoring and morphing has been given and the choices made for this dissertation to improve the state of the art have been presented.

Substantial research has been carried out over the past decades in both morphing and aeroelastic tailoring. However, there seems to be a lack of models suitable for the design of aircraft wings that, on the one hand, are sufficiently efficient to explore the design space, but, on the other hand, are sufficiently comprehensive to account for all factors relevant in the design of aircraft wings.

Based on the literate overview on aeroelastic tailoring, the following requirements have been identified for the aeroelastic analysis and optimisation framework:

- The jig twist of the wing should be included in the optimisation in order to ensure aircraft performance in cruise conditions, while still taking advantage of the benefits of aeroelastic tailoring for, for example, manoeuvre load alleviation.

- All laminates should have free fibre angles and thickness and the stiffness of the wing should be allowed to vary in both chordwise and spanwise direction to fully harvest the potential benefits of aeroelastic tailoring and not limit the design a priori.
- All relevant constraints should be included: (i) aeroelastic stability, (ii) strength, (iii) buckling, and (iv) aileron effectiveness.
- If necessary for the specific wing considered, the framework should be able to optimise the wing for both manoeuvre loads and gust loads.
- The complete wingbox structure including stringers and spars should be modelled.
- All relevant non-structural masses, such as the engine, main landing gear, leading edge and trailing edge masses, or fuel should be included.



Based on the literature overview on morphing aircraft, the following requirements were identified for the morphing analysis and optimisation framework:

- All relevant morphing concepts should be incorporated: (i) shear/sweep morphing, (ii) twist morphing, (iii) fold morphing, (iv) camber morphing, and (v) span morphing.
- Actuation forces and actuation energy should be obtained.
- The framework should be suitable for morphing aircraft optimisation, incorporating concept specific limitations, while still being applicable to generic morphing aircraft.

Furthermore, the influence of the flight condition and the order in which different parts of the wing are morphed on the required actuation force and energy remains to be assessed, since it is driving for the sizing of the actuation mechanism and ultimately for the performance of the morphing mechanism.

Finally, in order to combine aeroelastic tailoring and morphing and assess potential combined benefits, the aeroelastic analysis and optimisation framework and the morphing framework will be combined to investigate the use of morphing trailing edge devices on an aeroelastically tailored wing.

# PART I

# AEROELASTIC ANALYSIS AND OPTIMISATION FRAMEWORK

*Engineering is the art of modelling materials we do not wholly understand, into shapes we cannot precisely analyse so as to withstand forces we cannot properly assess, in such a way that the public has no reason to suspect the extent of our ignorance.*

**Dr. A.R. Dykes, British Institution of Structural Engineers, 1976**

# 3

# STRUCTURAL ANALYSIS[1]

As outlined in the introduction to this dissertation, in order to assess the potential benefits of aeroelastic tailoring and morphing, an aeroelastic model that incorporates the effects of aeroelastic tailoring and morphing is required. Therefore, a structural model is required that can analyze a composite wing structure and accounts for large shape changes introduced by morphing, especially in case of morphing mechanisms that effect the global wing geometry.

With the introduction of composite materials and the drive to lighter wing structures, wings become increasingly flexible, leading to, for example, a 25% tip deflection of the Boeing 787 under ultimate loads.[2] Geometrically linear structural models no longer capture the response of these wings accurately and, therefore, a geometrically nonlinear structural model is required. Furthermore, large wing shape changes introduced by morphing have to be accounted for by means of a geometrically nonlinear aeroelastic model, requiring a geometrically nonlinear structural model, to accurately capture the influence of these shape changes on the aeroelastic response of the aircraft wing.

This chapter is split into ten sections. First, Section 3.1 outlines the modelling approach used to obtain the structural response, followed by Sections 3.2 to 3.7

[1] Part of this chapter is based on the journal paper Werter, N.P.M. and De Breuker, R. (2016). *"A novel dynamic aeroelastic framework for aeroelastic tailoring and structural optimisation"*, Composite Structures, vol. 158, pp. 369-386.

[2] Source: `http://boeing.mediaroom.com/2010-03-28-Boeing-Completes-Ultimate-Load-Wing-Test-on-787`, accessed on July 14, 2016

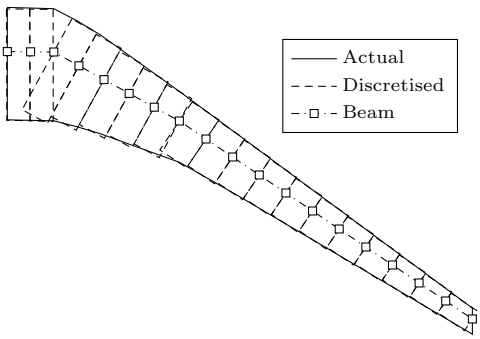


**Figure 3.1:** Schematic illustration of the discretised wingbox geometry versus the actual wingbox geometry.



discussing the different components of the model in detail. Finally, Section 3.8 presents the verification of the structural model, followed by a discussion of the limitations of the structural model in Section 3.9 and a synopsis in Section 3.10.

## 3.1 MODELLING APPROACH

The goal of the aeroelastic analysis and optimisation framework presented in this dissertation is to improve the conceptual design of aircraft wings by including aeroelasticity. Therefore, one of the key requirements of the framework is computational efficiency. For this purpose, the three-dimensional wing geometry is described by a one-dimensional structural model. First, the wing is split in several spanwise sections with a constant cross-sectional geometry. Varying geometry along the span is accounted for by modelling the wing using a sufficient number of sections, as illustrated in Figure 3.1. Each spanwise section can have its own composite laminate distribution throughout the wing cross-section to allow for aeroelastic tailoring along the span and throughout the cross-section.

The structural analysis module consists of four analysis components, as illustrated in Figure 3.2. First, the material properties and lamination parameters that describe the composite laminates in the structure are converted to the corresponding laminate properties, as introduced in Section 3.2.

In order to generate the beam model, these laminate properties, together with the cross-sectional geometry, are used to generate the Timoshenko cross-sectional stiffness matrix with respect to the beam reference axis, using the cross-sectional modeller developed by Ferede and Abdalla (2014). For completeness, a brief overview of this procedure will be given in Section 3.3.

As a third step, a geometrically nonlinear static analysis is carried out to obtain

the nonlinear static displacement field of the wing for the various load cases. The static model is a geometrically nonlinear Timoshenko beam model based on the co-rotational formulation, as developed by Battini and Pacoste (2002) and implemented by De Breuker (2011). In order to make this model suitable for the analysis of generic composite aircraft wings, in this dissertation the model is extended with the implementation of eccentric follower and non-follower forces to account for the effects of gravity and engine thrust, for example. A brief description of the original model, followed by a description of the implementation of eccentric forces, is given in Section 3.4.

As a final analysis step, the static structural model has been extended to a structural dynamics model, as presented in Section 3.5. The dynamic structural response is obtained by a linearised dynamic analysis around the nonlinear static equilibrium solution. The nonlinear structural stiffness matrix, obtained from the static analysis, is linearised and coupled to a linear mass matrix to obtain the structural dynamics model.



Finally, based on the static and dynamic response, the cross-sectional modeller is used to determine the three-dimensional wing strains to assess structural strength and a panel buckling analysis based on the work of Dillinger et al. (2013) is carried out to determine the buckling resistance of the wing, as presented in Sections 3.6 and 3.7, respectively.

## 3.2 Composites

Composites in the aerospace industry conventionally consist of several plies of unidirectional or woven fibres embedded in a polymer matrix stacked together in a stacking sequence to obtain the desired stiffness properties. Instead of analysing both components and each ply separately, fibre-matrix composites are commonly analysed using equivalent single layer properties in order to analyse structures build out of fibre-matrix composites efficiently. One of the methods commonly used to obtain the equivalent single layer properties from a stacking sequence is classical lamination theory (CLT), as presented in Section 3.2.1. Instead of describing a composite laminate by ply angles and a stacking sequence to obtain the stiffness properties, it can also be described as a function of lamination parameters, as introduced by Tsai and Pagano (1968) and presented in Section 3.2.2 for completeness. Lamination parameters provide a continuous parametrisation of the equivalent single layer properties, making them suitable for gradient-based optimisation. They will, therefore, serve as design variables in the aeroelastic optimisations. Finally, a method to visualise the stiffness properties of composite laminates is presented in Section 3.2.3 and will be used throughout this dissertation.

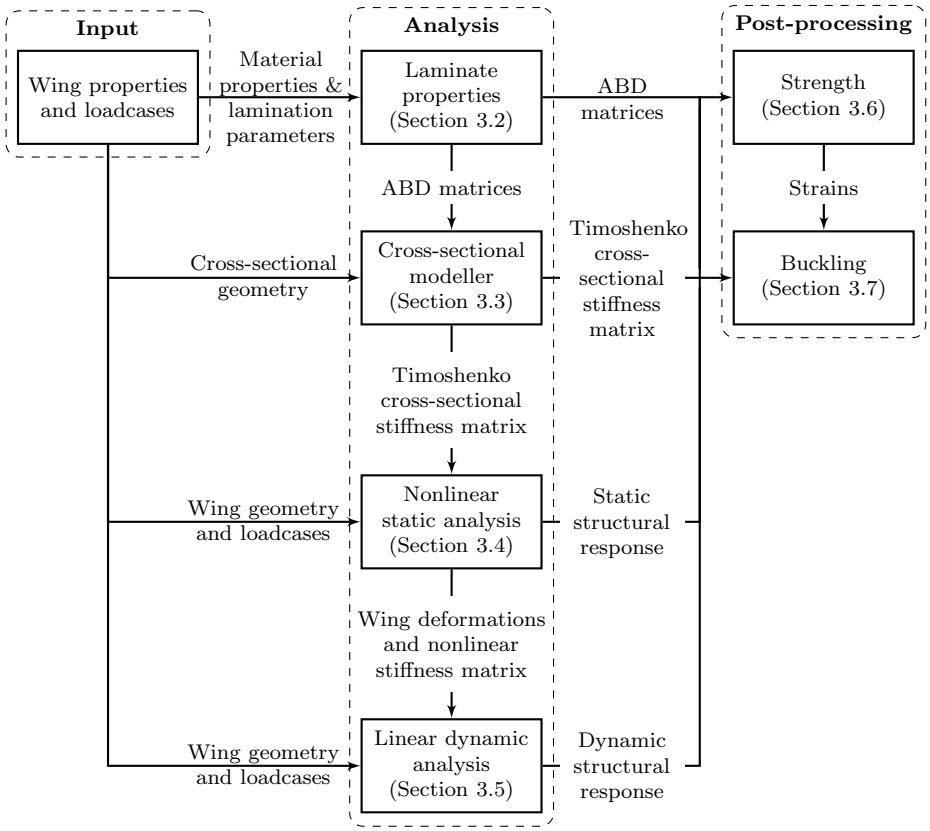


**Figure 3.2:** Schematic representation of the structural analysis module.

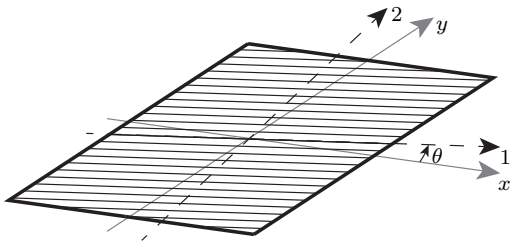


**Figure 3.3:** Laminate and ply coordinate systems.

### 3.2.1 CLASSICAL LAMINATION THEORY



The stiffness properties of composite laminates are conventionally described using classical lamination theory. The derivation of CLT can be found in many textbooks on composites (for example, Gürdal et al. (1999) or Daniel and Ishai (2006)) and is only given here for completeness. In CLT, through-the-thickness deformations are assumed to be zero and the out-of-plane stresses are considered negligible compared to the in-plane stresses. Under these assumptions, the stiffness properties of a single ply can be described using the following stress-strain relation:

$$\begin{pmatrix} \sigma_1 \\ \sigma_2 \\ \tau_{12} \end{pmatrix} = \begin{bmatrix} Q_{11} & Q_{12} & 0 \\ Q_{12} & Q_{22} & 0 \\ 0 & 0 & Q_{66} \end{bmatrix} \begin{pmatrix} \epsilon_1 \\ \epsilon_2 \\ \gamma_{12} \end{pmatrix} \tag{3.1}$$

where $\sigma_1$ is the longitudinal stress, $\sigma_2$ is the in-plane transverse stress, $\tau_{12}$ is the in-plane shear stress, $Q_{ij}$ are the reduced stiffness components, $\epsilon_1$ is the longitudinal strain, $\epsilon_2$ is the transverse strain, $\gamma_{12}$ is the shear strain, and the $1, 2$ coordinate system is defined according to Figure 3.3. The reduced stiffness components are related to conventional ply properties through the following relations:

$$Q_{11} = \frac{E_{11}}{1 - \nu_{12}\nu_{21}} \tag{3.2}$$

$$Q_{12} = \frac{\nu_{12}E_{22}}{1 - \nu_{12}\nu_{21}} \tag{3.3}$$

$$Q_{22} = \frac{E_{22}}{1 - \nu_{12}\nu_{21}} \tag{3.4}$$

$$Q_{66} = G_{12} \tag{3.5}$$

where $E$ is the Young's modulus, $G$ is the shear modulus, $\nu$ is the Poisson's ratio, and the subscripts $1, 2$ refer to the $1, 2$ coordinate system. Plies are generally

rotated with respect to the laminate coordinate system $x, y$ through a ply angle, $\theta$, as indicated in Figure 3.3. The lamina stresses and strains, defined in the $1, 2$ coordinate system, can be transformed to the laminate coordinate system through a transformation matrix, $\mathbf{T}$, defined by equation (3.6), resulting in the relations given by equation (3.7).

$$\mathbf{T} = \begin{bmatrix} \cos^2\theta & \sin^2\theta & 2\cos\theta\sin\theta \\ \sin^2\theta & \cos^2\theta & -2\cos\theta\sin\theta \\ -\cos\theta\sin\theta & \cos\theta\sin\theta & \cos^2\theta - \sin^2\theta \end{bmatrix} \tag{3.6}$$

$$\begin{pmatrix} \sigma_1 \\ \sigma_2 \\ \tau_{12} \end{pmatrix} = \mathbf{T} \begin{pmatrix} \sigma_x \\ \sigma_y \\ \tau_{xy} \end{pmatrix}, \qquad \begin{pmatrix} \epsilon_1 \\ \epsilon_2 \\ \epsilon_{12} \end{pmatrix} = \mathbf{T} \begin{pmatrix} \epsilon_x \\ \epsilon_y \\ \epsilon_{xy} \end{pmatrix} \tag{3.7}$$

3

Note that this transformation only holds for the tensorial shear strain, $\epsilon_{12}$, which is half the engineering shear strain, $\gamma_{12}$, introduced in equation (3.1). Therefore, the following relations are introduced, relating the engineering shear strain to the tensorial shear strain:

$$\mathbf{R} = \begin{bmatrix} 1 & 0 & 0 \\ 0 & 1 & 0 \\ 0 & 0 & 2 \end{bmatrix} \tag{3.8}$$

$$\begin{pmatrix} \epsilon_1 \\ \epsilon_2 \\ \gamma_{12} \end{pmatrix} = \mathbf{R} \begin{pmatrix} \epsilon_1 \\ \epsilon_2 \\ \epsilon_{12} \end{pmatrix}, \qquad \begin{pmatrix} \epsilon_x \\ \epsilon_y \\ \gamma_{xy} \end{pmatrix} = \mathbf{R} \begin{pmatrix} \epsilon_x \\ \epsilon_y \\ \epsilon_{xy} \end{pmatrix} \tag{3.9}$$

Introducing equations (3.7) and (3.9) into equation (3.1), the stress-strain relation of the ply in the $x, y$ coordinate system is obtained:

$$\begin{pmatrix} \sigma_x \\ \sigma_y \\ \tau_{xy} \end{pmatrix} = \mathbf{T}^{-1}\mathbf{Q}\mathbf{R}\mathbf{T}\mathbf{R}^{-1} \begin{pmatrix} \epsilon_x \\ \epsilon_y \\ \gamma_{xy} \end{pmatrix} \tag{3.10}$$

where the reduced stiffness matrix of the rotated ply, $\bar{Q}_{ij}$, is defined as:

$$\bar{\mathbf{Q}} = \mathbf{T}^{-1}\mathbf{Q}\mathbf{R}\mathbf{T}\mathbf{R}^{-1} \tag{3.11}$$

A laminate is obtained by bonding $N$ plies together, each having its own ply orientation angle, $\theta$. CLT assumes that the plies are bonded together with an infinitely thin bond line, the in-plane deformations across this bond line are continuous, and the strain distribution varies linearly through the thickness. Under

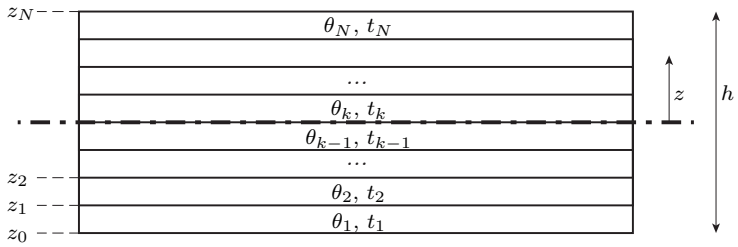


**Figure 3.4:** Schematic representation of a laminate consisting of $N$ plies having thickness $t_k$ and orientation angle $\theta_k$.

these assumptions, the strains in the $k^{th}$-ply at a location $z_{k-1} \leq z \leq z_k$, as illustrated in Figure 3.4, are given by the following relations:

$$\begin{pmatrix} \epsilon_x \\ \epsilon_y \\ \gamma_{xy} \end{pmatrix}_k = \begin{pmatrix} \epsilon_x^0 \\ \epsilon_y^0 \\ \gamma_{xy}^0 \end{pmatrix} + z \begin{pmatrix} \kappa_x \\ \kappa_y \\ \kappa_{xy} \end{pmatrix} \tag{3.12}$$

where $z$ is the through-the-thickness ply coordinate, $\kappa$ are the laminate curvatures, and the superscript 0 indicates the strains at the midplane of the laminate.

Loads on a laminate are generally defined by stress and moment resultants per unit laminate width. The stress and moment resultants are obtained by integrating the ply stresses over the thickness of the laminate, $h$:

$$\begin{aligned} \begin{pmatrix} N_x \\ N_y \\ N_{xy} \end{pmatrix} &= \int_{-h/2}^{h/2} \begin{pmatrix} \sigma_x \\ \sigma_y \\ \tau_{xy} \end{pmatrix} dz = \sum_{k=1}^{N} \int_{z_{k-1}}^{z_k} \begin{pmatrix} \sigma_x \\ \sigma_y \\ \tau_{xy} \end{pmatrix}_k dz \\ \begin{pmatrix} M_x \\ M_y \\ M_{xy} \end{pmatrix} &= \int_{-h/2}^{h/2} \begin{pmatrix} \sigma_x \\ \sigma_y \\ \tau_{xy} \end{pmatrix} z\, dz = \sum_{k=1}^{N} \int_{z_{k-1}}^{z_k} \begin{pmatrix} \sigma_x \\ \sigma_y \\ \tau_{xy} \end{pmatrix}_k z\, dz \end{aligned} \tag{3.13}$$

where $N_x$, $N_y$, and $N_{xy}$ are the stress resultants and $M_x$, $M_y$, and $M_{xy}$ are the moment resultants. Combining equations (3.10), (3.12), and (3.13), the ABD-

matrix is obtained:

$$\begin{pmatrix} N_x \\ N_y \\ N_{xy} \\ M_x \\ M_y \\ M_{xy} \end{pmatrix} = \left[\begin{array}{ccc:ccc} A_{11} & A_{12} & A_{16} & B_{11} & B_{12} & B_{16} \\ & A_{22} & A_{26} & & B_{22} & B_{26} \\ \text{sym.} & & A_{66} & \text{sym.} & & B_{66} \\ \hdashline & & & D_{11} & D_{12} & D_{16} \\ & \text{sym.} & & & D_{22} & D_{26} \\ & & & \text{sym.} & & D_{66} \end{array}\right] \begin{pmatrix} \epsilon_x^0 \\ \epsilon_y^0 \\ \gamma_{xy}^0 \\ \kappa_x \\ \kappa_y \\ \kappa_{xy} \end{pmatrix} \tag{3.14}$$

that describes the stiffness properties of a laminate, where the components of the ABD-matrix are given by:

$$\begin{aligned} A_{ij} &= \sum_{k=1}^{N} \left(\bar{Q}_{ij}\right)_k (z_k - z_{k-1}) \\ B_{ij} &= \frac{1}{2} \sum_{k=1}^{N} \left(\bar{Q}_{ij}\right)_k \left(z_k^2 - z_{k-1}^2\right) \\ D_{ij} &= \frac{1}{3} \sum_{k=1}^{N} \left(\bar{Q}_{ij}\right)_k \left(z_k^3 - z_{k-1}^3\right) \end{aligned} \tag{3.15}$$

The ABD-matrix illustrates several different types of coupling that can exist between applied loads and the deformation of a composite laminate that are not present for an isotropic material. For example, the B-matrix describes the coupling between the out-of-plane response of a laminate under in-plane loading, or vice versa, that is only present in case of a non-symmetric stacking sequence. Therefore, in this dissertation, as is conventional, a symmetric stacking sequence is used for composite laminates to prevent warping of the structure upon curing of the laminate caused by the coupling between in-plane thermal stresses and out-of-plane deformations.

In order to exploit composite laminates for aeroelastic tailoring, two effects are of particular interest. First, $A_{16}$ and $A_{26}$ describe the extension-shear coupling of a laminate. When these are non-zero, an applied tensile load, for example, will not only induce extensional strain, but also shear strain. When for every positive ply angle $\theta$, a corresponding negative ply angle $-\theta$ is present in a laminate, the laminate is balanced and no extension-shear coupling exists. Second, $D_{16}$ and $D_{26}$ describe the bend-twist coupling of a laminate. When these are non-zero an applied bending moment, for example, will not only induce a bending deformation, but will also induce twist. A more detailed discussion on these effects and how they affect the aeroelastic response of the wing will be presented in Chapter 8 dedicated to the aeroelastic optimisation of a composite wing.

### 3.2.2 LAMINATION PARAMETERS

Instead of describing a composite laminate by ply angles and a stacking sequence to obtain the stiffness properties, it can also be described as a function of lamination parameters. Lamination parameters were first introduced by Tsai and Pagano (1968) and provide a representation of a composite laminate as an integrated form. They are related to the ply angles and stacking sequence through the following relations:

$$(V_{1\mathbf{A}}, V_{2\mathbf{A}}, V_{3\mathbf{A}}, V_{4\mathbf{A}}) = \int_{-1/2}^{1/2} (\cos 2\theta, \sin 2\theta, \cos 4\theta, \sin 4\theta)\, d\bar{z} \tag{3.16}$$

$$(V_{1\mathbf{B}}, V_{2\mathbf{B}}, V_{3\mathbf{B}}, V_{4\mathbf{B}}) = 4 \int_{-1/2}^{1/2} \bar{z}\, (\cos 2\theta, \sin 2\theta, \cos 4\theta, \sin 4\theta)\, d\bar{z} \tag{3.17}$$

$$(V_{1\mathbf{D}}, V_{2\mathbf{D}}, V_{3\mathbf{D}}, V_{4\mathbf{D}}) = 12 \int_{-1/2}^{1/2} \bar{z}^2\, (\cos 2\theta, \sin 2\theta, \cos 4\theta, \sin 4\theta)\, d\bar{z} \tag{3.18}$$

where $V_{i\mathbf{A}}$, $V_{i\mathbf{B}}$, and $V_{i\mathbf{D}}$ are the in-plane, coupling, and bending lamination parameters and $\bar{z}$ is the normalised through-the-thickness coordinate. Commonly the ply angles are not a continuous function through the thickness, but a set of discrete angles, in which case the integrals in equation (3.18) are replaced by a summation. Once the lamination parameters are known, the ABD-matrix can be obtained through the following linear relations:

$$\mathbf{A} = h\, (\mathbf{\Gamma_0} + \mathbf{\Gamma_1} V_{1\mathbf{A}} + \mathbf{\Gamma_2} V_{2\mathbf{A}} + \mathbf{\Gamma_3} V_{3\mathbf{A}} + \mathbf{\Gamma_4} V_{4\mathbf{A}}) \tag{3.19}$$

$$\mathbf{B} = \frac{h^2}{4}\, (\mathbf{\Gamma_0} + \mathbf{\Gamma_1} V_{1\mathbf{B}} + \mathbf{\Gamma_2} V_{2\mathbf{B}} + \mathbf{\Gamma_3} V_{3\mathbf{B}} + \mathbf{\Gamma_4} V_{4\mathbf{B}}) \tag{3.20}$$

$$\mathbf{D} = \frac{h^3}{12}\, (\mathbf{\Gamma_0} + \mathbf{\Gamma_1} V_{1\mathbf{D}} + \mathbf{\Gamma_2} V_{2\mathbf{D}} + \mathbf{\Gamma_3} V_{3\mathbf{D}} + \mathbf{\Gamma_4} V_{4\mathbf{D}}) \tag{3.21}$$

where $\mathbf{\Gamma_i}$ are the material invariant matrices that are related to the material invariants through:

$$\mathbf{\Gamma_0} = \begin{bmatrix} U1 & U4 & 0 \\ U4 & U1 & 0 \\ 0 & 0 & U5 \end{bmatrix}, \quad \mathbf{\Gamma_1} = \begin{bmatrix} U2 & 0 & 0 \\ 0 & -U2 & 0 \\ 0 & 0 & 0 \end{bmatrix}, \quad \mathbf{\Gamma_2} = \begin{bmatrix} 0 & 0 & U2 \\ 0 & 0 & U2 \\ U2 & U2 & 0 \end{bmatrix}$$
$$\mathbf{\Gamma_3} = \begin{bmatrix} U3 & -U3 & 0 \\ -U3 & U3 & 0 \\ 0 & 0 & -U3 \end{bmatrix}, \quad \mathbf{\Gamma_4} = \begin{bmatrix} 0 & 0 & 2U3 \\ 0 & 0 & -2U3 \\ 2U3 & -2U3 & 0 \end{bmatrix} \tag{3.22}$$

which are in term related to the lamina stiffness matrices through:

$$U_1 = \frac{1}{8}\left(3Q_{11} + 3Q_{22} + 2Q_{12} + 4Q_{66}\right) \tag{3.23}$$

$$U_2 = \frac{1}{2}\left(Q_{11} - Q_{22}\right) \tag{3.24}$$

$$U_3 = \frac{1}{8}\left(Q_{11} + Q_{22} - 2Q_{12} - 4Q_{66}\right) \tag{3.25}$$

$$U_4 = \frac{1}{8}\left(Q_{11} + Q_{22} + 6Q_{12} - 4Q_{66}\right) \tag{3.26}$$

$$U_5 = \frac{1}{8}\left(Q_{11} + Q_{22} - 2Q_{12} + 4Q_{66}\right) \tag{3.27}$$

The use of lamination parameters as design variables in an optimisation to describe the stiffness properties of a laminate has several advantages over the use of ply angles and a stacking sequence. First of all, lamination parameters provide a smooth, continuous description of the stiffness properties of composite laminates, allowing for efficient gradient-based optimisers to be used. Secondly, any composite laminate is described by a fixed number of 12 lamination parameters and its thickness, while in case of ply angles and a stacking sequence, the number of design variables scales with the number of plies in the laminate, making optimisation more difficult as the size of the laminate grows. Finally, the feasible design space of lamination parameters is convex, while the design space in fibre angle space is highly irregular due to the highly nonlinear relation between the laminate stiffness matrices and the ply angles.

However, two main drawbacks exist for lamination parameters. First of all, lamination parameters require an additional post-processing step to obtain the corresponding set of ply angles and the stacking sequence. A set of ply angles that exactly matches a set of lamination parameters is only guaranteed in case of an infinite number of plies and research into finding the optimal stacking sequence that best matches a set of lamination parameters, given a certain discrete ply thickness, is still ongoing (see, for example, IJsselmuiden (2011), van Campen et al. (2012), Irisarri et al. (2014), or Raju et al. (2015)). As a consequence, the

performance predicted by lamination parameters results in a theoretical optimum and a drop in performance can be expected when converting back to ply angle space depending on the application and the number of plies in the laminate. The focus of this dissertation, however, is on the potential increase in performance by using composites for aeroelastic tailoring and will only address the continuous stiffness optimisation using lamination parameters.

The second drawback of lamination parameters is that no set of closed-form expression is known that fully defines the feasible region of lamination parameters. Hammer et al. (1997) derived a set of closed form expressions that define the feasible region of the in-plane, coupling, and bending lamination parameters separately, given by:

$$2V_1^2\left(1-V_3\right)+2V_2^2\left(1+V_3\right)+V_3^2+V_4^2-4V_1V_2V_4\leq 1 \tag{3.28}$$

$$V_1^2+V_2^2\leq 1 \tag{3.29}$$

$$-1\leq V_i\leq 1 \tag{3.30}$$



However, the in-plane, coupling, and bending lamination parameters cannot vary independently, as they are all defined by the same ply angles and stacking sequence for a given laminate. Recently, Raju et al. (2014) and Wu et al. (2015) used the Cauchy-Schwarz inequality to derive two closed-form expressions constraining a combination of in-plane and out-of-plane lamination parameters, as given in Appendix A. These equations, however, only provide a necessary condition and are not sufficient to fully contrain the lamination parameter feasibility region.

In order to approximate the full feasibility region of lamination parameters, two approaches exist in the literature. Bloomfield et al. (2009) obtained a set of constraints describing the convex hull of the lamination parameter design space by considering a set of predefined ply angles and Setoodeh et al. (2006) obtained a set of linear constraints by approximating the convex hull of the lamination parameter design space by generating feasible design points until the total volume of the convex hull has converged. Both approaches have not been considered in the present dissertation, since the approach by Bloomfield et al. (2009) constrains the design space a priori to a set of fixed ply angles, negating one of the benefits of the use of lamination parameters and the approach by Setoodeh et al. (2006) results in a large amount of constraints (i.e. 37126 for $V_{1\mathbf{A}}, V_{3\mathbf{A}}, V_{1\mathbf{D}}, V_{3\mathbf{D}}$) slowing down the optimisation process. A slightly reduced performance is expected when converting the lamination parameters to an actual stacking sequence. Most panels will, however, only be critical in either strength, which is driven by the in-plane properties of the laminate (i.e. the A-matrix), or buckling, which is driven by the out-of-plane properties of the laminate (i.e. the D-matrix). Therefore, when, for example, a laminate is critical in strength, the stacking sequence retrieval procedure can be used to find a best match between the in-plane lamination

parameters and the in-plane stiffness properties of the final composite stacking sequence, while sacrificing the match in out-of-plane stiffness properties.

### 3.2.3 LAMINATE STIFFNESS VISUALISATION

As introduced by Dillinger et al. (2013), in order to visualise the directional stiffness distribution of a laminate defined by a set of lamination parameters, the membrane and flexural modulus of elasticity of the laminate along a direction, $\theta$, are obtained from the laminate membrane stiffness matrix, A, and flexural stiffness matrix, D. The modulus of elasticity of a laminate along an axis rotated with an angle, $\theta$, with respect to the laminate axis is defined by:



$$E_{m_{11}}(\theta) = \frac{1}{A_{11}^{-1}(\theta)} \tag{3.31}$$

$$E_{f_{11}}(\theta) = \frac{1}{D_{11}^{-1}(\theta)} \tag{3.32}$$

where

$$A_{11}^{-1}(\theta) = T^T A_{11}^{-1} T \tag{3.33}$$

$$D_{11}^{-1}(\theta) = T^T D_{11}^{-1} T \tag{3.34}$$

and

$$T = \begin{bmatrix} \cos^2(\theta) & \sin^2(\theta) & 2\cos(\theta)\sin(\theta) \\ \sin^2(\theta) & \cos^2(\theta) & -2\cos(\theta)\sin(\theta) \\ -\cos(\theta)\sin(\theta) & \cos(\theta)\sin(\theta) & \cos^2(\theta) - \sin^2(\theta) \end{bmatrix} \tag{3.35}$$

Figure 3.5 shows an example of the corresponding stiffness distributions for several characteristic laminates using the composite material properties given in Table 3.1. First of all, as expected and illustrated in Figures 3.5a to 3.5d, when all fibres are oriented along a single fibre angle, the membrane and flexural stiffness distribution of the laminate are equal with a maximum normalised stiffness of 1.0 aligned with the fibre angle.

Secondly, as illustrated by Figures 3.5e and 3.5f showing the normalised membrane and flexural stiffness distribution for $[30/-30]_s$ and $[-30/30]_s$ laminates, the flexural stiffness distribution of a laminate is heavily dependent upon the stacking sequence, showing a stiffness of 0.89 aligned with the outermost plies and 0.20

**Table 3.1:** Material properties. (Source: Daniel and Ishai (2006))

| UD Carbon/Epoxy (AS4/3501-6) | |
|---|---|
| $E_{11}$ | 147.0 GPa |
| $E_{22}$ | 10.3 GPa |
| $G_{12}$ | 7.0 GPa |
| $\nu_{12}$ | 0.27 |
| $\rho$ | 1600 kg/m$^3$ |

aligned with the innermost plies, while, as expected, the membrance stiffness distribution shows an equal stiffness of 0.55 along both directions.

Finally, Figures 3.5g and 3.5h show the normalised membrane and flexural stiffness distribution of a quasi-isotropic (QI) laminate, showing, as expected, equal stiffness in all directions. However, as can be seen, the stiffness has reduced to 0.40.



## 3.3 CROSS-SECTIONAL MODELLING

The cross-sectional modeller, as mentioned in Section 3.1, has two functions. First, the cross-sectional properties have to be determined from the three dimensional wing model to obtain the equivalent one-dimensional properties. For this purpose a thin-walled cross-sectional modeller was developed by Ferede and Abdalla (2014). The cross-section is discretized using linear Hermitian shell elements having constant properties and can be any arbritrary open or closed, single-cell or multi-cell, thin-walled, composite cross-section. Using a variational asymptotic approach, the Timoshenko cross-sectional stiffness matrix, $\mathbf{C}$, around a chosen reference point can be determined, relating the strains, $\epsilon$, and curvatures, $\kappa$, at the reference point to the applied forces, $F$, and moments, $M$:

$$\begin{pmatrix} F_1 & F_2 & F_3 & M_1 & M_2 & M_3 \end{pmatrix}^T = \mathbf{C} \begin{pmatrix} \epsilon_{11} & \epsilon_{12} & \epsilon_{13} & \kappa_1 & \kappa_2 & \kappa_3 \end{pmatrix}^T \tag{3.36}$$

Note that the reference point of the cross-section can be any arbitrary point, so knowing the location of the shear centre and neutral axis is not required. The cross-sectional mass properties can be determined by simply determining the mass per unit length, the first mass moments, and the mass moments of inertia of the cross-section.

Secondly, once the aeroelastic analysis has been completed, the cross-sectional modeller is used to recover the skin strains throughout the cross-section from the one-dimensional beam strains to be able to assess potential skin failure and structural instability. The skin strains include both the Euler-Bernouilli strains

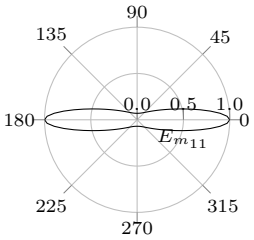


**(a)** [0]

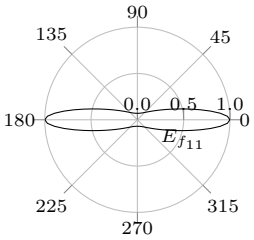


**(b)** [0]

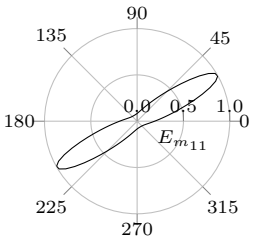


**(c)** [30]

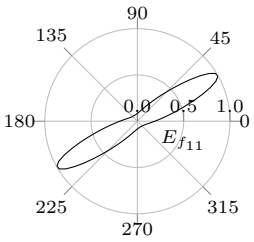


**(d)** [30]

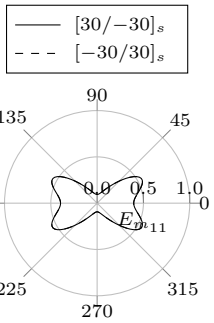


**(e)** $[30/-30]_s$ and $[-30/30]_s$

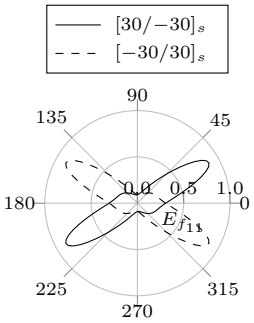


**(f)** $[30/-30]_s$ and $[-30/30]_s$

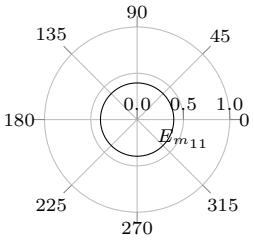


**(g)** QI: $[(0/45/-45/90)_{100}]_s$

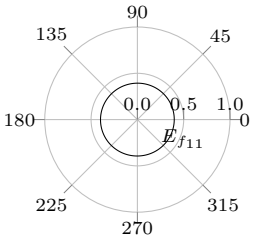


**(h)** QI: $[(0/45/-45/90)_{100}]_s$

**Figure 3.5:** Membrane and flexural stiffness distribution for several characteristic laminates normalised with respect to $E_{11}$.

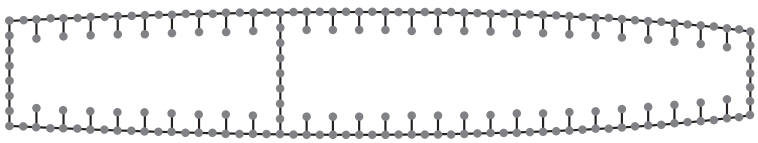

**Figure 3.6:** Illustration of the cross-sectional discretisation of a wingbox structure including stringers. The dots indicate the cross-sectional nodes.

and the second-order free warping solution.

Figure 3.6 shows an example of a cross-sectional discretisation of a wingbox structure. In case stringers are present in the cross-section, equally distributed blade stringer are introduced based on predefined stringer pitch. The stringers are defined by their material properties, height, extensional stiffness, and mass per unit length. The extensional stiffness and mass per unit length are matched by adjusting the thickness and mass density of the stringer laminate.



## 3.4 Static structural response

Once the cross-sectional properties have been determined, the static structural model can be defined. The static structural analysis module is based on the work of De Breuker et al. (2011). Section 3.4.1 provides a brief overview of the model implemented by De Breuker et al. (2011). In order to account for forces and moments induced by, for example, the engine or the main landing gear, in this dissertation, the structural model has been extended to include eccentric forces and moments, as presented in Section 3.4.2.

### 3.4.1 Geometrically nonlinear beam analysis

The structural model is a finite element beam model using linear Timoshenko beam elements. The elements are coupled in a co-rotational framework to obtain a geometrically nonlinear structural solution. The local element is a 20-degree of freedom shear flexible element with a constant cross-section that allows the use of anisotropic materials. In order to model, for example, a tapered wing that has a varying cross-section along the span, the wing has to be discretised in sufficient elements in order to ensure an accurate description of the variation in cross-section along the wing span. The beam strain energy, $\mathcal{U}$, of a Timoshenko beam element

is given by:

$$\mathcal{U} = \frac{L_0}{2} \int_0^1 \boldsymbol{\epsilon}^{\mathbf{T}} \mathbf{C} \boldsymbol{\epsilon} d\xi \tag{3.37}$$

where $L_0$ is the undeformed element length, $\boldsymbol{\epsilon}$ is the beam strain and curvature vector, $\mathbf{C}$ is the Timoshenko cross-sectional stiffness matrix given by the cross-sectional modeller, and $\xi$ is the beam axial coordinate non-dimensionalised with respect to $L_0$. The strain and curvature vector is related to the element deformation through the following relation:



$$\begin{aligned} \boldsymbol{\epsilon} &= \begin{pmatrix} \epsilon_{11} & \epsilon_{12} & \epsilon_{13} & \kappa_1 & \kappa_2 & \kappa_3 \end{pmatrix}^T \\ &= \begin{pmatrix} \frac{1}{L_0}\frac{\partial u}{\partial \xi} & -\psi + \frac{1}{L_0}\frac{\partial v}{\partial \xi} & \theta + \frac{1}{L_0}\frac{\partial w}{\partial \xi} & \frac{1}{L_0}\frac{\partial \phi}{\partial \xi} & \frac{1}{L_0}\frac{\partial \theta}{\partial \xi} & \frac{1}{L_0}\frac{\partial \psi}{\partial \xi} \end{pmatrix}^T \end{aligned} \tag{3.38}$$

where $u$ is the elongation of the beam element, $v$ and $w$ are the deflections of the beam element, $\kappa_1$ is the twist curvature, and $\kappa_2$ and $\kappa_3$ are the bending curvatures. The corresponding 123 coordinate system is illustrated in Figure 3.7. In order to obtain the strain energy of the beam element, the following shape functions are used to describe the local deformation of the beam element, as a function of the degrees of freedom:

$$\begin{aligned} u &= u_1(1-\xi) + u_2\xi + q_5\xi(1-\xi) \\ v &= v_1(1-\xi) + v_2\xi + q_1\xi(1-\xi) + q_3(1-\xi)(1/2-\xi) \\ w &= w_1(1-\xi) + w_2\xi + q_2\xi(1-\xi) + q_4(1-\xi)(1/2-\xi) \\ \phi &= \phi_1(1-\xi) + \phi_2\xi + q_6\xi(1-\xi) \\ \theta &= \theta_1(1-\xi) + \theta_2\xi + q_7\xi(1-\xi) \\ \psi &= \psi_1(1-\xi) + \psi_2\xi + q_8\xi(1-\xi) \end{aligned} \tag{3.39}$$

where the different degrees of freedom are defined according to Figure 3.7. The beam element stiffness matrix can now be obtained by introducing equation (3.38) and (3.39) into equation (3.37) and computing the Hessian of the strain energy with respect to the element degrees of freedom, $\mathbf{p_e}$:

$$\mathbf{K}_{\mathbf{e}ij} = \frac{\partial^2 \mathcal{U}}{\partial \mathbf{p}_{\mathbf{e}i} \partial \mathbf{p}_{\mathbf{e}j}} \tag{3.40}$$

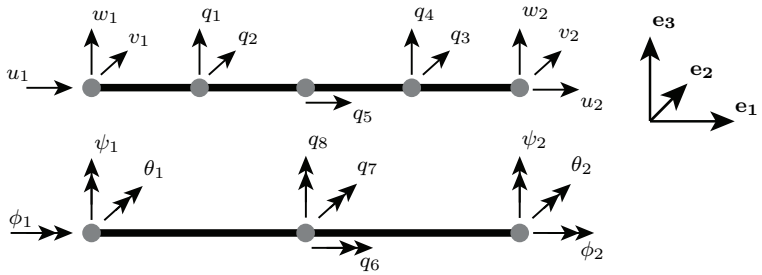


**Figure 3.7:** Element degrees of freedom. (Source: De Breuker (2011))

where

$$\mathbf{p_e} = \left(u_1, v_1, w_1, \phi_1, \theta_1, \psi_1, u_2, v_2, w_2, \phi_2, \theta_2, \psi_2, q_1, q_2, q_3, q_4, q_5, q_6, q_7, q_8\right)^T \tag{3.41}$$

In order to eliminate the internal nodes of the beam element, the method of static condensation is used (Guyan, 1965). By introducing all forces on the beam element at the end nodes and distinguishing between the internal degrees of freedom, $\mathbf{p_i}$, and the degrees of freedom at the end nodes of the beam element, $\mathbf{p_l}$, the equilibrium equation of the beam element can be partitioned as follows:

$$\begin{bmatrix} \mathbf{K_{ll}} & \mathbf{K_{li}} \\ \mathbf{K_{il}} & \mathbf{K_{ii}} \end{bmatrix} \begin{pmatrix} \mathbf{p_l} \\ \mathbf{p_i} \end{pmatrix} = \begin{pmatrix} \mathbf{F_l} \\ \mathbf{0} \end{pmatrix} \tag{3.42}$$

Using the second equation, the internal degrees of freedom, $\mathbf{p_i}$, can be written as a function of the nodal degrees of freedom, $\mathbf{p_l}$, in order to eliminate the internal degrees of freedom and reduce the element matrix from 20 degrees of freedom to 12 degrees of freedom, resulting in:

$$\mathbf{K_l p_l} = \mathbf{F_l} \tag{3.43}$$

where

$$\mathbf{K_l} = \mathbf{K_{ll}} - \mathbf{K_{li}} \mathbf{K_{ii}}^{-1} \mathbf{K_{il}} \tag{3.44}$$

In order to obtain a geometrically nonlinear equilibrium solution, the local beam elements are coupled using the co-rotational framework, derived by Battini and Pacoste (2002). In the co-rotational framework, the total beam deformation is decomposed in small elastic local element deformations and large rigid displacements and rotations of the beam elements. The relation between the local elastic

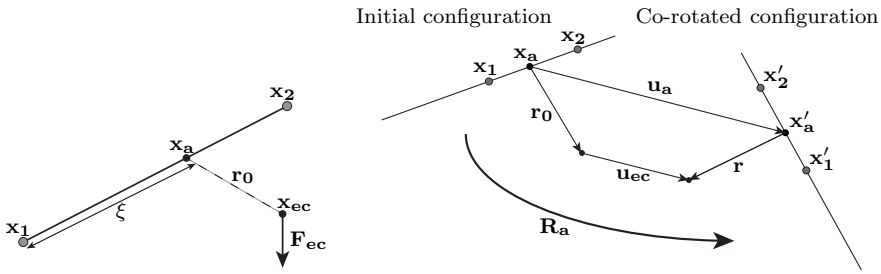


**(a)** Schematic illustration of an eccentric force or moment, $\mathbf{F_{ec}}$, acting at location $\mathbf{x_{ec}}$.

**(b)** Schematic illustration of the displacement of eccentric node, $\mathbf{x_{ec}}$.

**Figure 3.8:** Schematic illustration of the implementation of eccentric forces and moments.



deformations and the global beam deformations is derived by recognizing that the virtual work done by the internal forces expressed in the local frame has to be equal to the virtual work expressed in the global frame:

$$\mathcal{V} = \delta \mathbf{p_l}^T \mathbf{F_l} = \delta \mathbf{p}^T \mathbf{F} \tag{3.45}$$

Using this equation, following the derivation by Battini and Pacoste (2002), the global tangent stiffness matrix can be determined, which can be used to find the geometrically nonlinear structural equilibrium solution.

### 3.4.2 ECCENTRIC FORCES

In order to account for the effects of, for example, gravity and engine thrust, the static structural analysis module has been extended to account for both constant and follower eccentric forces and moments, based on the work of Battini and Pacoste (2002).

Consider an eccentric node at location, $\mathbf{x_{ec}}$, which is attached through a rigid link to $\mathbf{x_a}$, located on element $k$, as shown in Figure 3.8a. In order to link $\mathbf{x_{ec}}$ to $\mathbf{x_a}$, an eccentricity vector $\mathbf{r_0}$ is defined, such that:

$$\mathbf{x_{ec}} = \mathbf{x_a} + \mathbf{r_0} \tag{3.46}$$

where $\mathbf{r_0}$ is perpendicular to the beam axis. Since $\mathbf{x_{ec}}$ is attached to $\mathbf{x_a}$ through a rigid link, $\mathbf{r_0}$ is constant in the local element coordinate system. Therefore, defining the rotation from the local element coordinate system to the co-rotated coordinate system by a rotation matrix, $\mathbf{R_a}$, the co-rotated eccentricity vector is

given by:

$$\mathbf{r} = \mathbf{R_a r_0} \tag{3.47}$$

Using Figure 3.8b, the displacements of the eccentric node at location, $\mathbf{x_{ec}}$, can now be related to the deformations at location, $\mathbf{x_a}$, on the beam element, resulting in:

$$\mathbf{u_a} + \mathbf{r} = \mathbf{r_0} + \mathbf{u_{ec}} \tag{3.48}$$

$$\mathbf{u_{ec}} = \mathbf{u_a} + (\mathbf{R_a} - \mathbf{I})\,\mathbf{r_0} \tag{3.49}$$

In order to derive the equivalent nodal force vector and stiffness contribution corresponding to the applied eccentric forces and moments, the principle of virtual work is used. Recognizing that the virtual work done by the equivalent nodal forces, $\mathbf{F_e}$, should be equal to the virtual work done by the eccentric forces and moments, $\mathbf{F_{ec}}$, the following relation is obtained:

$$\boldsymbol{\delta}\mathbf{p}_{\mathbf{ec}}^{\mathbf{T}}\mathbf{F_{ec}} = \boldsymbol{\delta}\mathbf{p}^{\mathbf{T}}\mathbf{F_e} \tag{3.50}$$

where

$$\boldsymbol{\delta}\mathbf{p_{ec}} = \begin{pmatrix}\mathbf{u_{ec}} & \boldsymbol{\theta}_{\mathbf{ec}}\end{pmatrix}^T \tag{3.51}$$

$$\boldsymbol{\delta}\mathbf{p} = \begin{pmatrix}\mathbf{u_1} & \boldsymbol{\theta_1} & \mathbf{u_2} & \boldsymbol{\theta_2}\end{pmatrix}^T \tag{3.52}$$

where $\boldsymbol{\theta}_{\boldsymbol{ec}}$ is the total rotational pseudovector of the eccentric node, $\mathbf{u_1}$ and $\mathbf{u_2}$ are the displacement vectors of node 1 and node 2, and $\boldsymbol{\theta_1}$ and $\boldsymbol{\theta_2}$ are the total rotational pseudovectors of node 1 and node 2 respectively. Therefore, in order to find the nodal force vector corresponding to the eccentric force and moment vector, the variation of the deformation of the eccentric node has to be related to the variation of the nodal deformations of the corresponding beam element. Taking the variation of equation (3.49), and recognizing that $\mathbf{r_0}$ is constant, the following relation is obtained for the variation of the displacements at the eccentric node:

$$\boldsymbol{\delta}\mathbf{u_{ec}} = \boldsymbol{\delta}\mathbf{u_a} + \boldsymbol{\delta}\mathbf{R_a r_0} \tag{3.53}$$

The variation of a rotation matrix is related to its spatial angular variation, $\boldsymbol{\delta\vartheta_a}$, through:

$$\boldsymbol{\delta}\mathbf{R_a} = \boldsymbol{\delta}\tilde{\boldsymbol{\vartheta}}_{\mathbf{a}}\mathbf{R_a} \tag{3.54}$$

where the tilde indicates the skew symmetric representation of a vector and the spatial angular variation represents an infinitesimal rotation superimposed on $\mathbf{R_a}$. Using $\mathbf{a\tilde{b}} = -\mathbf{b\tilde{a}}$ and introducing equation (3.47), the variation of the displacements at the eccentric node can be related to the variation of the deformations of point $a$ through:

$$\begin{aligned} \boldsymbol{\delta u_{ec}} &= \boldsymbol{\delta u_a} + \boldsymbol{\delta \tilde{\vartheta}_a r} \\ &= \boldsymbol{\delta u_a} - \tilde{\mathbf{r}} \boldsymbol{\delta \vartheta_a} \end{aligned} \tag{3.55}$$

Recognizing that the rotations of the eccentric node are equal to the rotations of point $a$, because of the rigid link, the deformation vector of the eccentric node can be related to the deformations at point $a$ through:

$$\boldsymbol{\delta p_{ec}} = \begin{bmatrix} \mathbf{I} & -\tilde{\mathbf{r}} \\ \mathbf{0} & \mathbf{I} \end{bmatrix} \begin{pmatrix} \boldsymbol{\delta u_a} \\ \boldsymbol{\delta \vartheta_a} \end{pmatrix} \tag{3.56}$$

In order to relate the deformations of point $a$ to the deformations of node 1 and node 2, a linear interpolation is used, resulting in the following relation for the eccentric deformations as a function of the global deformations of node 1 and node 2:

$$\boldsymbol{\delta p_{ec}} = \underbrace{\begin{bmatrix} (1-\xi)\,\mathbf{I} & -(1-\xi)\,\tilde{\mathbf{r}} & \xi\mathbf{I} & -\xi\tilde{\mathbf{r}} \\ \mathbf{0} & (1-\xi)\,\mathbf{I} & \mathbf{0} & \xi\mathbf{I} \end{bmatrix}}_{\mathbf{B_{ex}}} \underbrace{\begin{pmatrix} \boldsymbol{\delta u_1} \\ \boldsymbol{\delta \vartheta_1} \\ \boldsymbol{\delta u_2} \\ \boldsymbol{\delta \vartheta_2} \end{pmatrix}}_{\boldsymbol{\delta p_g}} \tag{3.57}$$

where $\xi$ is the normalised location of the rigid link along the beam element.

The spatial angular variation and the total rotational pseudovector are not additive. In order to make the rotational vectors additive, the spatial angular variation needs to be transformed to the variation of the total rotational pseudovector, through:

$$\boldsymbol{\delta\theta} = \mathbf{T_s}\,(\boldsymbol{\theta})\,\boldsymbol{\delta\vartheta} \tag{3.58}$$

as derived by Ibrahimbegovic (1997). Introducing equation (3.58) in equation (3.57), the variations of the deformations of the eccentric node can be related to the variations of the nodal displacements, resulting in:

$$\boldsymbol{\delta p_{ec}} = \mathbf{B_{ex}}\,(\mathbf{p_g})\mathbf{H}\,(\mathbf{p})\boldsymbol{\delta p} \tag{3.59}$$

where $\mathbf{H}(\mathbf{p})$ is defined by, as derived by Battini and Pacoste (2002):

$$\mathbf{H}(\mathbf{p}) = \begin{bmatrix} \mathbf{I} & & & \mathbf{0} \\ & \mathbf{T_s}(\boldsymbol{\theta_1}) & & \\ & & \mathbf{I} & \\ \mathbf{0} & & & \mathbf{T_s}(\boldsymbol{\theta_2}) \end{bmatrix} \tag{3.60}$$

Inserting equation (3.59) in equation (3.50), the following equation for the nodal force vector as a function of the eccentric force vector can now be found:

$$\mathbf{F_e} = \mathbf{H^T B_{ex}^T F_{ec}} \tag{3.61}$$

The corresponding stiffness matrix is defined by:

$$\boldsymbol{\delta} \mathbf{F_e} = \mathbf{K_e} \boldsymbol{\delta} \mathbf{p} \tag{3.62}$$

and can be derived by taking the variation of equation (3.61), as shown in Appendix B, resulting in three different contributions to the total stiffness matrix. The first contribution comes from the variation of $\mathbf{H}$ and is commonly called the geometric moment stiffness, the second contribution comes from the variation of $\mathbf{B_{ex}}$ and is commonly called the geometric rotation stiffness, and the final contribution comes from the variation of the external force vector, $\mathbf{F_{ec}}$, and is commonly called the material stiffness. Note that the final contribution will only be non-zero in case of follower forces and moments.

Introducing the equivalent nodal force vector, $\mathbf{F_e}$, and stiffness matrix, $\mathbf{K_e}$, in the structural equilibrium equations, the static structural response including eccentric forces and moments can be obtained.

## 3.5 Dynamic structural response

In order to obtain the response of a wing to, for example, a gust, a structural dynamics model is required. Therefore, the static structural model introduced in Section 3.4 has been extended to a structural dynamics model. Assuming small dynamic disturbances with respect to the static equilibrium solution, a linear dynamic structural analysis is carried out around the geometrically nonlinear static equilibrium solution for computational efficiency. The derivation of the structural dynamics model of the wing is given in Section 3.5.1, followed by the introduction of nonstructural masses in Section 3.5.2.

### 3.5.1 BEAM ANALYSIS

At static equilibrium, the internal structural forces are equal to the applied external loads:

$$\mathbf{F_s} = \mathbf{F_{ext}} \tag{3.63}$$

Linearising equation (3.63) to obtain the small disturbance equation around the static equilibrium solution, the following equation is obtained:

$$\begin{aligned} \mathbf{F_{s_0}} + \mathbf{K_{s_0}}\boldsymbol{\Delta}\mathbf{p} &= \mathbf{F_{ext_0}} + \mathbf{K_{ext_0}}\boldsymbol{\Delta}\mathbf{p} + \boldsymbol{\Delta}\mathbf{F} \\ \mathbf{K_{s_0}}\boldsymbol{\Delta}\mathbf{p} &= \mathbf{K_{ext_0}}\boldsymbol{\Delta}\mathbf{p} + \boldsymbol{\Delta}\mathbf{F} \end{aligned} \tag{3.64}$$

where the subscript 0 indicates the static equilibrium solution and $\boldsymbol{\Delta}\mathbf{p}$ is the vector of structural disturbances $(\mathbf{p} - \mathbf{p_0})$ resulting from the applied disturbance forces, $\boldsymbol{\Delta}\mathbf{F}$. The linearised static equilibrium equation is augmented with a linear mass matrix of the deformed configuration to obtain the dynamic structural model. The dynamic structural model is based on the same linear Timoshenko beam elements as used for the static analysis. The kinetic energy, $\mathcal{T}$, of a structure is given by:

$$\mathcal{T} = \frac{1}{2}\int_V \rho \mathbf{v}^\mathbf{T}\mathbf{v} dV, \tag{3.65}$$

where $\rho$ is the mass density, $\mathbf{v}$ is the local velocity vector, and $\mathcal{V}$ is the volume. The local velocity vector, $\mathbf{v}$, at any location in the wing can be related to the velocity, $\dot{\mathbf{u}}$, and angular velocity, $\dot{\boldsymbol{\theta}}$, of the beam reference axis through:

$$\mathbf{v} = \dot{\mathbf{u}} + \dot{\boldsymbol{\theta}} \times \mathbf{r} \tag{3.66}$$

where $\mathbf{r}$ is the distance vector of a location in the wing with respect to the beam reference axis and a dot indicates a time derivative. Introducing beam cross-sectional properties, equation (3.65) can be rewritten in terms of the local degrees of freedom and the cross-sectional properties as:

$$\mathcal{T} = \frac{L}{2}\int_0^1 mA\dot{\mathbf{u}} \cdot \dot{\mathbf{u}} + 2\dot{\mathbf{u}}^\mathbf{t}\mathbf{m}\mathbf{Q}\dot{\boldsymbol{\theta}} + \dot{\boldsymbol{\theta}}^\mathbf{T}\mathbf{m}\mathbf{I}\dot{\boldsymbol{\theta}} d\xi \tag{3.67}$$

where $mA$ is the mass per unit length, $\mathbf{mQ}$ contains the first mass moments per unit length with respect to the beam reference axis, $\mathbf{mI}$ is the mass inertia tensor

per unit length with respect to the beam reference axis. By introducing the shape functions, as defined in equation (3.39), the element mass matrix is obtained by computing the Hessian of the kinetic energy with respect to the velocities of the degrees of freedom. Similar to the element stiffness matrix, the method of static condensation (Guyan, 1965) is used to eliminate the internal degrees of freedom and reduce the element matrix from 20 degrees of freedom to 12 degrees of freedom. Partitioning the mass matrix in degrees of freedom at the end nodes and internal degrees of freedom, the element mass matrix, corresponding to the degrees of freedom at the end nodes, becomes:

$$\mathbf{M_l} = \mathbf{M_{ll}} - \mathbf{M_{li}}{\mathbf{K_{ii}}}^{-1}\mathbf{K_{il}} - \left({\mathbf{K_{ii}}}^{-1}\mathbf{K_{il}}\right)^T\left(\mathbf{M_{il}} - \mathbf{M_{ii}}{\mathbf{K_{ii}}}^{-1}\mathbf{K_{il}}\right) \tag{3.68}$$

The global mass matrix can be obtained by transforming the local mass matrices from local to global (deformed) coordinates and using standard finite element approaches to assemble the global mass matrix from the local element matrices. Introducing the mass matrix in equation (3.64), the governing dynamic structural equation becomes:

$$\mathbf{M}\Delta\ddot{\mathbf{p}} + \mathbf{K_{s_0}}\Delta\mathbf{p} = \mathbf{K_{ext_0}}\Delta\mathbf{p} + \Delta\mathbf{F} \tag{3.69}$$

Note that in case of a fully nonlinear description of the beam kinetic energy, the kinetic energy also becomes a function of the beam displacements and rotations and not only of the beam velocities and angular velocities, thus introducing a damping term (commonly referred to as gyroscopic term) and an additional stiffness term (commonly referred to as centrifugal term) in the governing equation. In the current implementation, these terms have been neglected, so care should be taken in applying the present model to highly flexible wings undergoing large deformations. However, the present model is expected to provide a conservative approximation of the stability boundaries of the structure, since geometric structural nonlinearity introduces structural damping (Le et al., 2014).

## 3.5.2 Eccentric masses

Consider an eccentric mass with its centre of mass at location $\mathbf{x_{ec}}$, as defined in Figure 3.8a. The kinetic energy, $\mathcal{T}_{ec}$, of a lumped mass around its centre of mass is given by:

$$\mathcal{T}_{ec} = \frac{1}{2}m_{ec}\mathbf{v_{ec}^T}\mathbf{v_{ec}} + \frac{1}{2}\dot{\boldsymbol{\theta}}_{\mathbf{ec}}^{\mathbf{T}}\mathbf{I_{ec}}\dot{\boldsymbol{\theta}}_{\mathbf{ec}} \tag{3.70}$$

where $m_{ec}$ is the mass of the external mass, $\mathbf{v_{ec}}$ is the velocity vector of the centre of mass of the external mass, $\dot{\boldsymbol{\theta}}_{\mathbf{ec}}$ is the angular velocity vector of the

external mass, and $\mathbf{I_{ec}}$ is the inertia tensor of the external mass with respect to its centre of mass. Note that no coupling exists between the translational motion and rotation of the external mass, since all velocities are evaluated at the centre of mass. In order to relate the degrees of freedom of the external mass to the structural degrees of freedom, its location $\mathbf{x_{ec}}$ is projected orthogonally onto the closest structural element, similar to the implementation of eccentric forces, as discussed in Section 3.4.2 and shown in Figure 3.8a. The velocity vector of the eccentric node is related to the velocity on the beam element through the following relations:

$$\mathbf{v_{ec}} = \mathbf{v_a} + \dot{\boldsymbol{\theta}}_\mathbf{a} \times \mathbf{r} \tag{3.71}$$

$$\dot{\boldsymbol{\theta}}_\mathbf{ec} = \dot{\boldsymbol{\theta}}_\mathbf{a} \tag{3.72}$$



The degrees of freedom of point $a$ can then be related to the local element degrees of freedom, similar to the implementation of the eccentric forces, and by computing the Hessian of the kinetic energy with respect to the velocities of the degrees of freedom, the local eccentric mass matrix is obtained. Finally, the global eccentric mass matrix is obtained by transforming the local element matrices to the global coordinate system and assembling these using standard finite element approaches.

## 3.6 STRENGTH

In order to assess the structural strength, the cross-sectional modeller, developed by Ferede and Abdalla (2014) and introduced in Section 3.3, is used to convert the cross-sectional beam forces into strain in the cross-section. The cross-sectional forces, required as input for the cross-sectional modeller, can be obtained directly from the local element deformations given by the static and dynamic structural response presented in Sections 3.4 and 3.5:

$$\mathbf{F_l} = \mathbf{K_l p_l} \tag{3.73}$$

In case of the geometrically nonlinear static solution, the transformation from global beam deformations to local element deformations and vice versa are an inherent part of the computation of the stiffness matrix and all information is available to compute the cross-sectional beam forces. However, in case of the linearised dynamic simulation, the stiffness matrix and mass matrix are not updated during the analysis and, therefore, a separate transformation from the global beam deformations to the local element deformations is required.

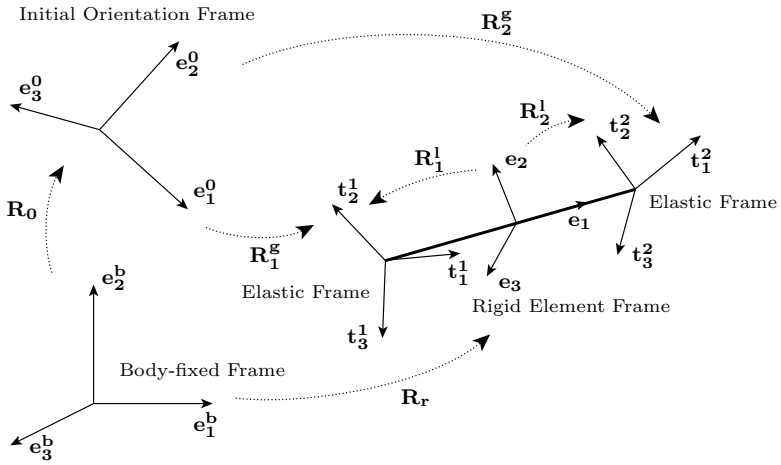


**Figure 3.9:** Definition of the different local and global coordinate frames. (Source: De Breuker (2011))

Considering a beam element with an undeformed orientation defined by a rotation matrix, $\mathbf{R_0}$, and a deformed orientation, $\mathbf{R_r}$, obtained from the geometrically nonlinear static equilibrium solution, as illustrated in Figure 3.9. Since displacements are vectorial, the local beam displacements can be obtained by rotating the global deformations from the deformed configuration to the local element configuration:

$$\mathbf{u_{l_i}} = \mathbf{R_r}^T \mathbf{u_{g_i}} \tag{3.74}$$

where $\mathbf{u}$ contains only displacements and the subscript $i$ indicates either the first node of the beam element or the second node of the beam element. Equation (3.74) is linear in the displacements and, thus, the local element displacements resulting from the dynamic disturbance can simply be computed by substituting the global dynamic disturbance displacement in equation (3.74). However, rotations are only pseudovectorial and, therefore, cannot be transformed through a rotation.

The local nodal orientation of the beam element can be obtained through two approaches: (i) a rotation from the element coordinate frame to the deformed coordinate frame, defined by $\mathbf{R_r}$ and a rotation from the deformed coordinate frame to the nodal coordinate frame, defined by $\mathbf{R_{l_i}}$ and (ii) a rotation from the element coordinate frame to the undeformed coordinate frame, defined by $\mathbf{R_0}$ and a rotation from the undeformed coordinate frame to the nodal coordinate frame, defined by $\mathbf{R_{g_i}}$. Both approaches should yield the same orientation, resulting in

the following relation:

$$\mathbf{R_r R_{l_i}} = \mathbf{R_{g_i} R_0} \tag{3.75}$$

Notice that the order of rotation between the left-hand side and right-hand side is different. The global deformations that define the nodal orientations with respect to the undeformed configuration, resulting in $\mathbf{R_{g_i}}$, are defined in the global coordinate system and follow the rotation from the element coordinate frame to the undeformed coordinate frame, $\mathbf{R_0}$, while the element rotations that define the nodal orientations with respect to the element, $\mathbf{R_{l_i}}$, are defined in the element coordinate frame and, therefore, precede the rotation from the element coordinate frame to the deformed coordinate frame, $\mathbf{R_r}$. The local element rotations are then obtained by computing the corresponding pseudo vector from $\mathbf{R_{l_i}}$ through the following relation, derived by Engø (2001):



$$\boldsymbol{\theta_i} = \log\left(\mathbf{R_{l_i}}\right) = \frac{\sin^{-1}\left(\|\mathbf{r}\|/2\right)}{\|\mathbf{r}\|}\mathbf{r} \tag{3.76}$$

where

$$\mathbf{r} = \text{axial}\left(\mathbf{R_{l_i}} - \mathbf{R_{l_i}}^T\right) \tag{3.77}$$

In case of the linearised dynamic simulation, the beam mesh is no longer updated during the simulation and, as a consequence, $\mathbf{R_r}$ is constant and equal to the geometrically nonlinear static equilibrium solution. However, the global nodal rotations are a combination of the static and dynamic deformation and $\mathbf{R_{g_i}}$ needs to be updated accordingly, consequently resulting in an update of the local element rotation matrix $\mathbf{R_{l_i}}$ according to equation (3.75). In order to obtain the local element rotations as a result of the dynamic disturbance only, the static local element rotations need to be subtracted from the total element rotations, resulting in:

$$\boldsymbol{\theta_{i}}_{dyn} = \log\left(\mathbf{R_{l_i}}\right)\big|_{stat+dyn} - \log\left(\mathbf{R_{l_i}}\right)\big|_{stat} \tag{3.78}$$

Combining the local element displacement and rotations to obtain the local element deformations, the corresponding cross-sectional forces can be obtained using equation (3.73). Note that the cross-sectional modeller assumes a constant cross-section, so sufficient beam elements should be used to obtain an accurate representation of the actual three-dimensional strain field. If more detailed strain information is required in further stages of the design process, a more detailed shell model can, for example, be used. The effect of the constant cross-sectional shape will be investigated in more detail in Section 3.8.

Once the cross-sectional forces have been determined, the Timoshenko cross-sectional stiffness matrix can be used to retrieve the corresponding beam strains and curvatures, as given by equation (3.36). Using the cross-sectional modeller, the corresponding strain field throughout the cross-section can be found, as introduced in Section 3.3.

Finally, structural failure is assessed by means of the failure envelope derived by IJsselmuiden et al. (2008). During the optimisation, classical composite strength failure criteria cannot be used, since the stacking sequence of the laminates is unknown. Therefore, IJsselmuiden et al. (2008) derived a failure envelope based on the Tsai-Wu failure criterion such that no failure occurs regardless of the ply angle. In this dissertation, the implementation of Khani et al. (2011) is used, who rederived the failure envelope in terms of principal strains.



## 3.7 BUCKLING

Structural stability is assessed by a buckling analysis of the different skin panels. Depending on the type of wing structure, buckling panels can be defined in several different ways:

- A conventional wingbox structure with ribs and stringers: the buckling panels are bounded by stringers and ribs and the ribs and stringers are expected to provide sufficient stiffness to prevent global buckling, as illustrated in Figure 3.10.
- A wingbox structure without stringers: the buckling panels are bounded by spars and ribs.
- A wing structure without spars and ribs: the complete outer shell acts a single buckling structure.

In case of a wingbox structure, in the present model, the stability of a panel in buckling is approximated based on an idealised buckling model under five assumptions.

First of all, the curvature of the load-carrying skin is assumed to be small and, therefore, the buckling panels can be approximated by their flat plate equivalent, resulting in a conservative approximation of the buckling load.

Secondly, since the wingbox is discretised using constant stiffness patches, each panel consists of a single laminate, resulting in a constant stiffness panel.

Thirdly, the load on the panel is assumed to be constant, as illustrated in Figure 3.10. In order to obtain a conservative approximation of the buckling load,

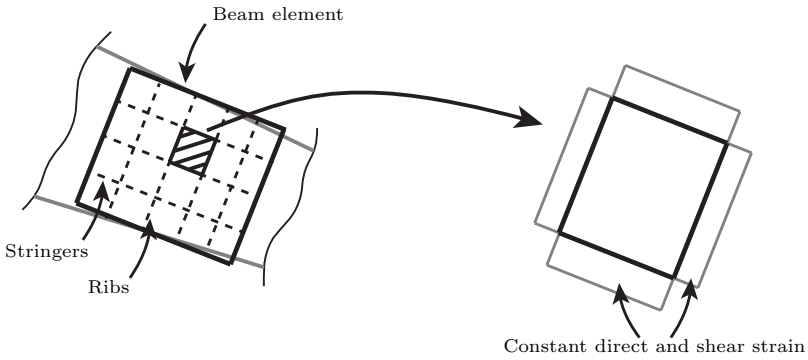


**Figure 3.10:** Schematic illustration of the selection of a buckling panel from the beam element discretisation.



first, the loads on each cross-sectional element are obtained from the cross-sectional modeller. Next, a buckling load is computed using the loads of each of the elements that define the buckling panel, as if they were acting along the complete panel. Finally the lowest buckling load is taken as the critical buckling load for the panel. When considering the wing skin, the resulting buckling load is expected to provide a good approximation of the actual buckling load, since the load distribution over a skin buckling panel is almost constant. However, when considering the spars, the bending loads will introduce a normal load distribution from tensile to compressive over the spar, and, therefore, the resulting buckling load, assuming a constant load, will be overly conservative. Therefore, it has been decided to compute the buckling load of the spars using the shear loads only and neglecting the effect of the normal load distribution. Since a significant part of the normal load is in tension, the buckling load under shear load only is still expected to provide a conservative approximation of the buckling load.

As a fourth approximation, the panel geometry is based on the beam approximation of the three-dimensional wing structure and not the actual wing structure, since the loads are also based on the beam approximation of the wing structure and not the actual wing structure.

Fifthly, the panels are considered to be simply supported. As a consequence, a detailed finite element simulation of panel buckling is not required, resulting in increased computational efficiency, while still providing a good approximation of the structural stability.

Under the aforementioned approximations, each buckling panel is approximated by a quadrilateral element. The buckling computation is based on the work by Dillinger et al. (2013). First, the panel geometry is projected onto a standard square using a bilinear transformation. The bending displacement over the panel

is approximated by multiplying one dimensional Lobatto (bubble) polynomials to obtain a set of hierarchical two-dimensional shape functions:

$$w(\xi,\eta) = \sum_p \sum_q a_{pq}\phi_p(\xi)\,\phi_q(\eta) \tag{3.79}$$

where $\phi$ are the Lobatto polynomials and $\xi$ and $\eta$ are the non-dimensional panel coordinates ranging from $-1$ to 1 corresponding to $x$ and $y$, respectively. Following an energy based approach, the strain energy, $\mathcal{U}$, and external potential energy, $\mathcal{V}$, are given by:

$$\mathcal{U} = \frac{1}{2}\mathbf{a}^T\mathbf{K}\mathbf{a} \tag{3.80}$$

$$\mathcal{V} = \frac{1}{2}\mathbf{a}^T\mathbf{K_g}\mathbf{a} \tag{3.81}$$



where $\mathbf{K}$ is the stiffness matrix, and $\mathbf{K_g}$ is the geometric stiffness matrix. The stiffness matrix, $\mathbf{K}$, is given by:

$$\mathbf{K} = \sum_{i=1,2,6} \sum_{j=1,2,6} D_{ij}\mathbf{K^{ij}} \tag{3.82}$$

where $D_{ij}$ are the components of the laminate out-of-plane stiffness matrix and the matrices $\mathbf{K^{ij}}$ are obtained by integrating the second derivatives of the shape functions. For example:

$$K^{11}_{pq} = \iint_A \frac{\partial^2\phi_p}{\partial x^2}\frac{\partial^2\phi_q}{\partial x^2}dA \tag{3.83}$$

The geometric stiffness matrix, $\mathbf{K_g}$, is given by:

$$\mathbf{K_g} = -N_x\mathbf{K^{xx}} - N_y\mathbf{K^{yy}} - N_{xy}\mathbf{K^{xy}} \tag{3.84}$$

with

$$K^{xx}_{pq} = \iint_A \frac{\partial\phi_p}{\partial x}\frac{\partial\phi_q}{\partial x}dA \tag{3.85}$$

$$K^{yy}_{pq} = \iint_A \frac{\partial\phi_p}{\partial y}\frac{\partial\phi_q}{\partial y}dA \tag{3.86}$$

$$K^{xy}_{pq} = \iint_A \frac{\partial\phi_p}{\partial x}\frac{\partial\phi_q}{\partial y}dA \tag{3.87}$$

The inverse buckling factor can then be obtained by solving the following eigenvalue problem:

$$(\mathbf{K_g} - r\mathbf{K})\,\mathbf{a} = \mathbf{0} \tag{3.88}$$

where $r$ is the inverse buckling factor. Hence, for a buckling-free panel, $r$ should be less than or equal to 1.

In case of a wing structure without any spars, ribs, or stringer, the complete outer shell acts as a single buckling surface and the assumption of flat buckling panels is no longer valid. However, since most conventional wing structures consist of a wingbox with spars, buckling of wing structures without spars has not been considered in the present dissertation. If the buckling load of wing structures without spars is required, a more detailed shell model that accounts for the curvature of the wing structure should be implemented.



## 3.8 VERIFICATION WITH LITERATURE

For verification of the structural analysis model, several verification cases were considered. First, Section 3.8.1 presents the verification of the nonlinear static structural model coupled to the cross-sectional modeller. Second, Section 3.8.2 presents the verification of the dynamic structural model including eccentric masses and, finally, Section 3.8.3 presents the verification of the assessment of structural strength, investigating the assumption of constant cross-section beam elements in more detail.

### 3.8.1 STATIC RESPONSE

First, in order to verify the link between the cross-sectional modeller and the structural model, the present nonlinear structural model is compared to experiments carried out by Chandra et al. (1990) for the structural response of anisotropic composite box beams. As an example, the beam with properties as given in Table 3.2 will be used, to verify and validate the present approach. The resulting comparison of the present approach to the experimental results and the different beam modelling approaches is shown in Figure 3.11. As can be seen, the present approach shows satisfactory agreement with the experimental results, and performs excellent compared to the other numerical approaches, thus verifying and validating the present approach.

In order to verify the implementation of external non-aerodynamic forces, the structural response of the present model is compared to a test case taken from Bathe and Bolourchi (1979), as shown in Figure 3.12a. The corresponding beam

**Table 3.2:** Composite beam properties used for verification and validation.

| Dimensions | | Layup* | | Material properties | | Loading | |
|---|---|---|---|---|---|---|---|
| Length | 0.762 m | Upper wall | $[45]_6$ | $E_{11}$ | 141.96 GPa | Tip load | 4.45 N |
| Width | 0.0242 m | Lower wall | $[-45]_6$ | $E_{22}$ | 9.79 GPa | | |
| Height | 0.0136 m | Right wall | $[45/-45]_3$ | $G_{12}$ | 6.00 GPa | | |
| | | Left wall | $[45/-45]_3$ | $\nu_{12}$ | 0.42 | | |
| | | | | $t_{ply}$ | 0.127 mm | | |

* Layup is defined with respect to the beam axis and positive with respect to the outward normal.



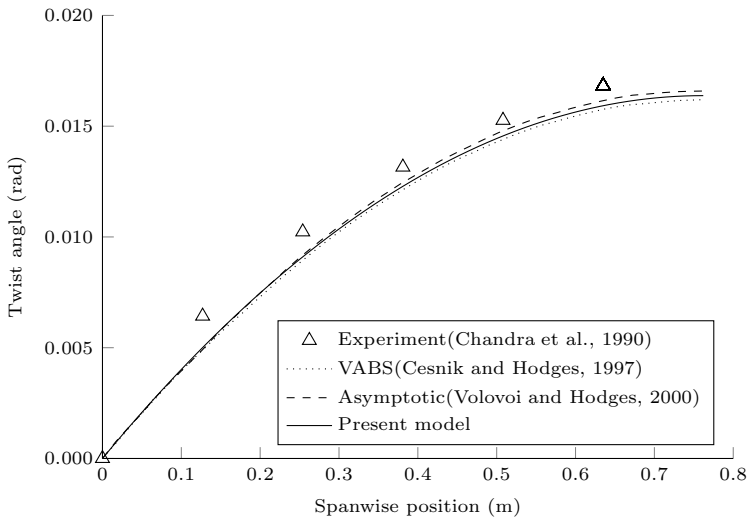


**Figure 3.11:** Verification and validation of the composite beam model with experiments and other numerical solutions.

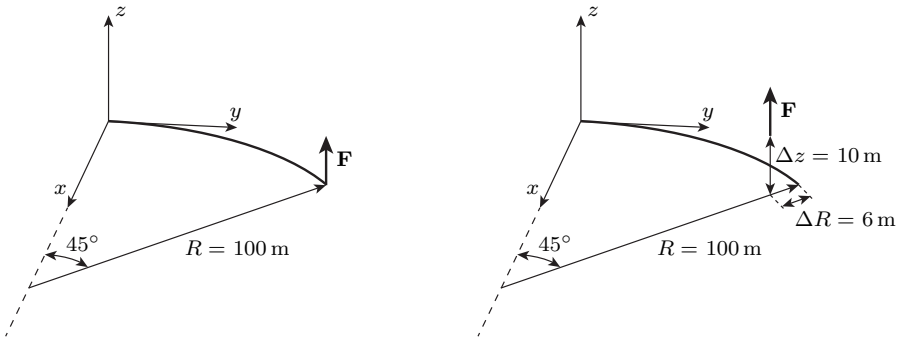


**(a)** Tip load. **(b)** Eccentric load.

**Figure 3.12:** 45 deg circular bend under tip and eccentric load.



properties and loads are given in Table 3.3. First, the resulting tip location after deformation under a constant tip load is compared to results in literature and, as can be concluded from Table 3.4, shows excellent agreement. Next, in order to verify the implementation of eccentric external forces and moments, the tip load is shifted 10 m in $z$-direction and 6 m in radial direction, as indicated in Figure 3.12b, and the results are compared to Abaqus, since to the best of the author's knowledge, no results are available in the literature. As can be seen in Figure 3.13, the resulting out-of-plane displacement and rotation about the $y-$axis shows excellent agreement with Abaqus for both a constant direction and follower force and moment, thus verifying the implementation of eccentric forces and moments.

**Table 3.3:** Beam properties.

| Cross-sectional properties | | Material properties | | Loading | | |
|---|---|---|---|---|---|---|
| Width | 1 m | $E$ | 10 MPa | Tip | $F_z = 600\,\mathrm{N}$ | $M_x = 0\,\mathrm{N\,m}$ |
| Height | 1 m | $G$ | 5 MPa | Constant eccentric | $F_z = 600\,\mathrm{N}$ | $M_x = -4000\,\mathrm{N\,m}$ |
| | | $\rho$ | $1000\,\mathrm{kg/m^3}$ | Follower eccentric | $F_z = 300\,\mathrm{N}$ | $M_x = -2500\,\mathrm{N\,m}$ |

**Table 3.4:** Comparison of the tip location (x,y,z) under various load levels.

| Load level | 300 | 450 | 600 |
|---|---|---|---|
| Present model | 22.12, 58.54, 40.48 | 18.37, 51.97, 48.70 | 15.56, 46.90, 53.60 |
| Bathe and Bolourchi (1979) | 22.5, 59.2, 39.5 | – | 15.9, 47.2, 53.4 |
| Crisfield (1990) | 22.16, 58.53, 40.53 | 18.43, 51.93, 48.79 | 15.61, 46.84, 53.71 |

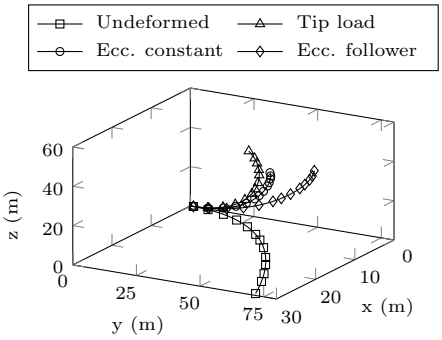


**(a)** Undeformed and deformed beam shape under different loads.

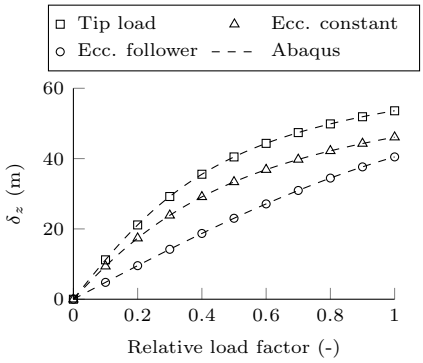


**(b)** Comparison of the out-of-plane tip displacement under different loads.

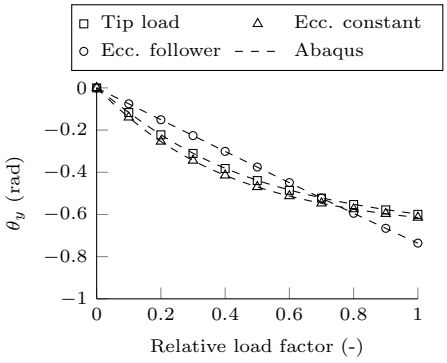


**(c)** Comparison of the rotation about the $y$-axis under different loads.

**Figure 3.13:** Verification of the implementation of eccentric forces and moments.

### 3.8.2 DYNAMIC RESPONSE

In order to verify the implementation of the linear mass matrix and the effect of the external masses, the model as described by Bathe and Bolourchi (1979), that was also used to verify eccentric loads, as specified in Table 3.3, has been extended with an eccentric tip mass, as specified in Table 3.5. The eccentric mass location is defined by Figure 3.12b. First, three different eccentric loads are applied to simulate a (non)linear static equilibrium solution, namely a force of 0 N (Linear), 75 N, and 150 N. Next, a dynamic simulation is carried out around the static equilibrium solution under a time dependent tip load, defined by:

$$F_{tip}(t) = 1000 \cdot \sin(2t)$$



**Table 3.5:** Eccentric mass properties.

| | |
|---|---|
| Mass | 10 000 kg |
| $I_{xx}$ | 30 000 kg m$^2$ |
| $I_{yy}$ | 50 000 kg m$^2$ |
| $I_{zz}$ | 100 000 kg m$^2$ |

The resulting time responses for different static equilibrium positions are given in Figure 3.14 and compared to the results obtained from Abaqus. As can be expected, in case no tip loads are applied, both models show good agreement, thus verifying the implementation of the linear mass matrix. However, as the level of nonlinearity increases, the difference between the fully nonlinear implementation in Abaqus and the quasi nonlinear implementation used in the present model increases. It should be noted, however, that for a tip load of 75 N, the tip deflection is already 16%, while the results still show good agreement. The corresponding structural frequencies show a maximum error in the first 10 eigenfrequencies of 0.3% in case no tip load is applied, 4.8% for a tip load of 75 N, and 7.8% for a tip load of 150 N, thus also showing good agreement up to a tip load of 75 N. Therefore, for general aircraft wings, the present model is expected to predict the dynamic behaviour adequately; however, care should be taken for extremely flexible aircraft wings. Furthermore, when considering dynamic aeroelastic stability, the present model is expected to give a conservative approximation of the stability boundaries, since geometric structural nonlinearity introduces structural damping (Le et al., 2014), which is not taken into account in the present model.

### 3.8.3 STRENGTH

In order to investigate the effect of the assumption of constant cross-section beam elements on the strain calculations, the present model is compared to several FEM shell models analysed in Abaqus. First, a wingbox with no sweep, taper,

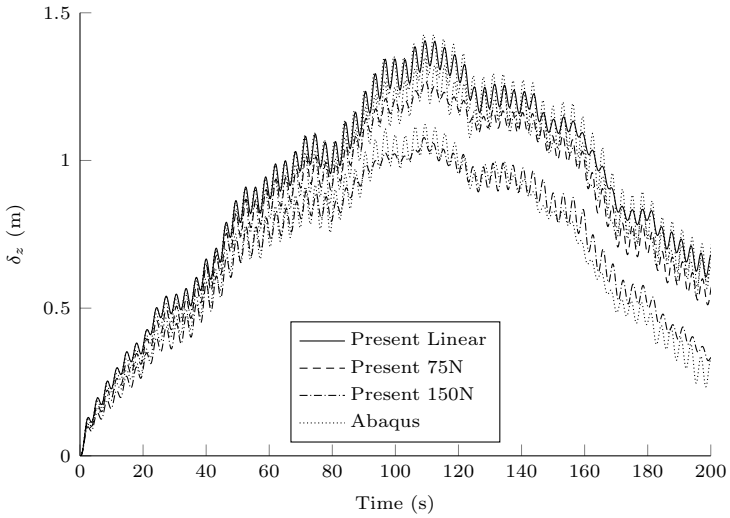


**Figure 3.14:** Tip displacement around the nonlinear static equilibrium position under a time dependent tip load.



or dihedral and a rectangular cross-section is analysed to investigate the effect of the warping restraint at the root on the strain distribution in the wing. The wing geometry and applied loads, and material properties and layups are given in Table 3.6 and Table 3.7, respectively.

**Table 3.6:** Rectangular wing geometry and applied loads used for verification of the strain calculations.

| Dimensions | | Loading | |
|---|---|---|---|
| Length | 1.0 m | Tip load* | 400 N |
| Width | 60 mm | | |
| Height | 20 mm | | |

* Load is applied in the centre of the cross-section.

Figure 3.15 and Figure 3.16 show the corresponding strain results for the quasi-isotropic and tailored wingbox, as defined by Table 3.6. For clarity, only the critical principal strains are shown for each of the components of the wingbox. Similar conclusions can be drawn for the other principal strain components. As is expected and can be seen in Figure 3.15, in case of a quasi-isotropic wing where no warping is present, the present beam model and Abaqus show excellent agreement. In Abaqus, the Poisson deformations in the cross-sectional plane are restricted at the wing root, resulting in slight stress concentrations that are not present in a beam model. However, in reality, the surrounding structure of the wing will allow

**Table 3.7:** Material properties and layups used for verification of the strain calculations.

| Material properties | | Layups* | |
|---|---|---|---|
| $E_{11}$ | 141.96 GPa | Quasi-isotropic | $[0/45/-45/90]_s$ |
| $E_{22}$ | 9.79 GPa | Tailored top/bottom | $[0/30/0/30]_s$ |
| $G_{12}$ | 6.00 GPa | Tailored spars | $[45/-45/45/-45]_s$ |
| $\nu_{12}$ | 0.42 | | |
| $t_{ply}$ | 0.25 mm | | |

* Layup is defined with respect to the beam axis and positive with respect to the outward normal.

for small cross-sectional deformations, thus alleviating these strains.



When looking at the results for the tailored wingbox shown in Figure 3.16, the effect of the warping restraint at the wing root can clearly be observed. However, the resulting wing strains are still within 10% of the Abaqus model and are, therefore, considered sufficiently accurate for the purpose of conceptual design. As expected, the strains in the remainder of the wing shows excellent agreement to the Abaqus results, thus verifying the present beam model.

Finally, in order to investigate the effect of constant cross-section beam elements on the strain distribution of a swept, tapered wing with wing dihedral, the wing geometry given in Table 3.8 has been analysed using the laminates as defined in Table 3.7. As expected, the error between the present model and Abaqus increases and the effect of the wing geometry can clear be observed. However, the resulting wing strains are within 15% of the Abaqus model and the correct spanwise strain distribution is still captured by the beam model. Therefore, the optimisation results are still expected to provide a good estimate of the potential benefits of aeroelastic tailoring. In order to find a design that still satisfies the structural strength requirements, an additional knockdown factor can, for example, be applied on the strain allowables during the conceptual design optimisation.

**Table 3.8:** Swept, tapered wing used for verification of the strain calculations.

| Dimensions | | Loading | |
|---|---|---|---|
| Length | 1.0 m | Tip load* | 100 N |
| Root width | 60 mm | | |
| Root height | 20 mm | | |
| Sweep | 30 deg | | |
| Dihedral | 10 deg | | |
| Taper ratio | 0.3 | | |

* Load is applied in the centre of the cross-section.

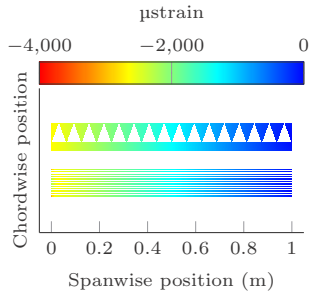


**(a)** $\epsilon_{min}$ on the top skin. (top: present model, bottom: Abaqus)

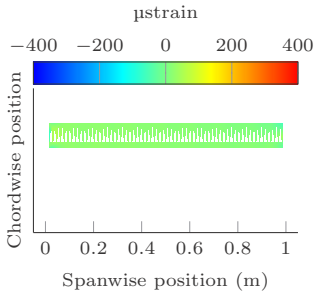


**(b)** Difference in $\epsilon_{min}$ on the top skin between the present model and Abaqus.

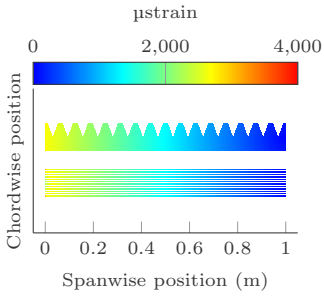


**(c)** $\epsilon_{max}$ on the bottom skin. (top: present model, bottom: Abaqus)

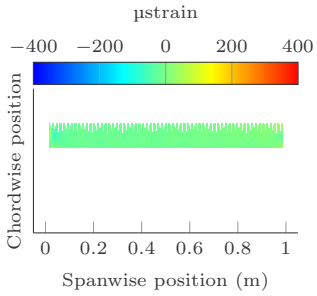


**(d)** Difference in $\epsilon_{max}$ on the bottom skin between the present model and Abaqus.

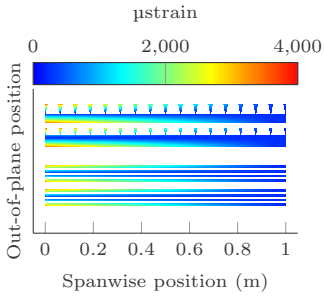


**(e)** $\gamma_{max}$ on the spars, front to rear from top to bottom. (top two: present model, bottom two: Abaqus)

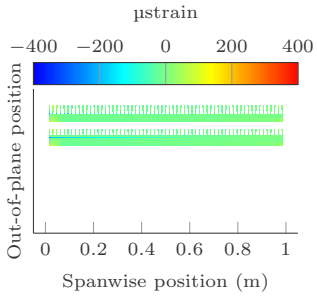


**(f)** Difference in $\gamma_{max}$ on the spars between the present model and Abaqus, front to rear from top to bottom.

**Figure 3.15:** Strain distribution of a rectangular wingbox structure with quasi-isotropic laminates. (Note: the wingbox width and height have been scaled by a factor 2 and 4, respectively, for better visualisation.)

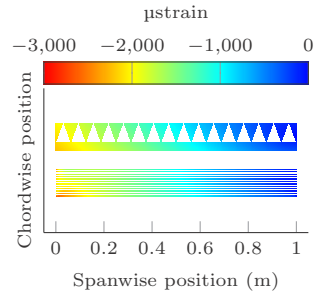


**(a)** $\epsilon_{min}$ on the top skin. (top: present model, bottom: Abaqus)

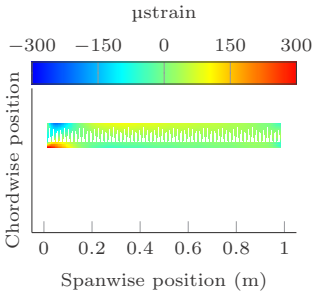


**(b)** Difference in $\epsilon_{min}$ on the top skin between the present model and Abaqus.

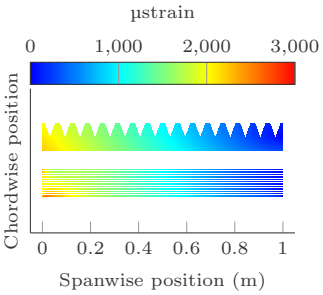


**(c)** $\epsilon_{max}$ on the bottom skin. (top: present model, bottom: Abaqus)

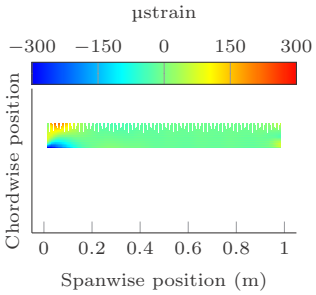


**(d)** Difference in $\epsilon_{max}$ on the bottom skin between the present model and Abaqus.

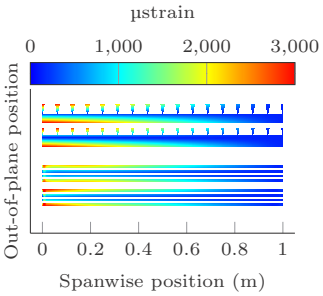


**(e)** $\gamma_{max}$ on the spars, front to rear from top to bottom. (top two: present model, bottom two: Abaqus)

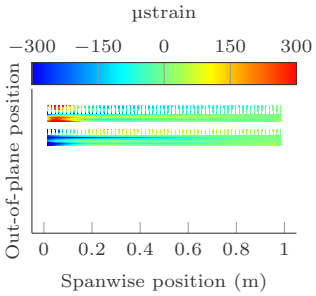


**(f)** Difference in $\gamma_{max}$ on the spars between the present model and Abaqus, front to rear from top to bottom.

**Figure 3.16:** Strain distribution of a rectangular wingbox structure with tailored laminates. (Note: the wingbox width and height have been scaled by a factor 2 and 4, respectively, for better visualisation.)

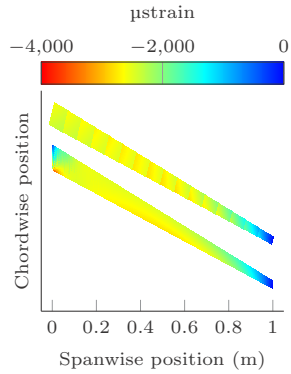


**(a)** $\epsilon_{min}$ on the top skin. (top: present model, bottom: Abaqus)

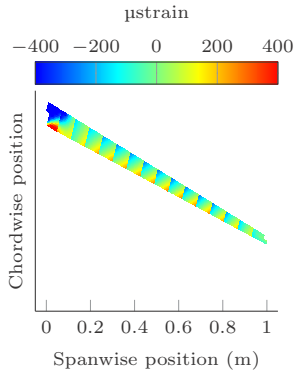


**(b)** Difference in $\epsilon_{min}$ on the top skin between the present model and Abaqus.

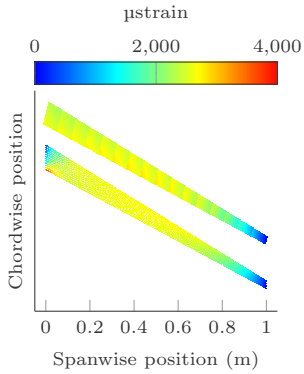


**(c)** $\epsilon_{max}$ on the bottom skin. (top: present model, bottom: Abaqus)

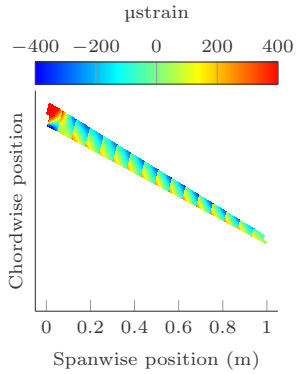


**(d)** Difference in $\epsilon_{max}$ on the bottom skin between the present model and Abaqus.

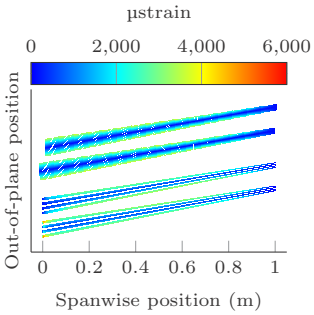


**(e)** $\gamma_{max}$ on the spars, front to rear from top to bottom. (top two: present model, bottom two: Abaqus)

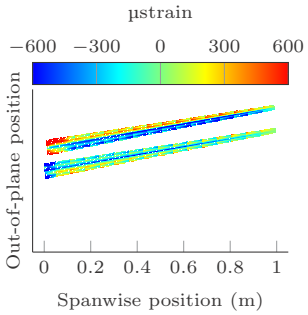


**(f)** Difference in $\gamma_{max}$ on the spars between the present model and Abaqus, front to rear from top to bottom.

**Figure 3.17:** Strain distribution of a swept tapered wingbox structure with tailored laminates. (Note: the wingbox width and height have been scaled by a factor 2 and 4, respectively, for better visualisation.)

## 3.9 LIMITATIONS OF THE MODEL

The goal of the aeroelastic analysis and optimisation framework presented in this dissertation is to improve the conceptual design of aircraft wings by including aeroelasticity. Therefore, the structural model was selected as a trade-off between computational efficiency and accuracy and, consequently, a number of assumptions have been made. In case of the structural model, this results in the following main limitations of the model:



- The composite laminates have been modelled using lamination parameters. As a consequence, a stacking sequence retrieval step is required, resulting in a slight loss of performance when converting the lamination parameters to an actual stacking sequence.
- The cross-sectional modeller assumes a rigid, constant cross-sectional geometry, which is valid for aircraft wing structures, as long as sufficient ribs are present to preserve the cross-sectional shape and the wing is modelled using a sufficient number of sections to model a varying geometry along the span.
- The stringers are modelled as equivalent blade stringers, which is only valid as long as the stringers are small with respect to the cross-sectional geometry.
- Small dynamic perturbations with respect to the static equilibrium solution are assumed, such that a linearised dynamic structural analysis can be carried out around the geometrically nonlinear static equilibrium solution for computational efficiency.
- The accuracy of the recovered three-dimensional strain field is affected by the assumption of a constant cross-sectional shape. The results show that, as long as a sufficient number of sections is used, the strain results are sufficiently accurate for conceptual design. However, if more detailed strain information is required in further stages of the design process, a more detailed shell model can, for example, be used.
- The ribs and stringers are assumed to provide sufficient stiffness to prevent global buckling, making panel buckling in between ribs and stringers the dominant buckling mode.
- For computational efficiency, the geometry of the buckling panels is assumed to be flat and based on the beam cross-sectional geometry and loads. If more detailed buckling information is required in further stages of the design process, a more detailed shell model can, for example, be used.

When interpreting the results obtained by the framework, one should always keep these limitations in mind.

## 3.10 SYNOPSIS

In this chapter, a structural model that can analyze composite wing box structures and is suitable for structural optimisation has been formulated.

- The wingbox is discretised in several spanwise beam sections with a constant cross-section.
- Each spanwise section can have its own composite laminate distribution throughout the wing cross-section to allow for aeroelastic tailoring along the span and throughout the cross-section.
- The composite laminates are described using lamination parameters to make the framework suitable for gradient-based optimisation.
- The Timoshenko cross-sectional stiffness matrix is obtained under a thin-walled assumption through a cross-sectional modeller that discretises the cross-section using linear Hermitian shell elements.
- A geometrically nonlinear model is obtained by embedding linear Timoshenko beam elements in a co-rotational framework.
- The dynamic response is obtained by carrying out a linear dynamic simulation around the nonlinear static equilibrium solution.
- The effects of eccentric forces, moments, and masses have been accounted for through a rigid link to the closest beam element.
- Structural strength is assessed by retrieving the three-dimensional wing strains from the one-dimensional beam strains through the cross-sectional modeller.
- Structural stability is assessed by an idealised buckling model under the assumption of flat, constant stiffness panels in between ribs and stringers.

*It always seems impossible until it's done.*
**Nelson Mandela**

# 4

# AERODYNAMIC ANALYSIS[1]

As outlined in the introduction to this dissertation, in order to assess the potential benefits of aeroelastic tailoring and morphing, an aeroelastic model that incorporates the effects of aeroelastic tailoring and morphing is required. One of the requirements of an aeroelastic model is an aerodynamic model. In order to account for dynamic aeroelastic instabilities and obtain the response of a wing to, for example, a gust, an unsteady aerodynamic model is required. Current models, however, are either computationally too expensive to be used for loads analysis in preliminary design, or do not allow for accurate time domain analyses of the gust response of any generic wing shape. Therefore, this chapter presents an unsteady aerodynamic model that is both computationally efficient and directly written in a continuous-time state-space form to allow for accurate time domain analyses of the gust response of a wing.

This chapter is split in ten sections. Section 4.1 presents an overview of aerodynamic modelling for loads analysis, illustrating the most commonly used models in loads analysis and their advantages and disadvantages. Next, Section 4.2 provides a brief explanation of potential flow theory in aerodynamics, which is used as the basis for the aerodynamic model. The vortex ring elements used to discretise the wing surface and trailing wake are presented in Section 4.3, after which the conventional steady aerodynamic solution is presented in Section 4.4 for com-

[1]This chapter is based on the journal paper Werter, N.P.M., De Breuker, R., and Abdalla, M.M., *"Continuous-time state-space unsteady aerodynamic modelling for efficient loads analysis"*, AIAA Journal, revision under review.

pleteness. The novel continuous-time formulation of the unsteady vortex lattice method (UVLM) that has been developed as lifting surface solution method to obtain the unsteady aerodynamic solution is discussed in Section 4.5, followed by the computation of the aerodynamic drag in Section 4.6. The model is verified by applying it to several steady, unsteady, and compressible benchmark solutions, which is discussed in Section 4.7. Next, in order to illustrate the benefits of the developed unsteady aerodynamic model, the model is applied to the discrete gust analysis of a wing, as discussed in Section 4.8. Finally, the limitations of the presented aerodynamic model and a synopsis are given in Section 4.9 and Section 4.10, respectively.

## 4.1 AERODYNAMIC MODELLING FOR LOADS ANALYSIS



There are several ways to predict the unsteady aerodynamic loads on an aircraft. Murua et al. (2012a) give an overview of unsteady aerodynamic modelling for loads analysis. The three most commonly used methods are two-dimensional unsteady airfoil theory, the doublet lattice method (DLM), and the unsteady vortex lattice method (UVLM). A brief overview of each of these methods will be given in the following paragraphs. More recently, also CFD-based methods have gained popularity for the analysis of, for example, limit-cycle oscillations (Beran et al., 2004; Kholodar et al., 2004; Thomas et al., 2002, 2004), flutter (Farhat, 2004; Geuzaine et al., 2003), gust response (Raveh, 2007, 2011; Raveh et al., 2001; Reimer et al., 2015), and transonic shock buffet (Iovnovich and Raveh, 2012; Raveh and Dowell, 2014). However, currently these methods are still computationally too costly to be applied for dynamic loads analysis in the preliminary design of aircraft.

Two-dimensional unsteady airfoil theory is generally referred to as strip theory. It uses closed-form solutions for several specific cases (i.e. impulsive flows, step gusts, harmonic oscillations, and sinusoidal gusts) in order to set up a state-space system to determine the unsteady aerodynamic loads. Strip theory has extensively been used for high-altitude, long-endurance (HALE) aircraft modelling (Patil and Hodges (2004); Patil et al. (2001b)). Two different methods to obtain a state-space system from the closed-form solutions are commonly used: Peters's finite-state method (Peters et al. (1995)) and the indicial method of Leishman (Leishman and Nguyen (1990)). The main advantages of strip theory are its simplicity and that it allows for easy corrections for, for example, stall. However, the main disadvantage of strip theory is that it is based on 2D unsteady airfoil theory with 3D corrections and thus it cannot give any accurate information about the spanwise loading distribution.

The doublet lattice method, introduced by Albano and Rodden (1969), is probably the most widely used method for unsteady loads analysis of aircraft. One of

the advantages of DLM is that compressibility is captured in the analysis. DLM assumes harmonic displacements on the natural vibration modes of the wing to determine the aerodynamic influence coefficients (AICs) for several reduced frequencies and flight conditions. The solution is converted from the frequency domain to the time domain by means of a rational function approximation (RFA). There are two well-known techniques for the RFA: Roger's approach using Padé approximants (Roger (1977)) and Karpel's minimum-state method (Karpel (1982)). The setup in the frequency domain makes the method especially suitable for flutter analysis. However, when time domain simulations are required, an incorrect selection of lag terms in the RFA can have a significant effect on the accuracy of the results. Especially when a discrete gust is modelled, the time lags, resulting from the convection of the gust over the wing, that are expressed as phase shifts in the frequency domain, make the approximation of the gust response in the time domain by means of a RFA problematic. In order to overcome this problem, two methods were introduced: (i) dividing the aerodynamic model into several aerodynamic zones, each having their own gust input (Karpel et al. (2005)) and (ii) the physical RFA introduced by Kier and Looye (2009), where instead of applying the RFA on the AICs in generalized coordinates, the RFA is applied to the AICs at a panel level resulting in a gust input per aerodynamic panel such that the time lags can be modelled directly. Both methods, however, result in an increase in the number of aerodynamic states and still use harmonic aerodynamic data to predict the transient aerodynamic response. Furthermore, a wide range of reduced frequencies has to be covered to ensure accurate results.



The unsteady vortex lattice method uses a distribution of vortex rings over the mean aerodynamic surface and wake to solve the potential flow equations. Katz and Plotkin (2001) give a good overview of the implementation of UVLM. The main advantages of UVLM are that it is written in time domain and thus the transient aerodynamic response is computed directly, and that it allows for modelling of a free wake and can thus be used for the computation of the flow around wings undergoing large motions. Therefore UVLM has recently become popular for the accurate analysis of HALE aircraft wings undergoing large deformations (Murua et al. (2012a)). Furthermore, UVLM can be written in a discrete-time state-space system (Hall (1994); Murua et al. (2012b)), allowing easy integration with other disciplines. More recently, Stewart et al. (2016) converted this discrete-time form of the wake-shedding equation to a continuous-time representation by means of a central differencing scheme, following a similar approach as introduced by Mohammadi-Amin et al. (2012) who used a backward Euler scheme to obtain a continuous-time representation for a boundary element solution based on constant strength doublet panels.

Within this field, the present dissertation proposes a continuous-time state-space formulation of UVLM, that, in contrast to Mohammadi-Amin et al. (2012) and Stewart et al. (2016), is directly derived through a discretisation of the governing advection equation for transport of vorticity in the wake by means of the

discontinuous Galerkin method and not based on an underlying discrete-time discretisation. In case the incompressible flow equations are solved, a continous-time system is directly obtained by only discretising the advection equation of wake vorticity in space, while retaining the derivative with respect to time. As a consequence, the present method can (i) be applied to any arbitrary flat or non-flat wake shape, (ii) be applied to a non-uniform wake discretisation taking advantage of the diminishing influence of vorticity as it is advected in the wake, and (iii) be easily extended to higher order panel methods.

Furthermore, in order to assess the range of validity of UVLM for unsteady subsonic compressible flows, i.e. neglecting the time-dependent terms in the governing equation, the Prandtl-Glauert transformation is applied to the presented continuous-time formulation and the incompressible flow solution procedures are applied to the transformed geometry. It should be noted that in case of a solution to the full compressible governing equation including time-dependent terms, the presence of time delays in the governing boundary integral equation requires a discretisation of the governing equations in both space and time (see Morino (1993)). Therefore, in this case, an equivalent continuous-time representation can only be sought through a discrete-time formulation.



## 4.2 POTENTIAL FLOW THEORY

When the flow conditions around a wing correspond to very high Reynolds numbers, exhibit no strong shocks, neglecting transonic effects, and under small angles of attack, the small disturbance velocity potential can be introduced and the Prandtl-Glauert equation is obtained (see, for example, Blair (1992), Morino (1993), or any textbook on aerodynamics). In order to investigate the validity of the proposed model for unsteady compressible flows, the Prandtl-Glauert transformation ($\bar{x} = x/\sqrt{1-M^2} = x/\beta$, $\bar{y} = y$, $\bar{z} = z$) is applied, resulting in the following governing equation:

$$\frac{\partial^2 \phi}{\partial \bar{x}^2} + \frac{\partial^2 \phi}{\partial \bar{y}^2} + \frac{\partial^2 \phi}{\partial \bar{z}^2} = \left( \frac{2M}{a\sqrt{1-M^2}} \right) \frac{\partial^2 \phi}{\partial \bar{x} \partial t} + \left( \frac{1}{a^2} \right) \frac{\partial^2 \phi}{\partial t^2} \tag{4.1}$$

where $M$ is the Mach number, $a$ is the speed of sound, and $\phi$ is the disturbance velocity potential defined as:

$$\mathbf{V} = \mathbf{V}_{\boldsymbol{\infty}} + \nabla_{\mathbf{x}} \phi \tag{4.2}$$

where $\mathbf{V}$ is the local velocity vector, $\mathbf{V}_{\boldsymbol{\infty}}$ is the free-stream velocity vector, and the subscript $\mathbf{x}$ indicates the $xyz$-coordinate system.

In case of steady flow, the right hand side reduces to zero and the Laplace equation is obtained such that incompressible flow solution procedures can be used to obtain the compressible flow solution. In case of unsteady flow, in order to find the compressible flow solution, the time dependent terms need to be considered as well. However, for low to moderate subsonic Mach numbers, the right-hand side is relatively small and the solutions to the unsteady Prandtl-Glauert equation can by approximated by solutions to the Laplace equation for the small disturbance velocity potential, which holds for both steady and unsteady flow conditions:

$$\nabla^2_{\bar{\mathbf{x}}}\phi = 0 \tag{4.3}$$

The validity of the Laplace equation for compressible unsteady aerodynamics is thus dependent upon the Mach number and the level of unsteadiness of the flow. A common measure for the level of unsteadiness in the flow is the reduced frequency, defined through:

$$k = \frac{\omega b}{V_\infty} \tag{4.4}$$



where $k$ is the reduced frequency, $\omega$ is the frequency of the flow perturbations and $b$ is the reference half-chord. As long as the either the reduced frequency or the Mach number is low to moderate, the incompressible flow solution is expected to approximate the unsteady compressible flow solution by applying the Prandtl-Glauert transformation and solving the Laplace equation, as supported by the numerical results in Section 4.7.3.

To complete the definition of the problem, boundary conditions need to be specified. For the aerodynamics of aircraft, these in general consist of a boundary condition enforcing flow tangency on the wing surface and a boundary condition at infinity that ensures the flow disturbance vanishes at infinity:

$$(\nabla_{\mathbf{x}}\phi + \mathbf{V_\infty} - \mathbf{V_b}) \cdot \mathbf{n} = 0, \text{ flow tangency on the wing surface} \tag{4.5}$$

$$\lim_{|\mathbf{x}-\mathbf{x_0}|\to\infty} \nabla_{\mathbf{x}}\phi = \mathbf{0}, \text{ far field condition} \tag{4.6}$$

where $\mathbf{n}$ is the surface unit normal vector, $\mathbf{x_0}$ is the position vector on the wing surface, $\mathbf{x}$ is the position vector of the location of interest, and $\mathbf{V_b}$ is the velocity of the wing surface with respect to the free-stream velocity as, for example, introduced by aeroelastic deformations.

In order to model a lifting surface by means of potential flow theory, a wake surface trailing the wing needs to be introduced, which is a surface of discontinuity for

$\phi$. The transport of vorticity on this wake surface is governed by the advection equation, as, for example, derived by Morino (1993):

$$\frac{\partial \Delta\phi}{\partial t} + \mathbf{V_w} \cdot \nabla \Delta\phi = 0 \tag{4.7}$$

where $\Delta\phi$ is the jump in velocity potential over the wake surface and $\mathbf{V_w}$ is the local velocity on the wake surface.

A common assumption in aeroelasticity (see, for example, Giesing et al. (1971)) is that the wake surface is rigidly connected to the wing and convected with the free-stream velocity such that equation (4.7) reduces to:

$$\frac{\partial \Delta\phi}{\partial t} + \mathbf{V}_\infty \cdot \nabla \Delta\phi = 0 \tag{4.8}$$



which is a valid assumption as long as the motions of the wing remain small with respect to the reference configuration.

In order to find a solution to the problem, the jump in velocity potential in the wake needs to be related to the velocity potential on the wing surface. For steady flow conditions, this relation can be found through the Kutta condition that states that the flow leaves the sharp trailing edge of an airfoil smoothly and the velocity there is finite, resulting in:

$$\Delta\phi_b|_{TE} = \Delta\phi_w|_{TE} \tag{4.9}$$

where $\Delta\phi_b$ is the potential difference on the body and $\Delta\phi_w$ is the corresponding potential difference in the wake along the same streamline. Katz and Plotkin (2001) provide a discussion on the validity of the Kutta condition for unsteady flow conditions, concluding that for small amplitude motions at a reduced frequency smaller than 0.6, the Kutta condition can be assumed to be valid. Most airplane manoeuvres comply with these conditions and, therefore, the use of the Kutta condition for unsteady aerodynamic flow around aircraft is justified.

### COMPRESSIBLE BOUNDARY CONDITIONS

In order to investigate the effect of compressibility, the Prandtl-Glauert transformation also needs to be applied to the boundary conditions. In case of compressibility, the boundary condition at infinity still holds, however the flow tangency condition, given by equation (4.5), is dependent on the induced velocity, $\nabla\phi$, at the wing surface and is therefore affected by the transformation. Defining the

wing surface as, $S(x, y, z, t) = 0$, such that the surface normal, $\mathbf{n}$, is given by $\nabla S$, the flow tangency condition, given by equation (4.5), can be written as:

$$(\mathbf{V_\infty} - \mathbf{V_b} + \nabla_\mathbf{x}\phi) \cdot \nabla_\mathbf{x} S = 0 \tag{4.10}$$

and introducing the Prandtl-Glauert transformation:

$$\left(\mathbf{V_\infty} - \mathbf{V_b} + \begin{bmatrix} \frac{1}{\beta}\frac{\partial\phi}{\partial\bar{x}} & \frac{\partial\phi}{\partial\bar{y}} & \frac{\partial\phi}{\partial\bar{z}} \end{bmatrix}\right) \cdot \nabla_\mathbf{x} S = 0 \tag{4.11}$$

$$(\mathbf{V_\infty} - \mathbf{V_b}) \cdot \nabla_\mathbf{x} S + \underbrace{\begin{bmatrix} \frac{\partial\phi}{\partial\bar{x}} & \frac{\partial\phi}{\partial\bar{y}} & \frac{\partial\phi}{\partial\bar{z}} \end{bmatrix}}_{\nabla_{\bar{\mathbf{x}}}\phi} \cdot \begin{bmatrix} \frac{1}{\beta}\frac{\partial S}{\partial x} & \frac{\partial S}{\partial y} & \frac{\partial S}{\partial z} \end{bmatrix} = 0 \tag{4.12}$$

As can be seen, the flow tangency boundary condition in the compressible flow solution can be computed using incompressible flow solution routines, as long as the Prandtl-Glauert transformation is applied to the wing geometry and the $x$-component of the surface normal is divided by $\beta$.



## 4.3 VORTEX RING ELEMENTS

In order to solve the potential flow problem, a collocation method is commonly used. In this dissertation, the wing is modelled by vortex ring elements on its camber surface under a thin-wing approximation. As illustrated in Figure 4.1, the camber surface of the wing, the first row of wake elements trailing the wing, and the free wake are discretised by $N_b$, $N_{w_0}$, and $N_w$ quadrilateral elements, respectively. Note that the jump in velocity potential over the wing surface and the wake, as present in the governing potential flow equations presented in Section 4.2, is equal to the vortex strength of the vortex ring elements (i.e. $\Delta\phi = \Gamma$).

First, Section 4.3.1 presents the discretisation of the camber surface of the wing and the corresponding wake by means of quadrilateral elements, after which Sections 4.3.2 and 4.3.3 present the corresponding discretised governing equations for the flow tangency condition and Kutta condition. Finally, Section 4.3.4 presents the computation of the aerodynamic forces and moments.

Once the flow tangency condition, Kutta condition, and computation of aerodynamic forces and moments have been discretised, the steady aerodynamic solution can be obtained, as will be presented in Section 4.4. In order to obtain the complete unsteady aerodynamic model, the transport of vorticity in the wake (equation (4.8)) also needs to be discretised, as will be presented in Section 4.5.

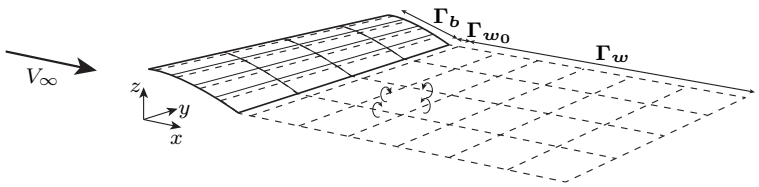


**Figure 4.1:** Example wing discretisation using vortex ring elements. The thick solid lines indicate the wing outer contour, the thin solid lines indicate the panel distribution, and the dashed lines indicate the vortex ring elements.

### 4.3.1 AERODYNAMIC DISCRETISATION

In case of vortex ring elements, as illustrated in Figure 4.1, each aerodynamic panel consists of a vortex ring with its leading segment on the panel's quarter chord line, and the collocation point at the centre of the three-quarter chord line. The vortex strength, $\Gamma$, is constant for each panel and is defined positive as illustrated by the vortex ring element in Figure 4.1.



The aerodynamic mesh is defined by a spanwise reference line (e.g. the quarter chord line of the wing), the wing twist distribution with respect to this reference line, and the wing camber distribution. The coordinate system is defined such that the $x$-direction is aligned with the free-stream velocity and the $xz$-plane is the aircraft symmetry plane.

In spanwise direction, the camber surface of the wing is discretised with a half-cosine distribution towards the wing tip to improve the accuracy of the solution at the wing tip. At each spanwise location, the aerodynamic mesh at zero aircraft angle of attack is defined through the chord vector, $\mathbf{c_0}$, and the section normal, $\mathbf{n}$, as illustrated in Figure 4.2. The section normal is defined as the vector perpendicular to the free-stream velocity and the spanwise reference axis. In order to obtain the chord vector, first, the deformed chord vector, $\mathbf{c_0^*}$, is obtained through two consecutive rotations: (i) the initial wing twist, defined by a rotation matrix, $\mathbf{R_{ini}}$, and (ii) the wing twist originating from the structural deformations, defined by a rotation matrix, $\mathbf{R_s}$, resulting in:

$$\mathbf{c_0^* = R_s R_{ini} c_{0_{ini}}} \tag{4.13}$$

with $\mathbf{c_{0_{ini}}} = \begin{pmatrix} 1 & 0 & 0 \end{pmatrix}^T$. In order to improve the efficiency of the aerodynamic model and ensure that all lift is generated by the leading vortices, the deformed chord vector, $\mathbf{c_0^*}$, is projected onto the plane spanned by the free-stream velocity, $\mathbf{V_\infty}$, and the section normal, $\mathbf{n}$, to obtain the chord vector, $\mathbf{c_0}$, as illustrated in Figure 4.2.

Given a normalised chordwise panel distribution, $\mathbf{x_{loc}}$, between the leading edge

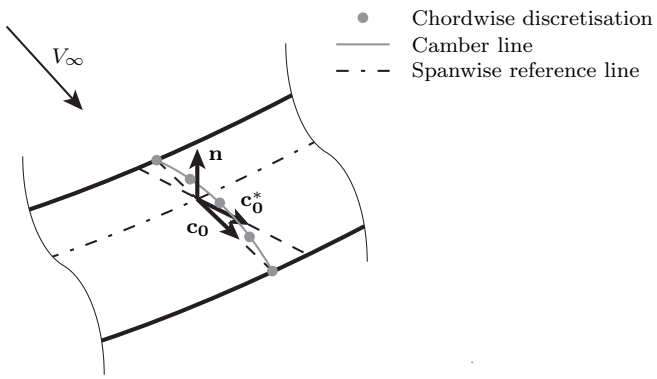


**Figure 4.2:** Wing segment illustrating the chordwise discretisation of the camber surface.

and trailing edge, the chord vector and section normal can be used to obtain the aerodynamic grid locations at each spanwise section, $i$, through:

$$\mathbf{x_{ij}} = \mathbf{x_{0_i}} + \left(\left(x_{loc_j} - x_{ref_i}\right) \cdot \mathbf{c_{0_i}} + z_{cam_{ij}} \cdot \mathbf{n_i}\right) \cdot c_i \tag{4.14}$$

where $\mathbf{x_0}$ is the location of the spanwise reference line, $\mathbf{x_{ref}}$ is the normalised location of the reference line with respect to the leading edge, $\mathbf{c}$ is the wing chord distribution, and $\mathbf{z_{cam}}$ is the normalised wing camber distribution. Figure 4.2 shows an example of the resulting chordwise discretisation. Next, the complete aerodynamic mesh is rotated with the aircraft angle of attack to align it with the global aerodynamic coordinate system.

Finally, the wake needs to be included. In case of a steady aerodynamic solution, the vortex strength in the wake is constant in flow direction and for each spanwise section only one semi-infinite wake element aligned with the free-stream flow is sufficient.

However, in case of unsteady aerodynamic flow, the vortex strength in the wake is no longer constant and the wake needs to be discretised in flow direction. In this case, two sections can be identified: (i) the panels directly trailing the wing, $\mathbf{\Gamma_{w_0}}$, and (ii) the free wake panels, $\mathbf{\Gamma_w}$, as illustrated in Figure 4.1.

Special care needs to be taken for the panels directly trailing the trailing edge. From a physical point of view, this can be interpreted by looking at the starting vortex. At the first time step, when the vortex strength in the wake is still 0, the closing vortex of the first wake panel can be interpreted as the starting vortex that develops and is a lumped representation of the continuous vortex sheet shed during the initial time step. As argued by Katz and Plotkin (2001), this vortex should be placed around 0.25 of the distance covered by the following wake panel. Under the assumption of small perturbations, the remaining wake is shed parallel

to the initial free stream flow and a rigid wake is obtained.

The only parameter that is left to be investigated is the distance at which the prescribed wake is truncated. As the distance between the shed vortices and the wing increases, their influence diminishes. Therefore, the wake can be truncated after a certain distance aft of the wing without a significant influence on the resulting aerodynamic forces and moments.

### 4.3.2 FLOW TANGENCY CONDITION

The flow tangency condition, given by equation (4.5), is satisfied at the $N_b$ collocation points on the wing surface, as defined in Section 4.3.1. The normal velocity induced by the vortex ring of panel $j$ on the collocation point of panel $i$, i.e. $(\nabla\phi \cdot \mathbf{n})_{ij}$, is defined by:

$$(\nabla\phi \cdot \mathbf{n})_{ij} = \underbrace{\nabla\phi^*_{ij} \cdot \mathbf{n_i}}_{A_{ij}} \Gamma_j \tag{4.15}$$



where $A_{ij}$ are the aerodynamic influence coefficients and $\nabla\phi^*$ is the velocity induced by a vortex ring of unit strength.

Taking advantage of the symmetry of the aerodynamic solution about the aircraft symmetry plane, the aerodynamic solution is obtained by modelling a single wing, while accounting for the effect of the symmetric wing through (Katz and Plotkin, 2001):

$$(\nabla\phi \cdot \mathbf{n})^{sym}_{ij} = \nabla\phi^*_{ij}\big|_{\mathbf{x_c}=(x_i,-y_i,z_i)} \cdot \begin{pmatrix} n_{x_i} \\ -n_{y_i} \\ n_{z_i} \end{pmatrix} \Gamma_j \tag{4.16}$$

where $(x_i, -y_i, z_i)$ is the location of the collocation point of the image of vortex ring element $i$ on the symmetric wing and the minus sign in front of $n_{y_i}$ accounts for the effect of symmetry on the induced velocity along the $y$-axis. The total induced velocity of $\Gamma_j$ on panel $i$ is then obtained by the sum of the influence of the modelled wing and the symmetric wing.

The velocity induced by a vortex ring is computed using the Biot-Savart Law, which describes the velocity induced at a point, $P$, by a vortex segment, $1-2$, as illustrated in Figure 4.3:

$$\nabla\phi^* = \frac{1}{4\pi} \frac{\mathbf{r_1} \times \mathbf{r_2}}{|\mathbf{r_1} \times \mathbf{r_2}|^2} \mathbf{r_0} \cdot \left( \frac{\mathbf{r_1}}{|\mathbf{r_1}|} - \frac{\mathbf{r_2}}{|\mathbf{r_2}|} \right) \tag{4.17}$$

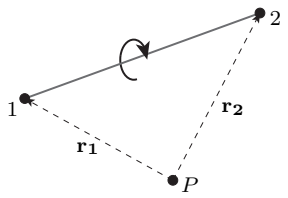


**Figure 4.3:** Nomenclature used for the velocity induced by a single vortex segment.

with

$$\mathbf{r_0} = \mathbf{r_1} - \mathbf{r_2} \tag{4.18}$$

Introducing equation (4.15) in equation (4.5), the following set of $N_b$ equations is obtained, as, for example, derived by Katz and Plotkin (2001):

$$\mathbf{K_1\Gamma_b} + \mathbf{K_2\Gamma_{w_0}} + \mathbf{K_3\Gamma_w} = -\mathbf{V}\cdot\mathbf{n} \tag{4.19}$$



where $\mathbf{V}\cdot\mathbf{n}$ represents the contribution of the free-stream velocity and any motion of the wing surface and $\mathbf{K_1}$, $\mathbf{K_2}$, and $\mathbf{K_3}$ are the matrices of aerodynamic influence coefficients defining the influence of the vorticity on the wing surface, $\mathbf{\Gamma_b}$, in the first row of wake elements, $\mathbf{\Gamma_{w_0}}$, and in the free wake, $\mathbf{\Gamma_w}$, on the collocation points on the wing surface.

Under the assumption of small disturbances with respect to the mean steady flow solution, the right hand side for a panel $p$ on the wing surface, reduces to:

$$-\mathbf{V_p}\cdot\mathbf{n_p} = \underbrace{-\mathbf{V_\infty}\cdot\mathbf{n_p}}_{\text{mean steady flow}} \quad \underbrace{-\Delta\mathbf{V_\infty}\cdot\mathbf{n_p}}_{\text{free-stream perturbation}} \quad \underbrace{-\mathbf{V_\infty}\cdot\Delta\mathbf{n_p} + \mathbf{V_b}\cdot\mathbf{n_p}}_{\text{motion of the wing surface}} \tag{4.20}$$

Introducing a small perturbation angle with respect to the mean free-stream flow, $\alpha$, as illustrated in Figure 4.4, $\Delta\mathbf{V_\infty}$ can be defined as a function of $\alpha$, resulting in:

$$-\mathbf{V_p}\cdot\mathbf{n_p} = -\mathbf{V_\infty}\cdot\mathbf{n_p} - V_\infty n_{z_p}\alpha - \mathbf{V_\infty}\cdot\Delta\mathbf{n_p} + \mathbf{V_b}\cdot\mathbf{n_p} \tag{4.21}$$

where, in this case, the perturbation angle, $\alpha$, is defined by a rotation about the $y-$axis. The same principle can, however, easily be extended to any arbitrary rotation in three dimensions, as long as the axis of rotation of interest for the perturbation angle, $\alpha$, is defined beforehand, e.g. in this example the $y$-axis or in case of wings with dihedral the projection of the spanwise reference axis on the

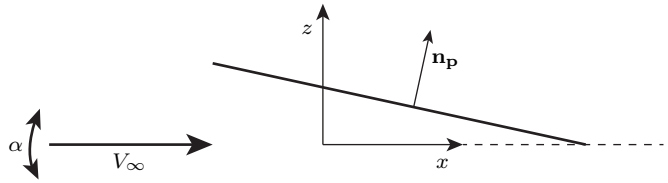


**Figure 4.4:** Schematic illustration of a panel $p$ with respect to the free-stream flow.

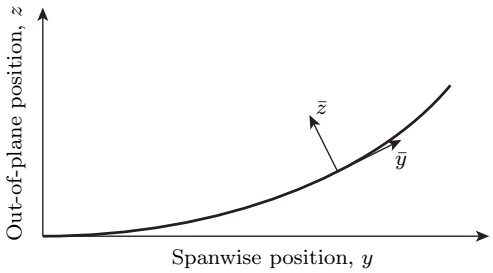


**Figure 4.5:** Schematic representation of the rear view of a wing.



$yz$-plane (i.e. $\bar{y}$ as illustrated in Figure 4.5). As a consequence, the influence of aeroelastic deformations can also be introduced through a perturbation angle of attack, $\alpha$, similar to the definition of downwash in the doublet-lattice method, as, for example, given by Giesing et al. (1971).

The first term in equation (4.21) represents the steady boundary condition, which is independent of time for a wing that is flying at a constant free stream velocity, $V_\infty$, with a fully developed wake, while the remaining terms represent the unsteady boundary conditions. Consequently, a solution can be found by splitting the problem in two sub-problems. First, a steady solution satisfying the first term in equation (4.21) is obtained assuming constant vorticity in the wake. Second, an unsteady solution satisfying the remaining terms in equation (4.21) is obtained by developing the wake vorticity in time. Finally, by the principle of superposition, the total aerodynamic forces and moments can be found.

### 4.3.3 KUTTA CONDITION

Using equation (4.9), a set of $N_{w_0}$ equations representing the Kutta condition can be derived, resulting in:

$$\mathbf{K_4\Gamma_b} + \mathbf{K_5\Gamma_{w_0}} = \mathbf{0} \tag{4.22}$$

where $\mathbf{K_4}$ and $\mathbf{K_5}$ are matrices containing ones and zeros to link each trailing edge panel to its corresponding wake panel, $\mathbf{\Gamma_b}$ is the vector of unknown vortex

ring strengths on the wing surface, and $\mathbf{\Gamma_{w_0}}$ is the vector of unknown vortex ring strengths at the start of the wake, as illustrated in Figure 4.1.

### 4.3.4 Aerodynamic forces and moments

Once the vortex strength distribution has been found, the aerodynamic forces and moments can be determined directly from the vortex strength of the vortex segments using the Kutta-Joukowski theorem, equivalent to the forces originating from horseshoe vortices in the unsteady lifting line theory (Drela, 1999). The computation of the aerodynamic forces and moments can be split in a steady component and an unsteady component, similar to Simpson et al. (2013).

The steady component of the aerodynamic forces is given by the steady component of the Kutta-Joukowski theorem and is computed for each of the vortices on the wing surface, under the assumption of small perturbations with respect to the free stream flow:



$$\mathbf{F_{st}} = \rho \mathbf{V}_\infty \times \mathbf{\Gamma} = \rho \mathbf{V}_\infty \times \mathbf{e_\Gamma} \Gamma \tag{4.23}$$

where $\mathbf{e_\Gamma}$ is the vector defining the vortex segment and $\Gamma$ is the vortex strength of the vortex segment. The resulting force acts at the midpoint of the vortex segment.

The unsteady component is computed per panel according to the unsteady component of the Kutta-Joukowski theorem:

$$\mathbf{F_{unst_i}} = \rho \hat{\mathbf{V}}_\infty \times \hat{\mathbf{e}}_\mathbf{\Gamma} \dot{\Gamma} S \tag{4.24}$$

where $\hat{\mathbf{V}}_\infty$ is the unit vector in the direction of the free stream flow velocity, $\hat{\mathbf{e}}_\mathbf{\Gamma}$ is the unit vector in the direction of the leading vortex segment of the panel, $S$ is the surface area of the panel, and the dot indicates a time derivative. Finally, the aerodynamic moments can be computed by:

$$\mathbf{M} = \mathbf{r} \times \mathbf{F} \tag{4.25}$$

where $\mathbf{r}$ is the distance between the location of the aerodynamic forces and the spanwise reference axis.

Using equations (4.23), (4.24), and (4.25) for the steady and unsteady forces and moments, the total aerodynamic forces and moments can be related to the vortex

strength distribution on the wing surface according to:

$$\begin{pmatrix} \mathbf{F} \\ \mathbf{M} \end{pmatrix} = \begin{pmatrix} \mathbf{F_{st}} \\ \mathbf{M_{st}} \end{pmatrix} + \begin{pmatrix} \mathbf{F_{unst}} \\ \mathbf{M_{unst}} \end{pmatrix} = \mathbf{L_1}\boldsymbol{\Gamma}_\mathbf{b} + \mathbf{L_2}\dot{\boldsymbol{\Gamma}}_\mathbf{b} \tag{4.26}$$

where $\mathbf{L_1}$ represents the contribution of the steady component of the Kutta-Joukowski theorem and $\mathbf{L_2}$ represents the contribution of the unsteady component of the Kutta-Joukowski theorem.

## 4.4 STEADY AERODYNAMIC SOLUTION

In case of steady aerodynamic flow, the vortex strength distribution in the wake is constant in flow direction and, therefore, the aerodynamic unknowns are the vortex strength distribution on the wing surface, $\boldsymbol{\Gamma}_\mathbf{b}$, and the spanwise vortex distribution in the wake, $\boldsymbol{\Gamma}_{\mathbf{w_0}}$, resulting in $N_b$ unknowns on the wing surface and $N_{w_0}$ unknowns in the wake. Introducing the Kutta condition, given by equation (4.22), in the flow tangency condition, given by equation (4.19), a systems of $N_b$ equations, is obtained for the mean steady flow solution defined by equation (4.20):

$$\mathbf{K_{st}}\boldsymbol{\Gamma}_\mathbf{b} = -\mathbf{V_\infty} \cdot \mathbf{n_p} \tag{4.27}$$

where $\mathbf{K_{st}}$ represents the combined influence coefficients of the wing and semi-infinite wake. Once the vortex strength distribution on the wing surface, $\boldsymbol{\Gamma}_\mathbf{b}$, has been obtained, equation (4.26) can be used to find the corresponding forces and moments.

## 4.5 CONTINOUS-TIME STATE-SPACE UNSTEADY AERODYNAMICS

As introduced in Section 4.2, the unsteady aerodynamic flow solution around aircraft wings is governed by the flow tangency condition, the Kutta condition, and the transport of vorticity. The discretised flow tangency condition and Kutta condition have been presented in Section 4.3. In order to obtain the complete system of equations, in this dissertation, the advection equation governing the transport of vorticity in the wake is discretised using the discontinuous Galerkin method, as presented in Section 4.5.1, after which a novel continuous-time state-space formulation describing the unsteady aerodynamic flow around aircraft wings can be obtained, as presented in Section 4.5.2.

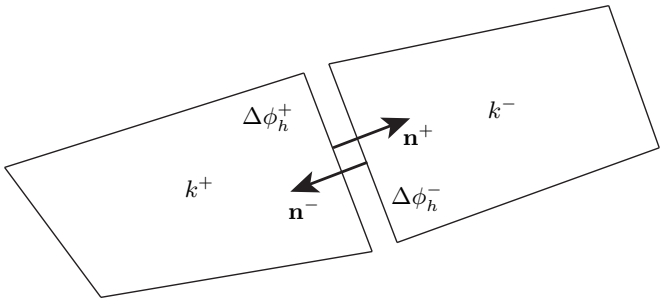


**Figure 4.6:** Schematic illustration for the definition of the numerical flux between element $\mathbf{k}$ ($\mathbf{k}^+$) and its neighbouring element $\mathbf{k}^-$.

### 4.5.1 Transport of vorticity in the wake

Once the vortex strength at the start of the wake is known, the transport of vorticity in the wake is governed by the advection equation, as introduced in Section 4.2 and given by equation (4.7). In order to solve equation (4.7), the discontinuous Galerkin method, as introduced by Reed and Hill (1973) and discussed in more detail by Li (2006), is used. The wake is discretised using finite elements that geometrically coincide with the wake panels and the solution, $\Delta\phi$, is approximated by an interpolation function, $\Delta\phi_h$, which is continuous within each element, but generally discontinuous across element boundaries.



First, equation (4.7) is multiplied with a test function, $w_h$, integrated by parts over each element individually, and, then, summed over all elements to obtain the weak formulation:

$$\sum_{k=1}^{N_w} \left( \int_{\Omega_k} w_h \frac{\partial \Delta\phi_h}{\partial t} - \mathbf{V_\infty} \cdot \nabla w_h \, \Delta\phi_h dS + \int_{\partial\Omega_k} w_h \, \Delta\phi_h \mathbf{V_\infty} \cdot \mathbf{n_k} ds \right) = 0 \quad (4.28)$$

where $k$ is the element index, $\Omega_k$ represents the surface of element $k$, $\partial\Omega_k$ represents the boundary of element $k$, and $\mathbf{n_k}$ is the outward unit normal on the element boundary.

Next, the flux of vorticity along the boundary of each element (i.e. $\Delta\phi_h \mathbf{V_\infty}$) is approximated by a numerical flux as a function of the interpolation function, $\Delta\phi_h$, on each side of the boundary, as illustrated in Figure 4.6. The numerical flux is typically defined as a function of the mean and jump of, in this case, $\Delta\phi$ across the boundary, defined by:

$$\overline{\Delta\phi_h} = \frac{1}{2}\left(\Delta\phi_h^+ + \Delta\phi_h^-\right); \qquad [\Delta\phi_h] = \Delta\phi_h^+ \mathbf{n}^+ + \Delta\phi_h^- \mathbf{n}^- \quad (4.29)$$

resulting in a numerical flux of:

$$\Delta\phi_h \mathbf{V}_\infty = \mathbf{V}_\infty \overline{\Delta\phi_h} + \mathbf{C}_\mathbf{V} \cdot [\Delta\phi_h] \tag{4.30}$$

where $\mathbf{C}_\mathbf{V}$ is a non-negative definite matrix dependent upon the value of $\mathbf{V}_\infty \cdot \mathbf{n}$.

Next, $\Delta\phi_h$ and $w_h$ are defined by an expansion using a set of $p$ (orthogonal) basis functions, $\psi$, on each element $k$:

$$\Delta\phi_h = \sum_{k=1}^{N_w} \sum_{m=1}^{p} \Delta\hat{\phi}_{k,m}(t)\psi_{k,m}(\mathbf{x}) \tag{4.31}$$

$$w_h = \sum_{k=1}^{N_w} \sum_{m=1}^{p} \hat{w}_{k,m}\psi_{k,m}(\mathbf{x}) \tag{4.32}$$



where the coefficients $\hat{w}_{k,m}$ can be chosen arbitrarily and $\Delta\hat{\phi}_{k,m}$ are unknown functions of time. A convenient choice for the coefficients $\hat{w}_{k,m}$ is to set one coefficient equal to 1, while setting all other coefficients equal to 0. Following this approach, a set of $p$ ordinary differential equations can be derived for the unknown coefficients $\Delta\hat{\phi}$ for each element $k$, as, for example, shown by Li (2006):

$$\mathbf{M}\frac{\partial \boldsymbol{\Delta}\hat{\boldsymbol{\phi}}_k}{\partial t} + \left(\mathbf{K} + \sum_{i=1}^{NS} \mathbf{K}_{B,i}\right) \boldsymbol{\Delta}\hat{\boldsymbol{\phi}}_k + \sum_{i=1}^{NS} \mathbf{N}_{B,i}\boldsymbol{\Delta}\hat{\boldsymbol{\phi}}_{(NB,i)} = \mathbf{0} \tag{4.33}$$

where the mass matrix, $\mathbf{M}$, and the stiffness matrix, $\mathbf{K}$ are defined by the volume integral in equation (4.28), $\mathbf{K}_{B,i}$ and $\mathbf{N}_{B,i}$ represent the contribution of the numerical flux defined by equation (4.30) across the boundary of the element, $\boldsymbol{\Delta}\hat{\boldsymbol{\phi}}_k$ are the degrees of freedom of element $k$, $\boldsymbol{\Delta}\hat{\boldsymbol{\phi}}_{(NB,i)}$ are the degrees of freedom of the neighbouring elements, and $NS$ is the number of sides along the boundary of the element.

In our implementation, a classical upwinding scheme given by $\mathbf{C}_\mathbf{V} = \frac{1}{2}(\mathbf{V}_\infty \cdot \mathbf{n})\mathbf{I}$ and piecewise constant basis functions (i.e. $\psi_{k,m}(\mathbf{x}) = 1$) have been selected, such that each wake element can be represented by an equivalent vortex ring element with strength, $\Gamma_k(t) = \Delta\phi_k(t)$. Recognizing that, as illustrated in Figure 4.1, $\mathbf{V}_\infty$ is oriented along the $x$-axis and always positive such that vorticity is transported in positive $x-$direction, the element equation (equation (4.33)) reduces to:

$$\dot{\boldsymbol{\Gamma}}_{\mathbf{w}_{i,j}} = \frac{\left(\boldsymbol{\Gamma}_{\mathbf{w}_{i,j}}(t) - \boldsymbol{\Gamma}_{\mathbf{w}_{i,j-1}}(t)\right) V_\infty}{\Delta x_{w_{i,j}}} \tag{4.34}$$

where $\Delta x_w$ is the wake panel length in flow direction, the element number $k$ has been replaced by a spanwise element index $i$ and a streamwise element index $j$ to reflect the transport of vorticity in streamwise direction, and the dot indicates a time derivative.

Finally, by assembling all element equations, the transport of vorticity in the wake is governed by the following matrix equation:

$$\dot{\mathbf{\Gamma}}_{\mathbf{w}} = \mathbf{K_6}\mathbf{\Gamma}_{\mathbf{w}} + \mathbf{K_7}\mathbf{\Gamma}_{\mathbf{w_0}} \tag{4.35}$$

where $\mathbf{K_6}$ represents the transport of vorticity throughout the wake and $\mathbf{K_7}$ introduces the influx of vorticity in the wake governed by the first row of wake elements.

Note that equation (4.7) has only been discretised in space and no assumptions are made regarding the time derivative. As a consequence, this approach allows for straight-forward implementation of arbitrary wake shapes, wake discretisations (structured and non-structured), or higher order panel methods, while retaining a continuous-time representation. Instead of a wake aligned with the undisturbed free-stream flow, the presented approach can, for example, also be applied to a prescribed wake geometry including the effects of wake roll-up, as, for example, used by Murua et al. (2012a) and Hesse and Palacios (2014) in their discrete-time formulation.



### 4.5.2 CONTINUOUS-TIME STATE-SPACE FORMULATION

The system of equations, given by equations (4.19), (4.22), and (4.35), can now be assembled in a continuous-time state-space form, following the derivation of Mohammadi-Amin et al. (2012); however, in this case, generalised to any generic wing shape and applicable to any arbitrary wake shape or discretisation. The resulting governing equation, as derived in Appendix C.1, is given by:

$$\dot{\mathbf{\Gamma}}_{\mathbf{w}} = \mathbf{K_8}\mathbf{\Gamma}_{\mathbf{w}} + \mathbf{K_9}\boldsymbol{\alpha} + \mathbf{K_{10}} \tag{4.36}$$

where $\boldsymbol{\alpha}$ is the perturbation angle of attack on the wing surface, $\mathbf{K_8}$ represents the contribution of the wing and wake, $\mathbf{K_9}$ represents the contribution of perturbing the free-stream flow, and $\mathbf{K_{10}}$ represents the contribution of the motion of the wing surface.

Similarly, the aerodynamic forces and moments can also be related to the vortex strength of the free wake panels, the perturbation angle of attack on the wing surface, and the motion of the wing surface, as derived in Appendix C.2, resulting

in:

$$\begin{pmatrix} \mathbf{F} \\ \mathbf{M} \end{pmatrix} = \mathbf{L_9}\boldsymbol{\Gamma}_\mathbf{w} + \mathbf{L_{10}}\boldsymbol{\alpha} + \mathbf{L_7}\dot{\boldsymbol{\alpha}} + \mathbf{L_{11}} \tag{4.37}$$

where $\mathbf{L_9}$ represents the contribution of the wing and wake, $\mathbf{L_7}$ and $\mathbf{L_{10}}$ represent the contribution of perturbing the free-stream flow, and $\mathbf{L_{11}}$ represents the contribution of the motion of the wing surface.

Identifying $\begin{pmatrix} \dot{\boldsymbol{\alpha}} & \mathbf{1} \end{pmatrix}^T$ as state-space input, $\mathbf{u}$, $\begin{pmatrix} \boldsymbol{\Gamma}_w & \boldsymbol{\alpha} \end{pmatrix}^T$ as state vector, $\mathbf{x}$, and $\begin{pmatrix} \mathbf{F} & \mathbf{M} \end{pmatrix}^T$ as output vector, $\mathbf{y}$, a standard continuous-time state-space system is obtained:

$$\dot{\mathbf{x}} = \underbrace{\begin{bmatrix} \mathbf{K_8} & \mathbf{K_9} \\ \mathbf{0} & \mathbf{0} \end{bmatrix}}_{\mathbf{A_{ss}}} \mathbf{x} + \underbrace{\begin{bmatrix} \mathbf{0} & \mathbf{K_{10}} \\ \mathbf{I} & \mathbf{0} \end{bmatrix}}_{\mathbf{B_{ss}}} \mathbf{u} \tag{4.38}$$

$$\mathbf{y} = \underbrace{\begin{bmatrix} \mathbf{L_9} & \mathbf{L_{10}} \end{bmatrix}}_{\mathbf{C_{ss}}} \mathbf{x} + \underbrace{\begin{bmatrix} \mathbf{L_8} & \mathbf{L_{11}} \end{bmatrix}}_{\mathbf{D_{ss}}} \mathbf{u} \tag{4.39}$$

where $\mathbf{1}$ is a vector of ones in all components. Note that a unique input can be specified for each wing panel, allowing for any arbitrary chordwise and spanwise gust distribution to be modelled. Finally, the unsteady aerodynamic response can be found by any standard state-space solver.

In conclusion, under the assumption of small perturbations of a thin wing around a steady-state reference configuration, the inviscid, (in)compressible, irrotational, unsteady aerodynamic forces and moments acting on any generic wing are computed using a continuous-time state-space model allowing for easy integration with structural or flight dynamic models for efficient aero(servo)elastic analysis using any arbitrary wake shape and discretisation and a time step solely governed by accuracy requirements. The input vector allows for a unique time dependent input for each panel on the wing surface, allowing for any arbitrary chordwise and spanwise gust distribution to be modelled. Once the unsteady aerodynamic response has been found, the total aerodynamic response can be found by the principle of superposition of the steady and unsteady aerodynamic solution.

## 4.6 AERODYNAMIC DRAG

In order to assess the aerodynamic performance of an aircraft, an estimate of the aircraft parasitic drag is made, as presented in Section 4.6.1, and the induced

drag of the wing is computed based on the potential flow solution, as presented in Section 4.6.2. For aerodynamic performance, only the steady aerodynamic drag is relevant and, therefore, no unsteady drag is computed.

### 4.6.1 PARASITIC DRAG

In order to account for the effect of parasitic drag on the performance of the aircraft while maintaining computational efficiency, the parasitic drag is estimated based on the work of Shevell (1989). The approach assumes that each component of the aircraft contributes to the total drag without interfering with each other.

In the present model, the parasitic drag is computed explicitly for the wing and fuselage, while the drag of any remaining components is included by an additional constant drag coefficient. The parasitic drag coefficient, $C_{D_0}$, of the wing and fuselage are approximated by:

$$C_{D_0} = \sum_i \frac{K C_{f_i} S_{wet_i}}{S_{ref}} \tag{4.40}$$



where $K$ is the form factor, $C_{f_i}$ is the skin friction coefficient of section $i$, $S_{wet_i}$ is the wetted area of section $i$, and $S_{ref}$ is the aircraft reference area. In case of wings, the form factor is dependent on the wing thickness and sweep angle, as given by Shevell (1989), and is approximated by the following cubic polynomial least-squares fit:

$$K = 0.99832 + 0.0001819\Lambda + 1.948\frac{t}{c} - 1.087 \cdot 10^{-5}\Lambda^2 - 0.001485\Lambda\frac{t}{c} - 1.154\left(\frac{t}{c}\right)^2 + 1.579e-07\Lambda^3 - 0.0002934\Lambda^2\frac{t}{c} - 0.00719\Lambda\left(\frac{t}{c}\right)^2 + 25.1\left(\frac{t}{c}\right)^3; \tag{4.41}$$

where $\Lambda$ is the quarter chord sweep angle in degrees and $\frac{t}{c}$ is the thickness over chord ratio of the corresponding airfoil.

The skin friction coefficient is given by:

$$C_{f_i} = \frac{0.455}{\left(\log_{10} Re_{L_i}\right)^{2.58}} \tag{4.42}$$

where $Re_{L_i}$ is the Reynolds number of section $i$ defined by:

$$Re_{L_i} = \frac{\rho V_\infty c_{mac_i}}{\mu} \tag{4.43}$$

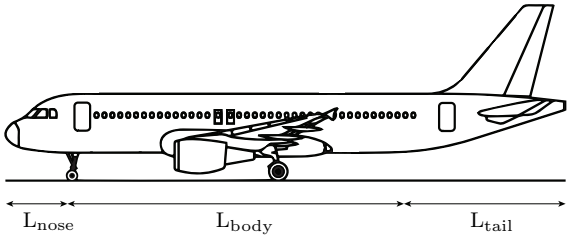


**Figure 4.7:** Schematic illustration of the different fuselage sections.

where $c_{mac_i}$ is the mean aerodynamic chord of section $i$, and $\mu$ is the air viscosity. Note that the skin friction coefficient should be corrected for surface roughness and imperfections. Since no information on this is available for the actual wings that will be analysed, a typical value of 6% increase of the skin friction coefficient is used (Bertin and Cummings, 2009).

Finally, to finish the calculation of the parasitic drag of the wing, the wetted area of each section is given by

$$S_{wet_i} = 2\left(1 + 0.2\left(\frac{t}{c}\right)\right) S_{exp_i} \tag{4.44}$$

where $\left(\frac{t}{c}\right)$ is the thickness ratio of the section airfoil, and $S_{exp_i}$ is the portion of the section planform that is exposed to the outside air.

In case of the fuselage, the skin friction coefficient is also defined by equation (4.42), but with the Reynolds number based on the total fuselage length. The fuselage form factor is dependent on the fineness ratio (length/diameter) of the fuselage, as given by Shevell (1989), and is approximated by the following fourth order least-squares polynomial fit:

$$K = 0.00032197\left(\frac{L}{D}\right)^4 - 0.010477\left(\frac{L}{D}\right)^3 + 0.12875\left(\frac{L}{D}\right)^2 - 0.74112\frac{L}{D} + 2.8843 \tag{4.45}$$

where $\frac{L}{D}$ is the fuselage fineness ratio.

Finally, in order to compute the wetted surface area of the fuselage, the fuselage is split in three sections, as illustrated in Figure 4.7. The nose section is approximated by a cone, the body is approximated by a cylinder, and the tail is approximated by a conical section, resulting in the following wetted surface area:

$$S_{wet} \approx S_{wet_{nose}} + S_{wet_{body}} + S_{wet_{tail}} \tag{4.46}$$

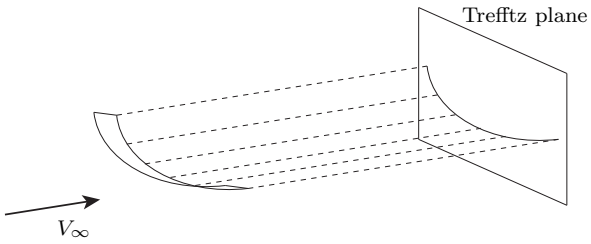


**Figure 4.8:** Schematic illustration of the Trefftz plane.

with

$$S_{wet_{nose}} = 0.75\pi DL_{nose} \tag{4.47}$$
$$S_{wet_{body}} = \pi DL_{body} \tag{4.48}$$
$$S_{wet_{tail}} = 0.72\pi DL_{tail} \tag{4.49}$$



In conclusion, the total parasitic drag is approximated as:

$$C_{D_0} = C_{D_{0_{wing}}} + C_{D_{0_{fus}}} + C_{D_{0_{rest}}} \tag{4.50}$$

### 4.6.2 Induced drag

Katz and Plotkin (2001) provide an excellent description of the computation of induced drag using vortex ring elements and a brief description is only included here for completeness. The induced drag of the steady aerodynamic solution can be computed by means of the Trefftz plane. The Trefftz plane is a plane perpendicular to the free stream flow and at a distance behind the wing such that the body vortex rings no longer influence the flow in this plane, as illustrated in Figure 4.8. Applying the integral form of the momentum equation, the resulting steady induced drag is then given by: (Katz and Plotkin (2001))

$$D = \frac{\rho}{2}\int_{-L/2}^{L/2} \Gamma(l)w(l)dl \tag{4.51}$$

where the downwash, $w$, is fully defined by the wake vortices and no longer influenced by the body vortices, the parameter, $l$, is defined according to Figure 4.9, and $L$ is the total length of the wing along the projection on the Trefftz plane.

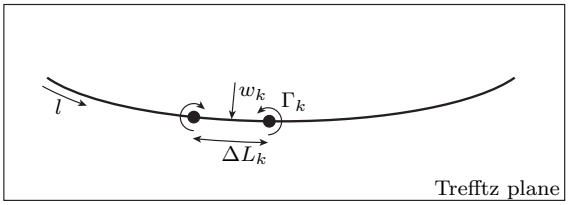


**Figure 4.9:** Schematic illustration of the discretisation of the Trefftz plane.

Discretising this equation, the steady induced drag becomes:

$$D = \frac{\rho}{2} \sum_{k=1}^{N_s} \Gamma_k w_k \Delta L_k \tag{4.52}$$

where $N_s$ is the number of spanwise elements, $w_k$ is the induced downwash at the centre of wake segment $k$, and $\Delta L_k$ is the length of wake segment $k$, as defined in Figure 4.9.



## 4.7 VERIFICATION WITH LITERATURE

In order to verify the aerodynamic model, the aerodynamic model is, first of all, assessed by applying the model to different steady and unsteady benchmark problems and comparing the results to the literature, as presented in Sections 4.7.1 and 4.7.2, respectively. Finally, the effect of compressibility and the validity of the assumptions made in Section 4.2 are assessed in Section 4.7.3. For all results presented, first a mesh convergence study has been carried out, but for clarity, only the results for a converged mesh will be shown.

### 4.7.1 STEADY AERODYNAMIC VERIFICATION

Aircraft wings in general are not rectangular, but have a combination of taper, sweep, dihedral, twist, and camber for optimal aerodynamic performance. Therefore, as a steady verification, the results obtained by the current model are compared to results found in literature for different taper ratios, sweep angles, dihedral, twist angles, and camber. For all cases presented in this section as a result of a convergence study, the wing has been been discretised using 16 spanwise and 32 chordwise elements.

First, Figure 4.10a shows the comparison of the current model to the results obtained by Bertin and Cummings (2009) using lifting-line theory for an untwisted wing with an aspect ratio of 7.28 and a NACA2412 airfoil at various taper ratios.

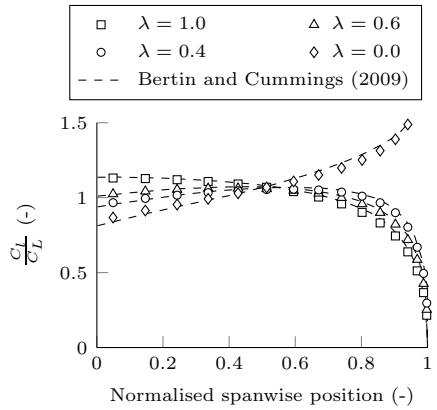


**(a)** An untwisted wing with a NACA2412 airfoil and an aspect ratio of 7.28 at different taper ratios.

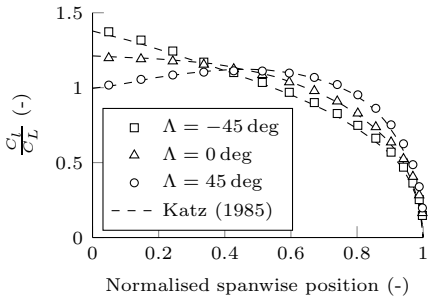


**(b)** An untwisted wing with an aspect ratio of 4 at different sweep angles.

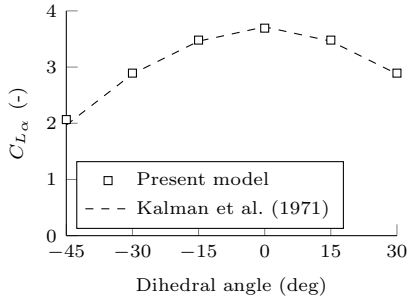


**(c)** An untwisted wing with an aspect ratio of 4 at different dihedral angles.

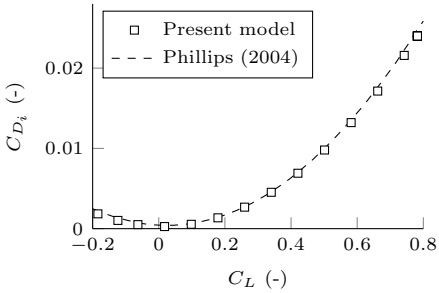


**(d)** A rectangular wing with an aspect ratio of 8 and an elliptic twist distribution.

**Figure 4.10:** Verification of steady aerodynamic results.

As can be seen, the results show excellent agreement for a taper ratio of 0.4, 0.6, and 1.0. Only for a taper ratio of 0.0, the difference becomes more pronounced. Note that using vortex rings, a taper ratio of 0.0 can only be approximated by selecting a very small taper ratio of, in this case, 0.001, since otherwise the length of vortices at the wing tip would become zero, resulting in numerical singularities when solving the system of equations.

Second, Figure 4.10b shows the comparison to the results obtained by Katz (1985) for an untwisted, untapered wing with an aspect ratio of 4.0 at different sweep angles. Since Katz's model is based on the unsteady vortex lattice method, and thus also uses vortex ring elements, as expected, the results show excellent agreement.

Next, in order to verify the model for dihedral, the results of the model were compared to the results by Kalman et al. (1971) for a rectangular wing with an aspect ratio of 4.0 at different dihedral angles. As can be seen in Figure 4.10c, the results show excellent agreement.

Finally, the implementation of twist in the model and the computation of the induced drag was verified by comparing the results of the present model to the results obtained by Phillips (2004) for a rectangular wing with an aspect ratio of 8.0 and an elliptic twist distribution with a twist angle of $-4.64$ deg at the wing tips and 0.00 deg at the wing root. The resulting induced drag polar is shown in Figure 4.10d, and, as can be seen, the results show excellent agreement.

In conclusion, the steady results show excellent agreement to results found in the literature for different taper ratios, sweep angles, dihedral, twist, and camber, thus verifying the current aerodynamic model for steady aerodynamic analysis.

### 4.7.2 UNSTEADY AERODYNAMIC VERIFICATION



In order to verify the unsteady aerodynamic response, the unsteady aerodynamic model is first compared to 2D unsteady results in the literature by modelling a wing with an aspect ratio of 200. In order to do a fair comparison to the 2D results, the results from the literature have been compared to the section lift coefficient at the centre of the wing.

Figure 4.11 shows the comparison of the present model to the lift and moment coefficient as predicted by Theodorsen (1935) for the harmonic pitch, plunge oscillation of a 2D flat plate at different reduced frequencies. The flat plate pitches around the quarter-chord axis with an amplitude of 1 deg, has a plunge amplitude of $\frac{h_0}{b} = \frac{0.02}{k}$, and has been investigated for $k = 0.1$, $k = 0.4$, $k = 1.0$, and $k = 3.0$. The wing is discretised using 8 spanwise and 32 chordwise elements. The wake is truncated at 20 times the chord and the wake is discretised using $\frac{\Delta x_w}{c} = \frac{1}{32}$. As can be seen the present model shows excellent agreement for $k = 0.1$ and $k = 0.4$. As the reduced frequency increases, it can be seen that the present model overpredicts the lift and moment coefficient, which can be explained by the fact that for the present model the wake needs to be discretised, while Theodorsen computes the lift and moment coefficient analytically. Especially at higher reduced frequencies, the effect of this discretisation becomes more pronounced, since the number of wake panels travelled per oscillation becomes smaller. It should be noted, however, that, for most practical applications, a reduced frequency of 0.4 is already high.

Aircraft in general have a combination of taper, sweep, dihedral, twist, and camber. However, to the authors knowledge, no results are available in literature on the unsteady aerodynamic response of panel methods for thin general aircraft wings. Therefore, in order to verify the 3D unsteady aerodynamic response, the

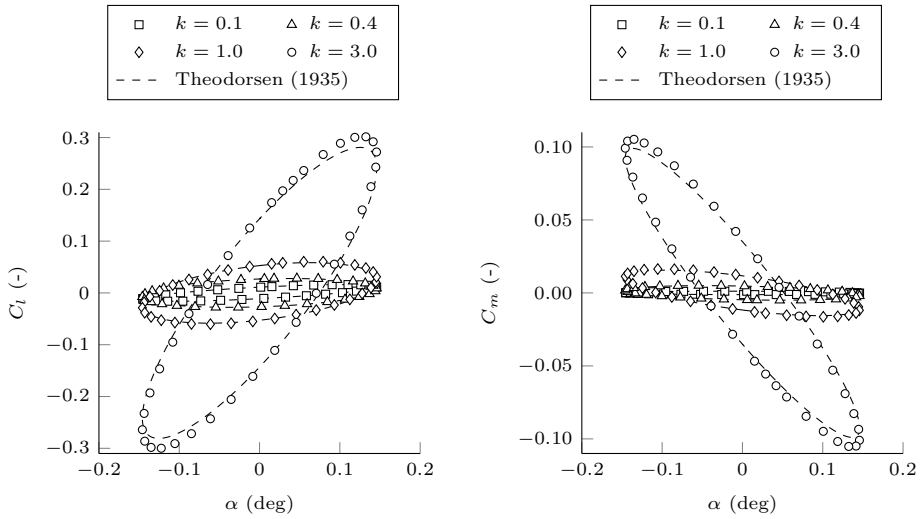


**(a)** Lift coefficient of a 2D flat plate undergoing a harmonic pitch, plunge oscillation at different reduced frequencies.

**(b)** Moment coefficient of a 2D flat plate undergoing a harmonic pitch, plunge oscillation at different reduced frequencies.

**Figure 4.11:** Verification of the 2D unsteady aerodynamic results.

present model is compared to the unsteady aerodynamic response for rectangular wings. Figure 4.12a shows the comparison of the present model to the sudden acceleration of a flat rectangular wing with an aspect ratio of 6 to the results obtained by Jones (1945). The wing is discretised using 8 spanwise and 32 chordwise elements. The wake is truncated at 10 times the chord and the wake is discretised using $\frac{\Delta x_w}{c} = \frac{1}{32}$. As was shown by Katz (1985) for UVLM, since the present model can only represent a finite acceleration rate due to its wake discretisation, while the solution by Jones accounts for the infinite acceleration rate, a moderately higher initial lift can be expected for the present model, after which the solution converges to the solution by Jones.

As a final verification for the unsteady aerodynamic response, the present model is compared to the results obtained by Wang et al. (2010) using UVLM for the gust response of the Goland wing under a 1-cosine gust. The wing is discretised using 8 spanwise and 32 chordwise elements. The wake is truncated at 10 times the chord and the wake is discretised using $\frac{\Delta x_w}{c} = \frac{1}{32}$. As can be seen in Figure 4.12b, the results show excellent agreement, thus verifying the present model.

In conclusion, the present model shows excellent agreement to results in the literature for the unsteady aerodynamic response of wings, thus verifying the present model.

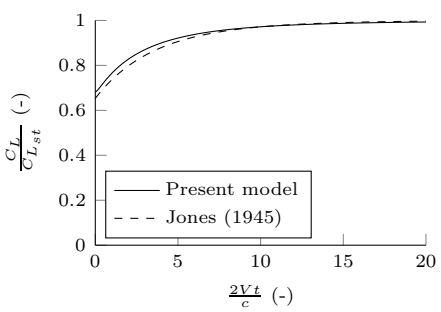


**(a)** Sudden acceleration of a rectangular wing with an aspect ratio of 6.

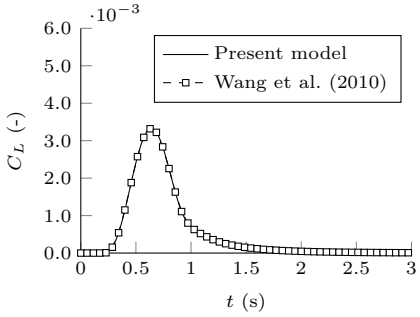


**(b)** Gust response of the Goland wing undergoing a 1-cosine gust.

**Figure 4.12:** Verification of the 3D unsteady aerodynamic results.

### 4.7.3 COMPRESSIBLE FLOW

4

In order to investigate the effect of reduced frequency and Mach number on the validity of the present model for unsteady compressible flow, the present model is compared to the approximate closed-form solution by Lin and Iliff (2000) to the Possio integral equation for the pressure distribution of a lifting surface in two-dimensional, oscillatory, subsonic compressible flow. The wing is discretised using 12 spanwise and 32 chordwise elements. The wake is truncated at 20 times the chord and the wake is discretised using $\frac{\Delta x_w}{c} = \frac{1}{32}$.

The resulting comparison in amplitude and phase for both lift coefficient and moment coefficient of an airfoil pitching with an amplitude of 1 deg about the 1/4 chord is shown in Figure 4.13 for different reduced frequencies and Mach numbers. As can be concluded from Figure 4.13a and Figure 4.13c, the present model shows excellent agreement to the closed-form solution in amplitude up to a reduced frequency of 1, after which the effects of compressibility are no longer captured by the present model. Regarding the phase angle, as expected, the present model results in a phase angle independent of Mach number, while the unsteady terms in the Prandtl-Glauert equation introduce a change in phase angle resulting from the effects of compressibility. However, at a Mach number of 0.8 and a reduced frequency of 1 the error in phase is still less than 10 deg.

Based on these results, it can be concluded that, as expected, with increasing reduced frequency and Mach number, the unsteady terms in the Prandtl-Glauert equation are no longer negligible and the present model can no longer capture the full effects of compressibility on the unsteady aerodynamic solution. However, although care should be taken, the results show that the present model provides sufficiently accurate dynamic load predictions at low to moderate Mach numbers and reduced frequencies encountered in the normal operating conditions of

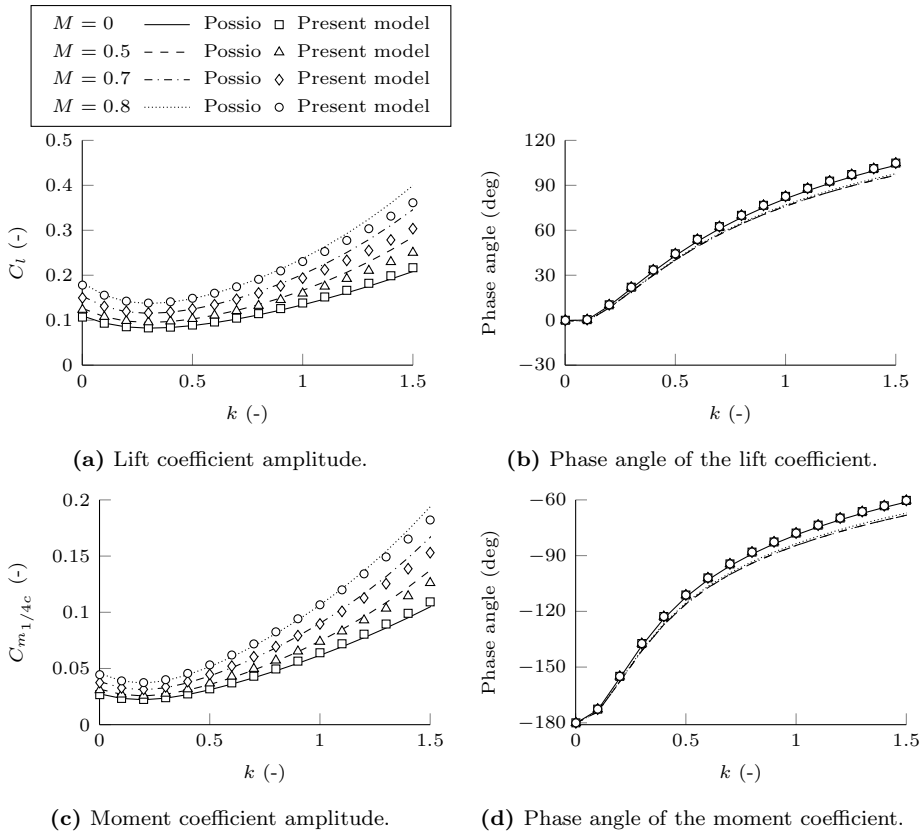


**(a)** Lift coefficient amplitude.

**(b)** Phase angle of the lift coefficient.

**(c)** Moment coefficient amplitude.

**(d)** Phase angle of the moment coefficient.

**Figure 4.13:** Comparison of the effect of Mach number and reduced frequency on the aerodynamic response between the present model and the closed-form solution of Lin and Iliff (2000) for a thin $2D$ airfoil pitching about 1/4 chord with an amplitude of 1 deg.

aircraft. Note, however, that at Mach numbers above 0.7 care should be taken in applying both the present model and the closed-form solution, since, depending on the wing geometry, the underlying assumptions of the linearised potential flow equations might no longer be valid and, for example, solutions to the Euler equations might be necessary for accurate results.

## 4.8 Numerical example: a discrete gust analysis

Finally, the model is applied to the analysis of a swept, tapered wing with the properties given in Table 4.1 under a 1-cosine gust of various lengths to illustrate

**Table 4.1:** Wing properties.

| | |
|---|---|
| Semispan | 5.0 m |
| Root chord | 1.0 m |
| Taper ratio | 0.3 |
| 1/4$c$ sweep angle | 30 deg |
| Dihedral angle | 5 deg |
| Camber | 0% |
| Mean aerodynamic chord | 0.713 m |

the advantages of the present continuous-time state-space model. The wing is flying at a steady angle of attack of 0 deg and free-stream velocity of 100 m/s at sea level. The gust is applied using the following input signal:

$$\alpha_g^i(t) = \begin{cases} \frac{1}{2}\frac{V_g}{V_\infty}\left(1 - \cos\left(\frac{\pi V_\infty (t - t_0^i)}{H}\right)\right) & \text{for} \quad 0 \leq t - t_0^i \leq \frac{2H}{V_\infty} \\ 0 & \text{otherwise} \end{cases} \tag{4.53}$$



where $\alpha_g^i$ is the angle of attack induced by the gust velocity on panel $i$, $V_g$ is the vertical gust velocity amplitude, $t_0^i$ is the time at which the gust reaches panel $i$, and $H$ is the half gust length. The gust lengths considered are 5, 10, 20, and 50 times the mean aerodynamic chord, equivalent to a reduced frequency of 0.628, 0.314, 0.157, and 0.063, respectively and the gust amplitude is 5.24 m/s such that the induced gust angle of attack is 3 deg. The number of spanwise and chordwise vortex ring elements is kept constant at 16 and the wake is truncated at 20 chords behind the wing. Two sets of analysis are run: (i) with constant size wake elements, while the wake discretisation is varied between $\frac{\Delta x_w}{c} = 2$ and $\frac{\Delta x_w}{c} = 32$ to provide a direct comparison to discrete-time simulations and (ii) with increasing wake element size aft of the wing to illustrate the possibility to improve the efficiency of the model by varying the wake element size. An additional analysis with a constant wake discretisation of $\frac{\Delta x_w}{c} = 64$ is used as the converged reference solution.

The resulting lift and moment coefficients for different gust lengths, at the finest constant size wake discretisation, are shown in Figure 4.14. In order to illustrate the effect of gust length on the level of unsteadiness in the flow, time has been normalised with respect to the time the gust needs to traverse the wing, i.e. at $\bar{t} = 0$ the gust hits the wing leading edge at the root and at $\bar{t} = 1$ the gust leaves the wing trailing edge at the tip. In case of a quasi-steady analysis, once the gust has left the wing ($\bar{t} \geq 1$), the gust no longer influences the aerodynamic flow around the wing, i.e. $C_L = C_M = 0$. As can be seen in Figure 4.14, for a long gust of 50 chords, this is a valid assumption. However, as the length of the gust is reduced, unsteady aerodynamic flow phenomena become more dominant, resulting in a lift coefficient that is still 10% of the maximum lift coefficient at $\bar{t} = 1$ for a gust length of 5 chords and are, therefore, not negligible. Furthermore,

**Table 4.2:** Maximum lift and moment coefficient for different gust lengths.

| Gust length | $C_{L_{max}}$ | $C_{M_{1/4c,max}}$ |
|---|---|---|
| $5c$ | 0.133 | −0.262 |
| $10c$ | 0.197 | −0.358 |
| $20c$ | 0.232 | −0.410 |
| $50c$ | 0.250 | −0.438 |
| Steady | 0.256 | −0.451 |

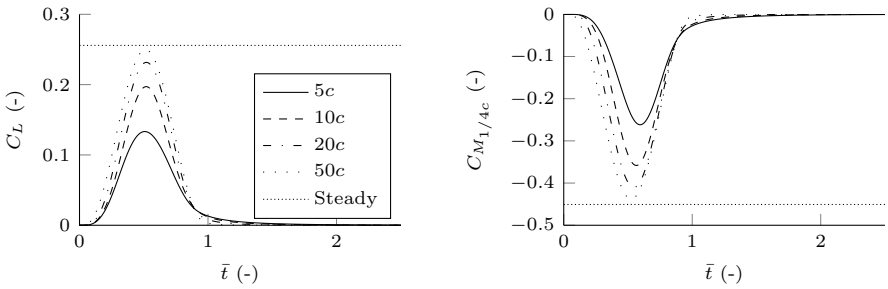


**(a)** $C_L$ of a 1-cosine gust of different lengths. **(b)** $C_M$ of a 1-cosine gust of different lengths.

**Figure 4.14:** Effect of gust length on the unsteady aerodynamic response. Time is normalised with respect to the time required for the gust to traverse the wing.



as can be expected, as the length of the gust is increased, the flow approaches a steady flow and the maximum lift coefficient approaches the equivalent steady lift coefficient. The corresponding maximum lift and moment coefficients are given in Table 4.2.

In order to investigate the effect of time step and wake discretisation on the accuracy of the results at different reduced frequencies, the remainder of this section will only focus on gust lengths of 5 chords (i.e. highly unsteady) and 50 chords (i.e. quasi-steady). Similar conclusions can be drawn for other gust lengths. It should be noted that in case of discrete-time state-space systems, the wake discretisation and time step are inherently linked and can not be varied independently, unlike the present model.

Figure 4.15 shows the effect of a varying time step on the maximum lift and moment coefficient for different wake discretisations. Note that, in this case, all simulations were run with a constant timestep; however, in contrast to discrete-time state-space systems, the continuous-time formulation of the present model also allows for an adaptive timestep to be used in the time integration, as required. The equivalent discrete-time state-space results, where the timestep matches the wake discretisation, are designated by the filled markers.

Several conclusions can be drawn on the effect of wake discretisation and timestep

on the accuracy of the results. First of all, as can be expected, the results for a gust length of 50 chords converge faster than the results for a gust length of 5 chords, since a shorter gust length implies a higher reduced frequency and therefore finer wake and time discretisations are required to obtain accurate results.

Second of all, the results clearly show the advantage of the present model, e.g. for a gust length of 5 chords, a wake discretisation of 8 panels per chord and the equivalent timestep of $\frac{V_\infty \Delta t}{c} = \frac{1}{8}$ results in an error of 2.5%, while a wake discretisation of only 4 panels per chord with a smaller timestep of $\frac{V_\infty \Delta t}{c} = \frac{1}{16}$ only results in an error of 1.8%, thus clearly showing the advantage of the variable timestep.

Finally, it is interesting to note that for the lift coefficient at a gust length of 5 chords, the best result is achieved with a wake discretisation of only 2 panels per chord and a timestep of $\frac{V_\infty \Delta t}{c} = \frac{1}{32}$. However, care should be taken, since depending on the gust length, both the convergence rate and the direction of convergence change. This can be explained by a combination of effects: first, depending on the gust length, the resulting aerodynamic forces are dominated by steady or unsteady effects and thus by the vorticity distribution in the wake or the time rate of change of the vorticity distribution in the wake and, second, as the wake is refined, the vorticity distribution in the wake is captured more accurately and depending on the vorticity distribution and its time rate of change, as the discretisation is improved, the resulting lift and moment coefficient might increase or decrease. In case of a wake discretisation of only 2 panels per chord, the combination of these effects results in a lift coefficient that is very close to the converged solution; however, as can be seen in Figure 4.15b, the error in moment coefficient is still 2.8%, clearly indicating a non-converged solution.



Figure 4.16 shows the effect of a non-constant wake discretisation on the maximum lift and moment coefficient for different sizes of the first wake panel, $\frac{\Delta x_w}{c}$, for a constant converged time step of $\frac{V_\infty \Delta t}{c} = \frac{1}{32}$. The number of streamwise wake panels is reduced from a constant wake to 1/16th of the number of streamwise wake panels in a constant wake, while maintaining the size of the first wake panel and increasing the element size of the remaining wake elements as the distance behind the wing increases. The ratio in size between two adjacent elements is kept constant through the following relation that maps a uniform element distribution, $\rho$ $(0 \leq \rho \leq 1)$, into a non-uniform element distribution, $r$ $(0 \leq r \leq 1)$, as given by Weatherill et al. (1998):

$$r = \frac{e^{A\rho} - 1}{e^A - 1} \tag{4.54}$$

where $A$ controls the ratio in size between two adjacent elements. The value of $A$ can be determined by solving equation (4.54) for the first wake element, based on the prescribed size of the first wake element, $\frac{\Delta x_w}{c}$, which defines $r$, and the

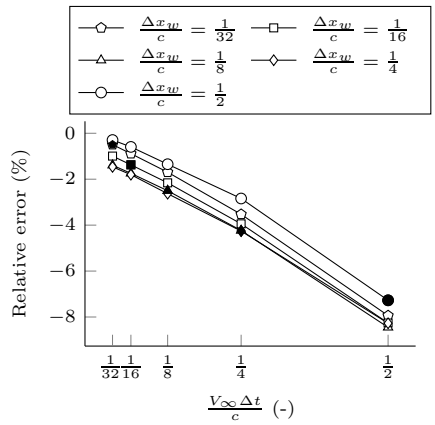


**(a)** Relative error in lift coefficient, $2H = 5c$.

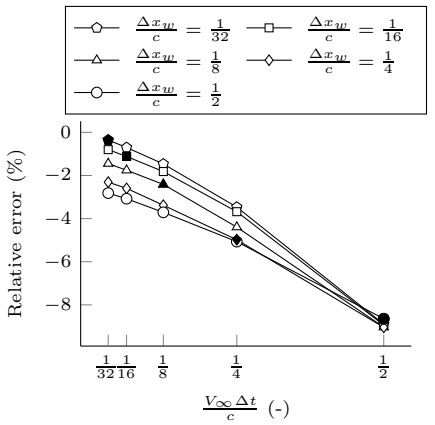


**(b)** Relative error in moment coefficient, $2H = 5c$.

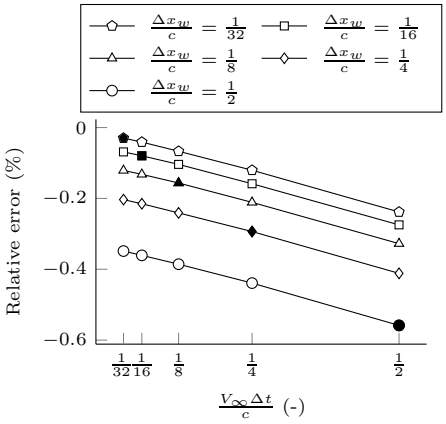


**(c)** Relative error in lift coefficient, $2H = 50c$.

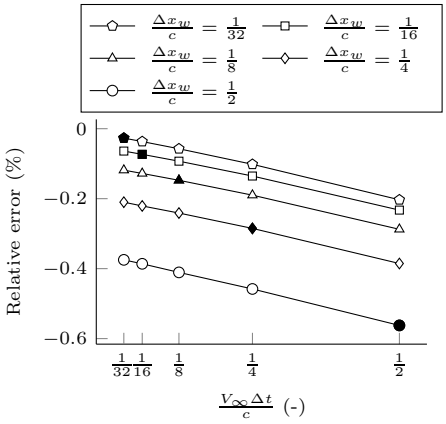


**(d)** Relative error in moment coefficient, $2H = 50c$.

**Figure 4.15:** Effect of varying the timestep for time integration on the maximum lift and moment coefficient for various wake discretisations at different gust lengths. The equivalent discrete-time results are indicated by the filled markers.

desired number of elements, which defines $\rho$.

The results clearly indicate the advantage of a variable wake element size on the efficiency of computation. The main conclusion that can be drawn from these results is the trade-off that can be made between model size and accuracy. For a small penalty in accuracy, the number of states in the system can be significantly reduced by reducing the number of wake panels. For example, for a gust length of 5 chords, the same accuracy can be achieved by a first wake element size of $\frac{\Delta x_w}{c} = \frac{1}{32}$ and a wake with 80 streamwise wake panels as for a constant wake discretisation of $\frac{\Delta x_w}{c} = \frac{1}{16}$ and 320 streamwise wake panels, resulting in a reduction in the number of states by a factor of 4.

In conclusion, the present model allows for unsteady aerodynamic simulations with increased efficiency with respect to discrete-time and available continuous-time approaches, by varying the wake element size and timestep, thus reducing the required system size for a given accuracy. Furthermore, in case of gust simulations for aircraft where many different load cases and gust lengths need to be run, a single, efficient model can be set up, while computational efficiency is maintained by varying the timestep as required.



## 4.9 LIMITATIONS OF THE MODEL

The goal of the aeroelastic analysis and optimisation framework presented in this dissertation is to improve the conceptual design of aircraft wings by including aeroelasticity. Therefore, the aerodynamic model was selected as a trade-off between computational efficiency and accuracy and, consequently, a number of assumptions have been made. In case of the aerodynamic model, this results in the following main limitations of the model:

- The aerodynamic model is based on potential flow theory, which restricts its applicability to very high Reynolds numbers, no strong shocks, no transonic effects, and small angles of attack. Therefore, care should be taken when applying the presented model to aircraft operating in transonic flight conditions, where higher fidelity aerodynamic models are typically required.
- Small unsteady perturbations with respect to the steady aerodynamics solution are assumed, such that a fixed wake geometry can be used and a continuous-time state-space formulation can be obtained for computational efficiency.
- Compressibility is accounted for by means of the Prandtl-Glauert correction, which is valid up to high subsonic Mach numbers for reduced frequencies up to 1, after which the effects of compressibility are no longer captured accurately by the present model.

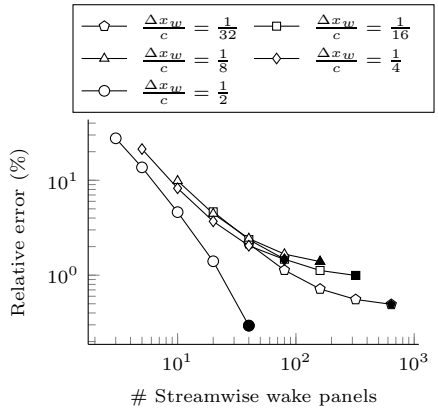


**(a)** Relative error in lift coefficient, $2H = 5c$.

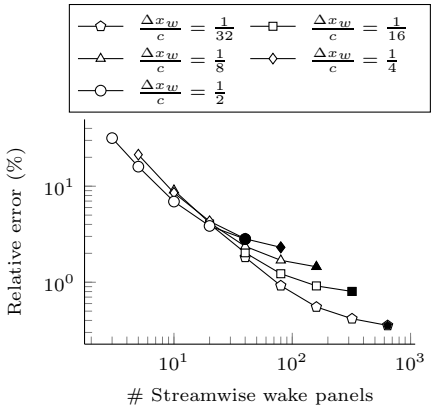


**(b)** Relative error in moment coefficient, $2H = 5c$.

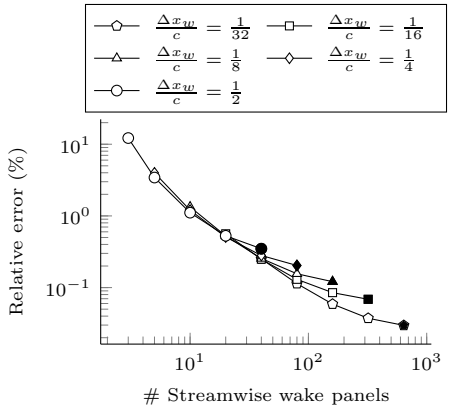


**(c)** Relative error in lift coefficient, $2H = 50c$.

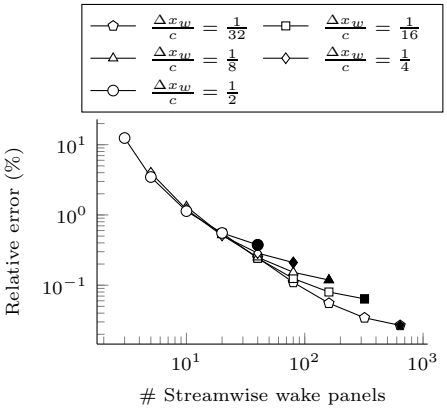


**(d)** Relative error in moment coefficient, $2H = 50c$.

**Figure 4.16:** Effect of varying the number of streamwise wake panels on the maximum lift and moment coefficient for various initial wake panel sizes at different gust lengths. The equivalent constant size wake discretisation results are indicated by the filled markers.

- The drag prediction is based on a semi-empirical viscous drag model and potential flow theory for induced drag, which is sufficiently accurate for conceptual structural and aeroelastic design. However, when design decisions are taken based on the drag results, care should be taken and a higher fidelity drag prediction might be required.

When interpreting the results obtained by the framework, one should always keep these limitations in mind.

## 4.10 SYNOPSIS

In this chapter, an aerodynamic model based on potential flow theory has been formulated that can analyze the high-subsonic steady and unsteady flow around aircraft wings.



- Under a thin-wing assumption, vortex ring elements are used to discretise the wing, as is common in the unsteady vortex lattice method (UVLM).
- Compressibility is accounted for by means of the Prandtl-Glauert transformation.
- By assuming small perturbations with respect to the steady solution and a fixed wake, the governing equations are obtained in continuous-time state-space form by only discretising the advection equation governing the transport of vorticity in the wake in space by means of the discontinuous Galerkin method, while making no assumptions regarding the time derivatives. The states of the system are the vortex strengths of the wake vortex elements and the perturbation angle of attack, the input of the system is the time derivative of the perturbation angle of attack, and the outputs of the system are the aerodynamic forces and moments acting on the wing.
- The approach for deriving the continuous-time form is applicable to any arbitrary wake shape and wake discretisation and can easily be extended to higher order panel methods.
- In order to assess the aerodynamic performance of an aircraft, the induced drag of the wing is computed based on the potential flow solution and an estimate of the aircraft parasitic drag is made using a semi-empirical approach.
- Verification of the model shows excellent agreement with incompressible steady and unsteady benchmark solutions.

- In case of compressibility, the model shows good agreement to the approximate closed-form solution of the Possio integral equation up to high subsonic Mach numbers for reduced frequencies up to 1, after which the effects of compressibility are no longer captured accurately by the present model.
- Application of the present model to a discrete gust analysis of a swept and tapered wing clearly illustrates the benefits of the continuous-time formulation for computational efficiency by varying the timestep independent of the spatial discretisation and introducing a non-constant wake element discretisation.

*Simplicity is the ultimate sophistication.*
**Leonardo da Vinci**

# 5

# AEROELASTICITY AND MORPHING[1]

The structural model and aerodynamic model used in this dissertation were presented in Chapter 3 and Chapter 4, respectively. In order to obtain the aeroelastic solution and incorporate the effects of morphing, these models have to be coupled and morphing needs to be taken into account in the solution process. Although models exist for the aeroelastic analysis of wings, neither of these includes both aeroelastic tailoring and morphing. Therefore this chapter presents an aeroelastic framework that incorporates all relevant static and dynamic aeroelastic effects for both aeroelastic tailoring and morphing.

First, Section 5.1 provides an overview of the state of the art in geometrically nonlinear aeroelastic analysis methods suitable for preliminary design. Next, Section 5.2 discusses the static aeroelastic model presenting the coupling between the structural and aerodynamic model, following De Breuker et al. (2011), and the assessment of aileron effectiveness and divergence. The dynamic aeroelastic model is formulated in a monolithic continuous-time state-space form, as is discussed in Section 5.3, presenting the coupled system that has been developed and the assessment of the flutter speed and discrete gust response. The implement-

[1]Part of this chapter is based on the journal paper Werter, N.P.M. and De Breuker, R. (2016). *"A novel dynamic aeroelastic framework for aeroelastic tailoring and structural optimisation"*, Composite Structures, vol. 158, pp. 369-386, and the conference paper Werter, N.P.M. and De Breuker, R. (2015). *"A framework for the aeroelastic analysis and design of generic morphing wings"*, in *Proceedings of the 23rd AIAA/AHS Adaptive Structures Conference*, pp. 1-15. Kissimmee, FL, USA.

ation of morphing is discussed in Section 5.4 extending the work of De Breuker et al. (2011) with camber and span morphing, after which Sections 5.5 and 5.6 presents a brief discussion on the computation of the sensitivities required for gradient-based optimisation and the implementation of the framework, respectively. The verification of the aeroelastic models is given in Section 5.7, after which Section 5.8 presents a discussion on the limitations of the framework. Finally, a brief synopsis is given in Section 5.9.

## 5.1 RECENT PROGRESS IN GEOMETRICALLY NONLINEAR AEROELASTIC ANALYSIS

With the introduction of composite materials and the drive to lighter wing structures, wings become increasingly flexible. As explained in Chapter 3, geometrically linear models no longer capture the response of these wings accurately and, therefore, a geometrically nonlinear aeroelastic model is required.

Since wing structures are typically slender structures, beam models are well suited for the geometrically (non)linear analysis of aircraft wings, as already introduced in Chapter 3. In order to obtain the geometrically nonlinear aeroelastic solution, the structural model needs to be coupled to an aerodynamic model accounting for the effects of wing deformation on the aerodynamic loads. Within the field of geometrically nonlinear aeroelasticity, a distinction can be made between models that incorporate a two-dimensional aerodynamic model (i.e. strip theory) and models that incorporate a three-dimensional aerodynamic model accounting for the effects of a finite wing.

Several examples of geometrically nonlinear aeroelastic models exist in the literature. Patil and co-workers (Patil et al., 1999; Patil and Hodges, 2004; Patil et al., 2000, 2001a,b) investigated the effect of geometric nonlinearity on both the static and dynamic aeroelastic response of a High-Altitude-Long-Endurance (HALE) aircraft wing by coupling a geometrically nonlinear intrinsic beam model to a strip theory aerodynamics using an unsteady finite state aerodynamics model. Their results clearly illustrate the importance of a geometrically nonlinear structural model for the analysis of very flexible wings, showing significant changes in flutter speed and frequency as a function of wing angle of attack and showing significant changes in the flight dynamic response resulting from wing flexibility. More recently, similar conclusions have been drawn by Su and Cesnik (2010) who also coupled a geometrically nonlinear intrinsic beam model to strip theory aerodynamics using an unsteady finite state aerodynamics model to investigate the aeroelastic stability and gust response of a flexible blended wing body.

Tang and Dowell (Tang and Dowell, 2001, 2002a,b, 2004; Tang et al., 2010) coupled a displacement-based geometrically nonlinear beam model to a strip theory aero-

dynamic model including the ONERA stall aerodynamic model to investigate, both numerically and experimentally, the effect of both geometric and aerodynamic nonlinearities on the flutter response and limit cycle oscillations of a HALE aircraft wing under different inertial, gravitational, and aerodynamic load conditions. Based on their results, similar conclusions can be drawn on the importance of geometrically nonlinear models for very flexible wing structures.

In contrast to the previous studies, Wang et al. (2010) and Murua et al. (2012a,b) coupled a geometrically nonlinear beam model to a three-dimensional unsteady aerodynamic model based on the unsteady vortex lattice method. Wang et al. investigated the effect of geometric and aerodynamic nonlinearities on the gust response of a HALE flying wing aircraft including the effects of wake rollup and wing stall. Murua et al. used a similar model and introduced flight dynamics to investigate the effect of flight dynamics on the aeroelastic stability and response of HALE aircraft. In order to improve the efficiency of the dynamic aeroelastic response computations, they introduce a linearised discrete-time state-space formulation of the coupled flight dynamic aeroelastic equations to compute the small perturbance response around the nonlinear equilibrium solution and assess the small perturbance aeroelastic stability. More recently, Ng et al. (2015) also applied this model to the aeroelastic analysis of wind turbine blades to investigate the effects of using flaps to reduce the root bending moment of a wind turbine blade.



Based on all these studies, it can be concluded that geometric nonlinearity can significantly influence the aeroelastic response of aircraft wings and has to be accounted for in case of very flexible wings. Within this field, the present model integrates the structural model described in Chapter 3 to the unsteady aerodynamic model described in Chapter 4 to obtain the dynamic aeroelastic response of composite aircraft wings.

Furthermore several morphing mechanisms will be introduced to investigate the influence of morphing on the aeroelastic response of aircraft wings and assess potential benefits that can be achieved. Especially in case of morphing mechanisms that effect the global wing geometry, these mechanisms can produce a morphing manoeuvre that causes large wing shape changes that have to be accounted for by means of a geometrically nonlinear aeroelastic model to accurately capture the influence of these shape changes on the aeroelastic response of the aircraft wing.

## 5.2 Static aeroelastic analysis

Static aeroelastic equilibrium is obtained by closely coupling the static structural model introduced in Section 3.4 to the steady aerodynamic solution introduced in Section 4.3 and Section 4.4, as explained in Section 5.2.1. Using the static

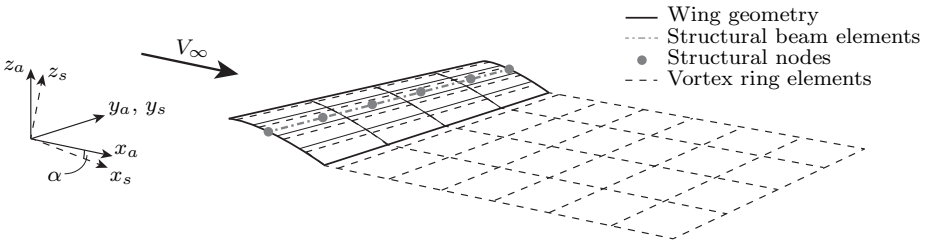


**Figure 5.1:** Example wing and wake discretisation using vortex ring elements illustrating the structural, $x_s y_s z_s$, and aerodynamic, $x_a y_a z_a$, coordinate systems.

aeroelastic equilibrium solution, the structural performance of the wing can be assessed for strength, as explained in Section 3.6, and buckling, as explained in Section 3.7. Furthermore, the static aeroelastic equilibrium solution is used to assess aileron effectiveness, as explained in Section 5.2.2, and static aeroelastic stability, i.e. divergence, as explained in Section 5.2.3.

### 5.2.1 AEROELASTIC EQUILIBRIUM



Aeroelastic equilibrium is governed by equilibrium of forces and moments between the internal structural forces and moments, $\mathbf{F_s}$, and the externally applied loads, $\mathbf{F_{ext}}$:

$$\mathbf{F_s} - \mathbf{F_{ext}} = \mathbf{F_s} - \mathbf{F_a} - \mathbf{F_e} = \mathbf{0} \tag{5.1}$$

where $\mathbf{F_a}$ are the aerodynamic forces and moments and $\mathbf{F_e}$ are the remaining external forces and moments (e.g. gravity or engine thrust), as defined in Section 3.4.2. In order to find geometrically nonlinear aeroelastic equilibrium, the aerodynamic mesh needs to be updated according to the structural deformations and the resulting aerodynamic forces need to be transferred to the structural nodes. Figure 5.1 shows a schematic illustration of the wing geometry, structural beam axis, aerodynamic vortex ring discretisation, and corresponding coordinate systems to assist the following paragraphs discussing the coupling of the structural and aerodynamic models.

The local structural deformations at the spanwise aerodynamic locations are found by linear interpolation of the nodal structural deformations, after which the aerodynamic mesh is created as explained in Section 4.3.1 and the aerodynamic solution can be found. In order to obtain the corresponding nodal force vector, $\mathbf{F_a}$, the resulting aerodynamic forces are first converted to statically equivalent forces and moments on the structural beam, after which they are converted into statically equivalent nodal forces and moments on the two closest structural nodes, as is illustrated in Figure 5.2 and described through a transformation matrix, $\mathbf{T_{AS}}$.

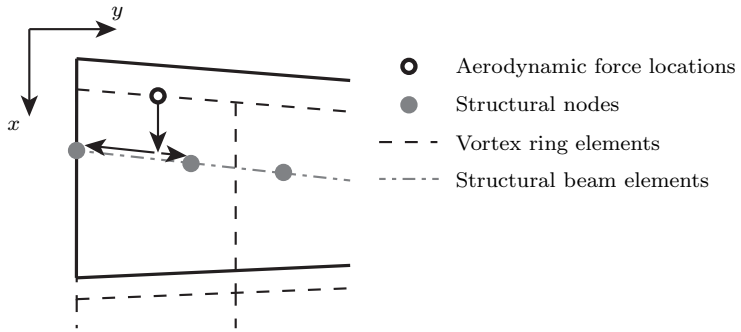


**Figure 5.2:** Schematic illustration of the transfer of the aerodynamic forces to the structural nodes.

Note that the aerodynamic forces are defined in the aerodynamic coordinate system, which is aligned with the free stream velocity vector, while the equivalent forces on the structure need to be defined in the body-fixed coordinate system. Therefore, the aerodynamic forces and moments need to be transformed through a coordinate transformation, $\mathbf{R_\alpha}$, rotating the aerodynamic forces through the aircraft angle of attack, $\alpha$, to the body-fixed coordinate system. Consequently, the equivalent nodal forces and moments are related to the aerodynamic forces and moments through the following transformation equation:



$$\mathbf{F_a} = \mathbf{T_{AS}} \mathbf{R_\alpha} \mathbf{F_a^a} \tag{5.2}$$

where the superscript $\mathbf{F_a^a}$ are the aerodynamic forces obtained from the aerodynamic solution, as defined in Chapter 4.

Finally, following De Breuker (2011), equilibrium is found by linearising equation (5.1), resulting in:

$$\underbrace{(\mathbf{K_a} + \mathbf{K_e} - \mathbf{K_s})}_{\mathbf{J}} \Delta\mathbf{p} = \mathbf{F_s}(\mathbf{p}) - \mathbf{F_a}(\mathbf{p}) - \mathbf{F_e}(\mathbf{p}) = \mathbf{R_0} \tag{5.3}$$

and solving this system using the Newton-Raphson root finding method until the residual force vector, $\mathbf{R_0}$, becomes the zero vector, resulting in the closely coupled static aeroelastic equilibrium solution, $\mathbf{p}$, for a given flight condition and angle of attack.

In general, the relevant static aeroelastic equilibrium solution is not given by a fixed angle of attack, but by trimming the aircraft for a certain flight condition, resulting in an additional equilibrium equation (i.e. the total lift generated equals the weight of the aircraft) and an additional degree of freedom (i.e. the aircraft

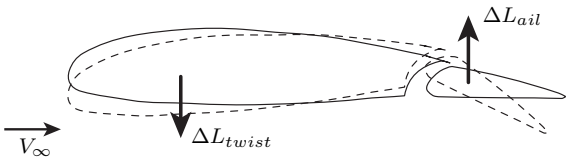


**Figure 5.3:** Schematic illustration of the forces introduced by the deflection of an aileron on a flexible wing structure.

angle of attack). Linearising the combined system of equations, the total set of equations that is solved by means of the Newton-Raphson root finding method, in case of a trimmed flight condition, becomes:

$$\begin{bmatrix} \mathbf{J} & -\mathbf{f}_\alpha \\ \frac{\partial L}{\partial \mathbf{p}} & \frac{\partial L}{\partial \alpha} \end{bmatrix} \begin{pmatrix} \Delta \mathbf{p} \\ \Delta \alpha \end{pmatrix} = \begin{pmatrix} \mathbf{R_0} \\ W - L\left(\mathbf{p}, \alpha\right) \end{pmatrix} \tag{5.4}$$

where $\mathbf{f}_\alpha$ is the partial derivative of the force residual with respect to the angle of attack, $L$ is the total lift generated, and $W$ is the aircraft weight. In this case, the static aeroelastic equilibrium solution is given by the structural equilibrium deformations, $\mathbf{p}$, and the required angle of attack for trim, $\alpha$.

5

### 5.2.2 AILERON EFFECTIVENESS

One of the important parameters in the performance of an aircraft is its controllability. In general, aircraft use ailerons to introduce a local change in aerodynamic load close to the wing tip and perform a roll manoeuvre. In case of a rigid wing structure, a downward deflection of the ailerons will locally induce an upward aerodynamic force, as illustrated in Figure 5.3, resulting in the desired rolling moment and roll manoeuvre. However, in case of a flexible wing structure, the twisting moment induced by the aileron deflection will induce a nose-down twist of the entire airfoil, thus inducing a downward aerodynamic force and reducing the effectiveness of the ailerons. As velocity is increased, this effect is amplified and undesired loss of control or eventually control reversal can occur.

One of the measures to assess the performance of the aileron is the aileron effectiveness defined as the negative ratio between the roll coefficient induced by the aileron deflection and the roll coefficient due to the resulting steady roll manoeuvre (Dillinger et al., 2013):

$$\eta_{ail} = -\frac{C_{m_\delta}}{C_{m_p}} = \frac{p_{roll} s}{\delta V_\infty} \tag{5.5}$$

where $s$ is the wing semispan, and $p_{roll}$ is the steady roll rate of the aircraft

corresponding to an aileron deflection angle, $\delta$. A positive aileron effectiveness indicates a desired positive roll rate for a positive aileron deflection, an aileron effectiveness of 0 indicates no control authority, and a negative aileron effectiveness indicates control reversal.

In the present framework, the assessment of aileron effectiveness has been implemented by computing the effectiveness of the ailerons around the static aeroelastic equilibrium solution. A roll manoeuvre is an anti-symmetric manoeuvre about the aircraft symmetry plane and, therefore, in order to obtain the aerodynamic loads introduced by the ailerons and the corresponding steady roll rate, an anti-symmetric aerodynamic analysis is carried out around the steady symmetric aerodynamic solution as presented in Sections 4.3 and 4.4. The anti-symmetric aerodynamic solution procedure is similar to the steady symmetric aerodynamic solution, with two main differences. First of all, in case of an anti-symmetric solution any positive vortex ring element on the modelled wing has a negative image on the other wing. This results in the following anti-symmetric induced velocities, similar to the symmetric induced velocities given by equation (4.16) (Katz and Plotkin, 2001):

$$(\nabla\phi \cdot \mathbf{n})_{i,j}^{asym} = -(\nabla\phi \cdot \mathbf{n})_{i,j}^{sym} = -\left.\nabla\phi_{i,j}^{*}\right|_{\mathbf{x_c}=(x_i,-y_i,z_i)} \cdot \begin{pmatrix} n_{x_i} \\ -n_{y_i} \\ n_{z_i} \end{pmatrix} \Gamma_j \tag{5.6}$$

Secondly, the right hand side of the flow tangency condition needs to be updated to account for the effect of the aileron deflection and the resulting wing deformation and roll rate. In this case, aileron effectiveness is assessed by finding the steady roll rate under an aileron deflection of 1 deg. The perturbation by the aileron can, thus, be assumed to be small and the effect of the aileron is only accounted for by an update of the normal vector of the corresponding aileron panels, while keeping the aerodynamic mesh unaffected when computing the influence coefficients. However, depending on the wing stiffness distribution, the effect of wing deformation is not necessarily small and, therefore, needs to be accounted for by an update of the aerodynamic mesh, similar to the static aeroelastic equilibrium solution. Finally, accounting for the effect of the aircraft roll rate, the right hand side of the flow tangency condition, given by equation (4.19), for the anti-symmetric aerodynamic solution becomes:

$$-\mathbf{V} \cdot \mathbf{n}|_{asym} = -\mathbf{V_\infty} \cdot (\mathbf{n_{ail}} - \mathbf{n_{st}}) + (\mathbf{p_{roll}} \times \mathbf{r}) \cdot \mathbf{n_{ail}} \tag{5.7}$$

where $(\mathbf{n_{ail}} - \mathbf{n_{st}})$ accounts for the update in normal vector from both the aileron deflection and the structural deformations with respect to the symmetric static equilibrium, $\mathbf{p_{roll}}$ is the roll rotational velocity vector, and $\mathbf{r}$ is the location of the collocation points with respect to the wing root.

In order to compute the aileron effectiveness, the roll rate, $p_{roll}$, that results in roll moment equilibrium needs to be determined. Starting from the static aeroelastic equilibrium solution, and introducing the roll rate, as additional degree of freedom and roll moment equilibrium as additional equation, the equilibrium equations are given by:

$$\mathbf{F_s}(\mathbf{p}) - \mathbf{F_e}(\mathbf{p}) - \mathbf{F_{a_{st}}}(\mathbf{p_{st}}, \alpha) - \mathbf{F_{a_{asym}}}(\mathbf{p}, \mathbf{p_{st}}, \alpha, p_{roll}) = 0 \tag{5.8}$$

$$M_{x_{root}}(\mathbf{p}, \alpha, p_{roll}) = 0 \tag{5.9}$$

where the subscript $st$ indicates the static equilibrium solution and $M_{x_{root}}$ is the reaction moment at the wing root about the longitudinal axis originating from the roll manoeuvre.

Subtracting the static equilibrium solution given by equation (5.1) from equation (5.8), and linearising the system of equations, the following linear system of equations is obtained:

$$\begin{bmatrix} \mathbf{J_{asym}} & -\mathbf{f}_{p_{roll}} \\ -\frac{\partial M_{x_{root}}}{\partial \mathbf{p}} & -\frac{\partial M_{x_{root}}}{\partial p_{roll}} \end{bmatrix} \begin{pmatrix} \Delta\mathbf{p} \\ \Delta p_{roll} \end{pmatrix} = \begin{pmatrix} \mathbf{R_{asym}} \\ M_{x_{root}}(\mathbf{p}, \alpha, p_{roll}) \end{pmatrix} \tag{5.10}$$



where $\mathbf{f}_{p_{roll}}$ is the partial derivative of the force residual, $\mathbf{R_{asym}}$, with respect to the roll rate and

$$\mathbf{J_{asym}} = \mathbf{K_{a_{asym}}} + \mathbf{K_e} - \mathbf{K_s} \tag{5.11}$$

$$\mathbf{R_{asym}} = \Delta\mathbf{F_s}(\mathbf{p}) - \Delta\mathbf{F_e}(\mathbf{p}) - \mathbf{F_{a_{asym}}}(\mathbf{p}, \alpha, p_{roll}) \tag{5.12}$$

where $\Delta\mathbf{F_s}(\mathbf{p})$ and $\Delta\mathbf{F_e}(\mathbf{p})$ are the update in the structural and external force vector originating from the anti-symmetric roll solution. Using the Newton-Raphson root finding method, the steady aeroelastic roll manoeuvre for a given aileron deflection can be found and the aileron effectiveness can be found through equation (5.5).

### 5.2.3 DIVERGENCE

One of the aeroelastic instabilities in aircraft is divergence. Consider a two-dimensional airfoil, as illustrated in Figure 5.4. The aerodynamic forces act at the centre of pressure close to the quarter-chord line of the airfoil, and, consequently, the elastic axis of the airfoil is typically located aft of the centre of pressure. Therefore, under aerodynamic loads, the airfoil will twist nose up, resulting in an increased angle of attack and increased aerodynamic forces. As long

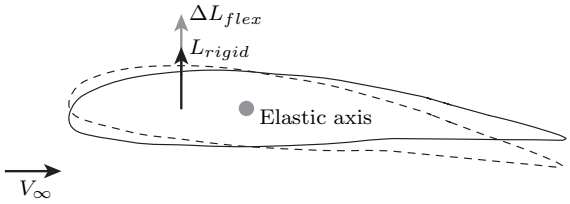


**Figure 5.4:** Schematic illustration of the forces introduced by the flexibility of the wing structure, potentially leading to divergence.

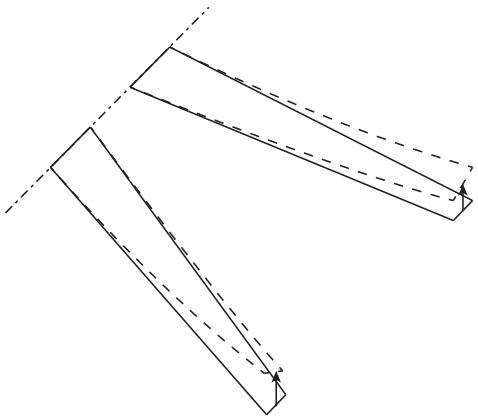

**Figure 5.5:** Schematic illustration of the twist induced by wing bending of forward and aft swept wings.



as the torsional stiffness of the wing structure is large enough, the wing structure will induce an opposing torsional moment which is sufficient to oppose the aerodynamic torsional moment and equilibrium is found. However, as velocity increases, the aerodynamic loads will increase until at one point, the torsional resistance of the wingbox is no longer sufficient to oppose the aerodynamic torsional moment and the system becomes unstable, i.e. an equilibrium between the structural and aerodynamic forces can no longer be found, and divergence will occur.

Extending this to three-dimensional wings, a clear relation between sweep angle and divergence speed can be observed. As illustrated in Figure 5.5, the geometric coupling between wing bending and wing twist for forward swept wings results in nose up twist when bending the wing upward, amplifying the coupling between aerodynamic loads and wing twist and, consequently, making forward swept wings prone to divergence. While, as illustrated, for aft swept wings, the opposite is observed resulting in an increase in divergence speed or even a divergence free wing.

In the present framework, divergence can be assessed by investigation the stability

of the linearised aeroelastic equilibrium equation, given by equation (5.3). Introducing $\lambda$ as the eigenvalue of the system, the stability of the static aeroelastic equilibrium is governed by the following eigenvalue problem:

$$(\lambda \mathbf{K_a} + \mathbf{K_e} - \mathbf{K_s})\,\Delta\mathbf{p} = \mathbf{0} \tag{5.13}$$

such that the static aeroelastic system is stable for $\lambda \geq 1$.

## 5.3 DYNAMIC AEROELASTIC ANALYSIS

The dynamic structural model introduced in Section 3.5 and the unsteady aerodynamic model introduced in Section 4.3 and Section 4.5 are monolithically coupled through a series of coupling matrices, as introduced in Section 5.3.1. Using these coupling matrices, a dynamic aeroelastic formulation in continuous-time state-space form has been developed that describes the dynamic aeroelastic response of a wing to external perturbations is discussed in Section 5.3.2. With this model, dynamic aeroelastic stability can be assessed, as discussed in Section 5.3.3, and the response of a wing to a discrete gust can be determined, as discussed in Section 5.3.4. Since dynamic perturbations around the static aeroelastic equilibrium solution are typically small, a linear dynamic aeroelastic analysis around the static aeroelastic equilibrium solution is carried out for computational efficiency.



### 5.3.1 COUPLING MATRICES

In order to couple the dynamic structural model and the unsteady aerodynamic model, the aerodynamic forces need to be transferred to the structural nodes as input to the structural model and the perturbation angle of attack and its time derivative induced by the structural deformations on the aerodynamic panels need to be determined as input to the unsteady aerodynamic model. Similar to the static aeroelastic model, the aerodynamic forces are first converted to statically equivalent forces and moments on the structural beam, after which they are converted into statically equivalent nodal forces and moments.

The perturbation angle of attack and its time derivative are composed of four components, as illustrated in Figure 5.6:

$$\alpha = \alpha_{air} + \theta - \frac{\dot{h}}{V_\infty} + \frac{\dot{\theta}\,(x - x_b)}{V_\infty} \tag{5.14}$$

where $\alpha_{air}$ is the perturbation angle of attack induced by the free stream flow, $\theta$ is the angle of attack introduced by the structural wing twist, $-\frac{\dot{h}}{V_\infty}$ is the

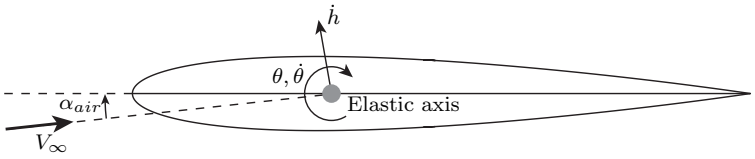


**(a)** Different components of the local angle of attack.

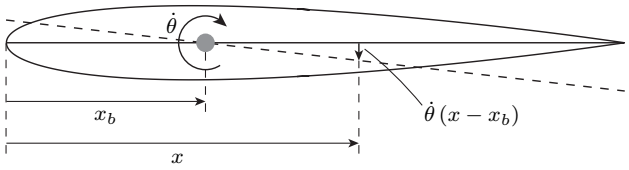


**(b)** Local angle of attack introduced by the pitch rate, $\dot{\theta}$.

**Figure 5.6:** Schematic illustrations of the dynamic perturbation angle of attack.

perturbation angle of attack introduced by the local plunge motion of the wing, and $\frac{\dot{\theta}(x-x_b)}{V_\infty}$ is the perturbation angle of attack introduced by the local pitch rate of the wing, where $x - x_b$ is the distance between the location of the aerodynamic panel and the pitch axis.

Given a static equilibrium solution and corresponding deformations, $\theta$, $\dot{\theta}$, $\ddot{\theta}$, $\dot{h}$, and $\ddot{h}$ need to be linked to the dynamic structural deformations to obtain the dynamic perturbation angle of attack. Note that, similar to the aerodynamic forces and moments, the structural degrees of freedom are first transformed through a coordinate transformation, $\mathbf{R}_{\boldsymbol{\alpha}}^T$, from the body-fixed coordinate system to the aerodynamic coordinate system.

First, in order to obtain the dynamic perturbation angle of attack induced by structural wing twist, $\theta$, the local angle of attack, $\alpha_l$, is linearised around the static aeroelastic equilibrium solution:

$$\alpha_l = \underbrace{\alpha_0}_{\text{static equilibrium}} + \underbrace{\frac{\partial \alpha_l}{\partial \boldsymbol{\theta}_\mathbf{s}} \Delta \boldsymbol{\theta}_\mathbf{s}}_{\text{dynamic perturbation, } \theta} \tag{5.15}$$

where $\boldsymbol{\theta}_\mathbf{s}$ are the structural rotational degrees of freedom and $\Delta\boldsymbol{\theta}_\mathbf{s}$ are the dynamic structural rotations around the static equilibrium solution.

Consider a spanwise aerodynamic section, $P_1 - P_2$, on the beam structural axis, as illustrated in Figure 5.7, defined by a tangent vector, $\mathbf{t}$. In order to find the angle of attack, $\alpha_l$, at the centre of the beam element, first, similar to the static aerodynamic model introduced in Section 4.3.1, the deformed chord vector is determined, given by a combination of, the wing angle of attack, the initial wing

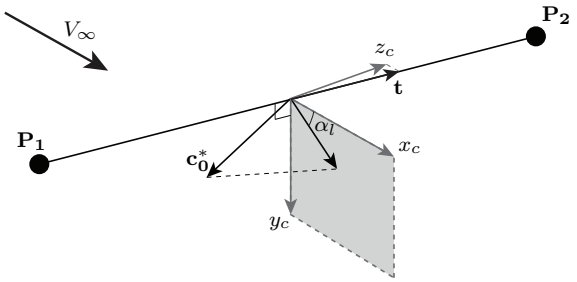


**Figure 5.7:** Schematic illustration of the effective angle of attack originating from the structural deformations.

twist, and the static structural deformations:

$$\mathbf{c_0^*} = \mathbf{R_s R_{ini} R_\alpha^T c_0} \tag{5.16}$$

In order to find the angle of attack induced by this deformation, the deformed chord vector is transformed to a new local coordinate system, $x_c y_c z_c$, defined by the direction of the free-stream velocity, $\mathbf{e_{V_\infty}}$, as $x_c-$direction and the normalised component of the tangent vector perpendicular to the free-stream velocity vector, $\mathbf{t}^*$, as $z_c-$direction, as illustrated in Figure 5.7. Finally, their cross-product defines the $y_c-$direction and is the normal to the projection of the beam axis on the plane perpendicular to the free-stream velocity. The resulting rotation matrix, $\mathbf{R_B}$, that transforms a vector in the global aerodynamic, $x_A y_A z_A$, coordinate system to the local, $x_c y_c z_c$, coordinate system, is given by:

$$\mathbf{R_B} = \begin{bmatrix} \mathbf{e}_{\mathbf{V_\infty}}^T \\ (\mathbf{t}^* \times \mathbf{e_{V_\infty}})^T \\ (\mathbf{t}^*)^T \end{bmatrix} = \begin{bmatrix} 1 & 0 & 0 \\ 0 & t_z^* & -t_y^* \\ 0 & t_y^* & t_z^* \end{bmatrix} \tag{5.17}$$

Transforming the deformed chord vector to the $x_c y_c z_c$ coordinate system:

$$\bar{\mathbf{c}}_\mathbf{0} = \mathbf{R_B c_0^*} = \mathbf{R_B R_s R_{ini} R_\alpha^T c_0} \tag{5.18}$$

the local angle of attack is defined by the angle between the deformed chord vector and the free-stream velocity vector in the $x_c y_c-$plane, as illustrated in Figure 5.7:

$$\alpha_l = \tan^{-1}\left(\frac{\bar{\mathbf{c}}_{\mathbf{0}_{y_c}}}{\bar{\mathbf{c}}_{\mathbf{0}_{x_c}}}\right) \tag{5.19}$$

Introducing equation (5.19) in equation (5.15), the dynamic perturbation angle of attack, $\theta$, induced by the dynamic structural rotations can be determined. Taking

the partial derivative of equation (5.19) with respect to the structural rotations, the following relation is obtained:

$$\frac{\partial \alpha_l}{\partial \boldsymbol{\theta_s}} = \frac{1}{1 + \left(\frac{\bar{\mathbf{c}}_{\mathbf{0}_{y_c}}}{\bar{\mathbf{c}}_{\mathbf{0}_{x_c}}}\right)^2} \frac{d\bar{\mathbf{c}}_{\mathbf{0}_y}\, \bar{\mathbf{c}}_{\mathbf{0}_x} - \bar{\mathbf{c}}_{\mathbf{0}_y}\, d\bar{\mathbf{c}}_{\mathbf{0}_{x_c}}}{\bar{\mathbf{c}}_{\mathbf{0}_x}^2} \tag{5.20}$$

with $d\bar{\mathbf{c}}_{\mathbf{0}}$ defined through equation (5.18):

$$d\bar{\mathbf{c}}_{\mathbf{0}} = \mathbf{R_B} \frac{\partial \mathbf{R_s}}{\partial \boldsymbol{\theta_s}} \mathbf{R_{ini}} \mathbf{R}_{\boldsymbol{\alpha}}^T \mathbf{c_0} \tag{5.21}$$

Next, considering the same spanwise aerodynamic section, $P_1 - P_2$, as illustrated in Figure 5.7, the structural velocities, $\dot{\mathbf{u}}_\mathbf{s}$, angular velocities, $\dot{\boldsymbol{\theta}}_\mathbf{s}$, accelerations, $\ddot{\mathbf{u}}_\mathbf{s}$, and angular accelerations, $\ddot{\boldsymbol{\theta}}_\mathbf{s}$ are projected along the relevant components of the local $x_c y_c z_c$ coordinate system to determine the remaining terms of the dynamic perturbation angle of attack, resulting in:

$$\dot{h} = -\left(\mathbf{R}_{\boldsymbol{\alpha}}^T \dot{\mathbf{u}}_\mathbf{s}\right) \cdot \left(\mathbf{t}^* \times \mathbf{e}_{\mathbf{V}_\infty}\right) \tag{5.22}$$

$$\dot{\theta} = \left(\mathbf{R}_{\boldsymbol{\alpha}}^T \dot{\boldsymbol{\theta}}_\mathbf{s}\right) \cdot \mathbf{t}^* \tag{5.23}$$

$$\ddot{h} = -\left(\mathbf{R}_{\boldsymbol{\alpha}}^T \ddot{\mathbf{u}}_\mathbf{s}\right) \cdot \left(\mathbf{t}^* \times \mathbf{e}_{\mathbf{V}_\infty}\right) \tag{5.24}$$

$$\ddot{\theta} = \left(\mathbf{R}_{\boldsymbol{\alpha}}^T \ddot{\boldsymbol{\theta}}_\mathbf{s}\right) \cdot \mathbf{t}^* \tag{5.25}$$

recognising that the plunge rate and acceleration are defined by a translation along $y_c$ and the pitch rate and acceleration are defined by a rotation about $z_c$.

Finally, similar to the static aeroelastic analysis, a linear interpolation of the nodal structural deformations to the spanwise aerodynamic sections is used to find the local structural deformations at each spanwise aerodynamic section. In order to assist the derivation of the coupled dynamic aeroelastic system in the next section, the relations linking the dynamic structural deformations and the different terms in equations (5.14), as governed by equations (5.15) and (5.22) to (5.25), are summarised by the following coupling matrices:

$$\begin{aligned}
\boldsymbol{\theta}_\mathbf{a} &= \mathbf{T}_{\boldsymbol{\alpha}} \boldsymbol{\theta}_\mathbf{s} \\
\dot{\boldsymbol{\theta}}_\mathbf{a} &= \mathbf{T}_\mathbf{t} \dot{\boldsymbol{\theta}}_\mathbf{s} \\
\ddot{\boldsymbol{\theta}}_\mathbf{a} &= \mathbf{T}_\mathbf{t} \ddot{\boldsymbol{\theta}}_\mathbf{s} \\
\dot{\mathbf{h}} &= \mathbf{T}_\mathbf{n} \dot{\mathbf{u}}_\mathbf{s} \\
\ddot{\mathbf{h}} &= \mathbf{T}_\mathbf{n} \ddot{\mathbf{u}}_\mathbf{s}
\end{aligned} \tag{5.26}$$

### 5.3.2 CONTINUOUS-TIME STATE-SPACE FORMULATION

Starting from the aerodynamic state-space system, as defined by equations (4.36) and (4.37), using equation (5.14), the aerodynamic state equation can be linked to the different components of the perturbation angle of attack, $\alpha$, resulting in:

$$\begin{pmatrix} \dot{\mathbf{\Gamma}}_\mathbf{w} \\ \dot{\boldsymbol{\alpha}}_\mathbf{air} \end{pmatrix} = \begin{bmatrix} \mathbf{K_1} & \mathbf{K_2} & -\frac{\mathbf{K_2 B_\alpha}}{V_\infty} & \mathbf{K_2 B_\alpha} & \mathbf{K_2 B_{pitch}} \\ \mathbf{0} & \mathbf{0} & \mathbf{0} & \mathbf{0} & \mathbf{0} \end{bmatrix} \begin{pmatrix} \mathbf{\Gamma}_\mathbf{w} \\ \boldsymbol{\alpha}_\mathbf{air} \\ \dot{\mathbf{h}} \\ \boldsymbol{\theta}_\mathbf{a} \\ \dot{\boldsymbol{\theta}}_\mathbf{a} \end{pmatrix} + \begin{bmatrix} \mathbf{0} \\ \mathbf{I} \end{bmatrix} \dot{\boldsymbol{\alpha}}_\mathbf{air} \quad (5.27)$$

where $\mathbf{B}_{\boldsymbol{\alpha}}$ links the spanwise pitch angle distribution, $\boldsymbol{\theta}_\mathbf{a}$, and plunge velocity distribution, $\dot{\mathbf{h}}$, to the corresponding aerodynamic panels, and $\mathbf{B_{pitch}}$ transforms the spanwise pitch rate, $\dot{\boldsymbol{\theta}}_\mathbf{a}$ to the local induced angle of attack of the corresponding aerodynamic panels, accounting for $\frac{x-x_b}{V_\infty}$ defined by equation (5.14). $\dot{\boldsymbol{\alpha}}_\mathbf{air}$ is selected as only external input to the state equation, since all other components are directly related to the structural degrees of freedom.

Inserting equation (5.26) into equation (5.27), the final aerodynamic state equation as a function of the external input and structural deformations becomes:

$$\begin{pmatrix} \dot{\mathbf{\Gamma}}_\mathbf{w} \\ \dot{\boldsymbol{\alpha}}_\mathbf{air} \end{pmatrix} = \underbrace{\begin{bmatrix} \mathbf{K_1} & \mathbf{K_2} & -\frac{\mathbf{K_2 B_\alpha T_n}}{V_\infty} & \mathbf{K_2 B_\alpha T_\alpha} & \mathbf{K_2 B_{pitch} T_t} \\ \mathbf{0} & \mathbf{0} & \mathbf{0} & \mathbf{0} & \end{bmatrix}}_{\mathbf{H_1}} \begin{pmatrix} \mathbf{\Gamma}_\mathbf{w} \\ \boldsymbol{\alpha}_\mathbf{air} \\ \dot{\mathbf{u}}_\mathbf{s} \\ \boldsymbol{\theta}_\mathbf{s} \\ \dot{\boldsymbol{\theta}}_\mathbf{s} \end{pmatrix} + \underbrace{\begin{bmatrix} \mathbf{0} \\ \mathbf{I} \end{bmatrix}}_{\mathbf{H_2}} \dot{\boldsymbol{\alpha}}_\mathbf{air} \quad (5.28)$$

Similarly the aerodynamic output vector, $\mathbf{F_a}$, can be related to the free stream perturbation angle of attack and the structural degrees of freedom, resulting in:

$$\mathbf{F_a} = \underbrace{\begin{bmatrix}\mathbf{L_1} & \mathbf{L_2} & -\frac{\mathbf{L_2 B_\alpha T_n}}{V_\infty} & \mathbf{L_2 B_\alpha T_\alpha} & (\mathbf{L_2 B_{pitch}} + \mathbf{L_3 B_\alpha})\,\mathbf{T_t}\end{bmatrix}}_{\mathbf{H_3}} \begin{pmatrix}\mathbf{\Gamma_w}\\ \boldsymbol{\alpha}_{\mathbf{air}}\\ \dot{\mathbf{u}}_\mathbf{s}\\ \boldsymbol{\theta}_\mathbf{s}\\ \dot{\boldsymbol{\theta}}_\mathbf{s}\end{pmatrix}$$
$$+ \underbrace{\begin{bmatrix}-\frac{\mathbf{L_3 B_\alpha T_n}}{V_\infty} & \mathbf{L_3 B_{pitch} T_t}\end{bmatrix}}_{\mathbf{H_4}} \begin{pmatrix}\ddot{\mathbf{u}}_\mathbf{s}\\ \ddot{\boldsymbol{\theta}}_\mathbf{s}\end{pmatrix} + \mathbf{L_3 B_\alpha}\dot{\boldsymbol{\alpha}}_{\mathbf{air}} \tag{5.29}$$

Introducing the aeroelastic state vector, defined as $\mathbf{x} = \begin{pmatrix}\mathbf{\Gamma_w} & \boldsymbol{\alpha}_{\mathbf{air}} & \dot{\mathbf{p}} & \mathbf{p}\end{pmatrix}^T$, the aerodynamic part of the aeroelastic state-space system is given by:

$$\begin{pmatrix}\mathbf{\Gamma_w}\\ \boldsymbol{\alpha}_{\mathbf{air}}\end{pmatrix} = \mathbf{H_1 T_1 x} + \mathbf{H_2}\dot{\boldsymbol{\alpha}}_{\mathbf{air}} \tag{5.30}$$
$$\mathbf{F_a} = \mathbf{H_3 T_1 x} + \mathbf{H_4 T_2}\dot{\mathbf{x}}_\mathbf{s} + \mathbf{L_3 B_\alpha}\dot{\boldsymbol{\alpha}}_{\mathbf{air}} \tag{5.31}$$

where $\mathbf{x_s}$ is the structural state vector defined as $\begin{pmatrix}\dot{\mathbf{p}} & \mathbf{p}\end{pmatrix}^T$, and $\mathbf{T_1}$ and $\mathbf{T_2}$ are matrices containing ones and zeros, selecting $\begin{pmatrix}\mathbf{\Gamma_w} & \boldsymbol{\alpha}_{\mathbf{air}} & \dot{\mathbf{u}}_\mathbf{s} & \boldsymbol{\theta}_\mathbf{s} & \dot{\boldsymbol{\theta}}_\mathbf{s}\end{pmatrix}^T$ from the state vector, $\mathbf{x}$, $\begin{pmatrix}\ddot{\mathbf{u}}_\mathbf{s} & \ddot{\boldsymbol{\theta}}_\mathbf{s}\end{pmatrix}^T$ from the time derivative of structural state vector, $\dot{\mathbf{x}}_\mathbf{s}$, respectively.

Next, considering the structural system of equations given by equation (3.69), using equation (5.2), the structural state-space system becomes:

$$\begin{pmatrix}\ddot{\mathbf{p}}\\ \dot{\mathbf{p}}\end{pmatrix} = \underbrace{\begin{bmatrix}\mathbf{0} & -\mathbf{M}^{-1}\mathbf{K}\\ \mathbf{I} & \mathbf{0}\end{bmatrix}}_{\mathbf{A_s}} \underbrace{\begin{pmatrix}\dot{\mathbf{p}}\\ \mathbf{p}\end{pmatrix}}_{\mathbf{x_s}} + \underbrace{\begin{bmatrix}\mathbf{M}^{-1}\\ \mathbf{0}\end{bmatrix}}_{\mathbf{B_s}} \mathbf{T_{AS} R_\alpha F_a^a} \tag{5.32}$$

Introducing the aerodynamic output equation, given by equation (5.31), the structural state-space system can be rewritten as:

$$\underbrace{(\mathbf{I} - \mathbf{B_s T_{AS} R_\alpha H_4 T_2})}_{\mathbf{H_5}}\dot{\mathbf{x}}_\mathbf{s} = \underbrace{(\mathbf{A_s T_3} + \mathbf{B_s T_{AS} R_\alpha H_3 T_1})}_{\mathbf{H_6}}\mathbf{x}$$
$$+ \underbrace{\mathbf{B_s T_{AS} R_\alpha L_3 B_\alpha}}_{\mathbf{H_7}}\dot{\boldsymbol{\alpha}}_{\mathbf{air}} \tag{5.33}$$
$$\dot{\mathbf{x}}_\mathbf{s} = \mathbf{H_5}^{-1}\mathbf{H_6 x} + \mathbf{H_5}^{-1}\mathbf{H_7}\dot{\boldsymbol{\alpha}}_{\mathbf{air}} \tag{5.34}$$

Finally, combining equations (5.30) and (5.34), the aeroelastic state equation is obtained as:

$$\dot{\mathbf{x}} = \underbrace{\begin{bmatrix} \mathbf{H_1 T_1} \\ \mathbf{H_5}^{-1}\mathbf{H_6} \end{bmatrix}}_{\mathbf{A_{ss}}} \mathbf{x} + \underbrace{\begin{bmatrix} \mathbf{H_2} \\ \mathbf{H_5}^{-1}\mathbf{H_7} \end{bmatrix}}_{\mathbf{B_{ss}}} \dot{\boldsymbol{\alpha}}_{\mathbf{air}} \tag{5.35}$$

In order to complete the dynamic aeroelastic state-space system, equation (5.34) is introduced in equation (5.31) to obtain the aerodynamic forces as a function of the aeroelastic states, resulting in:

$$\mathbf{F_a^a} = \underbrace{\left(\mathbf{H_3 T_1} + \mathbf{H_3 T_2 H_5}^{-1}\mathbf{H_6}\right)}_{\mathbf{H_8}} \mathbf{x} + \underbrace{\left(\mathbf{H_4 T_2 H_5}^{-1}\mathbf{H_7} + \mathbf{L_3 B_\alpha}\right)}_{\mathbf{H_9}} \dot{\boldsymbol{\alpha}}_{\mathbf{air}} \tag{5.36}$$

Including the structural degrees of freedoms as extra outputs, and rotating the aerodynamic forces to the structural coordinate system for consistency, the aeroelastic output equation becomes:

$$\begin{pmatrix} \mathbf{F} \\ \mathbf{p} \end{pmatrix} = \underbrace{\begin{bmatrix} \mathbf{R_\alpha H_8} \\ \mathbf{T_4} \end{bmatrix}}_{\mathbf{C_{ss}}} \mathbf{x} + \underbrace{\begin{bmatrix} \mathbf{R_\alpha H_9} \\ \mathbf{0} \end{bmatrix}}_{\mathbf{D_{ss}}} \dot{\boldsymbol{\alpha}}_{\mathbf{air}} \tag{5.37}$$

where $\mathbf{T_4}$ is a matrix containing ones and zeros selecting the structural degrees of freedom from the state vector.

In conclusion, equations (5.35) and (5.37) present a monolithic continuous-time state-space formulation of the dynamic aeroelastic response of an aircraft wing about the static aeroelastic equilibrium solution.

### 5.3.3 FLUTTER

Flutter is the dynamic aeroelastic instability of an aircraft, where the interaction between aerodynamic forces and structural deformations leads to an unstable oscillatory motion of the aircraft or parts of the aircraft. In the design of aircraft, it is one of the most important aeroelastic instabilities. Flutter is typically encountered for lifting surfaces, such as the wing, tail, or control surfaces. For a clamped, flexible wing, it typically occurs when the frequencies of the wing bending mode and wing torsional mode approach each other under the influence of aerodynamic loads, resulting in classical bending-torsion flutter.

In case of the present model, where the dynamic aeroelastic response is governed by a continuous-time state-space system, aeroelastic stability is governed by the

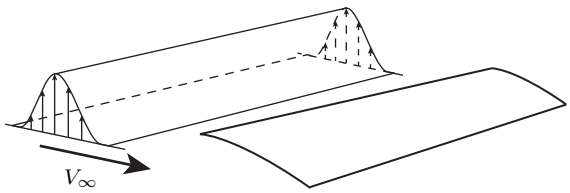


**Figure 5.8:** Schematic illustration of a wing encountering a discrete gust.

eigenvalues of the state matrix, $\mathbf{A_{ss}}$, defined by equation (5.35). The flutter speed can be determined by increasing the velocity until the eigenvalues of the state matrix become unstable, i.e. until the real part of one of the eigenvalues becomes positive.

### 5.3.4 Discrete gust analysis

One of the certification requirements for aircraft is that it should be able to sustain an encounter of positive and negative discrete '1-cosine' gusts of various lengths, as illustrated in Figure 5.8 and defined by:

$$V_g = \frac{V_{ds}}{2}\left[1 - \cos\left(\frac{\pi s}{H}\right)\right] \tag{5.38}$$



where $V_{ds}$ is the design gust velocity, $s$ is the distance penetrated in the gust, and $H$ is half of the gust length. For large aircraft, as certified according to CS-25 (EASA, 2016), the design gust velocity is given by:

$$V_{ds} = V_{ref} F_g \left(\frac{H}{107}\right)^{1/6} \tag{5.39}$$

where $H$ ranges from 9 m to 107 m, $V_{ref}$ is the reference gust velocity that must be considered, which decreases linearly from 17.07 m/s at sea level to 13.41 m/s at 4572 m and further to 6.36 m/s at 18 288 m, and $F_g$ is the flight profile alleviation factor, which must be increased linearly from the sea level value to a value of 1.0 at the maximum operating altitude. The flight profile alleviation factor at sea level is given by:

$$F_g = 0.5\,(F_{gz} + F_{gm}) \tag{5.40}$$

where

$$F_{gz} = 1 - \frac{Z_{mo}}{76\,200} \tag{5.41}$$

$$F_{gm} = \sqrt{R_2 \tan\left(\frac{\pi R_1}{4}\right)} \tag{5.42}$$

with $Z_{mo}$ the maximum operating altitude and:

$$R_1 = \frac{\text{Maximum landing weight}}{\text{Maximum take-off weight}} \tag{5.43}$$

$$R_2 = \frac{\text{Maximum zero fuel weight}}{\text{Maximum take-off weight}} \tag{5.44}$$

For a given free-stream velocity, $V_\infty$, under the assumption of small perturbations with respect to the mean free-stream flow, the angle of attack induced by a 1-cosine gust becomes:

$$\alpha_g = \frac{V_g}{V_\infty} = \frac{V_{ds}}{2V_\infty}\left[1 - \cos\left(\frac{\pi V_\infty t}{H}\right)\right] \quad \text{for } 0 \leq t \leq \frac{2H}{V_\infty} \tag{5.45}$$



where the distance penetrated into the gust at time, $t$, is equal to $V_\infty t$. Taking the time derivative of equation (5.45), the input to the dynamic aeroelastic state-space system for a 1-cosine gust on aerodynamic panel $i$ becomes:

$$\dot{\alpha}_g = \frac{\pi V_{ds}}{2H} \sin\left(\frac{\pi V_\infty \left(t - x_i/V_\infty\right)}{H}\right) \quad \text{for } 0 \leq t - \frac{x_i}{V_\infty} \leq \frac{2H}{V_\infty} \tag{5.46}$$

where $x_i$ is the $x-$location of the collocation point of panel $i$ with respect to the location where the gust first hits the wing.

In conclusion, using equation (5.46) as input, the dynamic aeroelastic state-space system defined by equations (5.35) and (5.37) can be used to find the dynamic response of a discrete gust encounter of an aircraft wing.

## 5.4 MORPHING

Current models to assess the benefits of morphing for aircraft performance either limit the design space a priori based on the specific concept they are designing or they don't limit the design space at all, leaving the question whether a feasible

morphing solution can be obtained. This dissertation introduces a novel approach in the aeroelastic modelling and conceptual design of morphing wings by means of a two-step approach. The first step is interchangeable depending on the morphing concept(s) to be analysed and is used to limit the design space of the generic morphing optimiser based on the morphing concept(s) that need to be analysed to ensure a feasibly morphing solution. The second step is the generic morphing analyser and optimiser that, based on the constraints given by the first step, will optimise the morphing wing parameters and return the required actuator energy. Based on the results of the optimisation, the validity of the initial feasibility constraints can be assessed and either an additional optimisation can be started with updated constraints or a feasible morphing solution has been found. A schematic overview of the design approach is shown in Figure 5.9.

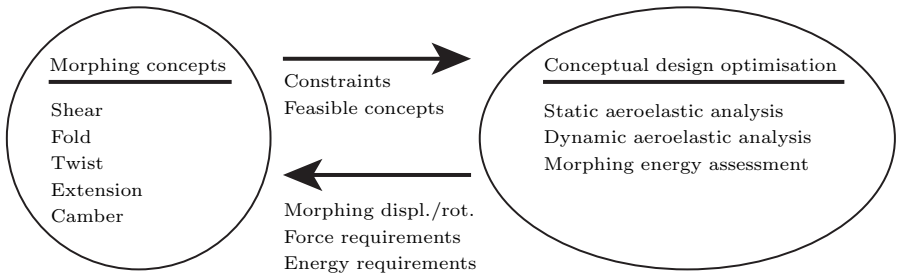


**Figure 5.9:** Two-step approach for morphing wing conceptual design.



Both steps of the approach will be discussed in more detail in the following subsections. First, the morphing wing discretisation adopted to reduce the number of design variables, while not constraining the design space a priori, is explained in Section 5.4.1, introducing the different morphing concepts that can be identified. Second, a detailed description of the implementation of five common morphing mechanisms in the aeroelastic analysis is given in Section 5.4.2 and, finally, the computation of the required morphing energy is explained in Section 5.4.3. The morphing energy can, for example, be used to assess the feasibility of the proposed morphing solution and, if necessary, the constraints on the morphing mechanisms can be updated and a new optimisation can be started to ensure a feasible morphing solution.

### 5.4.1 Morphing discretisation

The goal of the morphing analysis framework is to reduce the number of design variables while not constraining the design space a priori. As already introduced by De Breuker et al. (2011), in order to achieve this, the wing is discretised into several spanwise segments and a distinction is made between global and local morphing. Local morphing is defined as the morphing of the wing cross-section

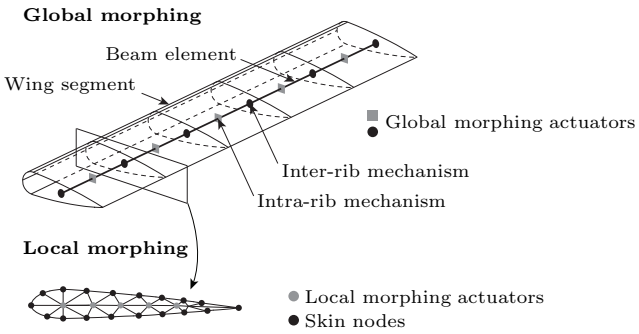


**Figure 5.10:** Global and local morphing and inter-segment and intra-segment morphing. (Source: De Breuker et al. (2011))

perpendicular to the wing span direction, thus affecting mainly the local aerodynamic flow around the wing, while global morphing is defined as morphing along the span of the wing thus affecting the overall aerodynamic flow around the wing. Within global morphing, a further distinction can be made between intersegment morphing and intrasegment morphing. In case of intersegment morphing, two spanwise segments can move with respect to one another by placing the actuators at the rib connecting these two segments, while in case of intrasegment morphing, both end ribs morph with respect to one another by placing the actuator in a specific wing segment. A schematic overview of these distinctions is given in Figure 5.10.



### 5.4.2 MORPHING WING MODELLING

Within the current morphing analysis framework, five different kinds of morphing are included, as illustrated in Figure 5.11: shear, twist, fold, camber, and span extension. Twist, shear and span extension are modelled as intrasegment morphing, where one end of a spanwise segment moves with respect to the other end, dihedral is modelled as intersegment morphing, where one spanwise segment can fold with respect to its neighbour, and finally camber is modelled as local morphing, where locally the camber line of the airfoil changes. Twist and shear morphing have already been implemented by De Breuker et al. (2011) and a brief description will only be given here for completeness. In this dissertation, the formulation by De Breuker et al. (2011) has been extended with camber and span morphing. Furthermore, fold morphing is introduced by imposing a fold angle, similar to the shear morphing formulation, instead of introducing additional degrees of freedom and additional constraint equations.

Shearing is another way of modelling wing sweep, as shown in Figure 5.11a. In the current aeroelastic framework, a shear angle, $\psi_s$, can be imposed on every

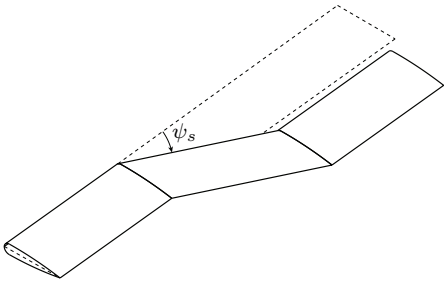


**(a)** Shear morphing of a wing. (Source: De Breuker et al. (2011))

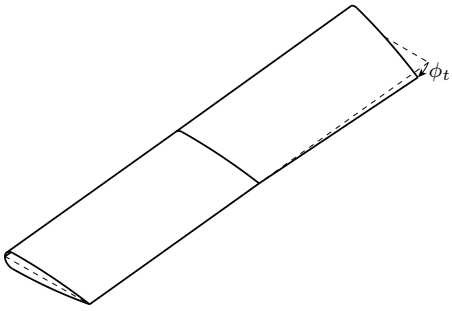


**(b)** Twist morphing of a wing. (Source: De Breuker et al. (2011))

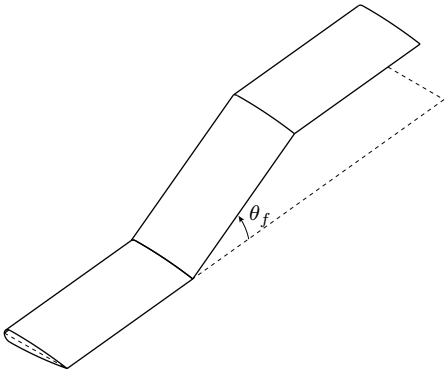


**(c)** Fold morphing of a wing. (Source: De Breuker et al. (2011))

**(d)** Camber morphing of an airfoil.

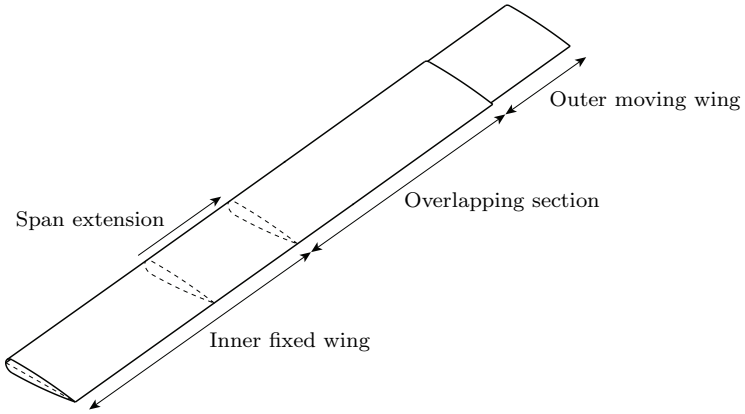


**(e)** Span extension of a wing. Each section has its own specific cross-section and gets elongated or retracted as required during span extension.

**Figure 5.11:** Schematic illustration of the different morphing mechanisms.

beam element individually around the wing normal axis. In principle, if the beam element would be sheared, while the cross-section at the two beam nodes would remain parallel, an elastic deformation would be introduced. However the use of a morphing mechanism means that shearing the wing should not introduce an elastic deformation. Therefore, the rotation of the beam elements in the global reference frame should be split in the rotation describing the shearing deformation and the rotation describing the elastic deformation:

$$\mathbf{R^g T_0} = \mathbf{R^g_{el} T_r R^{r,t}_{\psi}} \tag{5.47}$$

where $\mathbf{T_0}$ defines the initial beam orientation, $\mathbf{T_r}$ defines the deformed beam orientation, $\mathbf{R^g}$ is the rotation matrix of the total rotation, $\mathbf{R^g_{el}}$ is the rotation matrix of the elastic deformation in the global coordinate frame, and $\mathbf{R^{r,t}_{\psi}}$ is the rotation matrix of the shearing deformation in the local element coordinate frame. This implementation is similar to the co-rotational formulation introduced in Chapter 3 and illustrated in Figure 3.9.

Wing twist is introduced by imposing a twist angle, $\phi_t$, on the local element rotations, as illustrated in Figure 5.11b. This effectively rotates the cross-section at one end of the element with respect to the other end of the element, thus modifying the local angle of attack that is experienced at that cross section. Similar to shear morphing, these rotations are obtained without straining the element, so in the absence of external loads, this twisting angle is obtained in a force-free way.

In constrast to De Breuker et al. (2011), who introduced fold morphing by means of additional degrees of freedom and additional constraint equations to impose a fold angle, fold morphing is introduced, similar to shear, by imposing a fold angle, $\theta_f$, on every beam element individually around the element chord axis, resulting in a folding deformation as illustrated in Figure 5.11c. Similar to shear, the rotation of the beam elements in the global reference frame should be split in the rotation describing the folding deformation and the rotation describing the elastic deformation:

$$\mathbf{R^g T_0} = \mathbf{R^g_{el} T_r R^{r,t}_{\theta}} \tag{5.48}$$

In case of span extension, two different types of mechanism can be distinguished: (i) a mechanism with a compliant skin and (ii) a telescopic span extension mechanism where the outer wing slides over the inner wing. The change of stiffness due to span extension can be included in two ways depending on whether a compliant skin or a telescopic span morphing mechanism is used. In case of a compliant skin, either the material properties or the skin thickness can be updated to account for the change in stiffness upon extension. In case of a telescopic span extension mechanism, three sections are assigned for the mechanism: (i) the inner fixed

wing, (ii) the overlapping section, and (iii) the outer moving wing, as illustrated in Figure 5.11e. Each of these sections gets its own properties, where the overlapping section can be modelled as the sum of the cross-section of the outer moving wing and the inner fixed wing. This way, by extending or retracting the overlapping section and, correspondingly, the inner fixed wing and outer moving wing, the redistribution of stiffness due to a telescopic span extension mechanism can be modelled.

In order to incorporate camber morphing, two aerodynamic effects need to be taken into account: (i) the camber line of the wing changes and (ii) the wing chord changes. The change in camber line is governed by the airfoil, while the change in chord is determined by ensuring that the length of the camber line of the wing stays constant during camber morphing, as illustrated in Figure 5.11d. Note that in order to define the camber morphing displacement, each airfoil has a fixed location with respect to which the remainder of the airfoil morphs. The distribution of camber in spanwise direction is accounted for by assuming linear camber variation in between two airfoils.

### 5.4.3 Morphing actuation forces and energy

In order to assess the actuation and energy requirements of the different morphing concepts, an estimate is made of the required morphing actuation forces and energy to overcome the external forces. This section will explain the methods used to obtain this estimate for shear, twist, fold, camber, and span morphing. In case of shear, twist, and fold morphing, the morphing energy is computed based on the method proposed by De Breuker et al. (2011) which is briefly explained here for completeness.

The morphing energy required for shear morphing, $E_{\psi_s}$, is obtained by integrating the required shear moment times the corresponding shear angle over the morphing manoeuvre:

$$E_{\psi_s} = \int_0^1 M_{\psi_s} \psi_s d\lambda \tag{5.49}$$

The corresponding shear actuation moment consists of two components: (i) the required moment to overcome the external forces and (ii) the required moment to overcome the resistance in the morphing mechanism. First, the shear moment, $M_{\psi_s}$, to overcome the external forces is obtained by taking the derivative of the strain energy, $\mathcal{U}$, of the sheared element with respect to the shear angle, $\psi_s$:

$$M_{\psi_s}^{ext} = \frac{\partial \mathcal{U}}{\partial \psi_s} \tag{5.50}$$

Next, the shear moment required to overcome the structural stiffness is added to obtain the total shear moment, by assuming a linear relation between the shear resistance of the mechanism, $GA_s$, and the shear angle:

$$M_{\psi_s} = \frac{\partial \mathcal{U}}{\partial \psi_s} + GA_s\psi_s \tag{5.51}$$

Similar to shear morphing, the required morphing energy for twist morphing, $E_{\phi_t}$, is obtained by integrating the required twist moment times the corresponding twist angle over the morphing manoeuvre:

$$E_{\phi_t} = \int_0^1 M_{\phi_t}\phi_t d\lambda \tag{5.52}$$

The corresponding twist actuation moment, $M_{\phi_t}$, is obtained by taking the derivative of the strain energy of the twisted element, $\mathcal{U}$, with respect to the twist angle, $\phi_t$, and adding the twist moment required to overcome the torsional resistance of the mechanism, $GJ_t$:



$$M_{\phi_t} = \frac{\partial \mathcal{U}}{\partial \phi_t} + GJ_t\phi_t \tag{5.53}$$

In case of fold morphing, similar to shear and twist morphing, the required morphing energy, $E_{\theta_f}$, to overcome the aerodynamic forces is computed by integrating the required moment, $M_{\theta_f}$, times the fold angle, $\theta_f$, over the morphing manoeuvre:

$$E_{\theta_f} = \int_0^1 M_{\theta_f}\theta_f d\lambda \tag{5.54}$$

where the fold morphing actuation moment, under the assumption of no resistance in the mechanism, is given by:

$$M_{\theta_f} = \frac{\partial \mathcal{U}}{\partial \theta_f} \tag{5.55}$$

In contrast to the shear, twist, and fold morphing energy, the morphing energy required for camber morphing, $E_c$, is not given by a moment required to generate

morphing, but by integrating the work done by the aerodynamic forces on the wing over the camber morphing manoeuvre:

$$E_c = \int_0^1 \int_{S_w} \Delta p \mathbf{n} \cdot \mathbf{r} dS d\lambda \tag{5.56}$$

where $\Delta p$ is the aerodynamic pressure difference, $\mathbf{n}$ is the surface normal, $\mathbf{r}$ is the camber morphing displacement, and $S_w$ is the wing surface area. In order to compute the camber morphing displacement, each airfoil has a fixed location with respect to which the remainder of the airfoil morphs, as illustrated in Figure 5.11d. Note that in case of the vortex lattice method, the aerodynamic pressure difference can be approximated by dividing the aerodynamic force over the panel surface area, thus assuming a constant pressure distribution over the element. Based on this pressure distribution and the corresponding morphing displacement, the corresponding morphing energy can be determined using equation (5.56):

$$E_c = \int_0^1 \sum_{N_p} \frac{\mathbf{F_{a_i}}}{S_i} \cdot \int_{S_i} \mathbf{r} dS d\lambda \tag{5.57}$$



where $N_p$ is the number of aerodynamic panels on the wing surface, $\mathbf{F_{a_i}}$ is the aerodynamic force vector acting on panel $i$, and $S_i$ is the area of panel $i$. In order to improve the accuracy of the camber morphing energy assessment, while maintaining computational efficiency, aeroelastic equilibrium is first obtained using a coarse mesh, after which the aerodynamic force distribution, used to compute the camber morphing energy, is obtained through an additional aerodynamic analysis using a refined chordwise mesh.

For span extension, all energy required is given by the mechanical energy required to morph, since the aerodynamic forces act perpendicular to the morphing movement. Therefore, the magnitude of the shear force, bending moment, and torque at the end of the span extension mechanism are used as a measure for the actuation forces of the span extension mechanism, since these will determine the friction in the mechanism and, consequently, the required actuation forces.

In conclusion, the assessment of the morphing actuation forces and energy required for the different morphing manoeuvres allows for an assessment of the feasibility of different morphing concepts and an assessment of potential actuation requirements. Based on these results, an update of the feasibility constraints, set in the first step of the two-step design approach, might be required and a new design iteration can be started.

## 5.5 SENSITIVITIES

In order to make the framework suitable for gradient-based optimisation, the sensitivities of the objective and constraints with respect to the lamination parameters, laminate thicknesses, and morphing parameters are required. In the current framework, the sensitivities are computed for: the lamination parameter feasibility constraints, the Tsai-Wu strain factor, the buckling factor, aileron effectiveness, aeroelastic stability, the static aeroelastic response, the dynamic aeroelastic response, the local angle of attack to prevent stall, aerodynamic lift and drag, and the wing structural mass. Since the number of aeroelastic responses is significantly larger than the number of design variables, the sensitivities are computed using the direct method. All sensitivities are computed analytically for computational efficiency.

## 5.6 IMPLEMENTATION OF THE FRAMEWORK



The aeroelastic analysis and optimisation framework presented in this dissertation has been implemented in MATLAB[2]. The input consists of an Excel[3]-file defining the general aircraft data, the geometry of the wing, the location and magnitude of any non-structural masses and forces, the distribution of any morphing mechanisms that might be present, and the loadcases to be considered. Once the wing is defined, the globally convergent method of moving asymptotes (GCMMA) developed by Svanberg (2002) is used as a gradient-based optimiser to obtain the optimal wing design.

## 5.7 VERIFICATION WITH LITERATURE

For verification of the aeroelastic analysis framework, several verification cases were considered. First, Section 5.7.1 presents the verification of the geometrically nonlinear static aeroelastic analysis. Secondly, Section 5.7.2 presents the verification of the dynamic aeroelastic analysis and, finally, Section 5.7.3 presents the verification of the morphing actuation forces and moments and corresponding actuation energy.

[2]MATLAB®, The MathWorks, Inc., Natick, MA, USA
[3]Excel®, Microsoft Corporation, Redmond, WA, USA.

**Table 5.1:** HALE wing properties.

| | |
|---|---|
| Semispan | 16 m |
| Chord | 1 m |
| Elastic axis | 50% chord |
| Centre of gravity | 50% chord |
| Mass per unit length | 0.75 kg/m |
| Moment of inertia (around e.a.) | 0.1 kg m |
| Torsional stiffness | $1 \cdot 10^4$ N m$^2$ |
| Bending stiffness | $2 \cdot 10^4$ N m$^2$ |
| Chordwise bending stiffness | $\sigma \cdot 10^6$ N m$^2$ |

**Table 5.2:** Goland wing properties.

| | |
|---|---|
| Semispan | 6.096 m |
| Chord | 1.8288 m |
| Elastic axis | 33% chord |
| Centre of gravity | 43% chord |
| Mass per unit length | 35.72 kg/m |
| Moment of inertia (around e.a.) | 8.64 kg m |
| Torsional stiffness | $9.88 \cdot 10^5$ N m$^2$ |
| Bending stiffness | $9.77 \cdot 10^6$ N m$^2$ |

### 5.7.1 Static aeroelastic analysis



As a verification of the geometrically nonlinear static aeroelastic model, the present approach is compared to the results obtained by Murua et al. (2012b) for a HALE aircraft wing with properties given in Table 5.1 and $\sigma = 5$. The wing is flying at a speed of 25 m/s with an air density of 0.0889 kg/m$^3$. The geometrically nonlinear tip deflection at angles of attack of 2 deg and 4 deg is shown in Figure 5.12, showing excellent agreement, thus verifying the static aeroelastic model.

### 5.7.2 Dynamic aeroelastic model

In order to verify the dynamic aeroelastic model, first the flutter speed for the Goland wing (Goland, 1945), as defined in Table 5.2, and the HALE aircraft wing, as defined in Table 5.1 with $\sigma = 4$, are compared to the literature. The

**Table 5.3:** Flutter speed of the Goland wing.

| | $V_f$ | $\omega_f$ |
|---|---|---|
| Wang et al. (2006) | 163.8 m/s | - |
| ZAERO (Wang et al., 2006) | 174.3 m/s | - |
| Murua et al. (2012b) | 165 m/s | 69 rad/s |
| Present model | 168.3 m/s | 69.3 rad/s |

**Table 5.4:** Flutter speed of the HALE aircraft wing.

| | $V_f$ | $\omega_f$ |
|---|---|---|
| Patil and Hodges (2004) | 31.75 m/s | 23.60 rad/s |
| Murua et al. (2012b) | 33 m/s | 22 rad/s |
| Present model | 32.21 m/s | 23.14 rad/s |



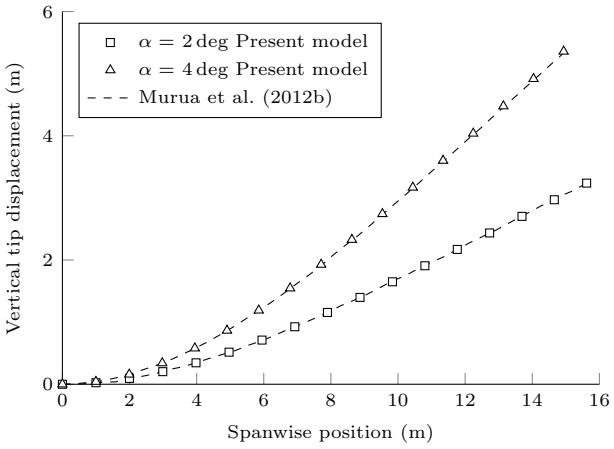


**Figure 5.12:** Static aeroelastic deflection of a HALE aircraft wing under different angles of attack.

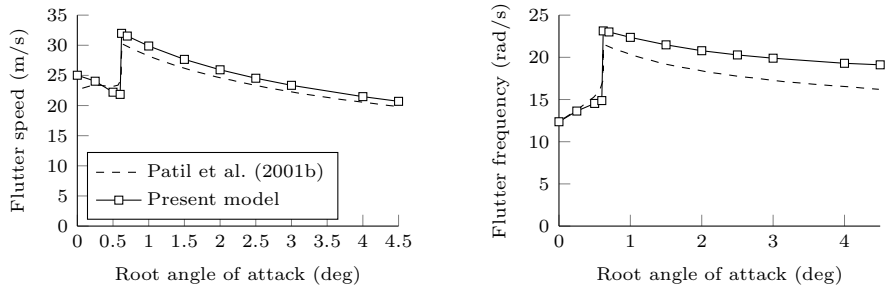


**(a)** Flutter speed. **(b)** Flutter frequency.

**Figure 5.13:** Non-linear flutter speed and frequency of the HALE aircraft wing at different root angles of attack.

flutter speed is determined by increasing the velocity until the eigenvalues of the state matrix, $\mathbf{A_{ss}}$, become unstable, i.e. until the real part of one of the eigenvalues becomes positive. As can be seen in Table 5.3, the results show excellent agreement.

Second, in order to verify the linear dynamic aeroelastic solution around the nonlinear static aeroelastic equilibrium solution, the present model is compared to the flutter speed and frequency obtained by Patil et al. (2001b) for the HALE aircraft wing with $\sigma = 4$ at different root angles of attack including the effects of gravity. The resulting flutter speed and frequency are shown in Figure 5.13. As can be seen, at low angles of attack, both models show excellent agreement. Furthermore, both models predict a change in flutter mode and corresponding jump in flutter speed and frequency at an angle of attack of 0.61 deg, originating from the geometrically nonlinear response of the wing. Note that, even at an angle of attack of 0 deg, the analysis is already geometrically nonlinear, because of the gravitational loads, resulting in a tip deflection of 17%.

However, at higher angles of attack, the present model predicts a higher flutter speed and frequency than Patil et al. (2001b). This can be explained by the two-dimensional aerodynamic model used by Patil et al. (2001b), compared to the three-dimensional aerodynamic model used in the present model. Similar discrepancies were also observed by Wang et al. (2010) and Murua et al. (2012b) when comparing the trim angle and the effects of flexibility on lift between aeroelastic models with two-dimensional and three-dimensional aerodynamic models. In conclusion, the same trends in flutter speed and frequency are observed between both models and good agreement is observed, especially at low angles of attack, thus verifying the present model.

Third, in order to validate the implementation of the eccentric masses, the aeroelastic stability, as predicted by the present model, is compared to the experi-

**Table 5.5:** Experimental wing properties. (Runyan and Sewall, 1948)

| | |
|---|---|
| Semispan | 1.2192 m |
| Chord | 0.2032 m |
| Elastic axis | 43.7% chord |
| Centre of gravity | 45.4% chord |
| Mass per unit length | 1.2943 kg/m |
| Moment of inertia (around e.a.) | $3.56 \cdot 10^{-3}$ kg m |
| Torsional stiffness | 198.6 N m$^2$ |
| Bending stiffness | 403.8 N m$^2$ |
| Eccentric mass | 1.44 kg |
| Chordwise location of the mass w.r.t. e.a. | −0.083 m |
| Moment of inertia (around mass c.g.) | $8.50 \cdot 10^{-3}$ kg m$^2$ |

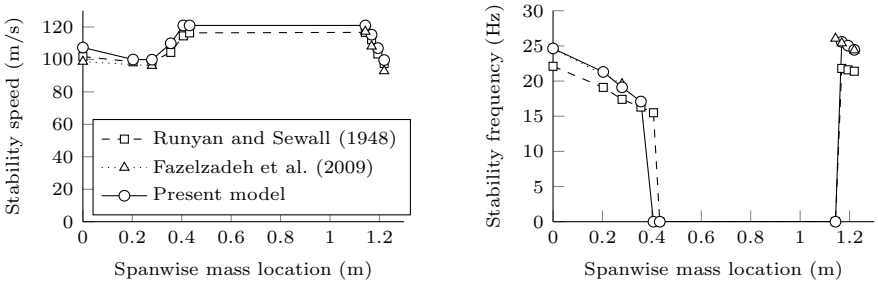


**(a)** Aeroelastic stability speed.

**(b)** Aeroelastic stability frequency.

**Figure 5.14:** Aeroelastic stability speed and frequency of a wing with an eccentric mass at different spanwise locations. (Experiment: Runyan and Sewall (1948), Numeric: Fazelzadeh et al. (2009))

mental results of Runyan and Sewall (1948) who experimentally investigated the effect of the spanwise location of an eccentric mass on the aeroelastic stability of a wing. The wing properties are given in Table 5.5 and the comparison is shown in Figure 5.14. When looking at the results, several things can be observed. First of all, the predicted flutter and divergence speeds show good agreement with the experiments, however, both the present model and Fazelzadeh et al. (2009) overpredict the flutter frequency by $10 - 15\%$, which can be explained by inaccuracies between the modelling of the experiment and the actual experiment. Second, the present model predicts transition from flutter to divergence already at 0.406 m, while in the experiment the wing was close to divergence, but still fluttering. In general, however, the present results show good agreement with the experiments, thus validating the implementation of eccentric masses in the present model.

As a final verification of the aeroelastic model, the implementation of the discrete gust response in the present model is verified by comparing the results obtained for a discrete gust analysis of the Goland wing, as defined by Table 5.2, under a 1-cosine gust to results obtained by Wang et al. (2010). The air density is

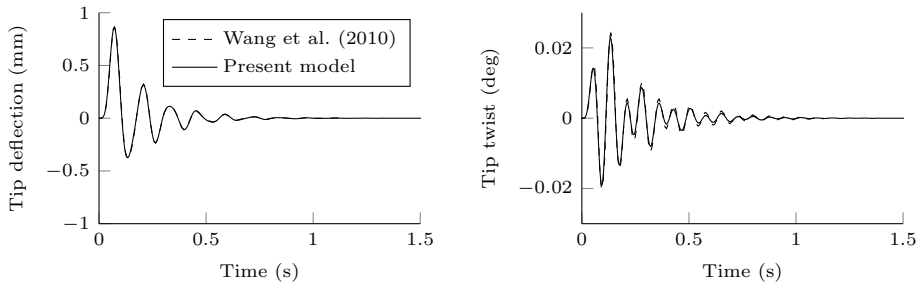


**(a)** Tip displacement. **(b)** Tip twist.

**Figure 5.15:** Gust response of the Goland wing under a 1-cosine gust.

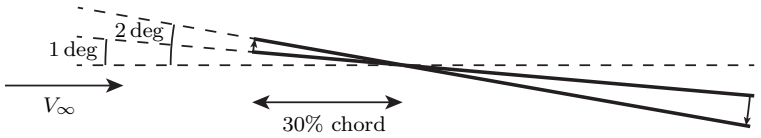


**Figure 5.16:** Camber morphing manoeuvre used for verification.

$1.229\,\mathrm{kg/m^3}$ and the mean free-stream flow velocity is $100\,\mathrm{m/s}$. The discrete gust has an amplitude of $V_g/V_\infty = 0.001$ and a length of $2H = 4$ chords. The resulting tip deflection and tip twist are shown in Figure 5.15. As can be expected, both results show excellent agreement, since both models are based on a beam model coupled to a UVLM-based aerodynamic model.



### 5.7.3 Morphing

The actuation moment required for fold morphing is verified by applying an out-of-plane tip load of $500\,\mathrm{N}$ to the HALE wing defined by Table 5.1 and $\sigma = 4$, resulting in a tip deflection of 75% of the beam length, which is clearly a nonlinear deflection. Similar to De Breuker (2011), the folding moment required to prevent a section of $1\,\mathrm{m}$ at the tip from folding is compared to the following analytical expression:

$$M_{\theta_f} = F_z \left(L_0 - \Delta y\right) \tag{5.58}$$

where $F_z$ is the applied tip load, $L_0$ is the undeformed length of the element, and $\Delta y$ is the end shortening of the element. The resulting comparison is shown in Figure 5.17a, showing excellent agreement and, thus, verifying the fold morphing moment required to compute the fold morphing energy.

The forces and energy required for camber morphing are verified by changing

the angle of attack of a rigid wing with a semispan of 50 m, a chord of 1 m, and no camber from 1 deg to 2 deg by means of a camber morphing manoeuvre, as illustrated in Figure 5.16. The corresponding free stream velocity is 10 m/s at sea level.

The morphing energy required is compared to the analytical solution, by starting from the analytical pressure distribution of a two-dimensional flat plate airfoil, given by:

$$C_p\left(x/c\right) = 1 - \left(\cos\left(\alpha\right) \pm \sin\left(\alpha\right)\sqrt{\frac{1-2\,x/c}{1+2\,x/c}}\right)^2 \tag{5.59}$$

where $\alpha$ is the airfoil angle of attack, $x/c$ is the normalised chordwise location ranging from $-0.5$ to 0.5, and the $\pm$ indicates top and bottom surface, respectively. The morphing energy required to overcome the forces induced by the pressure distribution is given by integrating the pressure distribution over the morphing manoeuvre:

$$E_c = \frac{1}{2}\rho V_\infty^2 \int_0^1 \int_{-0.5}^{0.5} C_p \cdot r\, x/c\, d\lambda \tag{5.60}$$

Note that the analytical expression is singular at the wing leading edge and care should be taken when integrating this expression. The reference morphing energy is obtained by numerically integrating equation (5.60) by means of the trapezoidal rule, while neglecting the contribution at the singularity. By refining the discretisation used for the trapezoidal rule, the effect of neglecting the contribution at the singularity diminishes and a converged reference morphing energy is found.

In order to do a fair comparison between the present three-dimensional solution and the two-dimensional analytical solution, the morphing energy required to morph a section of 1 m at the wing root is used for comparison. In order to obtain a more accurate solution at the leading edge singularity, the chordwise aerodynamic elements, $N_{el_c}$ are distributed by means of a $x^2$ distribution. The corresponding morphing energy required is given in Table 5.6 and Figure 5.17b shows the evolution of morphing energy over the morphing manoeuvre for various chordwise spatial discretisations.

As can be expected, the singularity at the leading edge heavily influences the accuracy of the computed morphing energy and a sufficiently refined aerodynamic mesh is required to obtain an accurate estimate of the morphing energy. As the mesh is refined, the present model converges to the analytical solution, thus verifying the present model. However, while applying the present model to obtain

**Table 5.6:** Camber morphing energy verification.

| | $E_c$ (N m) | Diff. |
|---|---|---|
| Analytical | $-8.79 \cdot 10^{-5}$ | - |
| $N_{el_c} = 16$ | $-6.30 \cdot 10^{-5}$ | 28.3% |
| $N_{el_c} = 32$ | $-7.51 \cdot 10^{-5}$ | 14.5% |
| $N_{el_c} = 64$ | $-8.10 \cdot 10^{-5}$ | 7.8% |
| $N_{el_c} = 128$ | $-8.39 \cdot 10^{-5}$ | 4.5% |

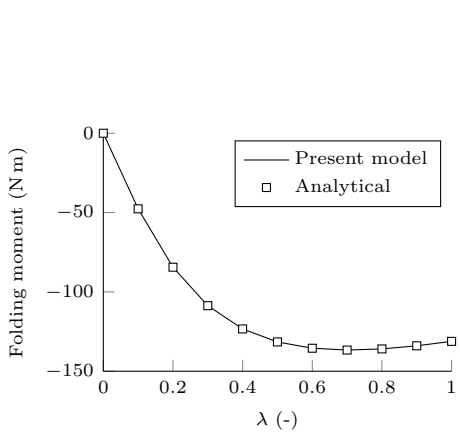


**(a)** Fold morphing moment over the morphing manoeuvre.

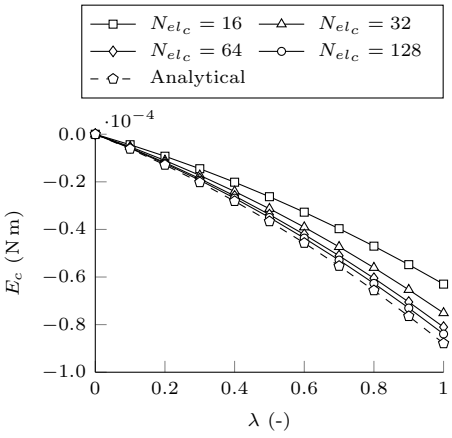


**(b)** Camber morphing energy over the morphing manoeuvre for various chordwise spatial discretisations.

**Figure 5.17:** Verification of the morphing energy computations.

an estimate of the required camber morphing energy, care should be taken to ensure a sufficiently refined mesh.

In conclusion, the present model shows excellent agreement with results found in the literature, thus verifying and validating the present dynamic aeroelastic model.

## 5.8 LIMITATIONS OF THE FRAMEWORK

The goal of the aeroelastic analysis and optimisation framework presented in this dissertation is to improve the conceptual design of aircraft wings by including aeroelasticity. Besides the assumptions made for the structural model, as discussed in Section 3.9, and the aerodynamic model, as discussed in Section 4.9, a number of assumptions have also been made for the aeroelastic model, resulting in the following additional limitations of the framework:

- The effects of the fuselage on the load distribution of the wing and the effects of the empennage on the trim equilibrium solution have not been accounted for, thus affecting the trim solution. The trends observed should, however, still be valid.
- The wing is clamped at the wing root and, as a consequence, the effects of control surfaces and flight dynamics on the dynamic aeroelastic response of the wing cannot be assessed.
- All morphing manoeuvres have been assumed to be quasi-steady, neglecting any structural dynamic or unsteady aerodynamic effects, which is only a valid assumption for slow morphing manoeuvres.

When interpreting the results obtained by the framework, one should always keep these limitations in mind.

## 5.9 SYNOPSIS

In this chapter, the structural and aerodynamic models discussed in Chapters 3 and 4 have been coupled to obtain a static and dynamic aeroelastic model suitable for the analysis of composite wings. In order to assess potential benefits of morphing, a morphing discretisation is introduced and five morphing mechanisms are incorporated in the aeroelastic analysis.

- A closely coupled geometrically nonlinear static aeroelastic model has been obtained using the Newton-Raphson root finding algorithm to obtain static aeroelastic equilibrium.

- The corresponding angle of attack required to trim the aircraft is found by appending the force equilibrium equations with an additional equation and solving for the angle of attack in conjunction with the wing deformations such that lift equals weight.

- Aileron effectiveness is assessed by solving for the steady state roll rate of the wing under a aileron deflection of 1 deg around the static aeroelastic equilibrium solution.

- The dynamic aeroelastic response is obtained by a linear dynamic aeroelastic analysis around the static equilibrium solution, formulated as a monolithic continuous-time state-space system that describes the response of a wing to external flow perturbations.

- Aeroelastic stability is assessed by investigating the stability of the eigenvalues of the aeroelastic state matrix.

- Morphing is introduced in the framework by a novel two-step approach for the modelling of morphing aircraft wings. The first step is concept-specific and is used to identify the different morphing mechanisms on the wing and their feasibility constraints. The second step is a generic morphing optimisation framework used to identify the optimal set of morphing parameters within the concept-specific bounds and assess whether a feasible morphing solution can be found. The main advantage of this approach is that the morphing optimisation framework is suitable for any morphing wing design, while concept-specific limitations can still be accounted for.

- Five morphing mechanisms (i.e. shear, twist, fold, camber, and span extension) are introduced by discretising the wing in several spanwise segments and introducing morphing in each wing segment or at the interface between segments, as required.

- In order to assess the feasibility of the final optimised morphing wing design, the required actuation forces and actuation energy are determined under the assumption of a slow, quasi-steady morphing manoeuvre. If necessary, the feasibility constraints derived in the first step are updated and a new optimisation is run until a feasible wing design has been found.

- The aeroelastic analysis and optimisation framework presented in this dissertation has been implemented in MATLAB® and the input consists of an Excel®-file defining the wing data. Once the wing is defined, the globally

convergent method of moving asymptotes (GCMMA) developed by Svanberg (2002) is used as a gradient-based optimiser to obtain the optimal wing design.

- Comparison of the present model to several linear, nonlinear, and morphing benchmarks in the literature shows good to excellent agreement, verifying the present implementation.

# PART II

# EXPERIMENTAL VALIDATION

*I think that in the discussion of natural problems we ought to begin not with the Scriptures, but with experiments, and demonstrations.*
**Galileo Galilei**

# 6

# AEROELASTIC TAILORING EXPERIMENTS[1]

Although aeroelastic experiments have been carried out that provide validation results for aeroelastic models, they are only partially sufficient for the validation of the aeroelastic analysis frameworks that use a load bearing skin or a wing box structure as design space for aeroelastic tailoring. Therefore, this chapter presents the design, manufacturing, and testing of aeroelastically tailored wings. In order to validate the aeroelastic framework, three wings were designed and built: a quasi-isotropic benchmark wing, and two aeroelastically tailored wings.

First, Section 6.1 presents a review of aeroelastic experiments, illustrating why additional experiments are required for the experimental validation of aeroelastic wing models for aeroelastically tailored wing structures. Next, Section 6.2 presents the design of the aeroelastically tailored wings that will be used for the experimental validation, followed by a brief description of the manufacturing process and the experimental setup in Section 6.3. Using the manufactured wings, first, a structural test was carried out to characterize the structural properties of the wings and provide a first level of model validation, as presented in Section 6.4. Next, static aeroelastic experiments were carried out in a low speed wind tunnel to provide experimental validation data for the static aeroelastic model, as presented

[1]This chapter is based on the journal paper Werter, N.P.M., Sodja, J. and De Breuker, R. (2017). *"Design and testing of aeroelastically tailored wings Under maneuver loading"*, AIAA Journal, vol. 55, no. 3, pp. 1012-1025.

in Section 6.5, followed by a brief synopsis in Section 6.6.

## 6.1 A REVIEW OF AEROELASTIC TAILORING EXPERIMENTS

Substantial research has been done on the potential benefits of aeroelastic tailoring; however, little experimental validation data is available. Sherrer et al. (1981) investigated the effect of aeroelastic tailoring on the divergence speeds using several composite plates at various sweep angles. Similar tests were carried out by Blair and Weisshaar (1982) investigating the effect of ply angle on the divergence speed of a wing at different sweep angles by varying the ply orientation of a composite plate covered by an aerodynamic fairing. Following this work, Dugundji and co-workers (Chen and Dugundji, 1987; Hollowell and Dugundji, 1984; Landsberger and Dugundji, 1985) performed several sets of experiments investigating the effect of aeroelastic tailoring on the divergence speed, flutter speed, and wing tip deflection of composite plates both cantilevered and with rigid-body-freedom.

Although these studies provide valuable experimental validation data, they are unsuitable for the validation of the aeroelastic analysis frameworks that use only a load bearing skin or a wing box structure as design space for aeroelastic tailoring, since these structures use the extension-shear coupling of the individual laminates of the wing cross-section to obtain bend-twist coupling at a wing level, while in a plate structure, the bend-twist coupling originates from the bend-twist coupling of the laminate. Therefore, the goal of the present experiments is to provide experimental validation data for the aeroelastic analysis of composite aeroelastically tailored wings with a closed-cell cross-sectional structure using the extension-shear coupling of the laminates to introduce the desired bend-twist coupling of the wing structure.



## 6.2 DESIGN OF AEROELASTICALLY TAILORED WINGS

Wing designs were created for two different cases, quasi isotropic (QI) and aeroelastically tailored using the aeroelastic analysis framework presented in Chapter 5. Note that, when designing the wings, the framework did not include an assessment of buckling of the wing designs. Section 6.2.1 presents the optimisation setup used to obtain the wing designs, followed by a discussion on the optimisation results in Section 6.2.2. The result of the optimisations is a set of lamination parameters that minimises the root bending moment of the wing. In order to manufacture the wings, these lamination parameters are converted to an actual stacking sequence, as presented in Section 6.2.3.

**Table 6.1:** Experimental wing geometry.

| | |
|---|---|
| Semispan (m) | 1.0 |
| Chord (m) | 0.2 |
| Aspect ratio (-) | 10 |
| Sweep angle (deg) | 0 |
| Taper ratio (-) | 1 |
| Airfoil | NACA0012 |

**Table 6.2:** Manoeuvre load cases.

| Load case | #1 | #2 | #3 |
|---|---|---|---|
| Flight speed (m/s) | 100 | 100 | 100 |
| Mach Number | 0.29 | 0.29 | 0.29 |
| Density (kg/m$^3$) | 1.225 | 1.225 | 1.225 |
| Load factor (-) | 1 | 2.5 | $-1$ |
| Half aircraft mass (kg) | 28 | 28 | 28 |
| Half wing lift (N) | 274.7 | 686.7 | $-274.7$ |

### 6.2.1 Optimisation setup

In order to find designs that can be used for experimental validation and in the process show potential benefits of aeroelastic tailoring for manoeuvre load alleviation, several optimisations were carried out. In order to test a wing that would fit in the wind tunnel and can serve as validation for the aeroelastic framework, a rectangular wing with a semispan of 1.0 m and an aspect ratio of 10 was selected, resulting in the wing dimensions given in Table 6.1.



The objective of the optimisation is to minimise the maximum root bending moment of the wing for several manoeuvre load conditions, as defined in Table 6.2. Constraints were put on the maximum skin strains (see Table 6.3), the trim angle of attack ($\leq$10 deg), and the lamination parameters to ensure a feasible structural design and a linear aerodynamic response. For manufacturing purposes, the optimisation was set up such that all composite laminates have a fixed skin thickness and their layup is symmetric to prevent any warping upon curing.

As introduced in Chapter 3, the composite laminates are described by lamination parameters. In case of the present design optimisation, for a symmetric laminate with a prescribed thickness where the laminate in-plane properties are dominant for the response, this results in 4 design variables, $V_{1\mathbf{A}} - V_{4\mathbf{A}}$, per laminate. The sensitivities of the objective and constraints to the lamination parameters are computed analytically and the globally convergent method of moving asymptotes (Svanberg, 2002) was used as the optimiser.

The quasi isotropic wing was built and analysed as a reference to be able to assess the potential benefits of the tailored wing. The tailored wing consists of two independent laminates that are constant along the span: one for the top skin

**Table 6.3:** Material properties.

| Material | CYCOM 977-2-35 12k HTS | CYCOM 977-2-35 12k HTS (Fibre volume corrected) | Epoxy resin | EPP Foam |
|---|---|---|---|---|
| $E_{11}$ (GPa) | 125.93* | 142.70 | 2.90 | $9.8 \cdot 10^{-3}$ |
| $E_{22}$ (GPa) | 7.72* | 8.72 | 2.90 | $9.8 \cdot 10^{-3}$ |
| $G_{12}$ (GPa) | 3.61† | 4.38 | 1.07 | $3.77 \cdot 10^{-3}$‡ |
| $\nu_{12}$ (-) | 0.336* | 0.336 | 0.35 | 0.3§ |
| $\rho$ (kg/m$^3$) | 1590 | 1620 | 1150 | 20 |
| $t_{ply}$ (mm) | 0.26 | 0.23 | - | - |
| $V_f$ (-) | 0.60 | 0.68 | - | - |
| $\epsilon_{x_{max}}$ (µstrain) | 4500¶ | - | - | - |
| $\gamma_{max}$ (µstrain) | 7000¶ | - | - | - |

* according to ASTM Standard D3039.
† according to ASTM Standard D3518.
‡ according to $G = \frac{E}{2(1+\nu)}$.
§ assumed.
¶ Including knockdown factors for environmental effects (0.8), barely visible impact damage (0.65), and material scatter (0.8) (Kassapoglou, 2013).

and one for the bottom skin, resulting in a total of 8 design variables.

6

### 6.2.2 OPTIMISATION RESULTS

The wings are made out of CYCOM 977-2-35 12k HTS carbon fibre epoxy with material properties as given in Table 6.3. Initially a tailored wing with a skin thickness of 3 layers was optimised to obtain a flexible wing with potential for aeroelastic tailoring. As expected, the critical load case for the wing was the 2.5g manoeuvre load, hence analysis results are only presented for this load case. Since no quasi-isotropic layup exists for a 3 layer wing, the performance of the optimised 3 layer wing has been compared to an equivalent quasi-isotropic set of lamination parameters with the same thickness and a 6 layer quasi-isotropic wing with a layup of $[60/0/-60]_s$ was built instead. When performing structural tests, the 3 layer tailored skin buckled and was unsuitable for further testing. Therefore, another design was created for a 4 layer tailored wing that was designed and manufactured based on the experience gained with the 3 layer tailored wing and the 6 layer quasi-isotropic wing. The optimum lamination parameters are given in Table 6.4 and the resulting root bending moments are given in Table 6.5. Note that the trim weight for all wings is based on an aircraft mass of 56 kg at 1g flight, resulting in similar root bending moments for all skin thicknesses.

**Table 6.4:** Optimum lamination parameters.

| | 3 Layers | | 4 Layers | |
|---|---|---|---|---|
| | Top skin | Bottom skin | Top skin | Bottom skin |
| $V_{1\mathbf{A}}$ | 0.282 | 0.283 | 0.382 | 0.290 |
| $V_{2\mathbf{A}}$ | 0.500 | 0.520 | 0.521 | 0.578 |
| $V_{3\mathbf{A}}$ | 0.395 | 0.341 | 0.409 | 0.310 |
| $V_{4\mathbf{A}}$ | 0.457 | 0.435 | 0.631 | 0.489 |

**Table 6.5:** Root bending moment results for the 2.5g load case for the optimised and actual laminates.

| Wing type | | Root bending moment (N m) | | | |
|---|---|---|---|---|---|
| | | Optimised | | Actual Laminates | |
| 6 layers | QI | 317.2 | | 317.2 | |
| 4 layers | QI | 317.3 | | 317.3 | |
| | Tailored | 290.0 | −8.58% | 290.8 | −8.34% |
| 3 layers | QI | 317.3 | | 317.3 | |
| | Tailored | 290.6 | −8.43% | 292.6 | −7.80% |

### 6.2.3 Final wing designs

The result of the optimisation is a set of lamination parameters. In order to find a corresponding laminate that can be manufactured, a sweep over the ply angles was done to find the laminate that best matches the stiffness properties obtained using the optimum lamination parameters. In order to evaluate the match between the stacking sequence and the optimised lamination parameters, the directional stiffness of the laminates is visualised by computing the modulus of elasticity along a direction, $\theta$, as presented in Section 3.2.3.

The resulting stiffness distributions of both the optimised laminates and the stacking sequences are shown in Figures 6.1a and 6.1b for the 3 layer and 4 layer wing, respectively. As can be seen, the stiffness distributions for the top and bottom skins are very close, so, for ease of manufacturing, it was decided to select a single laminate for both the top and bottom skins, resulting in a symmetric wing about the wing chord.

As can be concluded from Figure 6.1, upon converting from lamination parameters to an actual stacking sequence, a trade-off needs to be made to find the stacking sequence that best matches the lamination parameter optimum. In case of the 3 layer wing, this results in a stacking sequence that accurately captures the main stiffness direction by means of two 16 deg plies; however, at a reduced performance along the second stiffness direction, since only one additional ply is available. In case of the 4 layer wing, the restriction of a symmetric laminate results in a laminate with two ply directions with two plies per direction. As can be seen,

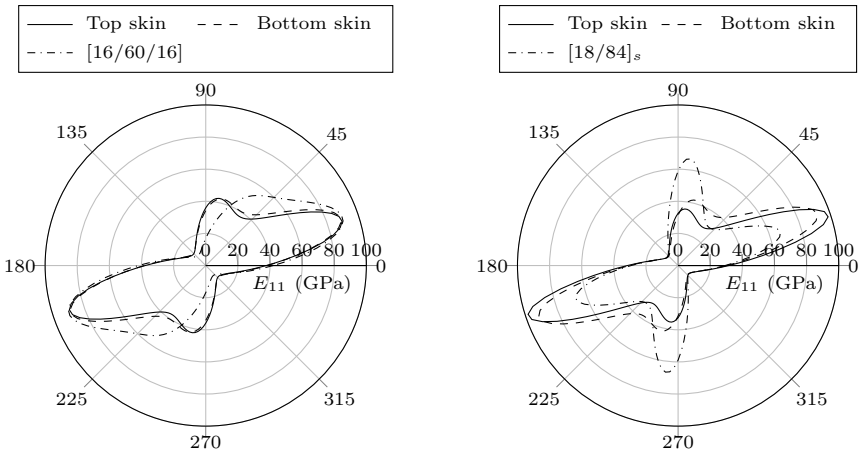


**(a)** 3 layer wing. **(b)** 4 layer wing.

**Figure 6.1:** Comparison of the extensional stiffness in different directions between the optimised results and the corresponding laminates. The 0 deg fibres are oriented along the wing axis and a layer with a positive angle is oriented forward.

**Table 6.6:** Wing laminates where the ply angle is defined positive with respect to the wing axis when the fibres are oriented forward when going from root to tip.

| Wing type | | Laminate |
|---|---|---|
| 6 layers | QI | $[60/0/-60]_s$ |
| 4 layers | Tailored | $[18/84]_s$ |
| 3 layers | Tailored | [16/60/16] |

6

this results in a stacking sequence that captures the two main stiffness directions; however, the ratio in stiffness between these two directions cannot be captured by the stacking sequence. As is expected, some performance is lost due to the transformation of lamination parameters to actual ply orientations, as can be seen in Table 6.5, but the actual laminates still show a clear benefit of aeroelastic tailoring for manoeuvre load reduction. The corresponding laminates can be found in Table 6.6.

Wash-out bend-twist coupling is introduced by orienting the fibres forward with respect to the wing axis, thus shifting the spanwise centre of pressure inboard and reducing the root bending moment. The bend-twist coupling on a wing level is not introduced by bend-twist coupling of the laminates, but by extension-shear coupling instead. Under bending, one skin will be in compression, while the other skin will be in tension, and, consequently both skins will shear in opposite direction. By constraining the relative shear deformation between individual skins, wing twist is introduced.

**Table 6.7:** Buckling load and tip deflection for various wing core configurations for a 4 layer tailored skin.

| Case | No ribs | Rib spacing 10 cm | Full core |
|---|---|---|---|
| Static load (N) | 200 | 200 | 200 |
| Buckling load (N) | 83.8 | 101.5 | 797.4 |
| Tip deflection (mm) | 67.7 | 67.5 | 64.8 |
| Tip twist (deg) | 5.19 | 5.17 | 4.81 |

In order to prevent flattening of the cross-section under deflection, four equally spaced EPP foam ribs, of which the material properties can be found in Table 6.3, with a width of 20 mm were installed as cross-sectional reinforcements in the 3 and 6 layer wings. Despite locally supporting the skins, the 3 layer wing buckled during the structural test and was, therefore, discarded from further testing. As mentioned, a 4 layer tailored wing was designed instead. In order to prevent the 4 layer wing from buckling, a FEM buckling analysis was done in ABAQUS with an equivalent tip load of 200 N at the quarter chord point to simulate a similar deflection and chordwise load introduction as anticipated in the wind tunnel experiments. The resulting wing tip deflection, tip twist, and buckling loads are presented in Table 6.7. For a rib spacing of 10 cm the EPP foam ribs still do not provide sufficient support to prevent skin buckling and, therefore, the 4 layer wings were completely filled with EPP foam, resulting in sufficient resistance to buckling, while only reducing the expected tip deflection by 4.3% and the expected tip twist by 7.3%.

## 6.3 Manufacturing and experimental test setup



As presented in Section 6.2.3, three wings were manufactured: a 3 layer tailored wing, a 4 layer tailored wing, and a 6 layer quasi-isotropic wing. The manufacturing process and the experimental setup are presented in more detail in the following sections.

### 6.3.1 Manufacturing

In order to ensure high geometrical accuracy and high quality surface finish, the wings were manufactured using a hand-layup moulding technique. Since unidirectional carbon fibre prepreg is used that has to be cured in the autoclave at elevated temperature and pressure, a female mould was CNC milled out of aluminium.

The manufacturing procedure consists of the following steps. First the prepreg tape is cut using a cutting robot into quadrilateral patches according to individual ply-orientation requirements. This way the different plies can be easily oriented in

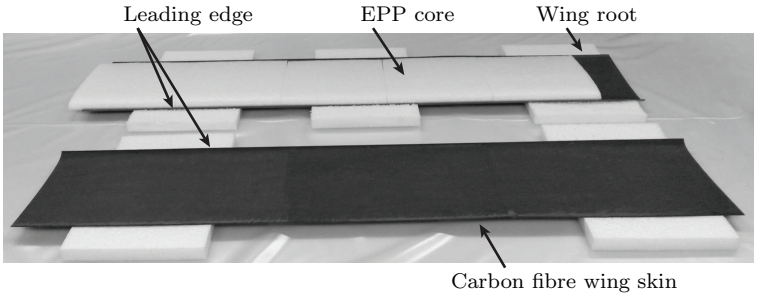


**(a)** Wing components before assembly.

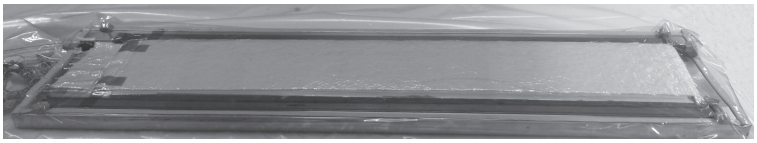

**(b)** Vacuum bagging of the assembled wings to ensure proper bonding of both wing halves.

**Figure 6.2:** Wing manufacturing.

the mould and the correct orientation of the fibres in the layup is ensured. After the layers have been stacked into the mould, the acquired layup is vacuum-bagged and cured in the autoclave. The cured skins are then trimmed down to final size, and the skin thickness is measured and used as an offset for manufacturing the EPP ribs and cores. The EPP foam was cut using a CNC hot-wire cutting machine. The ribs and cores are glued into the wing by means of epoxy. In order to connect the two wing halves, a strip of carbon fibre weave at an orientation of $\pm 45$ deg was glued in the leading edge on both the inside and the outside of the wing in order to transfer the loads. At the trailing edge, because of the larger contact surface, the wings were glued together by means of epoxy. Once the wing components are assembled, the wing is placed in the mould, packed in a vacuum bag and kept under vacuum as the epoxy cures in order to ensure good bonding. Figures 6.2a and 6.2b show the individual components before final assembly and the assembled wing in the vacuum bag.



### 6.3.2 STRUCTURAL TEST SETUP

As a first comparison between the experimental wings and the simulation results, two series of structural tests were carried out. The objective of these tests is twofold: (i) provide initial validation data for the numerical model and (ii) assess the importance of features in the experimental wings (e.g. the EPP foam and reinforcements for bonding) that are not included in the numerical model.

First, each wing was subjected to a load close to the wing tip at 97.5% span

**Table 6.8:** Laser measurement characteristics.

| Position | | Range (mm) | Resolution (mm) |
|---|---|---|---|
| Spanwise | Chordwise | | |
| 25.8% span | 30.0% chord | 20 | ±0.004 |
| 25.8% span | 92.5% chord | 20 | ±0.004 |
| 55.8% span | 30.0% chord | 50 | ±0.01 |
| 55.8% span | 92.5% chord | 50 | ±0.01 |
| 85.8% span | 30.0% chord | 100 | ±0.02 |
| 85.8% span | 92.5% chord | 100 | ±0.02 |

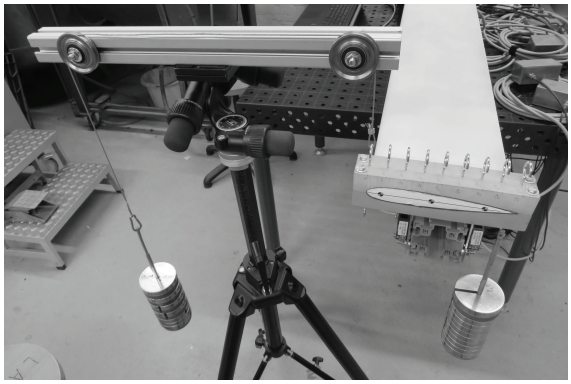

**Figure 6.3:** Picture of the structural test setup illustrating an applied tip torque.



introduced by a mass of up to 10 kg at different chordwise locations in order to validate the structural model. Figure 6.3 shows a picture of the load introduction during the structural tests. The wing deformation is measured by a VIC3D stereo digital image correlation (DIC) system (Correlated Solutions, Inc., 2015) yielding the 3D deformation field of the entire wing surface with a measurement accuracy of 0.1 - 0.2 mm.

Secondly, based on the comparison between the numerical model and the structural test results, an extra structural test was carried out for the 4 layer tailored wing subject to a pure torque of up to 20 N m introduced through a cable and pulley system, such that the wing tip is free to deflect, as shown in Figure 6.3. This test fully decouples the torsional stiffness and bend-twist coupling of the wing from the shear centre location and bending stiffness, resulting in a better structural characterisation of the 4 layer tailored wing. Since the anticipated deflections are in the range of 0.4 - 5.0 mm, the resolution of the VIC3D system is no longer sufficient and Micro-Epsilon optoNCDT 1302 laser distance sensors (Micro Epsilon, 2015) were used to measure deformations. The sensors were positioned in pairs at three different spanwise locations, as defined in Table 6.8.

### 6.3.3 WIND TUNNEL TEST SETUP

The wings were tested in the low turbulence wind tunnel of the Delft University of Technology, which has an octogonal cross-section of 1.80 m wide by 1.25 m high and a maximum wind speed of 120 m/s. The 4 layer tailored wing and the 6 layer quasi-isotropic wing have been tested at a range of angles of attack from −10 deg to 10 deg at wind tunnel speeds up to 80 m/s up until wing buckling. The aerodynamic forces and moments were measured by the mechanical six-component balance present in the wind tunnel.

Wing deformation was measured by two independent methods: a VIC3D DIC system and an optical marker tracking system. The corresponding wind tunnel test setup is shown in Figure 6.4. Optical marker tracking was carried out using a camera oriented along the span axis observing the wing tip. A set of distinctive markers was placed on the wing tip and were photographed during the experiment. In post-processing, the displacement of the markers is used to track the displacement and twist of the wing tip. The accuracy of the optical marker tracking system is ±0.05 mm. A set of captured frames with the recognized markers is shown in Figure 6.5. The position and orientation of the camera with respect to the wing is shown in Figure 6.4.

## 6.4 STRUCTURAL CHARACTERISATION



In the structural tests, the wings were first subjected to a load at 97.5% span at different chordwise locations. The load has been applied by masses in steps of 2 kg up to 10 kg. In order to reduce the effect of measurement errors, a load displacement curve is created for each of the measurement series and the equivalent stiffness of the wing to a specific load case is determined by means of a linear least-squares fit. This way, a single parameter is obtained for each load case that is used to compare the results of the structural test to the simulations.

The wing out-of-plane displacement and wing twist results of the structural tests are shown in Figures 6.6 and 6.7 for the tailored wing, and Figures 6.8 and 6.9 for the QI wing. As can be seen, the original numerical beam model predicts a more flexible wing than found in the experiment. In order to investigate the sources of discrepancy between the numerical beam model and the experimental wing, the tailored wing was cut to investigate the interior of the wing, as shown in Figure 6.10, revealing three sources of discrepancies. Upon investigation of the geometry of the experimental wing and the mould, a first source of discrepancy was found in the wing geometry, as illustrated in Figure 6.11.

A second source of discrepancy was identified by comparing the experimental wing to test samples that have been used previously to identify the material

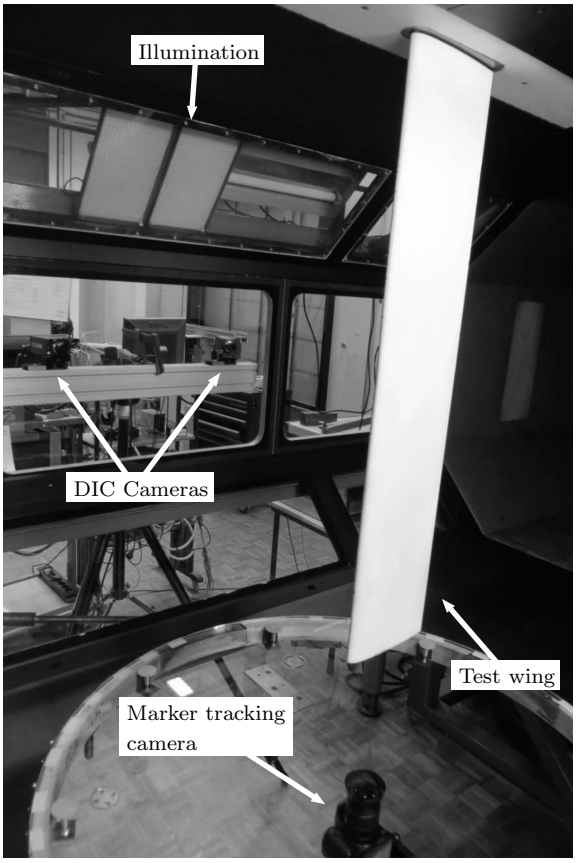


**Figure 6.4:** Wind tunnel test setup.

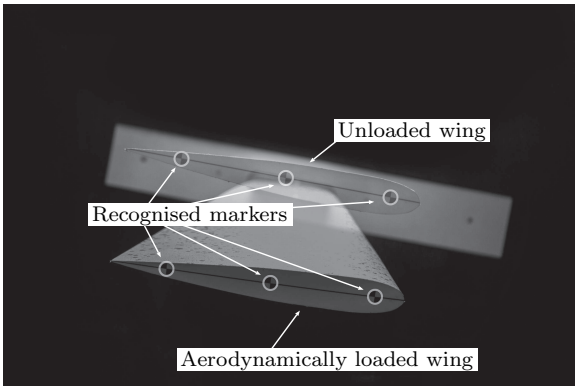


**Figure 6.5:** Overlay of tip photos of the unloaded and loaded 4 layer tailored wing at $\alpha = 10\,\text{deg}$ and $V = 80\,\text{m/s}$.

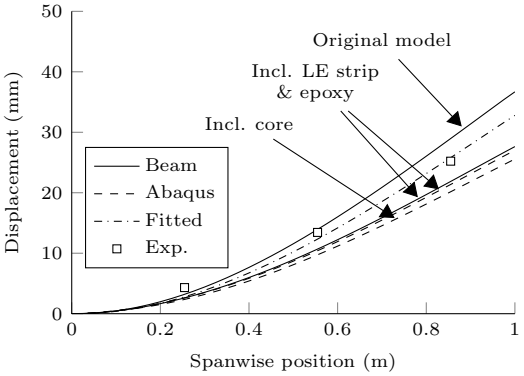


**(a)** 10 kg load at 97.5% span at the leading edge.

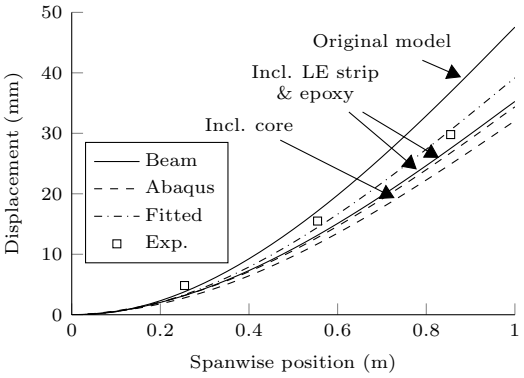


**(b)** 10 kg load at 97.5% span at the trailing edge.

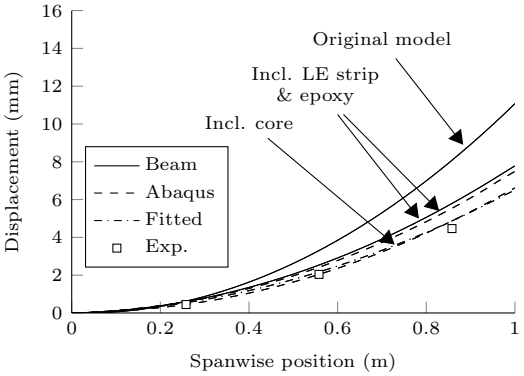


**(c)** Torque of 20 N m.

**Figure 6.6:** Comparison of the wing displacement of the tailored wing between the beam model, Abaqus, and the experiments.

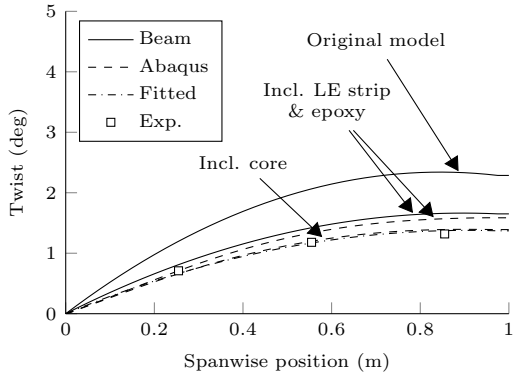


**(a)** 10 kg load at 97.5% span at the leading edge.

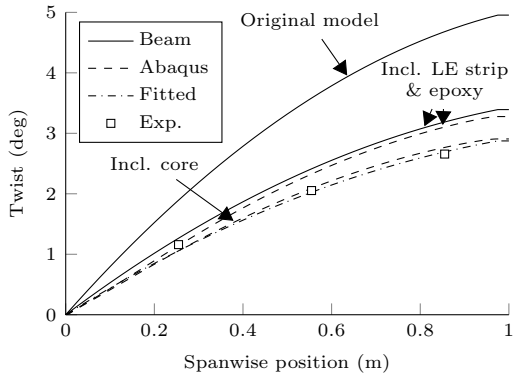


**(b)** 10 kg load at 97.5% span at the trailing edge.

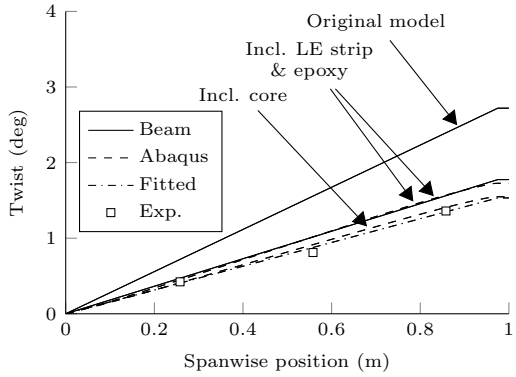


**(c)** Torque of 20 N m.

**Figure 6.7:** Comparison of the wing twist of the tailored wing between the beam model, Abaqus, and the experiments.

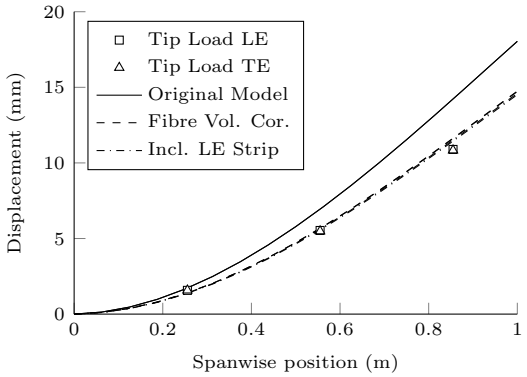


**Figure 6.8:** Wing displacement of the QI wing under a leading edge and trailing edge load at 97.5% span.



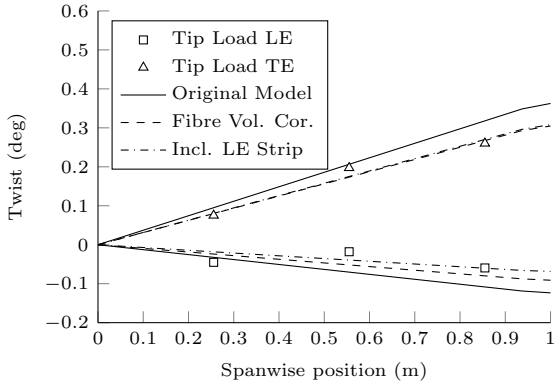


**Figure 6.9:** Wing twist of the QI wing under a leading edge and trailing edge load at 97.5% span.


**Figure 6.10:** Cross-section of the experimental wing.

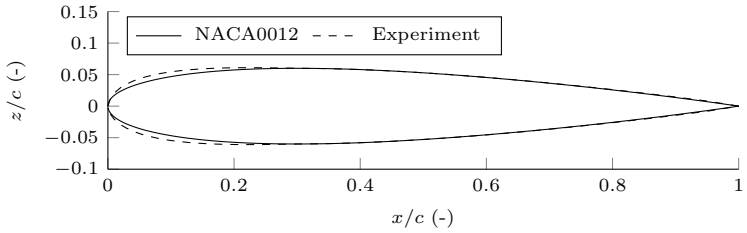


**Figure 6.11:** Comparison between the NACA0012 and the airfoil of the experimental wings.

properties. While the material test samples had a ply thickness of 0.26 mm, the experimental wing has a ply thickness of 0.23 mm instead of the expected 0.26 mm. This discrepancy can be explained by the difference in the manufacturing process between both the experimental wing and the material test samples. Even though both were manufactured using the same batch of material and under the same curing cycle, the material test samples were supported by an aluminium plate on the top and bottom, while the experimental wing skin was only supported by the mould on its outer surface and had a breather mesh on its inner surface, resulting in a loss of resin into the breather mesh during curing. This results in an increase in fibre volume fraction from 0.60 for the material test samples to 0.68 for the experimental wing under the assumption of equal fibre content per ply between both sets. Using the rule of mixtures (Daniel and Ishai, 2006) to estimate the change in material properties, this results in the fibre volume corrected properties as shown in Table 6.3.

Thirdly, as can be seen in Figure 6.10, three different regions on the wing surface can be identified: (i) the wing skin reinforced on the inside and outside with a strip of carbon fibre weave of 0.56 mm thickness for the first 2.5 mm oriented at $\pm 45$ deg, (ii) the wing skin reinforced only on the inside with a strip of carbon fibre weave of 0.56 mm thickness from 2.5 mm to 24 mm oriented at $\pm 45$ deg, and (iii) the remainder of the wing skin reinforced with a layer of 0.1 mm epoxy.

Based on these discrepancies, the airfoil geometry, material properties, and laminates have been updated to account for these effects, resulting in the additional beam results in Figures 6.6 to 6.9. As shown in Figures 6.8 and 6.9, the updated

simulation results of the QI wing show excellent agreement with the experimental results; however, as shown in Figures 6.6 and 6.7, the simulation results of the tailored wing still overpredict both the wing displacement and the wing twist. In order to investigate this in more detail, as mentioned in Section 6.3.2, a second series of structural tests has been carried out on the tailored wing under a pure tip torque to decouple the torsional stiffness and bend-twist coupling of the wing from the shear centre location and bending stiffness. The torque has been applied by a simultaneous upward force at the leading edge and downward force at the trailing edge at 97.5% span in steps of 2 kg up to 10 kg, resulting in a maximum tip torque of 20 N m. Similar to the applied load, a linear fit through the load displacement curve is used to obtain a single parameter to compare to the simulations. As can be seen in Figures 6.6c and 6.7c, the simulations also overpredict the wing displacement and wing twist for an applied tip torque.

Based on the structural test results, it was decided to do a structural characterisation of the tailored wing by finding the bending stiffness, torsional stiffness, bend-twist coupling and shear centre location that provide a best fit to the structural test results. For this purpose, an optimisation is set up that minimises the root mean squared error between the numerical beam simulations and the structural test results. The errors are normalised with respect to the maximum displacement or twist of the corresponding loadcase to weigh each measurement equally.

Consider the Timoshenko cross-sectional stiffness matrix, which relates the cross-sectional forces to the cross-sectional strains, as presented in Section 3.3:



$$\begin{pmatrix} F_1 & F_2 & F_3 & M_1 & M_2 & M_3 \end{pmatrix}^T = \mathbf{C} \begin{pmatrix} \epsilon_{11} & \epsilon_{12} & \epsilon_{13} & \kappa_1 & \kappa_2 & \kappa_3 \end{pmatrix}^T \tag{6.1}$$

In case of slender composite beams loaded in bending and twist, not all components of the Timoshenko cross-sectional stiffness have a significant impact on the resulting deformations. The extensional and shear deformations are small and, therefore, the deformations of the beam are mainly governed by the bending stiffness, torsional stiffness, bend-twist coupling and shear centre location. These are related to the components of the Timoshenko cross-sectional stiffness and compliance ($\mathbf{C}^{-1}$) matrices through the following relations:

$$EI = C_{55} \tag{6.2}$$

$$GJ = C_{44} \tag{6.3}$$

$$K = -C_{45} \tag{6.4}$$

$$e = -\frac{C_{34}^{-1}}{C_{44}^{-1}} \tag{6.5}$$

**Table 6.9:** Effect of different components of the experimental tailored wing on the wing stiffness. The last column shows the differences between the updated beam model and the Abaqus model including core, and the experimental properties.

| Property | | Fibre volume corrected | Incl. LE strips | Incl. epoxy | Incl. core | Fitted experiment | |
|---|---|---|---|---|---|---|---|
| EI ($\mathrm{N\,m^2}$) | Beam | 1715.0 | 1778.3 | 1786.8 | - | 1195.8 | 49.4% |
| | Abaqus | 1597.8 | 1565 | 1551.7 | 1704.4 | 1195.8 | 42.5% |
| | Difference | −6.8% | −12.0% | −13.2% | - | | |
| EI* ($\mathrm{N\,m^2}$) | Beam | 1001.5 | 1070.3 | 1086.8 | - | 924.9 | 17.5% |
| | Abaqus | 1051.0 | 1103.6 | 1099.2 | 1171.8 | 924.9 | 26.7% |
| | Difference | 4.9% | 3.1% | 1.1% | - | | |
| GJ ($\mathrm{N\,m^2}$) | Beam | 903.6 | 1058.8 | 1070.7 | - | 946.7 | 13.1% |
| | Abaqus | 794.4 | 886.9 | 883.4 | 1013.3 | 946.7 | 7.0% |
| | Difference | −12.1% | −16.2% | −17.5% | - | | |
| GJ* ($\mathrm{N\,m^2}$) | Beam | 527.7 | 637.2 | 651.3 | - | 732.2 | −11.1% |
| | Abaqus | 522.5 | 625.4 | 625.8 | 696.7 | 732.2 | −4.9% |
| | Difference | −1.0% | −1.9% | −3.9% | - | | |
| K ($\mathrm{N\,m^2}$) | Beam | −802.9 | −865.8 | −865.7 | - | −506.5 | 70.9% |
| | Abaqus | −659.1 | −639.7 | −632.2 | −734.6 | −506.5 | 45.1% |
| | Difference | −17.9% | −26.1% | −27.0% | - | | |
| e (%c) | Beam | 28.9 | 18.2 | 18.2 | - | 14.6 | 3.6 %c |
| | Abaqus | 21.1 | 12.1 | 12.0 | 19.6 | 14.6 | 5.0 %c |
| | Difference | −7.9 %c | −6.1 %c | −6.2 %c | - | | |

The results of the fitting process for these parameters are given in Table 6.9 and the corresponding match to the structural deformations is shown Figures 6.6 and 6.7.



In order to investigate the source of the discrepancy between the beam model and the experimental wing in more detail and investigate the effect of the different skin regions and the core on the cross-sectional properties, several finite element simulations were carried out in Abaqus, based on the updated airfoil shape shown in Figure 6.11: (i) the skin using the fibre volume corrected properties, (ii) the skin including the leading edge strips, (iii), the skin including the leading edge strips and the epoxy, and (iv) the full model including the core. The resulting wing displacement and twist are shown in Figures 6.6 and 6.7. For the sake of clarity, only the third and fourth Abaqus models are shown since similar conclusions can be drawn from the results of the first and second models. The cross-sectional stiffness properties were determined by extracting the Abaqus deformations at 10 equally spaced spanwise locations on the wing and applying the same fitting procedure as used for the experimental results. The resulting cross-sectional stiffness properties are given in Table 6.9.

Based on the structural characterisation, several conclusions can be drawn. First, when comparing the updated beam results with the LE strips and epoxy to the

corresponding Abaqus results, both results show good agreement in terms of wing displacement and wing twist, thus verifying the beam model. In case of wing twist, as expected, a slight offset is present caused by the warping restraint present in Abaqus, which is not accounted for in the beam model. When looking at the cross-sectional properties in Table 6.9, both models show significant differences. However, in case of wings that exhibit bend-twist coupling, care should be taken in interpreting these properties. As derived by Weisshaar (1987), the relation between applied bending moment and out-of-plane displacement, and applied torque and twist is no longer solely governed by bending stiffness and torsional stiffness, but also related to the bend-twist coupling, resulting in the following effective bending and torsional stiffnesses:

$$EI^* = EI\left(1 - \frac{K^2}{EI\,GJ}\right) \tag{6.6}$$

$$GJ^* = GJ\left(1 - \frac{K^2}{EI\,GJ}\right) \tag{6.7}$$

The resulting effective bending and torsional stiffnesses are also shown in Table 6.9 and show good to excellent agreement between the beam model and Abaqus with an errors of up to 4.9%.

In order to investigate the effect of the warping restraint on the equivalent beam properties in more detail, the beam cross-sectional properties of the Abaqus results for the first case (i.e. the skin using the fibre volume corrected properties) have been rederived excluding the effect of the warping restraint, by (i) only matching the region from 30% to 80% of the wing to remove the influence of the clamping region and load introduction region and (ii) matching the spanwise slope of deformation instead of the actual deformation values to remove the influence of the reduction in wing twist at the wing root because of the warping restraint. The resulting wing cross-sectional properties are given in Table 6.10 and an example of the corresponding wing deformations is shown in Figure 6.12 showing the reduction in wing twist at the wing root because of the warping restraint in the Abaqus simulations. As can be seen, when excluding the warping restraint, the cross-sectional properties of both models show good agreement, but in order to account for the effect of the warping restraint in the beam model, as illustrated in Figure 6.12 and can be observed in Table 6.10, a redistribution of stiffness between the different equivalent beam properties occurs. The remaining differences in the beam stiffness properties are probably related to the effect of inherent modelling differences between the beam model and the Abaqus shell model, such as cross-sectional deformations, on the equivalent beam properties. The influence of these effects on the aeroelastic response will be discussed in more detail when comparing the different numerical models to the wind tunnel test results.

Second, when comparing the numerical simulations and the experimental results,

**Table 6.10:** Influence of the warping restraint on the beam cross-sectional properties.

| Property | Beam | Abaqus (Value fit) | Diff. | Abaqus (Slope fit) | Diff. |
|---|---|---|---|---|---|
| EI ($\mathrm{N\,m^2}$) | 1715.0 | 1597.8 | −6.8% | 1781.1 | 3.9% |
| EI* ($\mathrm{N\,m^2}$) | 1001.5 | 1051.0 | 4.9% | 1044.7 | 4.3% |
| GJ ($\mathrm{N\,m^2}$) | 903.6 | 794.4 | −12.1% | 855.6 | −5.3% |
| GJ* ($\mathrm{N\,m^2}$) | 527.7 | 522.5 | −1.0% | 501.9 | −4.9% |
| K ($\mathrm{N\,m^2}$) | −802.9 | −659.1 | −17.9% | −793.8 | −1.1% |
| e (%c) | 28.9% | 21.1% | −7.9% | 30.2% | 1.2% |

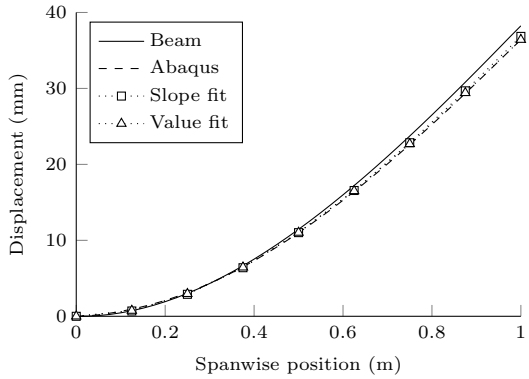


**(a)** Wing displacement.

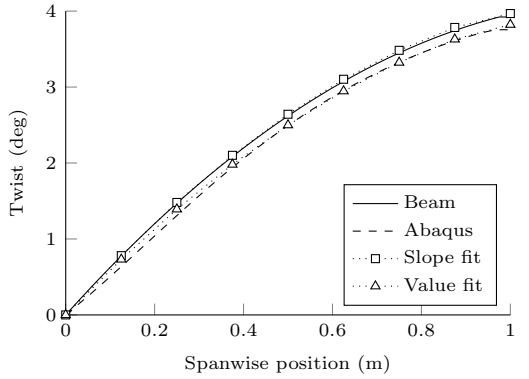


**(b)** Wing twist.

**Figure 6.12:** Effect of the warping restraint at the wing root on the beam deformations and the fitting procedure for the wing under a 10 kg load at 97.5% span at the trailing edge.

it can be concluded that excellent agreement is observed between the full model in Abaqus and the experimental results in terms of wing twist. In terms of wing displacement, excellent agreement is also observed under an applied torque. However, both Abaqus and the beam model predict a lower wing displacement than observed in the experiment under an applied load. Possible causes for this mismatch could, for example, be uncertainties in material properties, slight variations in wing geometry, or slight flexibility in the clamp mechanism, introducing additional wing deflection in the experiments. As can be expected, these differences are also clearly reflected in the fitted beam properties shown in Table 6.9.

In conclusion, while comparing the experimental wing deformations to numerical simulations, several causes for discrepancies were found. A difference in ply thickness between the material test samples and the experimental wings, a deviation from the NACA0012 profile, and the strip in the leading edge for bonding both skins resulted in a first set of discrepancies. By accounting for these, excellent agreement is observed for the QI wing, thus providing a first validation of the numerical results. Secondly, by additionally accounting for the effect of foam core, good agreement is also observed for the tailored wing in wing twist.

In the remainder of this chapter, the wind tunnel results will be investigated and the aeroelastic model will be validated using three sets of beam properties: (i) the properties from the cross-sectional modeller including leading edge strips and epoxy, (ii) the cross-sectional properties derived from the full Abaqus model, and (iii) the cross-sectional properties derived from the structural tests. Note that the cross-sectional modeller has been verified separately by Ferede and Abdalla (2014) and is, therefore, not considered here.



## 6.5 STATIC AEROELASTIC EXPERIMENTS

All wings were tested at a range of free stream velocities from $V = 10\,\mathrm{m/s}$ up to $V = 80\,\mathrm{m/s}$ and at a range of angles of attack from $\alpha = -10\,\mathrm{deg}$ up to $\alpha = 10\,\mathrm{deg}$. Because of the qualitatively similar behaviour at other velocities, only the results corresponding to $V = 40\,\mathrm{m/s}$, $V = 60\,\mathrm{m/s}$ and $V = 80\,\mathrm{m/s}$ are presented. The experimental wind tunnel results are compared to three sets of beam properties: (i) the properties from the cross-sectional modeller including leading edge strips and epoxy to validate the beam model, (ii) the cross-sectional properties derived from the full Abaqus model to investigate the effect of the core and the warping restraint at the root, and (iii) the fitted properties derived from the structural tests to validate the aeroelastic simulations. First, the comparison of the aerodynamic forces and moments is presented in Section 6.5.1, after which the comparison of the aeroelastic deformations is presented in Section 6.5.2.

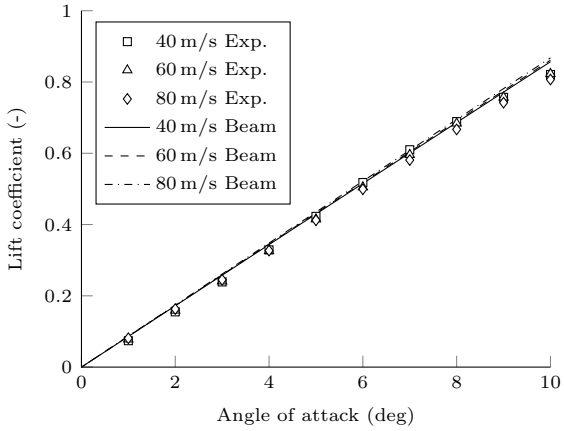


**Figure 6.13:** Lift coefficient of the QI wing.

### 6.5.1 Lift and root bending moment coefficient

A comparison between numerical beam results and experimental results for the lift and root bending moment coefficient of the QI wing is shown in Figures 6.13 and 6.14. In case of lift, the numerical and experimental results show good agreement with a slightly higher predicted lift curve slope than measured in the experiment. At angles of attack larger than 8 deg, a slight nonlinearity is observed in the measurements, most likely related to the onset of stall on the wing. Excluding the results with aerodynamic nonlinearities, which are not captured by the present simulations, the error ranges from 0.5% to 4.6%. In the case of the root bending moment, the numerical results show excellent agreement with the experimental results with an error ranging from 0.5% to 3.8%.

Figures 6.15 and 6.16 show the lift coefficient and root bending moment coefficient comparisons for the tailored wing. First of all, it is interesting to note that the differences between the fitted properties obtained from the structural tests, the cross-sectional properties derived from the full Abaqus model, and the beam model including LE strips and epoxy are negligible, thus showing that the foam core and the warping restraint at the wing root have negligible influence on the aeroelastic loads. Secondly, it can be concluded that, in terms of lift, the numerical results show excellent agreement with the experimental results with an error ranging from 0.2% to 4.7%. However, in terms of root bending moment coefficient, especially at 40 m/s and 60 m/s, and high angles of attack, the numerical results predict a slightly lower root bending moment coefficient than observed in the experiments with an error ranging from 1.2% to 7.5%.

In order to compare the two wings and investigate the effect of manoeuvre load alleviation, an important parameter is the spanwise location of the centre of pres-

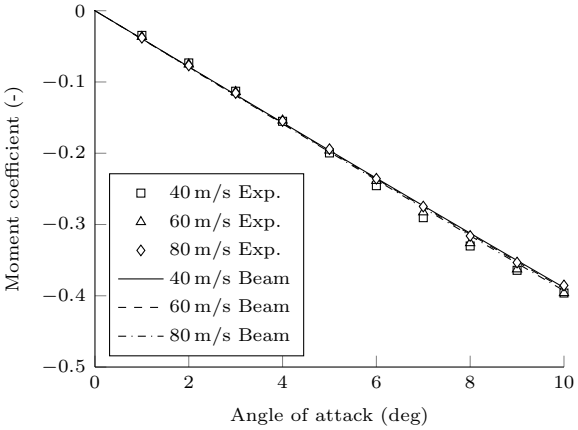


**Figure 6.14:** Root bending moment coefficient of the QI wing.



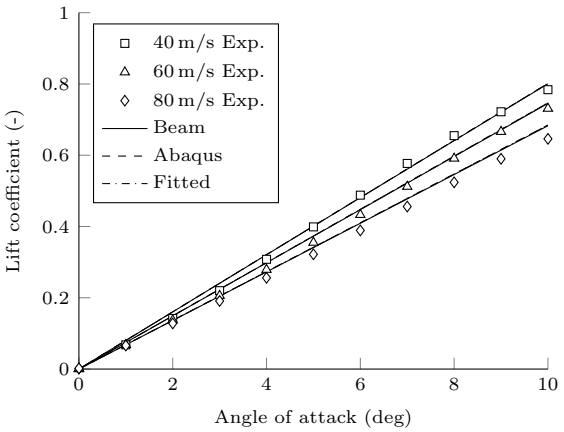


**Figure 6.15:** Lift coefficient of the tailored wing.

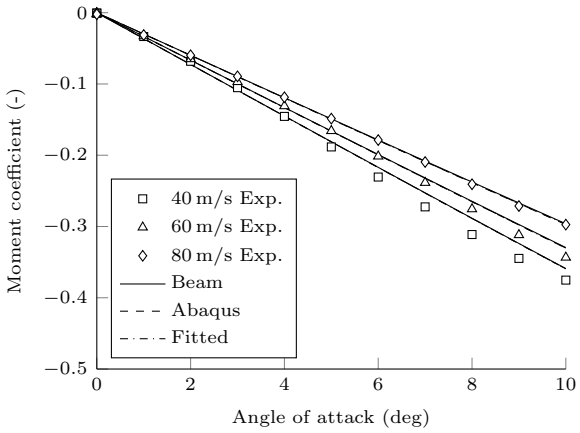


**Figure 6.16:** Root bending moment coefficient of the tailored wing.

sure of the wing shown in Figure 6.17, which has been obtained by dividing the root bending moment coefficient by the lift coefficient. From this figure, several conclusions can be drawn. First, both the experimental results and the numerical simulations show that the QI wing does not alleviate loads due to the lack of bend-twist coupling and a shear centre location of 23% chord, which is close to the quarter chord centre of pressure. The difference of up to 2.5% span between the numerical simulations and the experimental results is considered good agreement and can be explained by, for example, manufacturing quality, measurement inaccuracies, and assumptions made in the simulations.



Secondly, the tailored wing clearly shows manoeuvre load alleviation by shifting the centre of pressure inboard as the velocity is increased. Similar to the QI wing, a difference is observed between the numerical simulations and the experimental results. It is interesting to note that, although there is a difference between the numerical simulations and the experimental results, the relative shift in centre of pressure as the velocity increases shows good agreement, especially at higher angles of attack.

Finally, when comparing the tailored wing and the QI wing, the experimental results show less manoeuvre load alleviation than expected from the numerical simulations. This is most likely caused by slight geometrical differences between both wings.

It is interesting to note that manoeuvre load alleviation is almost independent of the angle of attack. For a symmetric wing without pre-twist, given a certain velocity, this can be explained by the fact that both the aerodynamic loads and the wing twist start from zero and are linear with respect to the angle of attack. Therefore, given a lift distribution for, for example, an angle of attack of 1 deg,

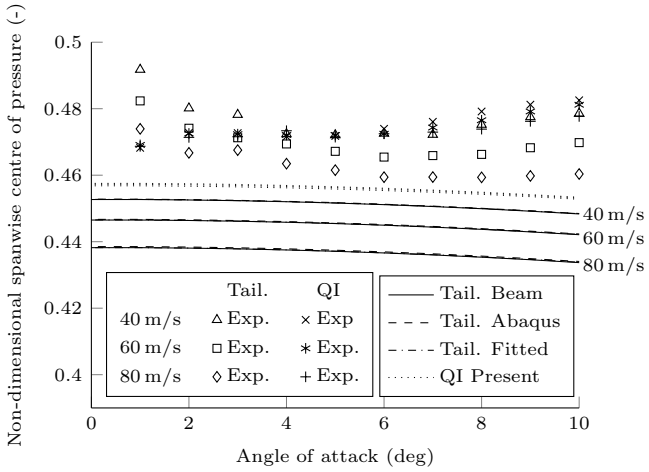


**Figure 6.17:** Location of the spanwise centre of pressure for the QI and tailored wing at different velocities.

doubling the angle of attack to 2 deg will double the resulting lift and wing twist; however, since both effects are linear, the resulting lift distribution is almost unaffected. However, a change in air speed does affect the lift distribution, as the aerodynamic loads are quadratic in air speed and, thus, for the same lift generated a different wing twist distribution and, consequently, lift distribution is obtained.

In conclusion, when including the effects of the fibre volume corrected properties, leading edge strips, and epoxy, the beam results show good agreement with the experimental results, thus validating the loads predicted by the aeroelastic analysis framework.



## 6.5.2 WING DEFORMATION

Figures 6.18 and 6.19 show the comparison of the wing tip deflection and wing tip twist between the DIC measurements, the optical marker tracking system (OMTS) and the numerical beam simulations for the QI wing. The wing deflection and wing twist results show good agreement for 40 m/s and 60 m/s with errors ranging from 1.0% to 7.5% for deflection and up to 0.1 deg for twist. At 80 m/s and an angle of attack larger than 7 deg, the wing buckled, resulting in differences between the experimental results and the numerical simulations. Figures 6.20 and 6.21 show the out-of-plane displacement and twist distribution along the span at an angle of attack of 10 deg. At 40 m/s and 60 m/s, the experimental results and the numerical simulations show good agreement, however, at 80 m/s, the wing buckled and thus the results clearly differ. Note that the experimental wing

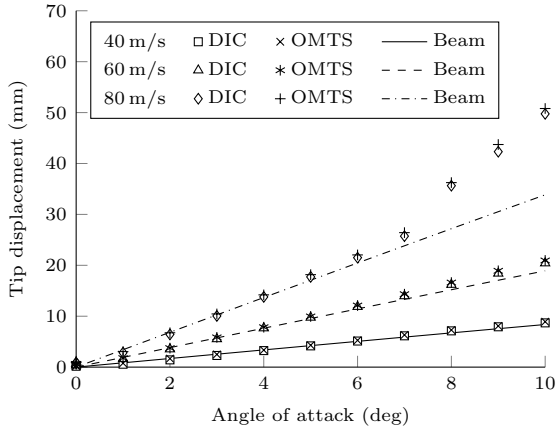


**Figure 6.18:** Out-of-plane tip deflection of the QI wing at different velocities.

twist is derived from the displacement measurements which is why close to the wing root, the experimental results show a small wing twist due to measurement inaccuracies, while the simulations predict almost no wing twist.

The comparison of the wing tip deflection and tip twist between the different measurement techniques and the numerical simulations for the tailored wing is shown in Figures 6.22 and 6.23. Similar to the results from the structural tests, the beam model including LE strips and epoxy and the full Abaqus model predict a stiffer wing in bending than obtained from the experimental results with errors ranging from 10% to 22% for the beam model and 7% to 19% for the Abaqus model. When looking at the wing twist, it is interesting to note that, even though all models have different cross-sectional properties, the difference in the resulting twist distribution under aerodynamic loads is negligible, showing that the effect of the core and warping restraint on the aeroelastic twist is negligible. When comparing the beam twist results to the experimental twist results, the beam results predict a tip twist which is 4% to 10% higher, which is consistent with the larger manoeuvre load alleviation observed in the root bending moment results in Figure 6.16.

The out-of-plane displacement and twist distribution along the span at an angle of attack of 10 deg are shown in Figures 6.24 and 6.25. Similar to the QI wing, at 40 m/s and 60 m/s, the experimental wing displacement and the numerical simulations using the fitted cross-sectional properties show excellent agreement, however at 80 m/s the wing buckled and thus the results clearly differ. It is interesting to note that, while the tip deflection is clearly affected by buckling, the wing twist is much less affected. As also observed in the structural tests, the beam and Abaqus simulations predict a stiffer wing in bending than the experimental results. When looking at the wing twist, as already concluded from

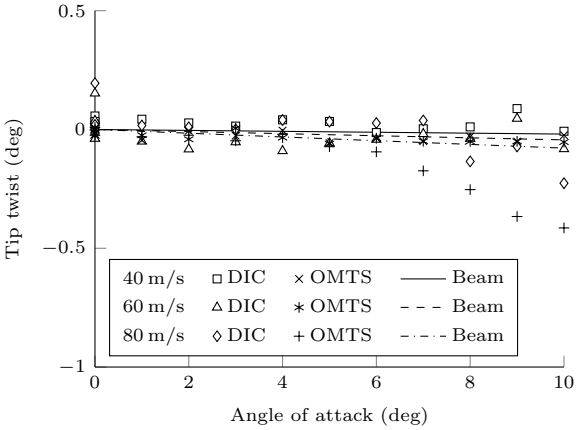


**Figure 6.19:** Tip twist of the QI wing at different velocities.



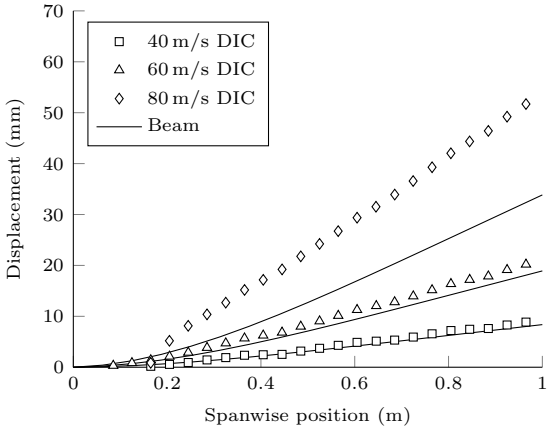


**Figure 6.20:** Out-of-plane deflection of the quarter-chord line of the QI wing at $\alpha = 10\,\text{deg}$.

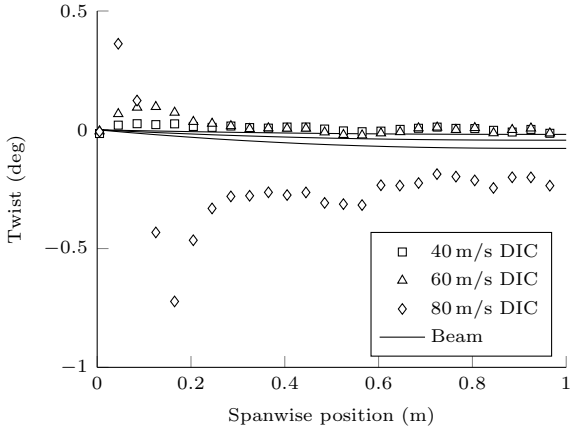


**Figure 6.21:** Twist of the QI wing at $\alpha = 10\,\text{deg}$.

the tip twist results, the numerical simulations predict a slightly higher wing twist than observed in the experiment.

Comparing the QI wing to the tailored wing, first of all, it can be seen that, as expected, the bend-twist coupling of the tailored wing results in manoeuvre load alleviation by a wash-out deformation, while negligible manoeuvre load alleviation is observed for the QI wing due to a lack of bend-twist coupling and a shear centre location of 23% chord, which is close to the quarter chord centre of pressure. Second of all, it is interesting to note that the QI wing buckled at a lower angle of attack than the tailored wing, even though its skin is thicker. This can be explained by two effects: (i) the tailored wing alleviates loads and thus the actual force and bending moment on the wing is smaller and (ii) the tailored wing skins are supported by a foam core over the entire surface, while the wing skins of the QI wing are only reinforced by foam ribs at discrete locations.

In conclusion, although the error in wing deflection of the tailored wing ranges from 10% to 22%, the wind tunnel results show reasonable to good agreement to the aeroelastic beam simulations in terms of wing twist with errors ranging from 4% to 10%, in terms of predicted loads with errors ranging from 0.2% to 7.5%, and in terms of wing deflection for the QI wing with errors ranging from 1.0% to 7.5%, thus validating the static aeroelastic analysis framework. Causes for the discrepancies in wing deflection of the tailored wing are slight variations in material properties or wing geometry, or some flexibility in the clamping mechanism resulting in additional wing deflection in the experiments. Furthermore, the results obtained using the cross-sectional properties derived from the Abaqus model show that the effect of the core and warping restraint on the aeroelastic response is negligible.

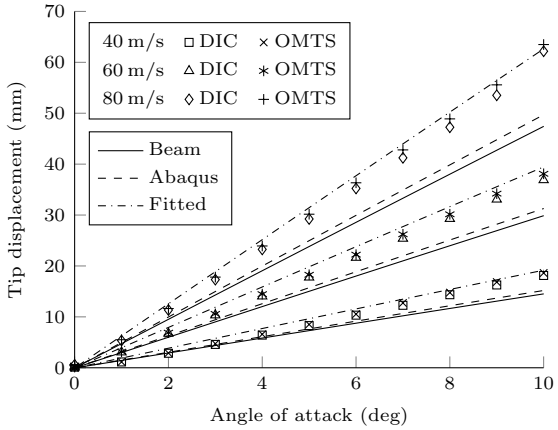


**Figure 6.22:** Out-of-plane tip deflection of the tailored wing at different velocities.



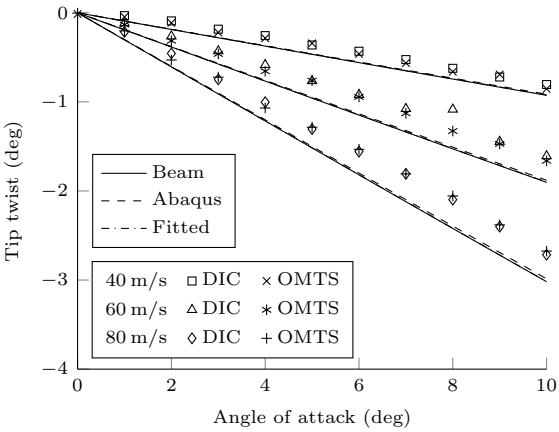


**Figure 6.23:** Tip twist of the tailored wing at different velocities.

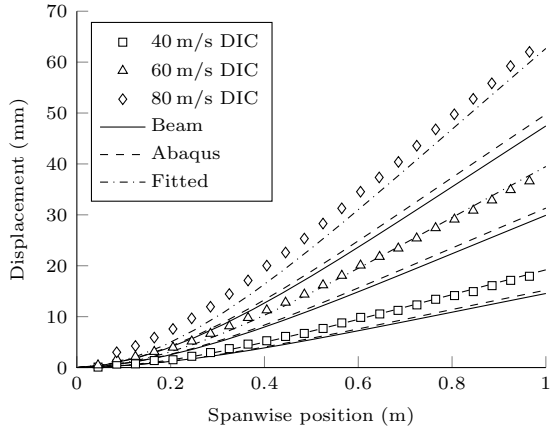


**Figure 6.24:** Out-of-plane deflection of the quarter-chord line of the tailored wing at $\alpha = 10\,\text{deg}$.

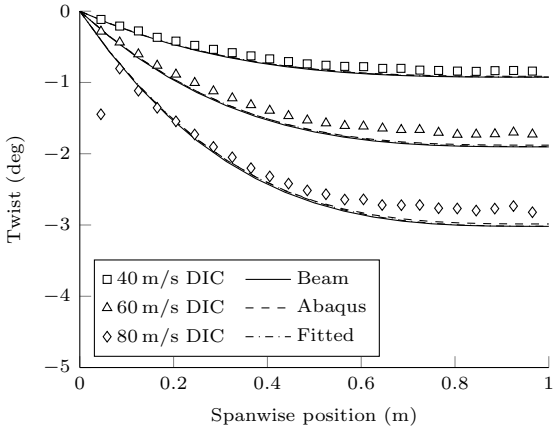


**Figure 6.25:** Twist of the tailored wing at $\alpha = 10\,\text{deg}$.

## 6.6 SYNOPSIS

In this chapter experimental validation data for composite aeroelastically tailored wings with a closed-cell cross-sectional structure is presented and used to validate the static aeroelastic analysis framework presented in the previous chapters.

- The framework has been used for the design of several aeroelastically tailored wings designed to alleviate loads by minimising the root bending moment.
- Two wings were tested: (i) a 6 layer quasi-isotropic wing to act as reference wing, and (ii) a 4 layer tailored wing.
- Structural tests were carried out to investigate the influence of the different components of the manufactured wings on the structural response and provide structural characterisation data.
- Wind tunnel tests were carried out at a range of angles of attack up to a wind speed of 80 m/s. The aerodynamic forces and moments have been measured using a six component balance, the wing deformation has been measured by a digital image correlation system, and the tip deflection and tip twist have been measured by an optical marker tracking system.
- The effect on the aeroelastic response of the foam core and the warping restraint at the wing root, which are not accounted for in the beam model, has been assessed by using cross-sectional properties derived from Abaqus simulations of the complete wing, showing that these effects had negligible influence on the aeroelastic response.
- Comparison of the experimental data and numerical simulations shows good agreement for the quasi-isotropic wing, both in terms of wing deformations with errors in the range of 1.0% to 7.5% and in terms of predicted loads with errors ranging from 0.5% to 4.6%.
- In case of the tailored wing, discrepancies were still observed in the wing deflection with errors in the range of 10% to 22%, even after accounting for the leading edge strips connecting the two wing halves and the epoxy used to glue in the core. However, reasonable to good agreement is observed in terms of wing twist with errors in the range of 4% to 10% and predicted loads with errors in the range of 0.2% to 7.5%. Causes for the discrepancies in wing deflection of the tailored wing are variations in material properties or wing geometry, or flexibility in the clamping mechanism resulting in additional wing deflection in the experiments.

In conclusion, structural tests and wind tunnel tests have been successfully performed on aeroelastically tailored wings, validating the static aeroelastic analysis and design framework.

# PART III

# APPLICATION TO WING STRUCTURAL DESIGN

*It is not the strongest; it is not the most intelligent who will survive; but the species that survives is the one that is able best to adapt and adjust to the changing environment in which it finds itself.*

**Prof. L.C. Megginson, paraphrasing Charles Darwin, 1963**

# 7

# MORPHING WING OPTIMISATION

Now that the aeroelastic analysis and optimisation framework, as described in Part I of this dissertation, has been validated, as described in Part II of this dissertation, the framework can be applied to design studies to illustrate the benefits of morphing. Therefore, this chapter presents the design optimisation of a morphing wing by means of the two-step morphing optimisation approach introduced in Section 5.4 using data from the EU FP7 Project CHANGE.

First, Section 7.1 presents the first step of the two-step morphing optimisation approach providing a description of the model and the distribution and limits of the morphing concepts on the wing. Based on this model description, two optimisations have been run in the second step of the two-step morphing optimisation approach, as presented in Section 7.2: one generating a fixed wing design to serve as a reference and one optimising a morphing wing.

Using the optimised morphing configurations for the different flight phases in the aircraft mission, the effect of two important parameters in the design of morphing aircraft has been investigated: (i) the effect of the flight condition at which morphing is carried out, as presented in Section 7.3, and (ii) the effect of the sequence in which the different morphing manoeuvres are carried out, as presented in Section 7.4. Based on the conclusions drawn on the importance of the flight condition and morphing sequence, Section 7.5 provides some general insights extrapolating these conclusions to the design of morphing aircraft, putting them into perspective, and addressing their impact. Finally, a brief synopsis is given in

**Table 7.1:** UAV properties.

| Planform | | Wing box | | General | |
|---|---|---|---|---|---|
| Semispan | 1.66 - 2.00 m | Front spar | 30% chord | Aircraft weight | 25 kg |
| Root chord | 0.60 m | Rear spar | 70% chord | | |
| Taper ratio | 1 | | | | |
| Sweep angle | 0 deg | | | | |

Section 7.6.

## 7.1 FIRST STEP: MORPHING WING DEFINITION

In order to illustrate the morphing optimisation framework, it has been applied to the optimisation of a wing based on the planform of the EU FP7 CHANGE wing, which is designed for a 25 kg unmanned aerial vehicle (UAV). The wing is described in more detail in the following sections, showing the wing planform, the layout of the morphing mechanisms, the CHANGE mission profile, and the optimisation setup and wing discretisation.

### 7.1.1 MODEL DESCRIPTION

Figure 7.1 shows the planform of the CHANGE wing and the corresponding data is given in Table 7.1. The wing is equipped with camber morphing mechanisms in the inboard section of the wing at locations 1 and 2, a span extension mechanism in the middle section, a twist mechanism in the outboard extended wing, and 3 shear morphing mechanisms, allowing the complete wing to shear, as is illustrated in Figure 7.1. The baseline wing has no twist and the NACA2510 airfoil was selected as the baseline airfoil. The wingbox is made out of carbon/epoxy with the material properties as given in Table 7.2 and a quasi-isotropic layup. The wing has a linearly varying thickness from 5 mm at the wing root to 2 mm at the wing tip.



### 7.1.2 MORPHING FEASIBILITY CONSTRAINTS

The CHANGE wing has 7 different morphing mechanisms, distributed over 4 types of morphing. As a consequence, the wing has 7 design parameters for each flight phase, as given in Table 7.3. The first step in the two-step optimisation approach consists of deriving the feasibility constraints for these design parameters based on the limitations of the morphing mechanisms and their location, as illustrated in Figure 7.1. This results in the following concept-specific feasibility

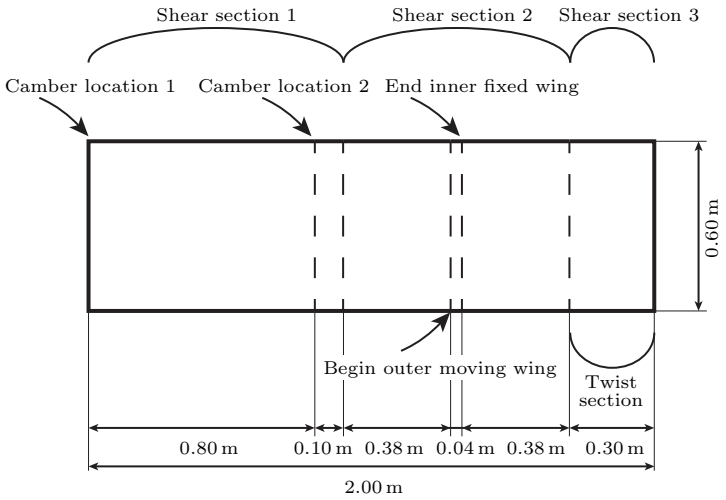


**Figure 7.1:** Initial wing planform and morphing sections.

**Table 7.2:** Material properties. (Source: Daniel and Ishai (2006))

| UD Carbon/Epoxy (AS4/3501-6) | |
|---|---|
| $E_{11}$ | 147.0 GPa |
| $E_{22}$ | 10.3 GPa |
| $G_{12}$ | 7.0 GPa |
| $\nu_{12}$ | 0.27 |
| $\rho$ | 1600 kg/m$^3$ |
| $X_t$ | 948.5 MPa$^*$ |
| $X_c$ | 717.6 MPa$^*$ |
| $Y_t$ | 23.7 MPa$^*$ |
| $Y_c$ | 94.8 MPa$^*$ |
| $S$ | 31.6 MPa$^*$ |

$^*$ Including knockdown factors for environmental effects (0.8), barely visible impact damage (0.65), and material scatter (0.8). (Kassapoglou, 2013)

**Table 7.3:** Number of design parameters per flight phase.

| | |
|---|---|
| Twist | 1 |
| Span extension | 1 |
| Camber | 2 |
| Shear | 3 |
| Total | 7 |

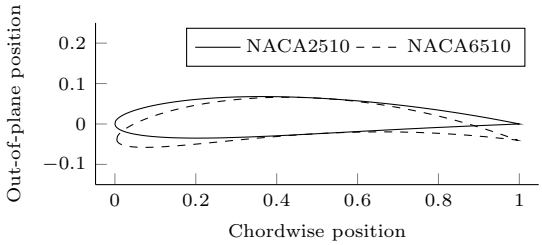


**Figure 7.2:** Camber morphing airfoils.

constraints for the CHANGE wing:

- Camber: between a NACA2510 (2% camber) and a NACA6510 airfoil (6% camber), as illustrated in Figure 7.2, with linearly interpolated airfoils between location 1 and location 2, and linearly interpolated airfoils in the 0.10 m transition region outboard of location 2.
- Semi-span extension: between 1.66 m and 2.00 m by a telescopic span extension mechanism positioned between 0.90 m and 1.70 m span.
- Twist: linearly varying from 0 deg at the end of the span extension mechanism at 1.70 m span to an angle of 0 to −5 deg (indicating nose down twist) at the wing tip.
- Shear: three independent sections shearing between 0 deg and 30 deg (indicating sweep back).

### 7.1.3 MISSION PROFILE

The CHANGE wing has been designed to fly a typical UAV mission consisting of five flight phases, as illustrated in Figure 7.3: (i) take-off, (ii) a high speed phase to the area of interest, (iii) a loiter phase to explore the area of interest, (iv) the second high speed phase to return the landing site, and (v) landing. The corresponding flight conditions are given in Table 7.4. As can be seen, the loiter and landing phase are essentially identical, leaving three unique flight conditions

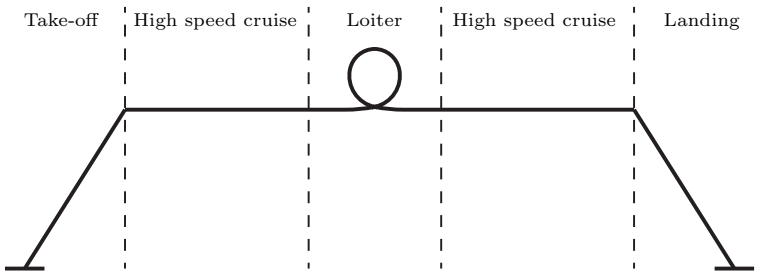


**Figure 7.3:** Schematic illustration of the CHANGE mission profile.

**Table 7.4:** Flight phases of the CHANGE UAV mission.

| | Flight speed (EAS) |
|---|---|
| Take-off | 21.25 m/s |
| High speed | 30.55 m/s |
| Loiter | 15.27 m/s |
| Landing | 15.27 m/s |

for which the CHANGE wing needs to be optimised: (i) take-off, (ii) high speed, and (iii) loiter.

### 7.1.4 WING DISCRETISATION



Based on a mesh convergence study, the CHANGE wingbox structure is discretised using 20 structural elements. Each cross-section is discretised using 89 cross-sectional elements. The aerodynamic panel distribution consists of 12 spanwise aerodynamic panels with a half-cosine distribution towards the wing tip and 16 equally distributed chordwise aerodynamic panels, resulting in a total of 192 aerodynamic panels on the wing surface. In order to improve the accuracy of the chordwise pressure distribution required for the assessment of the actuation forces and energy of the camber morphing manoeuvre, an additional aerodynamic analysis is carried out with a refined chordwise mesh of 32 elements once static equilibrium has been obtained. The unsteady aerodynamic wake for the dynamic aeroelastic simulations is discretised using $\frac{\Delta x_w}{c} = \frac{1}{8}$ and is truncated at 10 root chords behind the wing, resulting in a total of 960 wake panels in the unsteady wake.

## 7.2 SECOND STEP: OPTIMUM MORPHING PARAMETERS

This section presents the second step in the two-step morphing optimisation approach. Based on the feasibility constraints derived in the first step, as presented in Section 7.1.2, the generic morphing optimisation framework presented in Section 5.4 is used to find the optimum morphing parameters at each of the three different flight phases of the CHANGE mission. First, Section 7.2.1 presents the corresponding optimisation setup, after which the optimisation results are presented in Section 7.2.2.

### 7.2.1 OPTIMISATION SETUP

Based on the chosen mission profile, a morphing optimisation is done to investigate the optimum morphing parameters for each flight condition. Each flight phase has its own performance parameter and, therefore, its own objective. In case of take-off, the selected objective was to optimise the climb performance of the UAV, which in case of fixed weight aircraft is equivalent to minimising drag. In case of the high-speed phase, the objective is to maximise the range of the aircraft, which for a fixed weight aircraft powered by lithium-polymer batteries at a given velocity scales with $D^{-1.3}$ (Traub, 2011), and is, therefore, in this case also equivalent to minimising the aircraft drag. Finally, in case of the loiter phase, the objective is to maximise endurance, which for a given velocity is equivalent to maximising range and, thereby, in this case also equivalent to minimising drag.

In order to generate a fixed wing design to act as a reference for the optimised morphing wings, an additional optimisation is run with equal morphing parameters for all flight phases and a weighted objective with a focus on the high speed and loiter phases (both 40% and take-off 20%).



Besides the morphing feasibility constraints derived in Section 7.1.2, additional constraints are set on the aeroelastic stability of the wing and the local angle of attack on the wing to ensure a feasible final design. As explained in Section 5.3.3, the aeroelastic stability is governed by the eigenvalues of the state matrix, resulting in the following constraint on the real part of the eigenvalues for aeroelastic stability of the wing:

$$\Re(\lambda) \leq 0 \tag{7.1}$$

In order to reduce the number of constraints that are fed to the optimiser and improve the efficiency of the optimisation, only the 10 most critical eigenvalues for each loadcase are introduced as constraints in the optimisation, instead of all eigenvalues.

**Table 7.5:** Optimum morphing parameters.

| | Fixed wing | Morphing wing | | |
|---|---|---|---|---|
| | | Take-off | High speed | Loiter |
| Shear section 1 | 0 deg | 21.6 deg | 30.0 deg | 0 deg |
| Shear section 2 | 0 deg | 11.6 deg | 30.0 deg | 0 deg |
| Shear section 3 | 11.7 deg | 15.3 deg | 30.0 deg | 0 deg |
| Twist | −5.0 deg | −5.0 deg | −0.5 deg | −5.0 deg |
| Camber location 1 | 2.69% | 4.24% | 5.69% | 3.86% |
| Camber location 2 | 2.59% | 2.85% | 4.86% | 3.70% |
| Span | Extended | Extended | Retracted | Extended |

The local angle of attack is defined by the aircraft angle of attack, the initial wing twist, and the twist induced by the structural deformations, and is limited to ±12 deg to ensure attached aerodynamic flow, while still leaving design freedom to the optimiser, resulting in two constraints per aerodynamic cross-section per loadcase, which results in 24 constraints using the wing discretisation given in Section 7.2.

### 7.2.2 Optimisation results

The optimised planform and corresponding morphing parameters for each of the optimisations are shown in Figure 7.4 and Table 7.5, respectively. First, each wing design will be discussed separately, after which a comparison between the different wing designs is presented. For each wing design, the dynamic aeroelastic stability constraints and local angle of attack constraints are not active and are, therefore, not included in the discussion of the results.

#### Fixed wing reference configuration



When looking at the optimal morphing parameters in Table 7.5, it can be seen that, as is to be expected, the fixed wing optimal design is a compromise between the different flight phases. As can be concluded from Table 7.6, the optimum fixed wing design is a trade-off between minimising parasitic drag on the one hand and minimising induced drag on the other hand across the different flight phases, where, in this case, minimising induced drag is favoured with a sacrifice in parasitic drag. Induced drag is driven by the lift distribution and aspect ratio of the wing and is minimised by increasing the aspect ratio of the wing and obtaining an elliptic lift distribution. Parasitic drag, on the other hand, is reduced by reducing the surface area of the wing and increasing the sweep angle of the wing, as can be concluded from Section 4.6.1, illustrating the trade-off to be made.

The effect of the trade-off between induced drag and parasitic drag can, for ex-

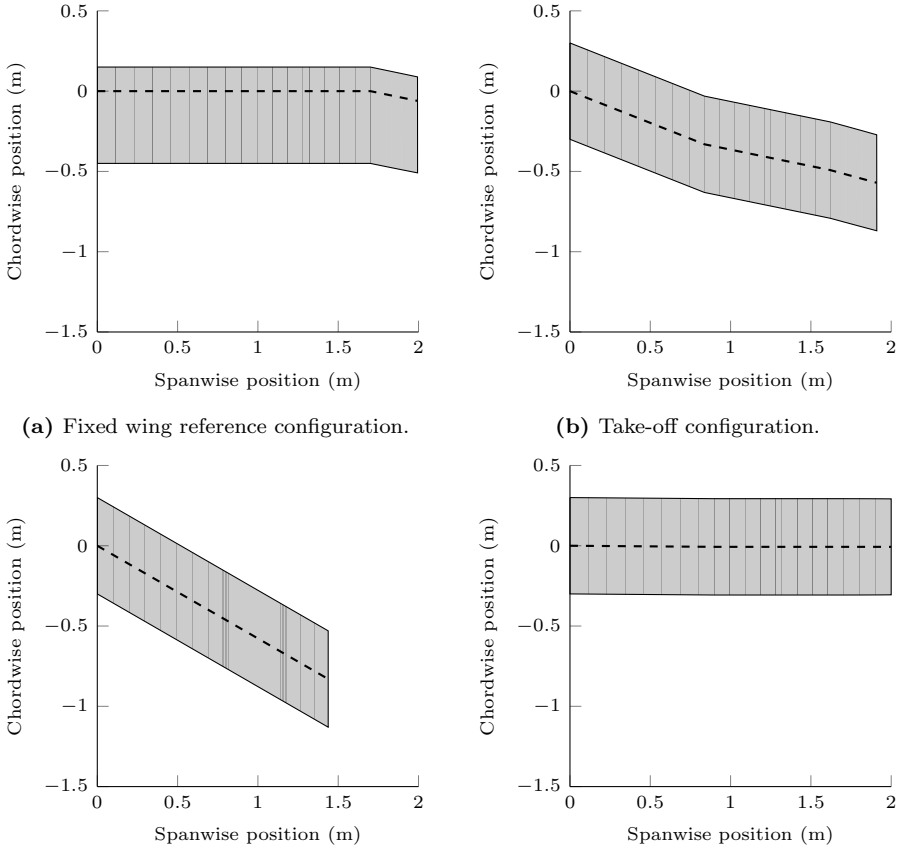


**(a)** Fixed wing reference configuration.

**(b)** Take-off configuration.

**(c)** High speed configuration.

**(d)** Loiter configuration.

**Figure 7.4:** Optimised wing planform for the fixed wing design and for each of the different flight conditions of the morphing wing.



**Table 7.6:** Optimised wing characteristics.

| | Fixed wing | | | Morphing wing | | |
|---|---|---|---|---|---|---|
| | Take-off | High speed | Loiter | Take-off | High speed | Loiter |
| $C_D{}^*$ | 0.01809 | 0.01263 | 0.03627 | 0.01803 | 0.01075 | 0.03597 |
| ${C_{D_p}}^*$ | 0.01193 | 0.01140 | 0.01270 | 0.01132 | 0.00780 | 0.01273 |
| ${C_{D_i}}^*$ | 0.00616 | 0.00149 | 0.02358 | 0.00671 | 0.00295 | 0.02323 |
| $C_{D_p}/{C_{D_i}}^*$ | 1.94 | 7.64 | 0.54 | 1.69 | 2.64 | 0.55 |
| Trim angle (deg) | 2.31 | −0.12 | 6.82 | 2.24 | −0.65 | 6.16 |
| Surface area ($m^2$) | 1.20 | 1.20 | 1.20 | 1.15 | 0.86 | 1.20 |

* Defined with respect to the reference area of the original wing of 1.20 $m^2$.

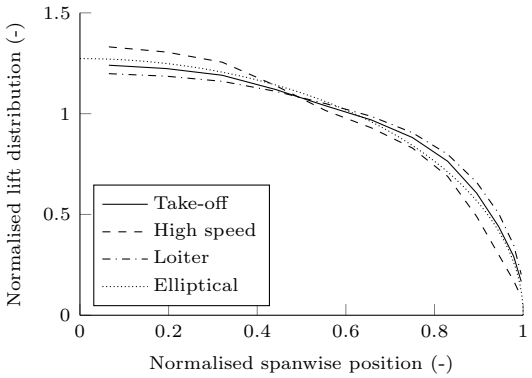


**Figure 7.5:** Lift distribution of the fixed wing design.

ample, be observed in the shear morphing parameters. Reducing the shear angle to 0 deg along the wing span would result in the minimum induced drag, but at the cost of an increase in parasitic drag by increasing the surface area of the wing and reducing the sweep angle. As a consequence, a trade-off has to be made, resulting a shear angle of 0 deg in sections 1 and 2 and a shear angle of 11.7 deg in section 3.

Finally, twist and camber morphing are used to approach an elliptical lift distribution over the wing across the different flight phases, as shown in Figure 7.5, to minimise the induced drag of the wing, resulting in a negative twist angle at the feasibility limit of $-5$ deg at the wing tip and a camber variation from 2.69% at the wing root to 2.59% at location 2.

### Take-off configuration

When looking at the optimal morphing parameters for the take-off configuration in Table 7.5, it can be seen that, except for camber morphing at location 2, the take-off configuration is an intermediate configuration between the high speed configuration and the loiter configuration, which is to be expected, since the take-off flight condition is an intermediate flight condition between the loiter and high speed flight conditions.

As can be concluded from Table 7.6, similar to the fixed wing design, the optimum take-off shape is a trade-off between minimising parasitic drag on the one hand and minimising induced drag on the other hand. The effect of this trade-off can, for example, be observed in the shear morphing parameters. Reducing the shear angle to 0 deg along the wing span would reduce the induced drag by $4.9 \cdot 10^{-4}$, but at the cost of an increase in parasitic drag of $6.5 \cdot 10^{-4}$. As a consequence, a trade-off has to be made, resulting in the shear angles given in Table 7.5.

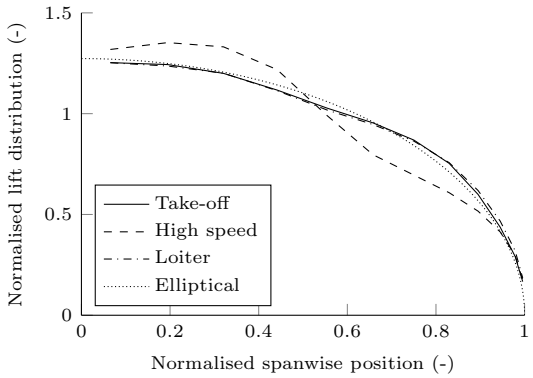


**Figure 7.6:** Lift distribution of the morphing wing design.

Finally, similar to the fixed wing design, twist and camber morphing are used to approach an elliptical lift distribution over the wing, as shown in Figure 7.6, to minimise the induced drag of the wing.

### HIGH SPEED CONFIGURATION

The optimal morphing parameters of the high speed configuration are shown in Table 7.5. As can be concluded from Table 7.6, in contrast to the take-off configuration, the high speed configuration is dominated by parasitic drag. Therefore, the shear angle of the wing is increased to its limit of 30 deg and the span extension mechanism is retracted, thereby minimising the surface area of the wing and maximising the sweep angle, thus, minimising the parasitic drag. As a consequence, the lift distribution over the wing is far from elliptical, as shown in Figure 7.6, thereby sacrificing the induced drag performance of the wing. Although, similar to the take-off configuration, twist and camber morphing are still used to improve the lift distribution of the wing and reduce the induced drag.



### LOITER AND LANDING CONFIGURATION

When looking at the drag breakdown in Table 7.6, it can be seen that the loiter configuration is dominated by induced drag because of the low velocity and corresponding high lift coefficient. Therefore, in this case, the wing is kept straight with no sweep and a fully extended span to maximise the aspect ratio of the wing and minimise the induced drag, while sacrificing parasitic drag performance.

Finally, twist and camber morphing are used to optimise the lift distribution of the wing and further minimise the induced drag, as shown in Figure 7.6.

### Comparison of the optimised wings

When comparing the optimal configurations for the different flight conditions, the main conclusion that can be drawn is that for each flight condition, a different trade-off is made between parasitic drag and induced drag, resulting in a different set of optimal morphing parameters. In case of the loiter configuration and high speed configuration, either induced drag (for loiter) or parasitic drag (for high speed) is clearly dominant and driving the design; however, in case of the take-off configuration a clear trade-off between induced drag and parasitic drag is observed. The fixed wing design shows similar performance to the morphing wing in case of take-off and loiter, but has a 17% higher drag and, consequently, 23% lower range at the high speed flight condition, thereby clearly illustrating the potential of morphing to optimise the performance of UAVs across a mission with highly varying flight conditions.

## 7.3 Effect of the flight condition on the morphing actuation requirements

One of the important aspects of morphing aircraft is the actuation system used to morph from configuration A to configuration B. In order to maximise the range or endurance of the morphing aircraft, minimising the weight of this actuation system for a given set of morphing manoeuvres is one of the objectives in designing a morphing aircraft. The weight of the actuation system is mainly driven by the maximum force the actuator has to transfer to the surrounding structure to morph the aircraft. The actuation forces required for morphing consist of three components: (i) friction within the actuation mechanism, (ii) forces required to deform the mechanism, and (iii) forces required to overcome the external forces acting on the mechanism. The friction within the mechanism and the forces required to deform the mechanism can be optimised by a proper design of the morphing mechanism. However, the forces required to overcome the external forces acting on the mechanism can only be assessed on a systems level.



As identified by De Breuker and Werter (2016), the actuation forces and moments required to overcome the external forces are significantly influenced by the morphing flight condition and the sequence of morphing manoeuvres. Therefore, based on the mission profile defined in Section 7.1.3 and the optimised morphing shapes for each of the flight conditions, as given in Section 7.2, two important questions need to be answered for the operation of the CHANGE morphing aircraft: (i) at what flight condition(s) should the morphing manoeuvres be carried out, and (ii) in what sequence should the different morphing manoeuvres be carried out. In order to obtain some insight in answering these questions, first, the effect of the flight condition(s) on the actuation requirements is discussed in this

section. Secondly, the effect of the morphing sequence on the actuation requirements will be discussed in Section 7.4.

Before continuing with the discussion of the results, it is important to note that, in this dissertation, a distinction is made between a morphing manoeuvre and a configuration change to prevent ambiguity when discussing the results. A morphing manoeuvre is defined as a morphing deformation of a single morphing type, so, for example, a twist morphing manoeuvre, while a configuration change is defined as the combination of morphing manoeuvres that, for example, morphs the wing from the take-off configuration to the high speed configuration.

In order to assess the actuation requirements for the different morphing mechanisms, the morphing actuation forces and moments to overcome the external forces are computed, as described in Section 5.4.3. Each morphing manoeuvre has been split in 10 equal morphing steps to assess the change of actuation forces or moments over the morphing manoeuvre.

In case of camber morphing, a distinction is made between leading edge and trailing edge morphing by computing separate actuation moments per unit span for the leading edge (i.e. 0% - 50% chord) and the trailing edge (i.e. 50% - 100% chord) with respect to the middle of the chord.

In case of span morphing, all energy required is given by the mechanical energy required to morph, since the aerodynamic forces act perpendicular to the morphing movement. Therefore, the magnitude of the shear force, bending moment, and torque at the end of the span extension mechanism at 1.32 m span are used as a measure for the actuation forces of the span extension mechanism, since these will determine the friction in the telescopic mechanism and, consequently, the required actuation forces.

In order to investigate the influence of the flight condition on the morphing actuation forces and moments, each configuration change is evaluated at 11 equally distributed velocities between flight phase 1 and flight phase 2. The resulting actuation moments and forces for each morphing manoeuvre in the CHANGE flight mission will be discussed separately in the following sections, and, finally, a comparison will be made between the different morphing manoeuvres.



### 7.3.1 MORPHING FROM THE TAKE-OFF CONFIGURATION TO THE HIGH SPEED CONFIGURATION

The first configuration change that needs to be carried out in the CHANGE flight mission is the change from the take-off configuration to the high speed configuration. The resulting actuation forces and moments are given in Table 7.7. For the sake of brevity only the results for the best and worst flight conditions for each morphing mechanism are given.

**Table 7.7:** Maximum actuation requirements when morphing from the take-off configuration to the high speed configuration.

| | Flight speed (m/s) | | Sequence* | | Angle of attack (deg) | Resisting force/moment |
|---|---|---|---|---|---|---|
| Twist | Best | 21.15 | Best | sp-sh-tw | 4.92 | −1.24 N m |
| | | | Worst | ca-tw | 1.33 | 0.48 N m |
| | Worst | 30.55 | Best | sp-sh-tw | 0.71 | 0.88 N m |
| | | | Worst | ca-tw | −1.40 | 3.85 N m |
| Shear section 1 | Best | 30.55 | Best | ca-sh | −1.00 | −5.67 N m |
| | | | Worst | sp-sh | 0.71 | −3.60 N m |
| | Worst | 21.15 | Best | tw-ca-sh | 2.18 | −1.75 N m |
| | | | Worst | sp-sh | 4.92 | 0.33 N m |
| Shear section 2 | Best | 30.55 | Best | ca-sh | −1.00 | −1.89 N m |
| | | | Worst | sp-sh | 0.71 | −0.77 N m |
| | Worst | 21.15 | Best | tw-ca-sh | 2.18 | −0.64 N m |
| | | | Worst | sp-sh | 4.92 | −0.01 N m |
| Shear section 3 | Best | 30.55 | Best | tw-sh | −0.09 | −0.15 N m |
| | | | Worst | sp-sh | 0.71 | −0.12 N m |
| | Worst | 21.15 | Best | tw-ca-sh | 2.18 | −0.07 N m |
| | | | Worst | sp-sh | 4.92 | −0.02 N m |
| Camber LE location 1 | Best | 30.55 | Best | tw-ca | −0.57 | −1.01 N m/m |
| | | | Worst | sp-sh-ca | 0.71 | 2.61 N m/m |
| | Worst | 21.15 | Best | tw-ca | 2.17 | 5.40 N m/m |
| | | | Worst | sp-sh-ca | 4.92 | 8.84 N m/m |
| Camber LE location 2 | Best | 30.55 | Best | tw-ca | −0.57 | 1.30 N m/m |
| | | | Worst | sp-sh-ca | 0.71 | 5.83 N m/m |
| | Worst | 21.15 | Best | tw-ca | 2.17 | 7.09 N m/m |
| | | | Worst | sp-sh-ca | 4.92 | 11.28 N m/m |
| Camber TE location 1 | Best | 21.15 | Best | tw-sh-ca | 2.18 | 6.34 N m/m |
| | | | Worst | sp-ca | 3.72 | 6.81 N m/m |
| | Worst | 30.55 | Best | tw-sh-ca | −1.12 | 11.35 N m/m |
| | | | Worst | sp-ca | −0.94 | 12.15 N m/m |
| Camber TE location 2 | Best | 21.15 | Best | tw-sh-ca | 2.18 | 4.64 N m/m |
| | | | Worst | sp-sh-ca | 3.72 | 5.47 N m/m |
| | Worst | 30.55 | Best | tw-sh-ca | −1.12 | 8.03 N m/m |
| | | | Worst | sp-ca | −0.94 | 9.60 N m/m |
| Span shear force | Best | 30.55 | Best | ca-sp | −1.40 | 3.15 N |
| | | | Worst | tw-sh-sp | −0.09 | 18.64 N |
| | Worst | 21.15 | Best | ca-sp | 1.33 | 14.67 N |
| | | | Worst | tw-sh-sp | 3.21 | 21.99 N |
| Span bending moment | Best | 30.55 | Best | ca-sp | −0.94 | 0.58 N m |
| | | | Worst | tw-sh-sp | −0.09 | 4.77 N m |
| | Worst | 30.55 | Best | ca-sp | −0.94 | 0.58 N m |
| | | | Worst | tw-sh-sp | −0.09 | 4.77 N m |
| Span torque | Best | 25.85 | Best | sh-ca-sp | 0.21 | 0.43 N m |
| | | | Worst | ca-sp | −0.41 | 2.52 N m |
| | Worst | 30.55 | Best | tw-sh-sp | −0.09 | 1.18 N m |
| | | | Worst | ca-sp | −1.40 | 6.08 N m |

* tw = twist, sp = span, sh = shear, and ca = camber.

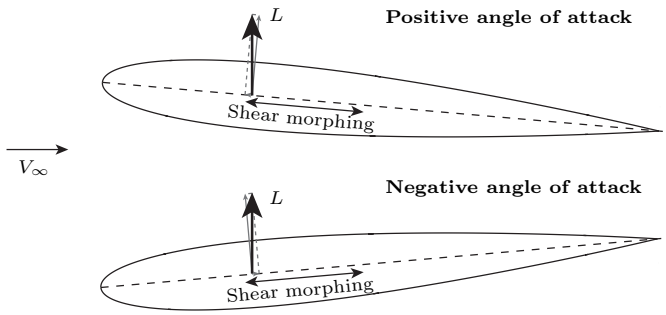


**Figure 7.7:** Schematic illustration of the influence of the angle of attack on the interaction of the lift force and shear morphing manoeuvre.

First of all, it can be concluded that depending on the morphing mechanism, the actuation requirements change significantly with flight condition, up to, for example, an increase in actuation moment of 630% for leading edge camber morphing at location 1. Furthermore, it can be seen that a trade-off has to be made when selecting the flight condition(s) at which to carry out the configuration change. For example, for the twist morphing manoeuvre, a low velocity and corresponding high angle of attack is beneficial, since this will generate a pitch up aerodynamic moment assisting in the pitch up twist morphing manoeuvre, resulting in a negative energy requirement. However, for shear morphing, a high angle of attack results in the highest actuation requirements, since, as illustrated in Figure 7.7, a positive angle of attack results in a lift force that resists shearing aft, while a negative angle of attack, results in a lift force that assists shearing aft. Hence, a high velocity is preferred for shear morphing.

Second of all, the contrast between leading edge and trailing edge camber morphing is interesting to note. In case of leading edge morphing, a low angle of attack, and thus high velocity, is preferred, since this reduces the upward forces, or even results in a negative force, at the leading edge, which is beneficial for increasing leading edge camber. However, since the overall wing lift remains equal, this results in an increased upward force at the trailing edge resisting an increase in camber at the trailing edge. Therefore, for trailing edge morphing, a low velocity and corresponding high angle of attack are preferred.

When looking at the different morphing mechanisms, for most mechanisms the lowest actuation requirements are obtained at either a velocity as low as possible or a velocity as high as possible and the highest actuation requirements are obtained at the other extreme, as is to be expected. However, two cases stand out: (i) the bending moment sizing the span morphing mechanism, and (ii) the torque sizing the span morphing mechanism.

In case of the bending moment, two different trends can be observed depending on the wing geometry when retracting the span: on the one hand, if the wing is

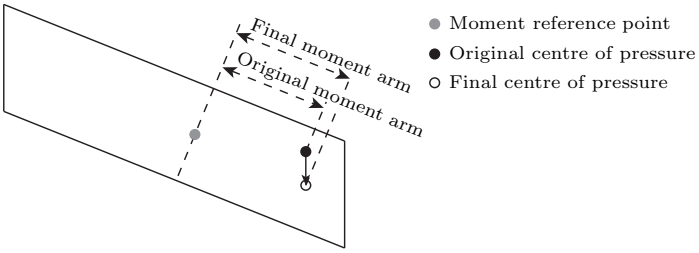


**Figure 7.8:** Schematic illustration of the influence of a shift of the lift towards the trailing edge on the bending moment acting on the span extension mechanism.

straight, an increase in velocity results in a reduced bending moment on the span extension mechanism, but, on the other hand, if the wing is swept, an increase in velocity results in an increased bending moment on the span extension mechanism. In both cases, an increase in velocity results in a corresponding decrease in angle of attack, reduced lift at the wing tip, and a chordwise centre of pressure that moves towards the trailing edge. However, the effect of these changes on the bending moment acting on the span extension mechanism is different. In case of a straight wing, a shift of the chordwise centre of pressure will only effect the torque on the span extension mechanism, but not the bending moment, and thus a reduced bending moment is observed resulting from the reduced lift at the wing tip. On the other hand, in case of a swept wing, a shift of the chordwise centre of pressure to the trailing edge also shifts the force away from the span extension mechanism, resulting in an increased bending moment, as illustrated in Figure 7.8. Hence, both the smallest bending moment and the largest bending moment are observed at the highest velocity.

When looking at the torque, the best flight condition at which to retract the span extension is neither the highest velocity nor the lowest velocity. Depending on the location of the centre of pressure on the outboard wing, either a positive or a negative torque acting on the span extension mechanism can be observed. Since the performance of the span extension mechanism is driven by the magnitude of the torque and is independent of its direction, the best flight condition, therefore, is found when, during the morphing manoeuvre, the torque changes from a pitch down torque to a pitch up torque, as can be seen in Figure 7.9, showing the change in torque while retracting the span extension at the best flight condition. Note that, in this case, 11 discrete velocities were investigated and the negative torque is slightly larger than the positive torque. As shown in Figure 7.9, a slight change in flight condition results in a slightly lower magnitude of the torque by finding the velocity at which both the positive and the negative torque are equal in magnitude.

Finally, it is interesting to note that the external forces acting on the wing do not always resist morphing and can actual be beneficial, depending on the flight

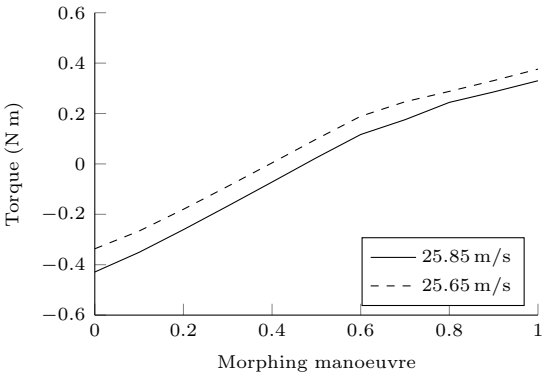


**Figure 7.9:** Change in the torque acting on the span extension mechanism during the span morphing manoeuvre. (Morphing sequence: sh-ca-sp)

condition, as, in this case, can be observed for leading edge camber morphing, shear morphing, and twist morphing.

### 7.3.2 MORPHING FROM THE HIGH SPEED CONFIGURATION TO THE LOITER CONFIGURATION

The second and fourth configuration change that needs to be carried out in the CHANGE flight mission is the change from the high speed configuration to the loiter or landing configuration. The resulting actuation forces and moments are given in Table 7.8. Similar conclusions can be drawn for this configuration change as for the change from the take-off configuration to the high speed configuration. For the sake of brevity, these will not be repeated here and the remainder of this section will focus on some of the differences observed.



When comparing the morphing parameters for both configuration changes, as given by Table 7.5, it can be seen that all morphing manoeuvres are in the opposite direction. As can be expected, in case of twist morphing, shear morphing, and camber morphing, the best flight condition when morphing from the take-off configuration to the high speed configuration becomes the worst flight condition when morphing from the high speed configuration to the loiter configuration and vice versa. However, in case of span morphing, the best and worse flight conditions are the same for both configuration changes, since the actuation requirements for span morphing are only driven by the magnitude of the shear force, bending moment, and torque acting on the span extension mechanism, while their direction is irrelevant. An important conclusion that can be drawn from this observation is that a different trade-off for the optimal flight condition will have to be made, since the flight condition that is optimal for the configuration change from the

take-off configuration to the high speed configuration will most likely not be the optimal condition for the configuration change from the high speed configuration to the loiter configuration.

### 7.3.3 Morphing from the loiter configuration to the high speed configuration

The third morphing manoeuvre that needs to be carried out in the CHANGE flight mission is the manoeuvre from the loiter configuration back to the high speed configuration. The resulting actuation forces and moments are given in Table 7.9. Since all morphing manoeuvres from the high speed configuration to the loiter configuration are similar to the morphing manoeuvres from the take-off configuration to the high speed configuration, similar conclusions can be drawn.

However, it is interesting to note that, even though morphing from the loiter configuration to the high speed configuration is the exact opposite manoeuvre as morphing from the high speed configuration to the loiter configuration, the best case in one direction is not necessarily the worst case in the other direction and vice versa. This will be discussed in more detail when discussing the effect of the morphing sequence on the actuation forces in Section 7.4.

### 7.3.4 Conclusion on the influence of flight condition

When investigating the influence of the flight condition on the morphing actuation forces and moments, several important conclusions can be drawn:

- The flight condition at which to morph has a significant influence on the actuation requirements of the different morphing mechanisms with changes of up to an order of magnitude. Therefore, it is something that should be incorporated in the design process of morphing mechanisms.

- When comparing the effect of the flight condition on the actuation requirements for the different morphing mechanisms, it is clear that no obvious optimal flight condition can be identified and a trade-off will have to be made depending on, for example, the actuation mechanism, actuator power limits, or UAV thrust limits.

- The optimal flight condition for morphing from configuration A to configuration B is not necessarily the optimal flight condition when morphing from configuration B back to configuration A. Therefore, a separate trade-off is required for each configuration change.

**Table 7.8:** Maximum actuation requirements when morphing from the high speed configuration to the loiter configuration.

| | Flight speed (m/s) | | Sequence* | | Angle of attack (deg) | Resisting force/moment |
|---|---|---|---|---|---|---|
| Twist | Best | 30.55 | Best | sp-sh-tw | −1.71 | −3.37 N m |
| | | | Worst | ca-tw | 0.40 | −0.21 N m |
| | Worst | 15.27 | Best | sp-sh-tw | 5.21 | 0.95 N m |
| | | | Worst | ca-tw | 12.14 | 2.30 N m |
| Shear section 1 | Best | 15.27 | Best | tw-ca-sh | 8.56 | 0.25 N m |
| | | | Worst | sp-sh | 5.21 | 0.82 N m |
| | Worst | 30.55 | Best | tw-ca-sh | −0.23 | 5.05 N m |
| | | | Worst | tw-sp-sh | −1.55 | 6.60 N m |
| Shear section 2 | Best | 15.27 | Best | tw-sp-ca-sh | 6.17 | 0.19 N m |
| | | | Worst | sp-sh | 5.21 | 0.37 N m |
| | Worst | 30.55 | Best | tw-sh | −1.22 | 0.90 N m |
| | | | Worst | sp-ca-sh | −0.91 | 2.31 N m |
| Shear section 3 | Best | 15.27 | Best | tw-ca-sh | 8.56 | 0.01 N m |
| | | | Worst | sp-sh | 5.21 | 0.07 N m |
| | Worst | 30.55 | Best | tw-sp-sh | −1.54 | 0.15 N m |
| | | | Worst | ca-sh | −0.48 | 0.19 N m |
| Camber LE location 1 | Best | 15.27 | Best | tw-sh-ca | 7.60 | −10.36 N m/m |
| | | | Worst | sp-sh-ca | 5.21 | −7.91 N m/m |
| | Worst | 30.55 | Best | tw-ca | −0.49 | 1.83 N m/m |
| | | | Worst | sp-sh-ca | −1.71 | 4.43 N m/m |
| Camber LE location 2 | Best | 15.27 | Best | tw-ca | 11.25 | −12.44 N m/m |
| | | | Worst | tw-sp-sh-ca | 5.37 | −7.72 N m/m |
| | Worst | 30.55 | Best | tw-ca | −0.49 | −1.55 N m/m |
| | | | Worst | sp-sh-ca | −1.71 | 4.21 N m/m |
| Camber TE location 1 | Best | 30.55 | Best | tw-sh-ca | −0.27 | −9.26 N m/m |
| | | | Worst | sp-ca | −0.24 | −8.36 N m/m |
| | Worst | 15.27 | Best | tw-ca | 12.30 | −3.72 N m/m |
| | | | Worst | sp-sh-ca | 6.01 | −3.28 N m/m |
| Camber TE location 2 | Best | 30.55 | Best | tw-sh-ca | −0.27 | −8.31 N m/m |
| | | | Worst | sp-ca | −0.24 | −6.70 N m/m |
| | Worst | 15.27 | Best | tw-sh-ca | 8.56 | −3.23 N m/m |
| | | | Worst | sp-ca | 8.93 | −2.79 N m/m |
| Span shear force | Best | 30.55 | Best | sh-sp | −1.71 | 2.33 N |
| | | | Worst | ca-sp | −0.24 | 17.69 N |
| | Worst | 15.27 | Best | tw-sh-sp | 5.37 | 16.31 N |
| | | | Worst | ca-sp | 8.93 | 23.28 N |
| Span bending moment | Best | 30.55 | Best | tw-sh-ca-sp | −0.58 | 0.19 N m |
| | | | Worst | ca-sp | −0.24 | 4.57 N m |
| | Worst | 30.55 | Best | tw-sh-ca-sp | −0.58 | 0.19 N m |
| | | | Worst | ca-sp | −0.24 | 4.57 N m |
| Span torque | Best | 27.49 | Best | tw-ca-sp | 1.46 | 0.43 N m |
| | | | Worst | tw-sh-sp | −1.00 | 4.96 N m |
| | Worst | 30.55 | Best | ca-sp | −0.24 | 1.35 N m |
| | | | Worst | tw-sh-sp | −1.54 | 7.53 N m |

* tw = twist, sp = span, sh = shear, and ca = camber.

**Table 7.9:** Maximum actuation requirements when morphing from the loiter configuration to the high speed configuration.

| | Flight speed (m/s) | | Sequence* | | Angle of attack (deg) | Resisting force/moment |
|---|---|---|---|---|---|---|
| Twist | Best | 15.27 | Best | sp-sh-tw | 12.28 | −2.13 N m |
| | | | Worst | ca-tw | 5.37 | −0.61 N m |
| | Worst | 30.55 | Best | sp-sh-tw | 0.55 | 0.96 N m |
| | | | Worst | ca-tw | −1.54 | 4.71 N m |
| Shear section 1 | Best | 30.55 | Best | ca-sh | −1.00 | −5.67 N m |
| | | | Worst | sp-sh | 0.55 | −3.81 N m |
| | Worst | 15.27 | Best | tw-ca-sh | 8.05 | 3.15 N m |
| | | | Worst | sp-sh | 12.28 | 5.20 N m |
| Shear section 2 | Best | 30.55 | Best | ca-sh | −1.00 | −1.89 N m |
| | | | Worst | sp-sh | 0.55 | −0.77 N m |
| | Worst | 15.27 | Best | tw-sp-ca-sh | 9.05 | 0.55 N m |
| | | | Worst | sh | 11.10 | 1.50 N m |
| Shear section 3 | Best | 30.55 | Best | tw-sh | −0.24 | −0.15 N m |
| | | | Worst | ca-sh | −1.00 | −0.12 N m |
| | Worst | 15.27 | Best | tw-ca-sh | 8.05 | 0.00 N m |
| | | | Worst | sp-sh | 12.28 | 0.11 N m |
| Camber LE location 1 | Best | 30.55 | Best | tw-ca | −0.91 | −0.94 N m/m |
| | | | Worst | sp-sh-ca | 0.55 | 2.30 N m/m |
| | Worst | 15.27 | Best | tw-ca | 6.01 | 8.81 N m/m |
| | | | Worst | sp-ca | 8.56 | 11.42 N m/m |
| Camber LE location 2 | Best | 30.55 | Best | tw-ca | −0.91 | −1.13 N m/m |
| | | | Worst | sp-sh-ca | 0.55 | 4.83 N m/m |
| | Worst | 15.27 | Best | tw-ca | 6.01 | 8.50 N m/m |
| | | | Worst | sp-sh-ca | 12.28 | 13.20 N m/m |
| Camber TE location 1 | Best | 15.27 | Best | tw-sh-ca | 8.05 | 4.08 N m/m |
| | | | Worst | sp-sh-ca | 11.25 | 4.44 N m/m |
| | Worst | 30.55 | Best | tw-sh-ca | −1.12 | 11.36 N m/m |
| | | | Worst | sp-ca | −1.23 | 12.60 N m/m |
| Camber TE location 2 | Best | 15.27 | Best | tw-sh-ca | 8.05 | 3.11 N m/m |
| | | | Worst | sp-ca | 7.60 | 3.77 N m/m |
| | Worst | 30.55 | Best | tw-sh-ca | −1.12 | 8.03 N m/m |
| | | | Worst | sp-ca | −1.23 | 10.44 N m/m |
| Span shear force | Best | 30.55 | Best | tw-ca-sp | −1.71 | 2.33 N |
| | | | Worst | tw-sh-sp | −0.24 | 17.69 N |
| | Worst | 15.27 | Best | ca-sp | 5.37 | 16.31 N |
| | | | Worst | tw-sh-sp | 8.93 | 23.28 N |
| Span bending moment | Best | 30.55 | Best | sp | −0.58 | 0.19 N m |
| | | | Worst | tw-sh-sp | −0.24 | 4.57 N m |
| | Worst | 30.55 | Best | sp | −0.58 | 0.19 N m |
| | | | Worst | tw-sh-sp | −0.24 | 4.57 N m |
| Span torque | Best | 27.49 | Best | sh-sp | 1.46 | 0.43 N m |
| | | | Worst | ca-sp | −1.00 | 4.96 N m |
| | Worst | 30.55 | Best | tw-sh-sp | −0.24 | 1.35 N m |
| | | | Worst | ca-sp | −1.54 | 7.53 N m |

* tw = twist, sp = span, sh = shear, and ca = camber.

It should be noted that the maximum and minimum actuation forces and moments given in this section are based on a set of 11 flight conditions and 25 morphing sequences between configuration A and configuration B to illustrate the importance of incorporating the flight condition at which morphing is carried out in the design of morphing aircraft. No conclusions can, therefore, be drawn on the optimality of these flight conditions. Further possibilities could, for example, include morphing different mechanisms at different flight conditions or morphing partially at one flight condition and then continue morphing at a different flight condition.

As a final remark on the optimal flight condition, since the actuation requirements of the different morphing mechanisms are heavily dependent on the flight condition, a question that arises is: which flight condition should the morphing mechanism be designed for? One could argue that the worst flight condition should drive the design of the mechanism, but one could also, for example, decide to limit a certain morphing manoeuvre only to a limited set of flight conditions, thereby reducing the requirements on the morphing mechanism and potentially obtaining a more efficient morphing aircraft.

## 7.4 EFFECT OF THE SEQUENCE OF MORPHING ON THE MORPHING ACTUATION REQUIREMENTS

As introduced in Section 7.3, besides the flight condition that has already been discussed, the second parameter that affects the morphing actuation requirements is the sequence of the different morphing manoeuvres. The influence of the morphing sequence on the actuation requirements for each of the configuration changes will, first, be discussed separately in the following sections, after which conclusions will be drawn in the final section.



In principle, by allowing for, for example, partial morphing manoeuvres and alternating between different morphing mechanisms, an infinite number of morphing sequences can be found to morph from one configuration to another configuration[1]. However, in order to limit the amount of results, while still being able to draw the important conclusions, only the 24 permutations of the 4 different morphing mechanisms and 1 case of carrying out all morphing manoeuvres in parallel have been investigated, resulting in a total of 25 unique morphing sequences. Each morphing sequence has been investigated at a set of different flight conditions (i.e. the 11 flight conditions specified in Section 7.3), resulting in a total number of 275 unique morphing cases per configuration change. For the sake of brevity, only the best and worst morphing sequence at the best and worst flight condition for

[1]For example, 25% twist-25% shear-75% twist-75% shear and 25% shear-75% twist-75% shear-25% twist result in the same configuration change.

each morphing mechanism are shown and discussed.

Note that for a given morphing manoeuvre (e.g. twist morphing), any morphing manoeuvres executed before the morphing manoeuvre of interest can be interchanged, while still obtaining the same actuation requirements (e.g. camber-shear-twist is equal to shear-camber-twist, when looking at the actuation moment for twist morphing).

### 7.4.1 Morphing from the take-off configuration to the high-speed configuration

The best case and worst case actuation forces and moments for the first configuration change from the take-off configuration to the high speed configuration are given in Table 7.7. First of all, as can be seen, the actuation requirements of a morphing mechanism are heavily dependent on the morphing sequence with changes up to 500% in the actuation requirements and changes from assisting external forces to resisting external forces. This clearly illustrates the importance of accounting for the sequence of morphing in the design process of morphing aircraft.

Furthermore, as is expected, in most cases, the best and worst morphing sequences are complementary. For example, in case of twist morphing, the lowest actuation moment is obtained when both the angle of attack is highest during the twist morphing manoeuvre and the twist section is most heavily loaded, such that the aerodynamic forces provide the largest assistance to the twist morphing manoeuvre. This results in a best morphing sequence, where first the span extension is retracted and the wing is sheared aft before carrying out the twist morphing manoeuvre and a worst morphing sequence when the wing is first cambered.

However, in a few cases, the best and worst morphing sequence are actually not complementary, illustrating that in making a trade-off between different morphing sequences identifying the effect of one morphing mechanism on the actuation loads of another morphing mechanism is not necessarily a trivial task. For example, in case of shear morphing of sections 1 and 2, increasing camber through camber morphing is beneficial for the shear morphing actuation moments, while retracting the span is detrimental. Twist morphing, on the other hand, can be both beneficial (in case of a combination of span and twist morphing before shear morphing) and detrimental (in case of camber and twist morphing before shear morphing). When looking at the effect of twist morphing on shear morphing of sections 1 and 2, two effects can be identified: (i) increasing the twist angle reduces the angle of attack, which, as already illustrated in Figure 7.7, is beneficial for shearing aft, and (ii) increasing the twist angle shifts load to the twist section, reducing the loads on sections 1 and 2, which is detrimental for shearing sections 1 and 2 aft.

In case of camber morphing combined with twist morphing, the resulting net

effect is detrimental, thereby making camber morphing, followed by shear morphing the best morphing sequence for shear morphing of sections 1 and 2. On the other hand, in case of span morphing combined with twist morphing, the net effect of twist morphing is beneficial, making span morphing followed by shear morphing the worst morphing sequence. This illustrates that the effect of one morphing mechanism on the actuation requirements of another morphing mechanism is not necessarily always beneficial, or always detrimental, but might be dependent on the morphing sequence, thus, showing the importance of selecting the right morphing sequence when morphing from one configuration to another configuration.

Furthermore, it is interesting to note that for shearing of section 3, a different trade-off needs to be made: in this case, twist morphing is always beneficial, while camber morphing can be both beneficial and detrimental, illustrating that the optimal morphing sequence is not only dependent on the types of morphing and how these interact with each other, but also on the location and distribution of morphing mechanisms on the wing.

When comparing leading edge camber morphing and trailing edge camber morphing, it can be seen that in both cases, twist morphing is beneficial, since it shifts load away from the camber morphing region to the outboard section of the wing and span morphing is detrimental, since it shifts load towards the camber morphing region. However, in case of shear morphing, an interesting conflict is observed, where shear morphing is beneficial for trailing edge morphing, but detrimental for leading edge morphing. When shearing aft, an increased angle of attack is required for trim equilibrium, which for a cambered airfoil results in a shift of load towards the leading edge. This illustrates another trade-off that has to be made and, in this case, the overall lowest camber morphing actuation moments are obtained through a sequence consisting of alternating shear and camber morphing or, if the morphing mechanism allows, performing leading edge morphing and trailing edge morphing independently.



When looking at span morphing, another interesting conflict can be observed: camber morphing before span morphing results in the lowest shear force and bending moment acting on the span extension mechanism, but also in the highest torque acting on the mechanism. The camber morphing manoeuvre from the take-off configuration to the high speed configuration results in an increased lift inboard that is compensated for by a negative lift close to the wing tip. This results in a reduced shear force and bending moment, since the negative lift cancels out some of the shear force and bending moment generated by the positive lift. However, in case of the torque applied to the span extension mechanism, the negative twist angle in the take-off configuration already introduces a negative torque, so decreasing the angle of attack, and thereby the torque, only results in a more negative torque, increasing its magnitude.

As a final remark, it is interesting to note that the optimum morphing sequence for

a given morphing mechanism can be dependent on flight condition. For example, in case of shear morphing, twist morphing is beneficial for sections 1 and 2 at low velocities, while, as discussed, in case of a high velocity it is not, clearly illustrating that the effect of different morphing mechanisms on the actuation forces and moments of other morphing mechanisms is not only dependent on the morphing sequence, but also on the flight condition.

### 7.4.2 Morphing from the high speed configuration to the loiter configuration

The best case and worst case actuation forces and moments for the second morphing manoeuvre from the high speed configuration to the loiter or landing configuration are given in Table 7.8. First of all, it is interesting to note that, contrary to what one might intuitively think, in most cases for twist, shear, and camber morphing, the optimum morphing sequence when morphing from the high speed configuration to the loiter configuration is identical to the optimum morphing sequence when morphing from the take-off configuration to the high speed configuration, even though the direction of the morphing manoeuvres is inverted. However, when looking at, for example, twist morphing, retracting the span extension and shearing the wing aft is beneficial for increasing twist, as explained in Section 7.4.1. Consequently, increasing the wing span and shearing the wing forward is beneficial for decreasing twist. Therefore, when morphing from the high speed configuration to the loiter configuration, and thus decreasing the twist angle, first increasing the wing span and shearing the wing forward reduces the twist actuation moments. As a consequence,the same optimal morphing sequence is obtained, as was already obtained for the configuration change from the take-off configuration to the high speed configuration: performing shear morphing and span morphing before the twist morphing manoeuvre.

In case of span morphing, however, similar to what has already been observed for the optimal flight conditions, the opposite holds. While the actuation loads of twist, shear, and camber morphing are dependent on the direction and magnitude of the external loads, the actuation loads of the span extension mechanism are only dependent on the magnitude of the external loads. For example, in case of the shear force acting on the span extension mechanism, camber morphing is beneficial when morphing from the take-off configuration to the high speed configuration (i.e. increasing camber), since it shifts lift inboard away from the span extension mechanism, but is detrimental when morphing from the high-speed configuration to the loiter configuration (i.e. decreasing camber). Therefore, morphing manoeuvres that are beneficial for span morphing when morphing from the take-off configuration to the high speed configuration are detrimental when morphing from the high speed configuration to the loiter configuration, and vice versa.

Interestingly, when looking at the actuation moments for shear morphing of section 2, span morphing is both beneficial (i.e. in combination with twist and camber morphing) and detrimental (i.e. when only morphing the span). This can be explained by a number of conflicting effects of extending the wing span on the shear morphing actuation requirements of section 2: (i) an increase in span increases the size of section 2, which increases both the lift acting on section 2 (which assists in shearing the wing forward) and drag acting on section 2 (which resists the shearing manoeuvre), (ii) an increase in span also reduces both the lift (since the wing surface area increases) and drag acting on section 2 (since the aspect ratio of the wing increases), and, finally, (iii) an increase in span reduces the angle of attack, thereby reducing the component of lift that assists shearing and increasing the component of drag that resists shearing. As a consequence, depending on the wing geometry at the start of the morphing manoeuvre, the net effect might be positive (in combination with twist and camber morphing) or negative (when only morphing the span), once again illustrating that the effect of one morphing mechanism on the actuation requirements of another morphing mechanism are heavily dependent on the morphing sequence, and, therefore, the morphing sequence should be accounted for in the design process of morphing aircraft.

### 7.4.3 MORPHING FROM THE LOITER CONFIGURATION TO THE HIGH SPEED CONFIGURATION

Finally, the best case and worst case actuation forces and moments for the fourth morphing manoeuvre from the loiter configuration to the high speed configuration are given in Table 7.9. As can be seen and is to be expected, the best and worst morphing sequences that are found when morphing from the loiter configuration to the high speed configuration are, in most cases, equal to the best and worst morphing sequences when morphing from the take-off configuration to the high speed configuration, since the morphing manoeuvres are similar.



However, it is interesting to compare this morphing manoeuvre from the loiter configuration to the high speed configuration to its inverse manoeuvre from the high speed configuration back to the loiter configuration. In case of shear, twist, and camber morphing, the best and worst morphing sequences remain similar. Therefore, once the optimum morphing sequence from the high speed configuration to the loiter configuration has been identified, one would want to select the same morphing sequence for the inverse morphing manoeuvre. However, as already explained in Section 7.4.2, in case of span morphing, the best and worst morphing sequences are actually inverted, so one would want to select the inverse morphing sequence when the inverse morphing manoeuvre is carried out. Therefore, irrespective of whether a different flight condition is chosen for a morphing manoeuvre and its inverse morphing manoeuvre, a different trade-off will

have to be made to obtain the optimal morphing sequence for both the morphing manoeuvre and its inverse morphing manoeuvre.

### 7.4.4 Conclusion on the influence of morphing sequence

When investigating the influence of the morphing sequence on the morphing actuation forces and moments, several important conclusions can be drawn:

- Actuation forces and moments are dependent on the morphing sequence with changes up to an order of magnitude including changes from assisting external forces to resisting external forces.
- When comparing the best and worst morphing sequences among the different mechanisms, it is clear that no obvious best morphing sequence can be identified and a trade-off will have to be made, depending on, for example, the actuation mechanism, actuator power limits, or UAV thrust limits.
- Depending on the type of morphing mechanism, the optimum morphing sequence might either invert or remain the same when inverting the morphing manoeuvre, illustrating the need for a different trade-off when morphing from configuration A to configuration B, as compared to morphing from configuration B to configuration A.
- The optimum morphing sequence for a specific type of morphing is dependent on the location and distribution of the morphing mechanism(s) on the wing. Consequently, when a the morphing type is split among different morphing mechanisms on the wing, the optimum sequence for one mechanism might actually be detrimental for another mechanism of the same morphing type at a different location on the wing.
- The optimum morphing sequence is dependent on the flight condition.

The possible morphing sequences investigated in this section are only a limited set of 25 morphing sequences between configuration A and configuration B to illustrate the importance of the morphing sequence on the actuation forces and moments of the different morphing manoeuvres. Further possibilities could, for example, include the possibility to alternate different morphing mechanisms, where instead of morphing from configuration A to configuration B in one step, one first morphs to an intermediate configuration.

As a final remark, when designing a morphing controller to morph from one configuration to another configuration, one could, for example, decide to limit a certain morphing manoeuvre to a specific morphing sequence or a limited set of morphing

sequences, avoiding the worst morphing sequences for a specific morphing manoeuvre, thereby reducing the actuation requirements and potentially obtaining a more efficient morphing aircraft.

## 7.5 IMPACT ON THE DESIGN OF MORPHING AIRCRAFT

As can be concluded from the previous sections, the flight condition and morphing sequence have a significant influence on the actuation requirements of a morphing manoeuvre. This shows the importance of accounting for these in the design and development of a morphing aircraft and corresponding morphing controller. Based on these conclusions, this section highlights some of the choices to be made and questions to be answered when designing a morphing aircraft and corresponding morphing controller for operating the aircraft to illustrate the possible impact of these conclusions on the design process of a morphing aircraft.

When designing a morphing aircraft with multiple morphing mechanisms, the corresponding optimal flight conditions and morphing sequences for different morphing manoeuvres will probably be different and, as already concluded, a trade-off will have to be made to identify the final morphing sequence and flight condition(s) at which a configuration change is carried out. As a first step in identifying the possible final morphing sequence and flight condition(s) for a given configuration change, several limitations should be accounted for and several parameters should be determined:

- The actuator limits of the morphing mechanisms, possibly limiting morphing manoeuvres to a range of flight conditions or a set of morphing sequences.
- The thrust and flight envelope limitations of the aircraft limiting the range of flight conditions that can be flown in a certain configuration.
- The range of desired morphing configurations: should all intermediate configurations be possible or is a limited set of configurations sufficient?
- The range of flight conditions at which morphing is allowed: should morphing be possible at all flight conditions between flight phase A and flight phase B or can this be limited to a range of flight conditions?
- Do the morphing mechanisms have a locking mechanism carrying the external loads while not morphing or should these be carried by the actuators at all times?
- Do all morphing manoeuvres require energy or are some morphing manoeuvres assisted by external forces across a range of morphing sequences and flight conditions, providing a possible trade-off by allowing an increase

in actuation requirements of these manoeuvres to reduce the actuation requirements of other manoeuvres?

- How sensitive is each morphing mechanism to a change of configuration of the other morphing mechanisms, i.e. how sensitive is a morphing mechanism to a change in morphing sequence?

Once these limitations have been accounted for and these questions have been answered, a first selection of possible morphing sequences and corresponding flight conditions can be made for each configuration change in the flight mission. At this stage, two possible outcomes can be obtained: (i) a set of feasible flight conditions and morphing sequences is found or (ii) no feasible flight condition(s) and morphing sequence(s) are found, resulting in an infeasible design.

When a set of feasible flight conditions and morphing sequences is found, the next step is to select the flight condition(s) and morphing sequence at which a configuration change is carried out. This requires the definition of an objective weighing the actuation requirements of the different morphing mechanisms on, for example, their margin of safety in order to be able to make a trade-off and find the final morphing sequence and corresponding flight condition(s).

On the other hand, when no feasible flight condition and morphing sequence are found for a specific configuration change, compromises will have to be sought. In this case, some possibilities for compromise to consider are:

- Do all morphing mechanisms on the wing provide sufficient benefits to justify their presence on the wing?
- Is it possible to change the layout of the morphing mechanism or change the actuator to increase the resulting actuation forces and moments, possible at the cost of reducing the stroke or bandwidth of the mechanism, while still justifying the presence of the mechanism?
- Can the infeasible morphing mechanism be interchanged for a morphing mechanism of a different morphing type with lower actuation requirements? For example, both twist and camber morphing can be used to optimise the lift distribution over the wing and can, therefore, possible be interchanged.
- Is the full range of morphing deformations required at all flight conditions or in all morphing configurations? One could, for example, decide to limit the morphing capabilities of specific concepts to a range of flight conditions or a set of morphing sequences to reduce the actuation requirements.

One question, that needs to be answered and might limit some of the choices, is: what range of flight conditions and what set of morphing sequences should

the morphing mechanisms be designed for as a worst case scenario? Depending on the choices made a this stage, a new set of feasibility constraints might have to be derived for the morphing mechanisms of the wing and a new iteration of the two-step morphing optimisation approach might be necessary to update the optimal morphing solution.

To conclude, unfortunately, answering these questions and finding these limitations is very case specific, so it is difficult to define a set of general design guidelines when designing a morphing aircraft and its corresponding morphing controller. This illustrates that the challenge of designing a morphing aircraft does not stop with designing a morphing mechanism, but requires a systems level approach, where flight condition and morphing sequence are an integral part of the design process.

## 7.6 SYNOPSIS

In this chapter, the two-step morphing optimisation appproach, introduced in Section 5.4, has been applied to the morphing optimisation of a wing based on the EU FP7 CHANGE wing designed for a 25 kg UAV. Based on the optimised morphing configurations for the different flight phases, the effect of flight condition and sequence of morphing manoeuvres on the actuation requirements of the different morphing mechanisms has been investigated to illustrate their importance in the design process of a morphing aircraft.

- The morphing optimisations clearly show the benefits of the two-step morphing approach by separating the concept-specific limitations from the generic morphing optimisation problem. In the first step, the wing is equipped with 7 morphing mechanisms, distributed over 4 types of morphing (camber, span, twist, and shear/sweep), thereby defining the feasibility constraints for the generic morphing optimisation problem, after which the optimal morphing parameters for the different flight phases are determined using the generic morphing optimisation framework in the second step.

- The optimised morphing wing shows an increase in range in the high speed flight phase of 23% over an equivalent fixed wing design, while maintaining endurance in loiter, thereby illustrating the potential benefits of integrating morphing mechanisms on a UAV.

- Both the flight condition at which a morphing manoeuvre is carried out and the morphing sequence in which the manoeuvres are carried out have a significant influence on the actuation requirements of the morphing mechanisms with changes up to an order of magnitude, illustrating the need to

incorporate the choice of morphing flight condition and morphing sequence in the design process of a morphing aircraft.

- It was shown that the optimal morphing flight condition and sequence is dependent on the morphing mechanism and its location on the wing and is not necessarily the same for all morphing mechanisms. Therefore, a trade-off is required to obtain the optimal morphing flight condition and sequence on a systems level.
- In designing a morphing aircraft, a different trade-off will have to be made for the optimal morphing sequence and flight condition(s) of each configuration change since the effect of one morphing manoeuvre on the actuation requirements of another morphing manoeuvre is dependent on the morphing configuration and can include a combination of beneficial and detrimental effects, resulting in a positive influence in some cases and a negative influence in other cases.
- Depending on the type of morphing mechanism, the optimum morphing sequence and flight condition might either change or remain the same when inverting the morphing manoeuvre, illustrating the need for a different trade-off when morphing from configuration A to configuration B, as compared to morphing from configuration B to configuration A.

In conclusion, the results shown in this chapter illustrate that the challenge of designing a morphing aircraft does not stop with designing a morphing mechanism, but requires a systems level approach where flight condition and morphing sequence are an integral part of the design process.

*The man who has no imagination has no wings.*
**Muhammad Ali**

# 8

# AEROELASTIC TAILORING OF THE COMMON RESEARCH MODEL

In order to investigate the potential benefits of aeroelastic tailoring for the design of wing structures, the aeroelastic analysis and optimisation framework presented in Part I of this dissertation is applied to the design of a wing structure for the NASA Common Research Model (CRM). After discussing the potential benefits of aeroelastic tailoring separately, trailing edge camber morphing devices are installed on the CRM to investigate the potential benefits of combining aeroelastic tailoring and morphing.

This chapter consists of eight sections. The first two sections present the properties of the CRM and the corresponding optimisation setup used for the different design studies. Four design studies have been carried out to address the influence of different parameters on the design of aeroelastically tailored wings: (i) a "conventional" weight minimisation with a fixed jig shape under static loads, as presented in Section 8.3, (ii) a weight minimisation with a free jig twist distribution to investigate the influence of the jig shape, as presented in Section 8.4, (iii) a weight minimisation with a free jig twist distribution under a combination of static loads and discrete gust loads to investigate the influence of discrete gust loads, as presented in Section 8.5, and (iv) a weight minimisation with a free jig twist distribution and manoeuvre load alleviation by means of trailing edge camber morphing devices to investigate the combined benefits of aeroelastic tailoring and morphing.

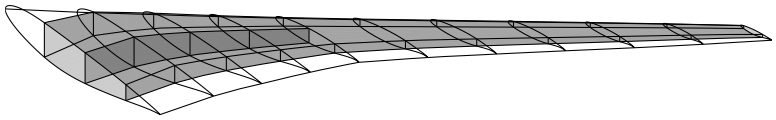

**Figure 8.1:** CRM Wing geometry.

**Table 8.1:** Wing box properties.

| Spar locations | | | |
|---|---|---|---|
| Spanwise location | Front | Middle | Rear |
| 0.00 m | 25.5% chord | 51.6% chord | 77.7% chord |
| 2.94 m | 12.0% chord | 41.8% chord | 71.5% chord |
| 10.87 m | 9.2% chord | 40.0% chord | 70.9% chord |
| 29.38 m | 10.0% chord | - | 70.2% chord |

Based on the conclusions drawn from these design studies, Section 8.7 presents some general insights for the design of aircraft wings highlighting some important observations that have been made and putting these into perspective. Finally, a brief synopsis is given in Section 8.8.

## 8.1 MODEL DESCRIPTION

In order to assess the use of the aeroelastic optimisation framework for conceptual design and assess the potential benefits of aeroelastic tailoring, the aeroelastic optimisation framework is applied to the stiffness and thickness optimisation of the NASA Common Research Model (CRM)[1] designed by NASA as a contemporary transonic supercritical wing to be used for the fourth AIAA CFD Drag Prediction Workshop[2]. The corresponding wing geometry is shown in Figure 8.1. The aircraft has a wing span of 58.9 m, leading edge sweep of 37.0 deg, and a wing surface area of 383.7 $m^2$.

The wing planform and wing box dimensions are given in Figure 8.2a and Table 8.1. The beam reference axis is placed at 46% chord at the wing root and varies linearly to 35% chord at the first kink in the wingbox at 2.94 m, after which the chordwise position of the beam reference axis is kept constant at 35% chord. The corresponding spanwise twist distribution is given in Figure 8.3a. The aircraft mass excluding the wing and any non-structural masses on the wing is 130 202 kg, distributed among the different aircraft components according to Table 8.2. The wing has two ailerons, as shown in Figure 8.2a and defined in Table 8.3.

[1]For more information on the NASA Common Research Model see (Vassberg et al., 2008) and: `https://commonresearchmodel.larc.nasa.gov/`

[2]4th AIAA CFD Drag Prediction Workshop; San Antonio, TX, USA; June 20-21, 2009

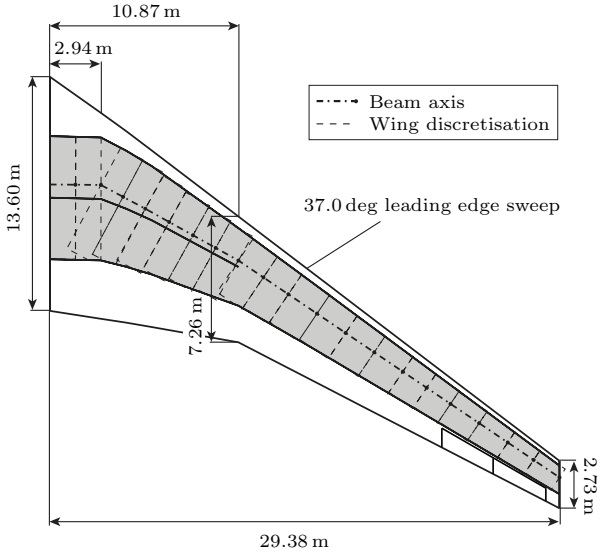


**(a)** Wing planform.

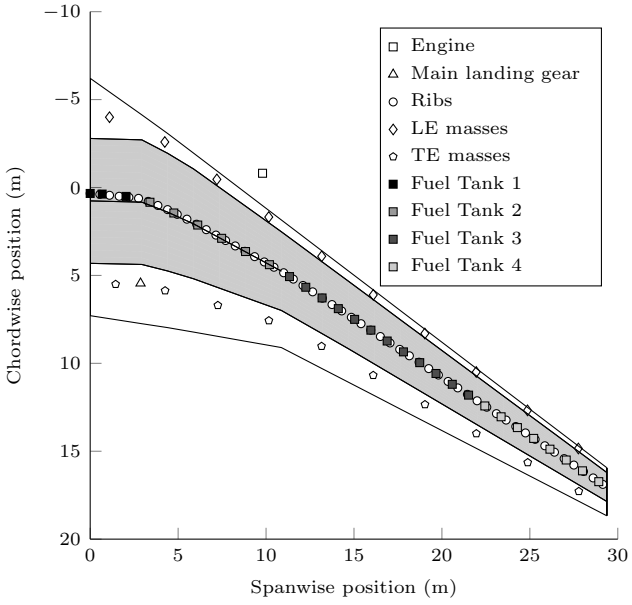


**(b)** Non-structural mass locations.

**Figure 8.2:** CRM wing properties.

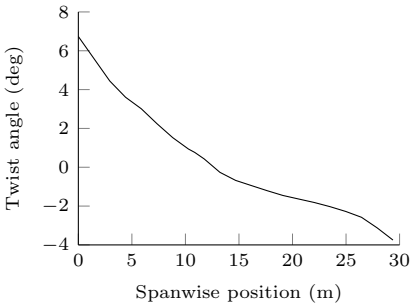


**(a)** Twist distribution of the cruise shape.

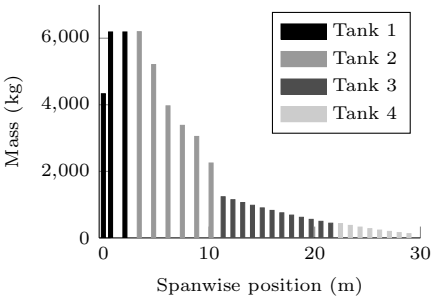


**(b)** Fuel mass distribution.

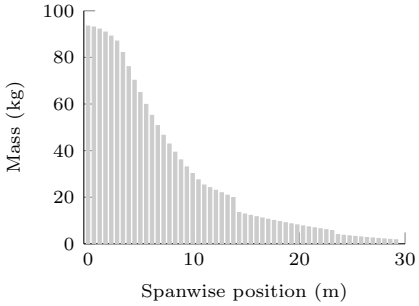


**(c)** Rib mass distribution.

**Figure 8.3:** Twist distribution and rib and fuel mass distribution of the CRM.

**Table 8.2:** CRM aircraft mass excluding the wing. (Source: Klimmek (2014))

| | Mass |
|---|---|
| Fuselage | 25 157 kg |
| Horizontal tail plane | 2267 kg |
| Vertical tail plane | 1564 kg |
| Nose landing gear | 1560 kg |
| Systems | 44 200 kg |
| Passengers | 25 194 kg |
| Payload | 30 260 kg |
| Total | 130 202 kg |

**Table 8.3:** Aileron locations. (Source: Klimmek (2014))

| Spanwise location | Chordwise hinge location |
|---|---|
| 22.04 - 24.97 m (75% - 85% span) | 75% chord |
| 24.97 - 27.91 m (85% - 95% span) | 75% chord |

**Table 8.4:** Non-structural masses on the wing.

| | Mass | $x$-location | $y$-location | $z$-location |
|---|---|---|---|---|
| Engine | 9730 kg | −0.81 m | 9.80 m | −1.87 m |
| Main landing gear | 4810 kg | 5.45 m | 2.86 m | 0.24 m |
| Leading edge mass 1 | 145 kg | −4.00 m | 1.10 m | 0.73 m |
| Leading edge mass 2 | 145 kg | −2.59 m | 4.24 m | 0.80 m |
| Leading edge mass 3 | 145 kg | −0.46 m | 7.20 m | 0.76 m |
| Leading edge mass 4 | 145 kg | 1.68 m | 10.15 m | 0.72 m |
| Leading edge mass 5 | 145 kg | 3.91 m | 13.16 m | 0.69 m |
| Leading edge mass 6 | 145 kg | 6.11 m | 16.10 m | 0.68 m |
| Leading edge mass 7 | 145 kg | 8.30 m | 19.03 m | 0.68 m |
| Leading edge mass 8 | 109 kg | 10.49 m | 21.95 m | 0.68 m |
| Leading edge mass 9 | 109 kg | 12.67 m | 24.87 m | 0.68 m |
| Leading edge mass 10 | 109 kg | 14.84 m | 27.76 m | 0.66 m |
| Trailing edge mass 1 | 381 kg | 5.50 m | 1.45 m | −0.07 m |
| Trailing edge mass 2 | 381 kg | 5.87 m | 4.26 m | 0.22 m |
| Trailing edge mass 3 | 381 kg | 6.70 m | 7.26 m | 0.45 m |
| Trailing edge mass 4 | 381 kg | 7.57 m | 10.16 m | 0.59 m |
| Trailing edge mass 5 | 381 kg | 9.03 m | 13.16 m | 0.68 m |
| Trailing edge mass 6 | 381 kg | 10.68 m | 16.09 m | 0.70 m |
| Trailing edge mass 7 | 381 kg | 12.34 m | 19.04 m | 0.72 m |
| Trailing edge mass 8 | 64 kg | 13.99 m | 21.96 m | 0.70 m |
| Trailing edge mass 9 | 64 kg | 15.64 m | 24.88 m | 0.70 m |
| Trailing edge mass 10 | 64 kg | 17.28 m | 27.78 m | 0.70 m |

**Table 8.5:** Fuel mass distribution.

| Tank ID | Max. fuel mass | Spanwise location |
|---|---|---|
| 1 | 16 700 kg | 0 - 2.93 m |
| 2 | 24 050 kg | 2.93 - 10.87 m |
| 3 | 9705 kg | 10.87 - 22.00 m |
| 4 | 2125 kg | 22.00 - 29.38 m |

The wing has 54 equally spaced ribs with a rib spacing of 0.55 m that are taken into account as concentrated masses to account for their effect on the wing mass distribution. The resulting rib mass distribution is given in Figure 8.3c. The stiffening effect of the ribs on the cross-section is inherently taken into account in the beam model under the assumption of a rigid cross-section. The properties of the engine, pylon, main landing gear, and leading edge and trailing edge masses are given in Table 8.4 and are also accounted for as concentrated masses. Finally, the wing fuel distribution is taken into account by including 4 fuel tanks, as specified by Table 8.5 and Figure 8.3b. The fuel level in the different tanks is accounted for by changing the mass of the fuel accordingly. The corresponding location of the different fuel masses is given in Figure 8.2b.

The wing top skin and bottom skin are reinforced using stringers that run along the span of the wing from root to tip. As introduced in Section 3.3, the stringers are introduced as isotropic blade stringers, where the thickness and density are

**Table 8.6:** CRM stringer data.*

| Spanwise location | Pitch | $EA$ (N m$^2$) | $mA$ (kg/m) |
|---|---|---|---|
| 0 - 12.10 m | 0.279 - 0.141 m | $7.83 \cdot 10^7$ | 3.17 |
| 12.10 - 21.45 m | 0.141 - 0.093 m | $2.35 \cdot 10^7$ | 0.95 |
| 21.45 - 29.38 m | 0.093 - 0.061 m | $1.13 \cdot 10^7$ | 0.46 |

* Source: NASA Common Research Model, `https://commonresearchmodel.larc.nasa.gov/fem-file/wingbox-fem-files/`, CRM_V15wingbox_1_noHM, accessed June 2016.

adjusted such that the blade stringers match the extensional stiffness, $EA$, and mass per unit length, $mA$, of the actual stringers. The properties of the stringers used for the CRM are given in Table 8.6.

## 8.2 ANALYSIS AND OPTIMISATION SETUP

This section presents the analysis and optimisation setup used to investigate the benefits of aeroelastic tailoring for the CRM wing. First, Section 8.2.1 presents the design loadcases for the CRM, followed by the design variables and responses in Section 8.2.2. The initial design used in the optimisation and the wing discretisation are presented in Sections 8.2.3 and 8.2.4, respectively. Finally, Section 8.2.5 presents the different design studies that have been carried out.

### 8.2.1 LOADCASES

The wing is designed for three static loadcases: one cruise condition and two manoeuvre load conditions, one symmetric pull up and one symmetric push down. The two manoeuvre loadcases were selected by NASA for the structural design of the CRM wing based on the FAR25 regulations (FAA, 2016). The resulting loadcases and corresponding fuel levels are specified in Table 8.7. In order to make a preliminary assessment of the influence of discrete gusts on the design of aircraft wings and show the integration of dynamic loadcases in the optimisations, a fourth dynamic loadcase is introduced in Section 8.5. Note that the present framework does not incorporate the effect of flight dynamics on the discrete gust loads acting on the wing, so care should be taken when interpreting the results, especially for long gust lengths. However, the model is still expected to provide a first assessment of the relative sensitivity of the wings to discrete gust loads, while showing the integration of dynamic loadcases in the optimisations. Furthermore, note that loadcase 1 and loadcase 2 are at the limit of applicability of the aerodynamic model, so care should be taken when interpreting the results. However, the model is still expected to provide a good approximation of the aeroelastic

**Table 8.7:** Loadcases.

| ID | Description | EAS | Altitude | Mach | $n_z$ | Fuel level (Tank 1-4) | | | |
|---|---|---|---|---|---|---|---|---|---|
| 1 | Cruise | 136 m/s | 11 000 m | 0.85 | 1.0 | 0.7 | 0.7 | 0.7 | 0.7 |
| 2 | Symm. pull up | 240 m/s | 3000 m | 0.85 | 2.5 | 0.8 | 0.8 | 0.8 | 0.8 |
| 3 | Symm. push down | 198 m/s | 0 m | 0.60 | −1.0 | 0.8 | 0.8 | 0.8 | 0.8 |

response of the wing and show the potential benefits of aeroelastic tailoring. In future work, a possible approach to account for the transonic aerodynamic effects in the present framework is through a defect-correction approach as introduced by Dillinger et al. (2015) and Jovanov and De Breuker (2015), thereby maintaining the efficiency of potential flow solutions when possible, while integrating the accuracy of high-fidelity CFD solutions when required. All analyses are done at a trimmed flight condition with the effects of gravity included.

### 8.2.2 Design variables and responses

In order to investigate how aeroelastic tailoring can be used to optimise the performance of a wing structure and how this is affected by various aspects, a range of optimisations was run for two cases: (i) a thickness optimisation of a composite wing with predefined laminates with $[0_{60\%}/\pm 45_{30\%}/90_{10\%}]_s$ for the top and bottom skins and a quasi-isotropic laminate for the spars, which serves as a baseline design based on conventional composite design practices, and (ii) a complete thickness and stiffness optimisation of a composite wing to investigate the potential benefits of aeroelastic tailoring for wing structural design. The 0 deg axis for the wing with predefined laminates is defined such that it aligns with the global $y$-axis for the section of the wingbox in the fuselage (0 - 2.94 m span) and aligns with the quarter chord sweep angle of 35 deg for the remainder of the wing, resulting in a spanwise stiffness distribution as illustrated in Figure 8.4 and visualised using stiffness rosettes as introduced in Section 3.2.3. In case of the spars, the 0 deg axis aligns with the dihedral of the wing. Table 8.8 shows the material properties used throughout the optimisation.



#### Objective and design variables

The objective of the optimisations is to minimise structural weight. The wing is split in 10 spanwise laminate sections: one section covering the area between the wing root and the first kink, three equally spaced sections covering the area between the first and the second kink, and six equally spaced sections covering the area between the second kink and the wing tip. Each section consists of several laminates: two laminates for the top skin in chordwise direction, two laminates for the bottom skin in chordwise direction, and one laminate for each of the spars.

**Table 8.8:** Material properties. (Source: Daniel and Ishai (2006))

| UD Carbon/Epoxy (AS4/3501-6) | |
|---|---|
| $E_{11}$ | 147.0 GPa |
| $E_{22}$ | 10.3 GPa |
| $G_{12}$ | 7.0 GPa |
| $\nu_{12}$ | 0.27 |
| $\rho$ | 1600 kg/m$^3$ |
| $X_t$ | 948.5 MPa* |
| $X_c$ | 717.6 MPa* |
| $Y_t$ | 23.7 MPa* |
| $Y_c$ | 94.8 MPa* |
| $S$ | 31.6 MPa* |

* Including knockdown factors for environmental effects (0.8), barely visible impact damage (0.65), and material scatter (0.8). (Kassapoglou, 2013)

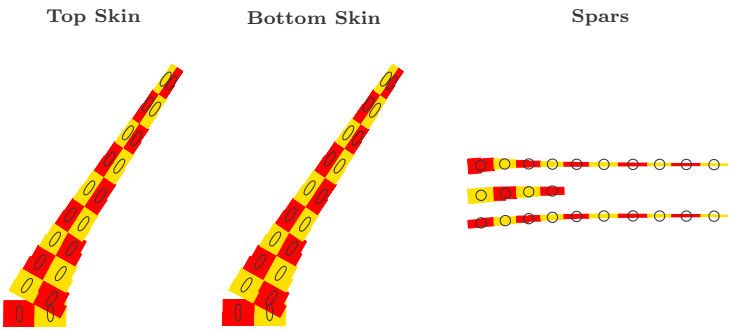


**Figure 8.4:** CRM laminate distribution and corresponding stiffness directions of the wing with predefined laminates.



The resulting laminate distribution contains 64 unique laminates and is shown in Figure 8.4.

In case of the wing with predefined laminates, the design variables are the thicknesses of the different material patches along the wing, resulting in a total number of 64 design variables. In case of the wing with unbalanced laminates, the design variables consist of eight lamination parameters, describing the in-plane and out-of-plane behaviour of the composite laminates, as introduced in Section 3.2.2, and the thicknesses of the different material patches along the wing, resulting in a total number of 576 design variables.

### CONSTRAINTS

The lamination parameters of each laminate are constrained by 6 feasibility equations, resulting in a total number of 384 lamination parameter feasibility constraints. For all optimisations, the thickness is limited between 1 mm and 50 mm.

In order to ensure a feasible final design, additional constraints are set on the aeroelastic stability, the local angle of attack, aileron effectiveness, structural strength, and buckling load. As explained in Section 5.3.3, the aeroelastic stability is governed by the eigenvalues of the state matrix, resulting in the following constraint on the real part of the eigenvalues for aeroelastic stability of the wing:

$$\Re(\lambda) \leq 0 \tag{8.1}$$

The local angle of attack is defined by the aircraft angle of attack, the initial wing twist, and the twist induced by the structural deformations, and is limited to $\pm 12$ deg to ensure attached aerodynamic flow, while still leaving design freedom to the optimiser, resulting in two constraints per aerodynamic cross-section per loadcase. The aileron effectiveness for each of the loadcases is constrained at 0.1 to ensure sufficient control authority in all flight conditions, resulting in a non-dimensional roll rate ($p \cdot s/V_\infty$) of 0.0017 per degree of aileron deflection. In cruise, this is equivalent to a roll rate of 0.46 deg/s per degree of aileron deflection. Finally, constraints are set on the Tsai-Wu strain factor and the buckling factor, as introduced in Sections 3.6 and 3.7.

In order to reduce the number of constraints that are fed to the optimiser and improve the efficiency of the optimisation, not all responses computed for aeroelastic stability, strain, and buckling are introduced as constraints in the optimisation, but a selection of the most critical responses is made. The number of aeroelastic stability constraints is reduced by only introducing the 10 most critical eigenvalues for each loadcase as constraints in the optimisation instead of all eigenvalues.

The number of strain constraints is reduced by investigating the strain responses per structural element. For each structural element, two cross-sections can be identified, one at each end of the element, and the corresponding strain distribution in each cross-section can be computed using the cross-sectional modeller, as presented in Section 3.3. In order to identify the most critical strain responses, for each laminate in a cross-section, the four most critical Tsai-Wu strain factors are identified and introduced as constraints. This results in a total number of 8 strain constraints per laminate for each structural element.

The number of buckling constraints is reduced by selecting the 8 most critical buckling panels for each laminate. As introduced in Section 3.7, the buckling factor of a buckling panel is computed under the assumption of a constant load on the panel. In order to obtain a conservative approximation of the buckling

**Table 8.9:** Number of optimisation constraints.

| Type | Number |
|---|---|
| Lamination parameter feasibility | 384 |
| Aeroelastic stability | 10 per loadcase |
| Local angle of attack | 34 per loadcase |
| Aileron effectiveness | 1 per loadcase |
| Tsai-Wu strain factor | 1024 per loadcase |
| Buckling factor | 4096 per loadcase |
| Total | 384 + 5165 per loadcase |

load, first, the loads on each cross-sectional element are obtained from the cross-sectional modeller presented in Section 3.3. Next, a buckling load is computed using the loads of each of the elements that define the buckling panel, as if they were acting along the complete panel. Finally, for each of these buckling panels, the two most critical buckling modes are selected for the two most critical loads obtained from the load distribution acting on the two ends of the panel, resulting in 8 ($2 \times 2 \times 2$) buckling constraints per buckling panel per loadcase. When selecting the 8 most critical buckling panels for each laminate, this results in a total of 64 buckling constraints per laminate per loadcase.

Based on the wing discretisation defined in Section 8.2.4, reducing the number of constraints results in a total of 384 constraints + 5165 constraints per loadcase, as given in Table 8.9.

#### OPTIMISER

The globally convergent method of moving asymptotes (GCMMA) developed by Svanberg (2002) is used as a gradient-based optimiser. Since the number of constraints is significantly larger than the number of design variables, direct sensitivities are used and all sensitivities of the objective and constraints with respect to the design variables are obtained analytically.

8

### 8.2.3 INITIAL DESIGN

Unless stated otherwise, the initial design for each of the optimisations has a thickness distribution starting with 20 mm at the wing root, increasing linearly to 40 mm at the engine location, and, finally, decreasing linearly to 10 mm at the tip for both the skin and the spars. This results in an initial wing structural mass excluding stringers of 13 700 kg for both composite wings. The stringers add 3268 kg to the wing structural mass, resulting in a total wing structural mass of 16 968 kg. The laminates of the initial design for the wings with unbalanced laminates are quasi-isotropic. Note that the initial design is a heavy, but feasible

design and not representative of an actual wing design. Therefore, the initial design should not be used as a reference to evaluate the potential of aeroelastic tailoring. The potential of aeroelastic tailoring is assessed by directly comparing the optimisation results of the wing with predefined laminates to the optimisation results of the wing with unbalanced laminates.

### 8.2.4 WING DISCRETISATION

The CRM wingbox structure is discretised using 20 structural elements, as illustrated in Figure 8.2a, resulting in two structural elements per spanwise laminate section. Each cross-section is discretised using 120 - 130 cross-sectional elements depending on the size of the spars compared to the size of the top and bottom skin. The aerodynamic panel distribution consists of 16 spanwise aerodynamic panels with a half-cosine distribution towards the wing tip and 12 chordwise aerodynamic panels with a full-cosine distribution, resulting in a total of 192 aerodynamic panels on the wing surface. The unsteady aerodynamic wake for the dynamic aeroelastic simulations is discretised using $\frac{\Delta x_w}{c} = \frac{1}{8}$ and is truncated at 10 root chords behind the wing, resulting in a total of 1280 wake panels in the unsteady wake.

### 8.2.5 OPTIMISATION CASES

In order to investigate how aeroelastic tailoring influences the different aspects that are important for the design of aircraft wings, as identified in Section 2.1, four sets of optimisations have been run:

- "Conventional" weight minimisation with a fixed jig shape under static loads and aileron effectiveness, strength, and buckling constraints.
- Weight minimisation with a free jig twist distribution under static loads and cruise twist, aileron effectiveness, strength, and buckling constraints to show the importance of the jig twist distribution for the design of aircraft wings to ensure optimal aerodynamic performance in cruise flight conditions, while taking advantage of aeroelastic tailoring in off-cruise conditions.
- Weight minimisation with a free jig twist distribution under a combination of static loads and discrete gust loads and cruise twist, aileron effectiveness, strength, and buckling constraints to illustrate the integration of dynamic loadcases in the optimisation and make a preliminary assessment of the sensitivity of the wing designs to discrete gust loads.
- Weight minimisation with a free jig twist distribution of the CRM wing with trailing edge camber morphing devices under static loads and cruise twist,

aileron effectiveness, strength, and buckling constraints to investigate the combined benefits of aeroelastic tailoring and trailing edge camber morphing for the design of aircraft wings.

Each of these optimisation cases will be discussed separately in the following sections, after which Section 8.7 presents some general insights for the design of aircraft wings based on the optimisation results.

## 8.3 AEROELASTIC TAILORING FOR MINIMUM WEIGHT

The conventional input to the design of wing structures is the flight shape in cruise conditions for optimal aerodynamic performance. An inverse method is typically used to identify the corresponding jig shape for a given wing structure, as required for manufacturing and aeroelastic analyses. As concluded from the literature overview in Section 2.1, the common approach for aeroelastic tailoring is to use this jig shape as the undeformed wing shape and optimise the wing structure for a given objective (e.g. minimum weight) without updating the jig shape during the optimisation.

Following this approach, this section shows the optimisation results for the CRM wing using the analysis and optimisation framework described in Part I to investigate the potential benefits of aeroelastic tailoring. The jig twist and deflection used in the optimisations have been identified by Klimmek (2014), and are shown in Figure 8.5.

A brief overview of the optimisation setup is given in Table 8.10, resulting in 576 design variables and 15 879 constraints, as defined in Section 8.2. As mentioned, two sets of optimisations are run: (i) a wing design with predefined laminates to act as a baseline based on conventional composite design practices and (ii) a wing design with unbalanced laminates to investigate the potential benefits of aeroelastic tailoring. In the following subsections, both wing designs are first discussed separately, after which a comparison is made between both wing designs and initial conclusions are drawn on the benefits of aeroelastic tailoring for wing structural design. All optimisation cases converged within 30 to 60 iterations. For each of the wing designs, the dynamic aeroelastic stability constraints and local angle of attack constraints are not active and are, therefore, not included in the discussion of the results. The corresponding wing structural mass, aileron effectiveness, and trim angles of attack of the optimised wing designs are given in Tables 8.11 to 8.13, respectively.

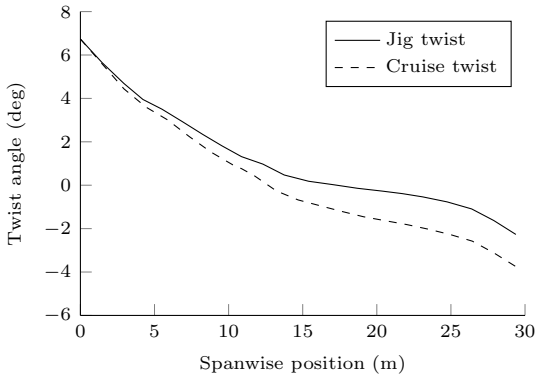


**(a)** Wing twist distribution.

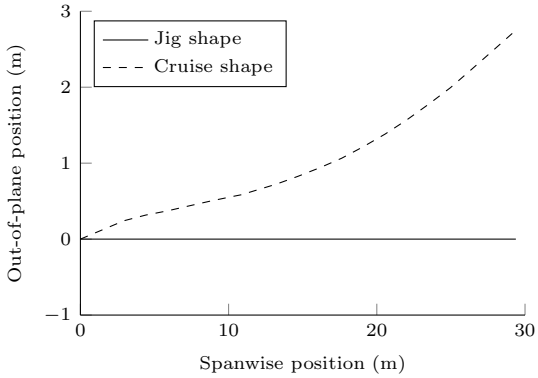


**(b)** Wing shape

**Figure 8.5:** CRM jig shape as identified by Klimmek (2014).

**Table 8.10:** Optimisation setup for the "conventional" optimisation.

| | |
|---|---|
| Objective | Minimum weight |
| Design variables | Lamination parameters<br>Laminate thickness |
| Constraints | Laminate feasibility<br>Aeroelastic stability<br>Maximum local angle of attack<br>Tsai-Wu strain failure criterion<br>Buckling |
| Optimiser | GCMMA |

**Table 8.11:** Wing structural mass of the optimised wing designs.

| Optimisation case | | | Wing structural mass excl. stringers | | |
|---|---|---|---|---|---|
| Case ID | Description (Section) | Design | Value (kg) | Diff. | Compared to |
| 1a | Fixed jig twist (8.3) | Predefined | 6877.2 | | |
| 1b | | Unbalanced | 4784.3 | −30.4% | 1a |
| 2a | Fixed jig twist excl. | Predefined | 4803.6 | −30.2% | 1a |
| 2b | ail. effectiveness (8.3) | Unbalanced | 3022.1 | −36.8% | 1b |
| 3a | Free jig twist (8.4) | Predefined | 6727.4 | −2.2% | 1a |
| 3b | | Unbalanced | 4516.5 | −5.6% | 1b |
| 4a | Free jig twist excl. | Predefined | 4720.9 | −29.8% | 3a |
| 4b | ail. effectiveness (8.4) | Unbalanced | 3349.8 | −25.8% | 3b |
| 5a | Incl. dynamic loadcases | Predefined | 6784.9 | 0.9% | 3a |
| 5b | (8.5) | Unbalanced | 4849.9 | 7.4% | 3b |
| 6a | Incl. morphing (8.6) | Predefined | 6280.9 | −6.6% | 3a |
| 6b | | Unbalanced | 3215.8 | −28.8% | 3b |
| 7a | Incl. morphing excl. | Predefined | 3116.9 | −34.0% | 4a |
| 7b | ail. effectiveness (8.6) | Unbalanced | 2346.8 | −29.9% | 4b |

**Table 8.12:** Aileron effectiveness of the optimised wing designs.

| Optimisation case | | | Aileron effectiveness | | |
|---|---|---|---|---|---|
| Case ID | Description | Design | LC 1 | LC 2 | LC 3 |
| 1a | Fixed jig twist | Predefined | 0.178 | 0.100 | 0.152 |
| 1b | | Unbalanced | 0.178 | 0.100 | 0.151 |
| 2a | Fixed jig twist excl. | Predefined | 0.146 | 0.025 | 0.101 |
| 2b | ail. effectiveness | Unbalanced | 0.066 | −0.092 | −0.005 |
| 3a | Free jig twist | Predefined | 0.178 | 0.100 | 0.152 |
| 3b | | Unbalanced | 0.179 | 0.100 | 0.151 |
| 4a | Free jig twist excl. | Predefined | 0.145 | 0.023 | 0.099 |
| 4b | ail. effectiveness | Unbalanced | 0.107 | −0.046 | 0.045 |
| 5a | Incl. dynamic loadcases | Predefined | 0.178 | 0.100 | 0.152 |
| 5b | | Unbalanced | 0.179 | 0.100 | 0.152 |
| 6a | Incl. morphing | Predefined | 0.177 | 0.100 | 0.152 |
| 6b | | Unbalanced | 0.182 | 0.100 | 0.156 |
| 7a | Incl. morphing excl. | Predefined | 0.111 | −0.058 | 0.047 |
| 7b | ail. effectiveness | Unbalanced | 0.083 | −0.100 | 0.008 |

**Table 8.13:** Trim angle of attack of the optimised wing designs.

| Optimisation case | | | Trim angle of attack (deg) | | |
|---|---|---|---|---|---|
| Case ID | Description | Design | LC 1 | LC 2 | LC 3 |
| 1a | Fixed jig twist | Predefined | 2.37 | 2.49 | −7.14 |
| 1b | | Unbalanced | 2.24 | 2.39 | −6.85 |
| 2a | Fixed jig twist excl. | Predefined | 2.52 | 2.76 | −7.10 |
| 2b | ail. effectiveness | Unbalanced | 3.12 | 3.41 | −7.27 |
| 3a | Free jig twist | Predefined | 2.54 | 2.59 | −7.00 |
| 3b | | Unbalanced | 2.44 | 2.52 | −6.67 |
| 4a | Free jig twist excl. | Predefined | 2.44 | 2.66 | −7.17 |
| 4b | ail. effectiveness | Unbalanced | 2.39 | 2.78 | −7.26 |
| 5a | Incl. dynamic loadcases | Predefined | 2.54 | 2.58 | −7.01 |
| 5b | | Unbalanced | 2.47 | 2.60 | −6.82 |
| 6a | Incl. morphing | Predefined | 2.53 | 2.49 | −4.33 |
| 6b | | Unbalanced | 2.41 | 1.00 | −3.18 |
| 7a | Incl. morphing excl. | Predefined | 2.39 | 1.27 | −3.98 |
| 7b | ail. effectiveness | Unbalanced | 2.38 | 0.77 | −5.18 |

### 8.3.1 Predefined laminate optimisation

The optimised thickness distribution of the weight optimised CRM wing with predefined laminates is shown in Figure 8.6. The corresponding stiffness distribution can be found in Figure 8.4, as introduced in Section 8.2. When looking at the thickness distribution, two wing regions can be identified: (i) the region from the wing root up to the engine location and (ii) the region from the engine location to the wing tip.

In case of the first region, as expected, a thickness increase from the wing root to the engine location is observed and the wing design is driven by the strain and buckling constraints, as can be seen in Figure 8.7. Furthermore, in chordwise direction, the leading patches are thicker than the trailing patches, thus shifting the elastic axis forward and introducing wash-out twist upon wing bending, which is beneficial for manoeuvre load alleviation[3] and, consequently, results in a reduced wing weight.

In case of the second region, the opposite is observed and the trailing patches are thicker than the leading patches, thus shifting the elastic axis aft. Furthermore, the wing design in the second region is no longer driven by strain and buckling constraints, but by the aileron effectiveness constraint that is active for loadcase 2, as can be seen in Table 8.12.

In order to investigate the effect of the aileron effectiveness constraints on the

[3] as already observed by Weisshaar (1987) and illustrated in Figure 2.1

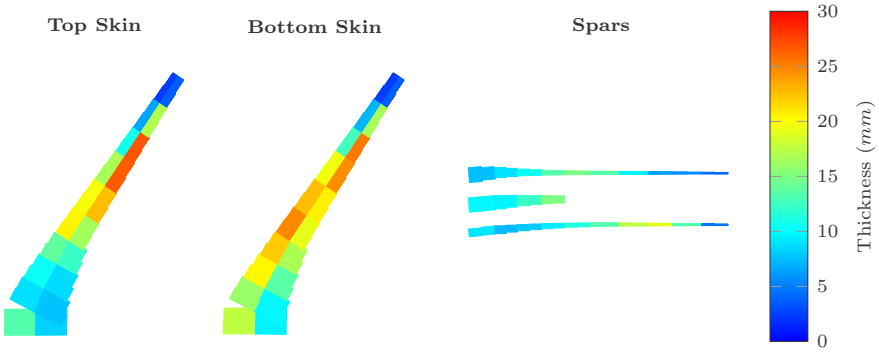


**Figure 8.6:** Thickness distribution of the optimised CRM wing with predefined laminates. (The spars are displayed front to rear with the front spar at the top.)

optimised wing design, a second optimisation without aileron effectiveness constraints has been run. The resulting thickness distribution is shown in Figure 8.8. As can be seen and is as expected, the thickness distribution shows an increase in thickness from the wing root up to the engine location, followed by a decrease in thickness towards the wing tip. Similar trends have recently also been observed by Stanford et al. (2016) for a thickness optimised aluminium wing design for the CRM under manoeuvre loads. In contrast to the optimised wing with aileron effectiveness constraints, no thickness increase close to the ailerons is observed. Furthermore, the leading patch is thicker across the entire wing and not only in the first region. Consequently, as can be seen in Figure 8.9a, showing the wing twist distribution in loadcase 2, more wash-out twist is observed in the second region, resulting in improved manoeuvre load alleviation by shifting load inboard, as shown in Figure 8.9b and a reduction in weight of 30.2%. As can be expected, in this case, the design of the complete wing is driven by the strain and buckling constraints, as can be seen in Figure 8.10.

As a final remark, it should be noted, however, that, depending on the aircraft, outboard ailerons might not always be the active control surfaces used for roll control. Spoilers or inboard ailerons might, for example, be more effective at high speeds, where outboard ailerons show reduced effectiveness or even reversal. Therefore, further investigation of the effect of aileron effectiveness constraints on the wing designs is required before pertinent conclusions can be drawn. The results, however, clearly show the importance of control effectiveness for the design of aircraft wings.

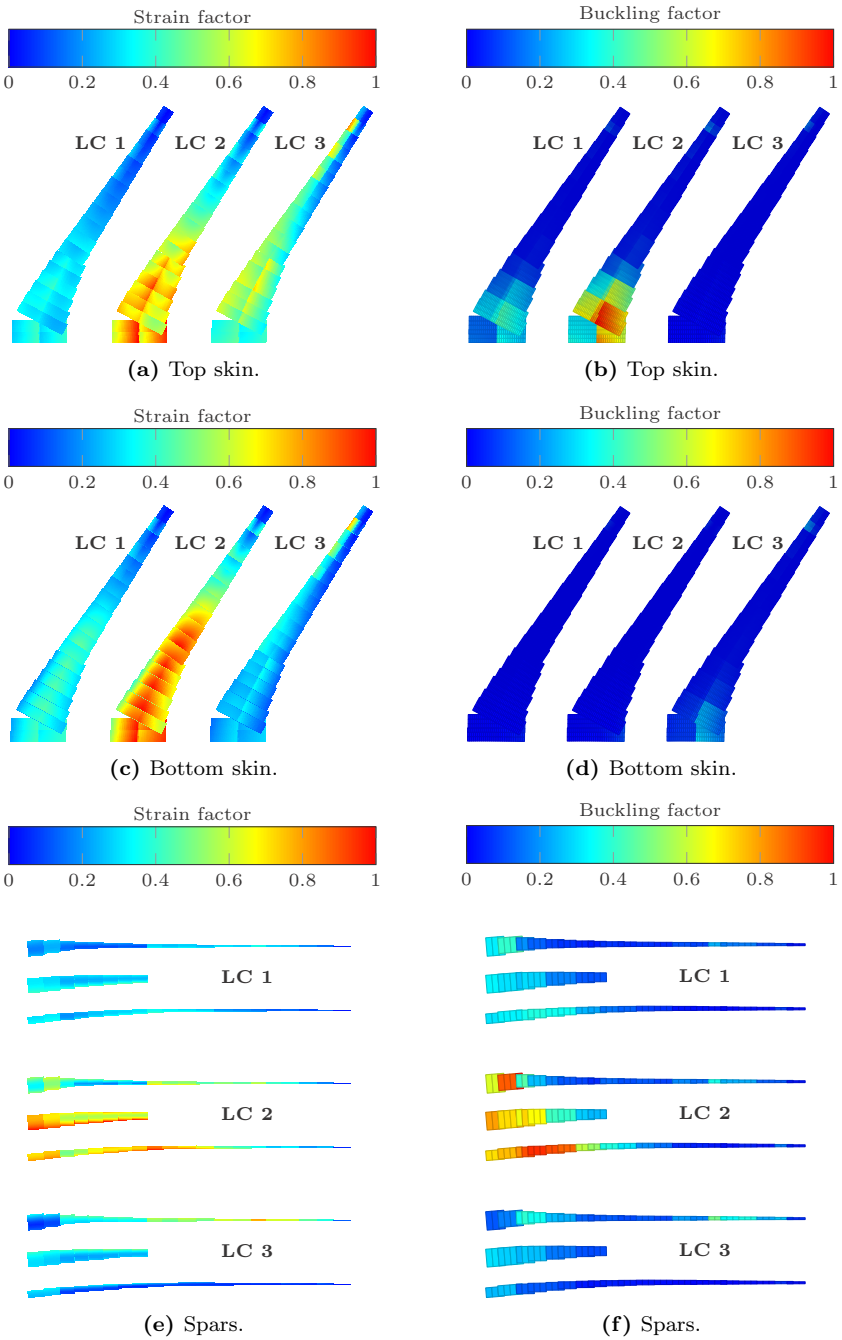


**(a)** Top skin. **(b)** Top skin.

**(c)** Bottom skin. **(d)** Bottom skin.

**(e)** Spars. **(f)** Spars.

**Figure 8.7:** Strain and buckling factor distribution of the optimised CRM wing with predefined laminates. (The spars are displayed front to rear with the front spar at the top.)

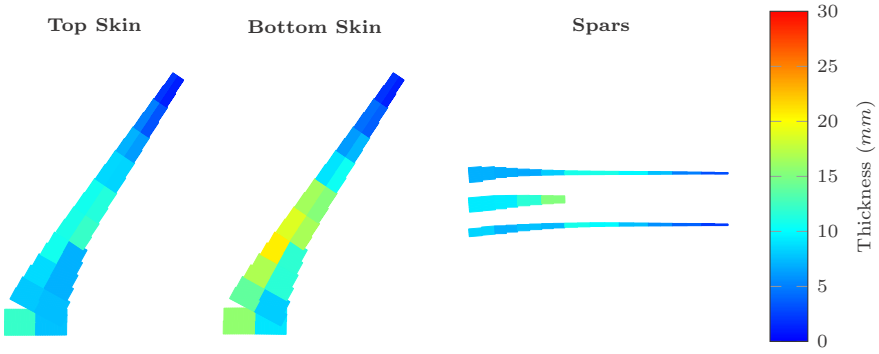


**Figure 8.8:** Thickness distribution for the optimised CRM wing with predefined laminates without aileron effectiveness constraints.

### 8.3.2 UNBALANCED LAMINATE OPTIMISATION

The optimised stiffness and thickness distributions of the unbalanced wing design are shown in Figure 8.11. The stiffness distribution has been visualised using stiffness rosettes, as introduced in Section 3.2.3. The corresponding strain and buckling factor distributions for the different loadcases are shown in Figure 8.12. Based on these results, three wing regions can be identified: (i) the buckling critical region close to the wing root, (ii) the region from the buckling critical region up to the engine location, and (iii) the region from the engine location up to the wing tip.

When comparing the buckling critical region[4] to the other wing regions, first of all, it is interesting to note that the buckling critical region, as expected, is dominated by the out-of-plane properties, resulting in pronounced optimal stiffness directions for the out-of-plane properties, while sacrificing the in-plane properties. The other two wing regions, on the other hand, are dominated by the in-plane properties that drive the global wing response and, consequently, pronounced stiffness directions are observed for the in-plane properties, while sacrificing the out-of-plane properties.

When looking at the stiffness distribution of the top skin close to the wing root, a significantly different out-of-plane stiffness is observed for the leading patch than for the trailing patch. In case of the leading patch, the buckling response is dominated by in-plane compression in loadcase 2, resulting in optimal cross-ply stiffness properties, while in case of the trailing patch, the buckling response is dominated by shear, resulting in a preferred stiffness direction resisting the diagonal shear buckling pattern. This illustrates the potential use of aeroelastic tailoring to optimise the stiffness distribution as required.

[4] the middle and rear spar and the top skin close to the wing root

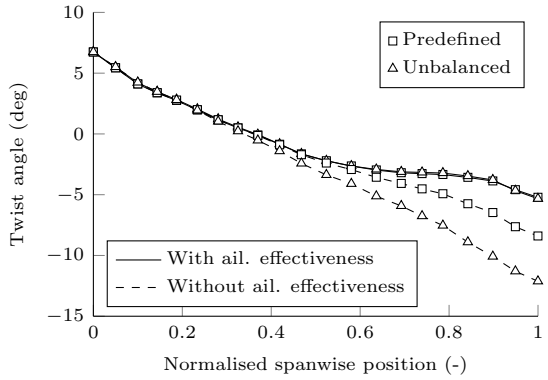


**(a)** Twist distribution.

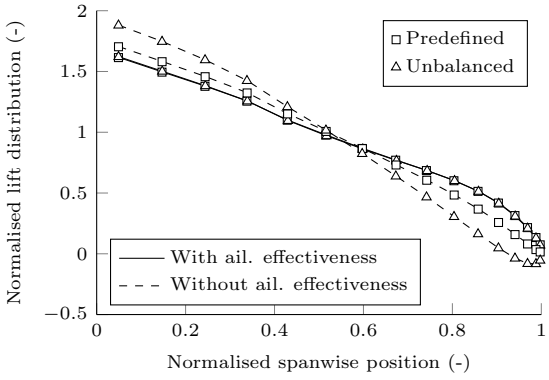


**(b)** Lift distribution.

**Figure 8.9:** Lift distribution and twist distribution for loadcase 2 for the optimised wings with unbalanced laminates and the optimised wings with predefined laminates with and without aileron effectiveness constraints.

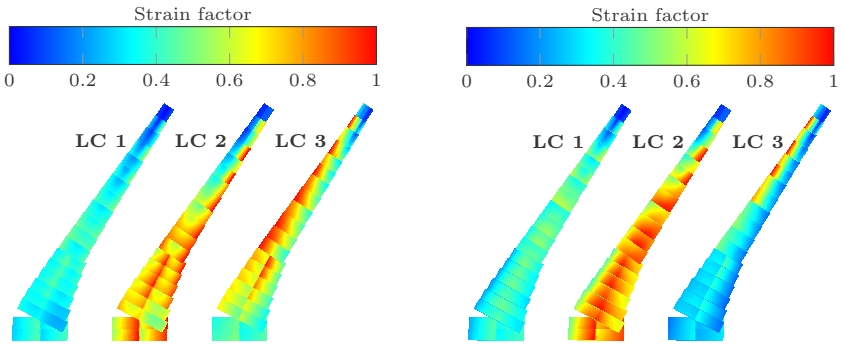


**(a)** Top skin. **(b)** Bottom skin.

**Figure 8.10:** Strain factor distribution of the optimised CRM wing with predefined laminates without aileron effectiveness constraints.

When looking at the second wing region outboard of the buckling critical region, the wing design is clearly strain driven, as can be concluded from Figure 8.12, and the in-plane stiffness is oriented along the wing axis to maximise the load carrying capabilities of the wing, thereby minimising the wing weight.

In the third wing region outboard of the engine location, the wing design with unbalanced laminates is driven by aileron effectiveness, similar to the wing design with predefined laminates. Therefore, the in-plane stiffness is oriented aft to increase the aileron effectiveness[5]. In order to investigate this in more detail, an additional optimisation without aileron effectiveness constraints has been carried out. The resulting stiffness and thickness distribution is shown in Figure 8.13.

As can be seen, when aileron effectiveness is no longer constraining the structural design, aeroelastic tailoring can be fully used for manoeuvre load alleviation by orienting the in-plane stiffness forward. This increases the wash-out twist deformation and shifts load inboard. Consequently, a weight reduction of 36.8% is obtained.

It is interesting to note that both optimised wings show a similar stiffness distribution in the buckling critical region on the top skin and in the strain critical region on the bottom skin up to the engine, indicating that, as expected, aileron effectiveness is mainly driving the wing design of the outboard wing.

When comparing the present results to the results by Stanford et al. (2016), who optimised the CRM wing by varying the number of plies using a fixed set of ply angles along the wing, as well as Stodieck et al. (2017), who optimised the CRM wing by rotating and varying the thickness of a fixed stacking sequence along the wing, several observations can be made. First, all studies show that, as expected,

[5] as already observed by Weisshaar (1987) and illustrated in Figure 2.1

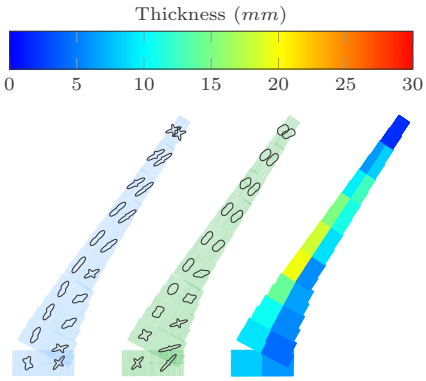


**(a)** Top skin.

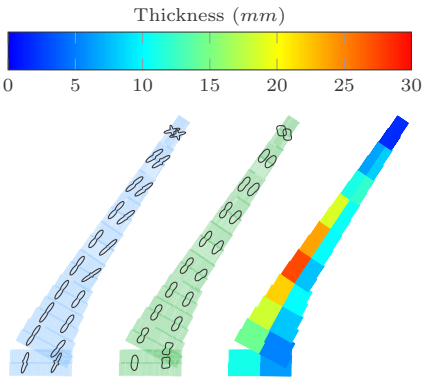


**(b)** Bottom skin.

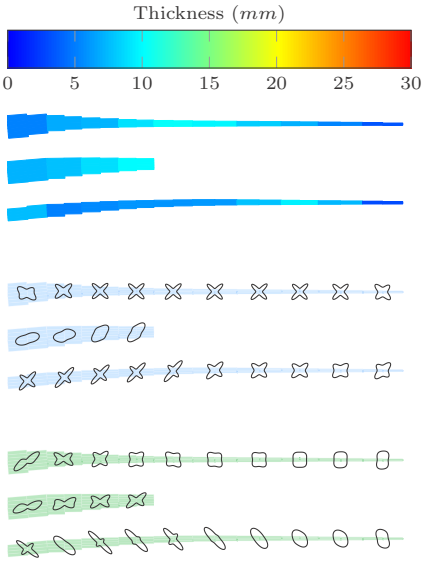


**(c)** Spars.

**Figure 8.11:** Stiffness and thickness distribution for the optimised CRM wing with unbalanced laminates. (In-plane stiffness: blue, out-of-plane stiffness: green. The spars are displayed front to rear with the front spar at the top.)

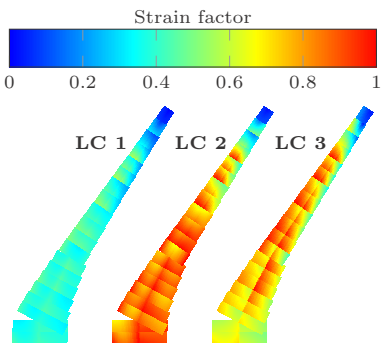


(a) Top skin.

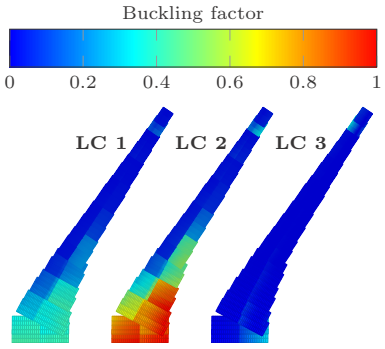


(b) Top skin.

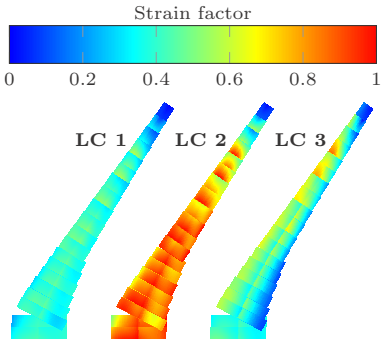


(c) Bottom skin.

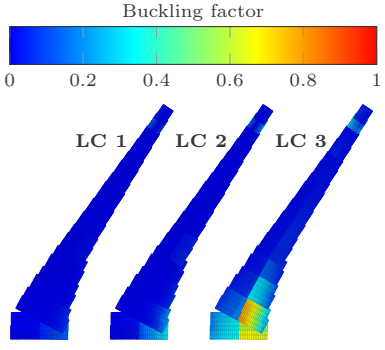


(d) Bottom skin.

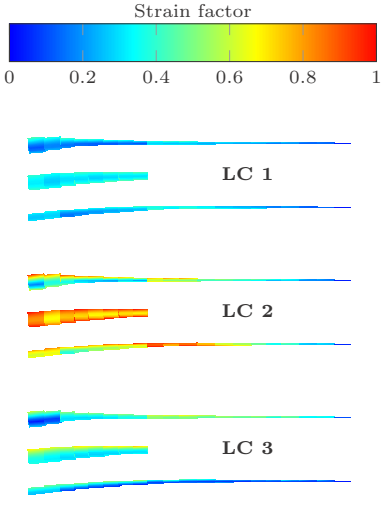


(e) Spars.

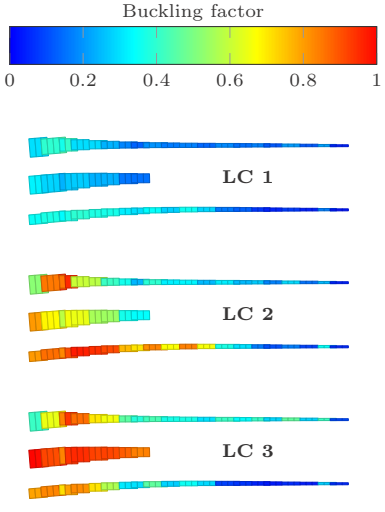


(f) Spars.

**Figure 8.12:** Strain and buckling factor distribution of the optimised CRM wing with unbalanced laminates. (The spars are displayed front to rear with the front spar at the top.)

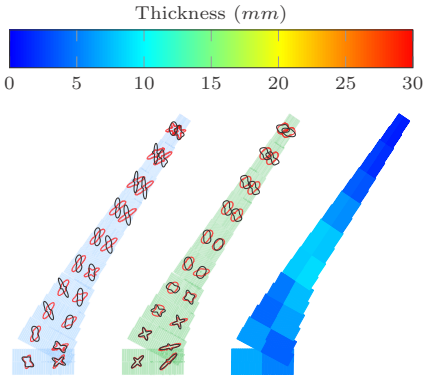


**(a)** Top skin.

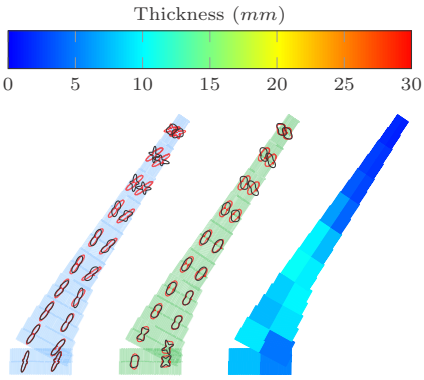


**(b)** Bottom skin.

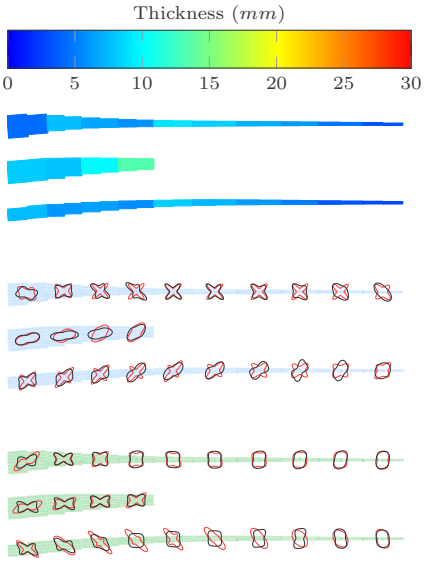


**(c)** Spars.

**Figure 8.13:** Stiffness and thickness distribution for the optimised CRM wing with unbalanced laminates without aileron effectiveness constraints. The stiffness distribution for the wing with unbalanced laminates with aileron effectiveness constraints is displayed in red for comparison. (In-plane stiffness: blue, out-of-plane stiffness: green. The spars are displayed front to rear with the front spar at the top.)

the structural weight of the wing can be reduced by orienting the primary stiffness direction of the laminate towards the leading edge when a wing design is driven by manoeuvre load alleviation.

Furthermore, excluding the aileron effectiveness constraint, both Stodieck et al. (2017) and the present results show, as expected, a bottom skin that is sized by the 2.5g manoeuvre loadcase and driven by strength constraints. However, both Stodieck et al. (2017) and Stanford et al. (2016) decided to reduce the number of stringers in the wingbox to reduce computational effort and, as a consequence, they observe a top skin that is completely driven by buckling constraints, while the present model, which includes all stringers, shows a more balanced design that is driven by a combination of strength and buckling constraints, as is to be expected in a realistic wing structure.

Finally, it is interesting to note that similar observations have been made by Stodieck et al. (2017) for the effect of the stiffness distribution on aileron effectiveness, showing reduced effectiveness when orienting the fibres towards the leading edge and increased effectiveness when orienting the fibres towards the trailing edge.

As a final remark on the present results, it should be noted that, in case of the wing with unbalanced laminates without aileron effectiveness constraints, both loadcase 2 and loadcase 3 are beyond the control reversal speed, clearly showing the importance of control effectiveness in the optimisation of aeroelastically tailored wings.

### 8.3.3 COMPARISON

Several conclusions can be drawn when comparing the wing design with unbalanced laminates including the aileron constraints to the wing design with predefined laminates including the aileron constraints. First of all, the benefits of aeroelastic tailoring can clearly be observed, resulting in a weight reduction of 30.4%. It is interesting to note that, as shown in Figure 8.14, the wing with unbalanced laminates has thicker leading patches in some regions on the wing such that more weight can be saved in other regions, resulting in a net weight reduction.



Second of all, when comparing the wing deformation and load distribution for both wing designs, as shown in Figure 8.15, it can be seen that both wing designs show a similar twist distribution for loadcase 2 under 2.5g loads, but a difference in wing deflection of 27%. In both cases, the wing twist distribution is constrained by the aileron effectiveness constraint, while wing deflection is free as long as the strain and buckling constraints are satisfied. In case of the wing with unbalanced laminates, as already observed, the twist is constrained by orienting the in-plane stiffness aft, while, in case of the wing with predefined laminates, the twist is

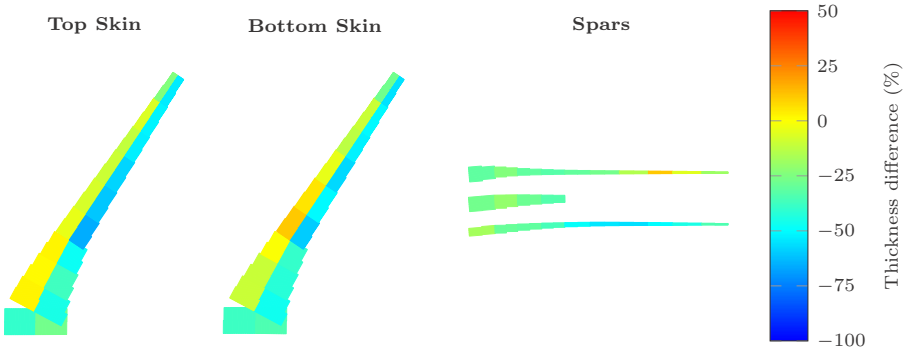


**Figure 8.14:** Thickness comparison of the optimised CRM wing with unbalanced laminates to the optimised wing with predefined laminates. (The spars are displayed front to rear with the front spar at the top.)

constrained by increasing the skin thickness of the trailing patches. Consequently, both wings have a different stiffness distribution that results in a similar twist distribution and corresponding load distribution, but a significantly different wing deflection.

Finally, when comparing the strain and buckling factor distributions of both wings shown in Figures 8.7 and 8.12, it can clearly be seen that the wing with unbalanced laminates is critical in strain and buckling over larger regions of the wing for both loadcase 2 and loadcase 3, indicating a more optimised wing design that shows more efficient load carrying capabilities.

In conclusion, when comparing the optimised wing with unbalanced laminates to the optimised wing with predefined laminates, the potential of aeroelastic tailoring to tailor the stiffness as required, and thereby optimise the wing structure for conflicting design requirements, can clearly be observed. As a result, a more optimised wing design is obtained, resulting in significant weight reductions, thereby illustrating the benefits of aeroelastic tailoring over conventional wing design approaches.



## 8.4 On the importance of the jig twist distribution for wing structural design

As identified in the literature overview presented in Section 2.1, one of the important parameters to consider in the aeroelastic design of wing structures is the jig shape of the wing, or, more specifically, the jig twist distribution. The wing dihedral has a negligible effect on the load distribution over the wing, and

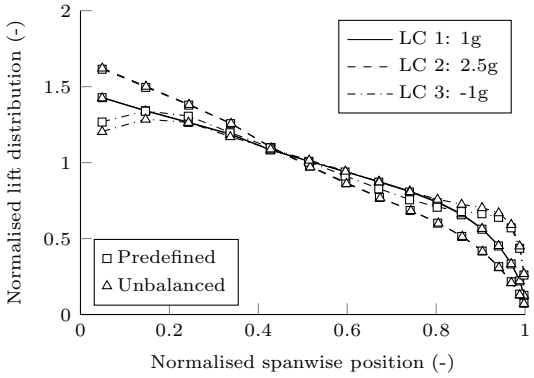


**(a)** Lift distribution.

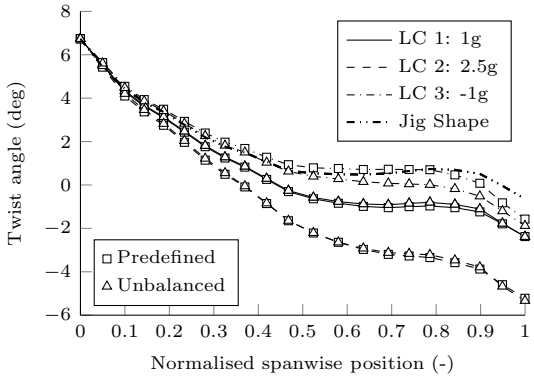


**(b)** Twist distribution.

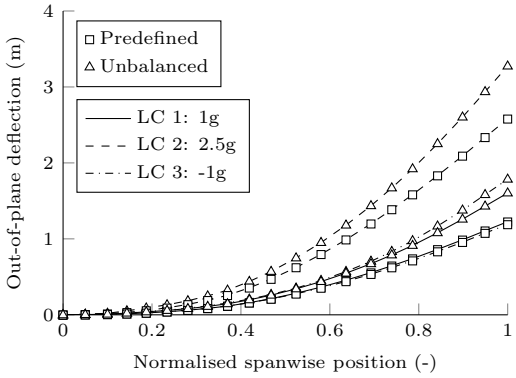


**(c)** Out-of-plane deflection. (Note that for LC 3, the negative tip deflection is displayed for clarity.)

**Figure 8.15:** Lift distribution, twist distribution, and out-of-plane deflection for the optimised wings for different loadcases.

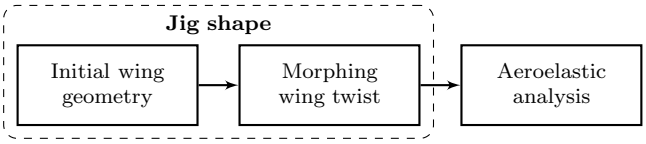


**Figure 8.16:** Schematic representation illustrating the modelling approach used to update the jig twist distribution in the aeroelastic analysis and optimisation.

consequently the aeroelastic response of the wing, and is mainly important for lateral stability of the aircraft, which would require a flight dynamic analysis to assess it. The jig twist distribution, however, can be used to modify the load distribution of the wing in order to ensure optimal aircraft performance in cruise flight conditions, while taking full advantage of aeroelastic tailoring in off-cruise conditions. Therefore, the focus in this dissertation is on the influence of the jig twist distribution on the aeroelastic response.

The remainder of this section is split in two parts. First, Section 8.4.1 presents the modelling approach used to modify the jig twist distribution and the corresponding optimisation setup, followed by a discussion of the corresponding optimisation results in Section 8.4.2.

### 8.4.1 Modelling approach and optimisation setup

In order to account for the effect of the jig twist distribution on the aeroelastic response of the wing, the aeroelastic analysis and optimisation framework and the morphing analysis and optimisation framework are combined, as illustrated in Figure 8.16. A morphing twist angle is introduced for each structural element as additional design variable, resulting in 20 additional design variables that allow the optimiser to modify the twist distribution of the wing. Optimal cruise performance is maintained by constraining the deformed wing twist distribution at cruise conditions (i.e. loadcase 1) to $\pm 0.1$ deg of the desired cruise twist distribution, which is the NASA CRM cruise flight shape. The corresponding optimisation setup is summarised in Table 8.14, resulting in a total of 596 design variables and 15 919 constraints. The final jig twist distribution can be obtained by analysing the initial wing geometry combined with morphing wing twist, but in the absence of external loads, as illustrated in Figure 8.16.

Similar to Section 8.3, two sets of optimisations have been carried out with and without aileron effectiveness constraints: (i) a wing design with predefined laminates and (ii) a wing design with unbalanced laminates.

**Table 8.14:** Optimisation setup including jig twist design variables.

| Objective | Minimum weight |
|---|---|
| Design variables | Lamination parameters<br>Laminate thickness<br>Morphing twist variables |
| Constraints | Laminate feasibility<br>Aeroelastic stability<br>Maximum local angle of attack<br>Tsai-Wu strain failure criterion<br>Buckling<br>Cruise twist distribution |
| Optimiser | GCMMA |

### 8.4.2 OPTIMISATION RESULTS

Similar to the "conventional" weight minimisations, the optimisation cases converged within 30 to 60 iterations and the dynamic aeroelastic stability constraints and local angle of attack constraints are not active and are, therefore, not included in the discussion of the results. The wing structural mass, aileron effectiveness, and trim angles of attack of the optimised wing designs are given in Tables 8.11 to 8.13 on pages 216 to 217, respectively. The jig twist distribution required for the desired wing twist at cruise conditions is shown in Figure 8.17a. The jig twist distributions obtained by Klimmek (2014) for his structural designs of the CRM is included for comparison. Similar twist distributions have, for example, also been obtained by Kenway et al. (2014) and Stodieck et al. (2017) in their designs for the CRM wing.

As can be seen, when the aileron effectiveness constraints are included in the optimisation, the same jig twist is obtained for both the optimised wing with predefined laminates and the wing with unbalanced laminates. This is caused by a combination of two effects. First of all, aileron effectiveness is mainly driven by the torsional stiffness of the wing. Therefore, both in case of the wing with predefined laminates and the wing with unbalanced laminates, a similar torsional stiffness towards the wing tip is expected, when, for a given flight condition, the aileron effectiveness constraint is active. This similar torsional stiffness is confirmed by the similar tip twist induced by an aileron deflection of 1 deg, as shown in Table 8.15. Second of all, the twist distribution of loadcase 1 is constrained to ensure optimal aerodynamic performance in cruise conditions. Therefore, under the assumption of a quasi-linear structural response, combining a similar torsional stiffness and prescribed twist distribution at cruise conditions, the same jig twist distribution is obtained for both wing designs. It should be noted, however, that the corresponding structural mass of the wing with unbalanced laminates is 32.9% lower than the structural mass of the wing with predefined laminates.

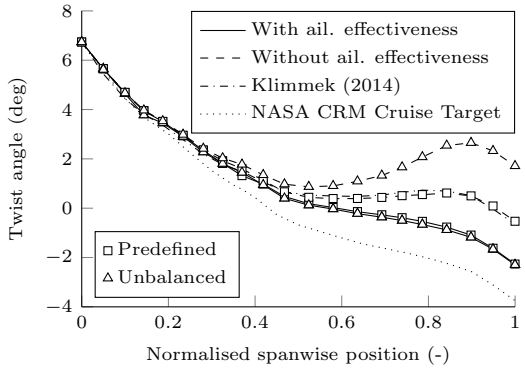


**(a)** Comparison of the jig twist between Klimmek (2014) and the optimised CRM wings including a cruise twist constraint. The cruise target shape is shown to illustrate the corresponding twist deformations.

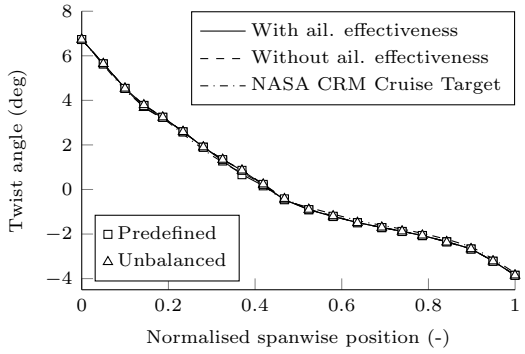


**(b)** Comparison of the twist distribution of the optimised wings in cruise flight to the target CRM twist distribution.

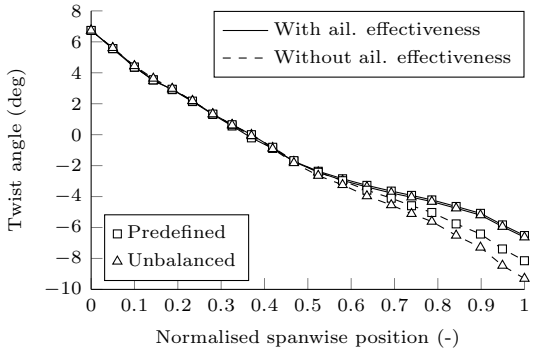


**(c)** Twist distribution of the optimised wings for loadcase 2 under 2.5g loads.

**Figure 8.17:** Twist distributions for the optimised CRM wings including a cruise twist constraint.

**Table 8.15:** Tip twist induced by an aileron deflection of 1 deg in loadcase 2.

| Case | Value |
|---|---|
| Predefined with aileron effectiveness | −0.183 deg |
| Predefined without aileron effectiveness | −0.381 deg |
| Unbalanced with aileron effectiveness | −0.180 deg |
| Unbalanced without aileron effectiveness | −0.554 deg |

When the aileron effectiveness constraints are not included in the optimisation, a significant difference in the jig twist distribution of both wing designs can be observed in Figure 8.17a, while still obtaining the same optimal twist distribution in cruise conditions, as shown in Figure 8.17b. As a result, the wing with unbalanced laminates shows significantly more wash-out in loadcase 2, as can be seen in Figure 8.17c, increasing the manoeuvre load alleviation and resulting in a root bending moment reduction of 5.1% over the wing with predefined laminates. The corresponding stiffness and thickness distributions of the wings without aileron effectiveness constraints are given in Appendix D.1.

In conclusion, Figure 8.17a, shows 5 different jig twist distributions that, with their corresponding wing structures, all result in the same optimal twist distribution at cruise conditions to ensure optimal aerodynamic performance, but show a significantly different twist distribution, and corresponding load distribution, at off-cruise conditions, illustrating the importance of the jig twist distribution for the aeroelastic analysis and design of wing structures.

Another important conclusion can be drawn when comparing the load distribution of the optimised wings with fixed jig twist, as presented in Section 8.3, to the optimised wing with free jig twist as presented in this section, shown in Figure 8.18. As can be seen, the jig twist is not only important for the aerodynamic performance in cruise conditions, but also to obtain the correct wing design loads, since changing the jig twist distribution changes the aerodynamic load distribution on the wing, and thereby the design loads for the wing.

The importance of this observation can be seen when comparing the optimised stiffness and thickness distribution of the wings with a free jig twist distribution, as shown in Figures 8.19a and 8.20c, to the optimised wing design with a fixed jig twist distribution, as presented in Section 8.3 and shown in Figures 8.6 and 8.11. For clarity, the difference in thickness between both sets of optimised wing designs is shown in Figure 8.19b for the wings with predefined laminates and in Figure 8.21 for the wings with unbalanced laminates. As can be seen, although the load distribution for the wings with free jig twist shows more manoeuvre load alleviation by shifting load inboard, resulting in a weight reduction of 2.2% for the wing with predefined laminates and 5.6% for the wing with unbalanced laminates, significant portions of the wing skins show an increased thickness, indicating increased design requirements and, more importantly, a potentially

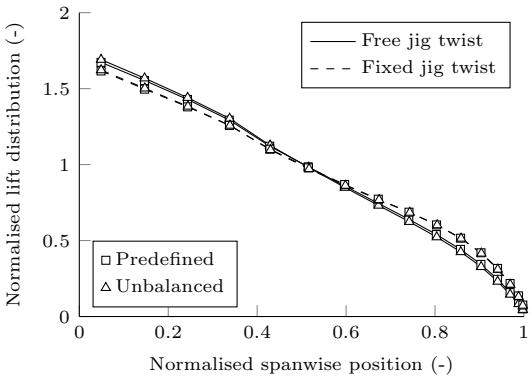


**Figure 8.18:** Comparison of the lift distribution for loadcase 2 for the optimised wings with a free jig twist distribution and a cruise twist constraint to the wings with a fixed jig twist distribution without a cruise twist constraint.

non-conservative wing structural design when the jig twist distribution is not included in the design and optimisation of wing structures.

To conclude this section on the influence of the jig twist distribution on the design of wing structures, the results clearly show the importance of the jig twist distribution, not only for optimal aerodynamic performance at cruise conditions, but also in obtaining the correct design loads. Therefore, it is paramount to include the jig twist distribution in the design of wing structures, especially when taking advantage of the increased design freedom of aeroelastic tailoring.

## 8.5 On the importance of discrete gust loads in wing structural design

The use of composite materials in the design of aircraft wings and the corresponding increase in design allowables has resulted in an increased flexibility of wing structures, making them more susceptible to dynamic loads such as discrete gusts. In order to investigate the effect of discrete gust loads on the optimisation of the NASA CRM wing structure, first, the statically optimised wing designs with a free jig twist distribution, as presented in Section 8.4, are used to identify the critical dynamic flight condition(s) and corresponding critical gust lengths. This is presented in Section 8.5.1.

Based on these critical flight condition(s) and corresponding critical gust lengths, Section 8.5.2 presents the expanded optimisation setup including dynamic loadcases that is used to find the optimal wing designs under both static and dynamic loads.

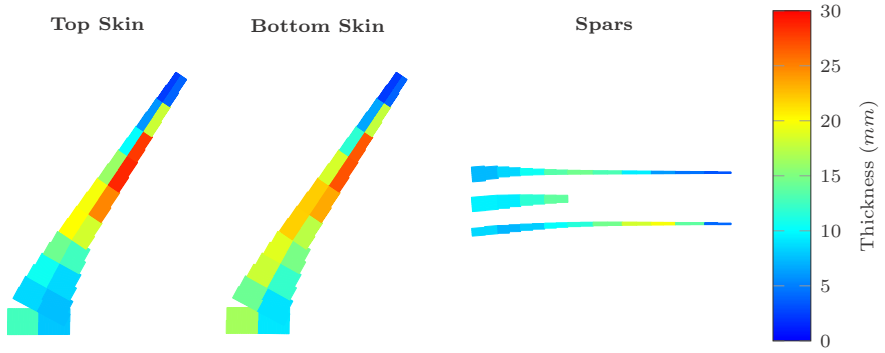


**(a)** Thickness distribution.

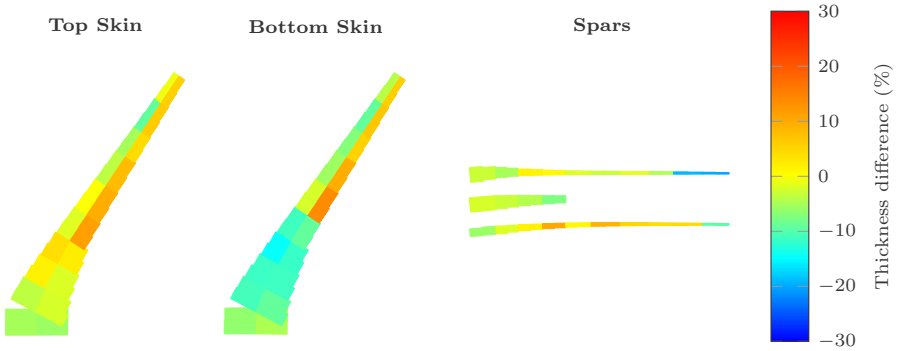


**(b)** Thickness comparison of the optimised CRM wing with predefined laminates with a free jig twist distribution and a cruise twist constraint to the wing with a fixed jig twist distribution without a cruise twist constraint.

**Figure 8.19:** Thickness distribution and thickness comparison for the optimised CRM wing with predefined laminates with a free jig twist distribution and a cruise twist constraint. (The spars are displayed front to rear with the front spar at the top.)

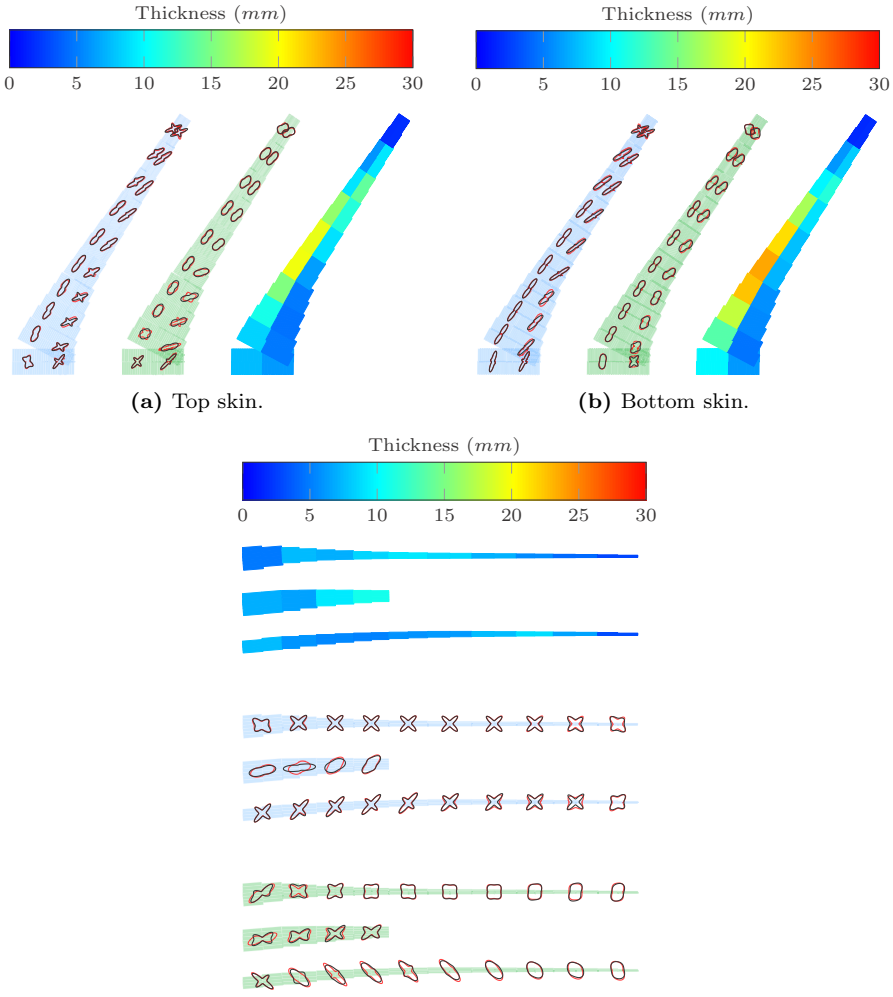


**(a)** Top skin. **(b)** Bottom skin.

**(c)** Spars.

**Figure 8.20:** Stiffness and thickness distribution for the optimised CRM wing with unbalanced laminates with a free jig twist distribution and a cruise twist constraint. The stiffness distribution for the wing with unbalanced laminates with a fixed jig twist distribution without a cruise twist constraint is displayed in red for comparison. (In-plane stiffness: blue, out-of-plane stiffness: green. The spars are displayed front to rear with the front spar at the top.)

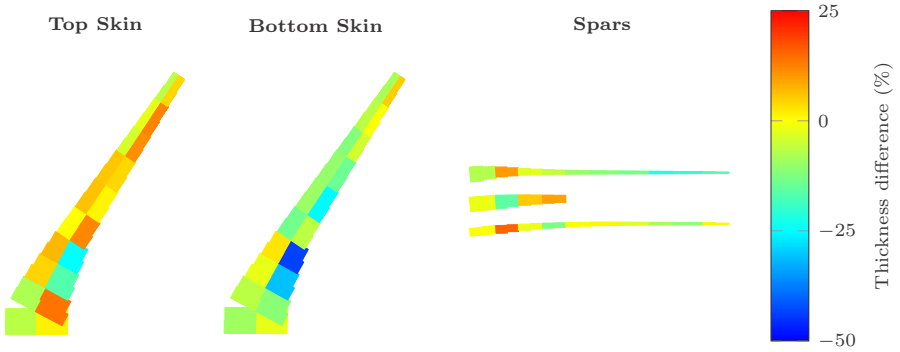


**Figure 8.21:** Thickness comparison of the optimised CRM wing with unbalanced laminates with a free jig twist distribution and a cruise twist constraint to the wing with a fixed jig twist distribution without a cruise twist constraint. (The spars are displayed front to rear with the front spar at the top.)

Finally, Section 8.5.3 presents the corresponding optimisation results, showing the influence of discrete gust loads on the design of aeroelastically tailored wings.

In the remainder of this section, for the sake of brevity, the optimised wing designs obtained under static loads only will be referred to as statically optimised wings, while the newly optimised wings including the influence of discrete gust loads will be referred to as dynamically optimised wings.

Note that, as mentioned, the present framework is limited to clamped wings only and all results in this section have been generated for a clamped wing, excluding the effects of coupled flight dynamic motions on the discrete gust loads acting on the wing. Therefore, further research is required before definitive conclusions can be drawn and care should be taken when interpreting the results. However, the model is still expected to provide a first assessment of the relative sensitivity of the wings to discrete gust loads while showing the integration of dynamic loadcases in the optimisations.

8

### 8.5.1 IDENTIFICATION OF THE CRITICAL DYNAMIC LOAD CONDITIONS

Starting from the statically optimised wings, as presented in Section 8.4, first, a set of analyses has been carried out across the flight envelope of the NASA CRM given in Figure 8.22, for a range of positive and negative discrete gusts from a gust length of 9 m to 107 m in straight, level, 1g flight, as prescribed by the CS25 regulations and already discussed in Section 5.3.4. The required aircraft data to obtain the gust amplitudes is given in Table 8.16. First of all, for the present CRM designs, no negative gusts were critical in any of the flight conditions and,

**Table 8.16:** CRM aircraft data.

| Parameter | Value |
|---|---|
| Maximum operating altitude | 13 140 m |
| Maximum zero fuel weight | 197 680 kg |
| Maximum landing weight | 208 200 kg |
| Maximum take-off weight | 302 850 kg |

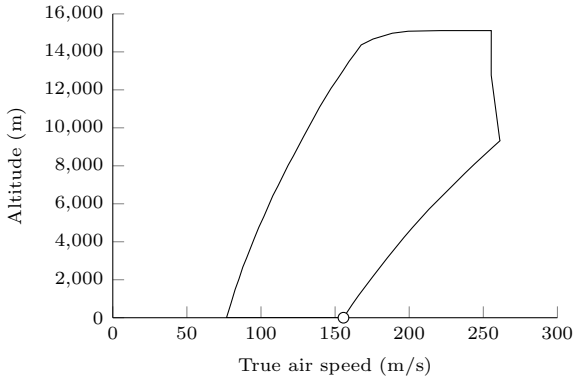


**Figure 8.22:** Flight envelope of the NASA CRM based on the EASA CS25 regulations (EASA, 2016). The marker indicates the critical flight condition for discrete gust loads.

therefore, the remainder of this section will only focus on the wing response to positive gusts.

The largest gust loads are obtained at the highest air speed for a given altitude, and, consequently, the most critical gust responses are observed along the edge of the flight envelope at the highest air speeds. When looking at the effect of altitude on the gust response, one might expect to observe the critical gust response at the same altitude as where the static loads are critical, driven by a combination of dynamic pressure and Mach number. However, certification requirements prescribe the largest gust amplitudes at sea level, after which the reference gust velocity decreases as a function of altitude. Therefore, in case of the CRM wing designs presented here, the most critical gust response is observed at sea level at the corner of the flight envelope, as shown in Figure 8.22, resulting in an equivalent air speed of 155.65 m/s and a corresponding Mach number of 0.46.

When investigating the gust response of both wing designs in more detail, several things can be observed. When looking at Figure 8.23, showing the critical gust length for each laminate on the wing, it can be seen that the critical gust length is not unique and, as can be expected, a different gust length is critical depending on the wing design and the location on the wing. A clear trend can, however, be observed for both wing designs. Close to the wing root, long gusts that show

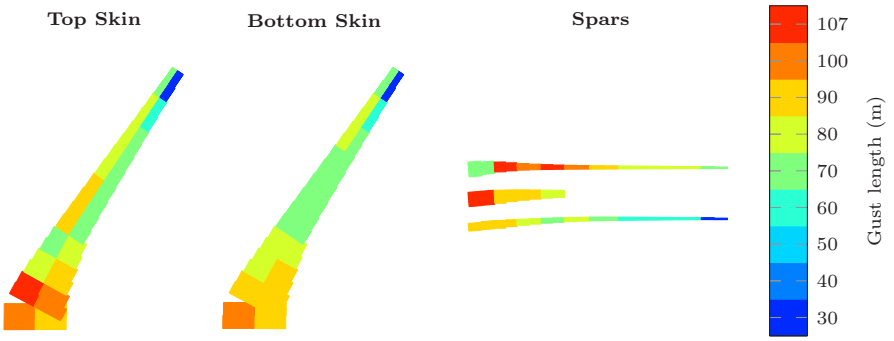


**(a)** Wing with predefined laminates.

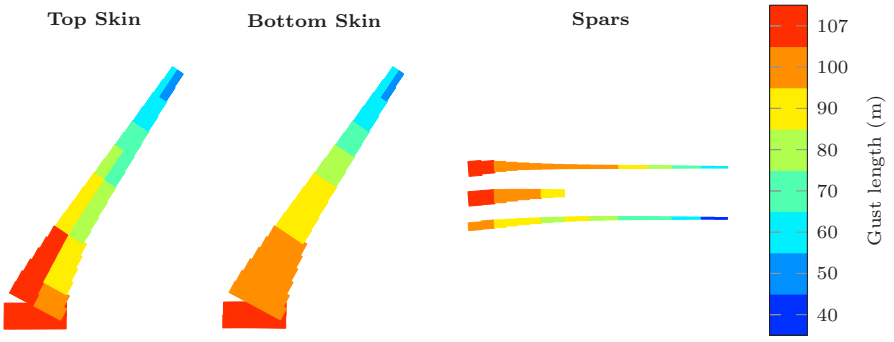


**(b)** Wing with unbalanced laminates.

**Figure 8.23:** Critical gust lengths for the statically optimised CRM wings with a free jig twist distribution. (The spars are displayed front to rear with the front spar at the top.)

a quasi-steady response are the most critical gust cases and, then, showing a reduction in critical gust length towards the wing tip driven by the dynamic response of the wing.

In order to investigate this trend in more detail, Figure 8.24 shows the wing displacement and twist distribution of the wing with unbalanced laminates for a long gust (107 m), a medium length gust (80 m), and a short gust (50 m) at their critical time instances. Similar observations can be made for the wing with predefined laminates. The static wing deformation for loadcase 2 is shown for comparison. It is interesting to see that the flexibility of the wing with unbalanced laminates results in a larger wing tip displacement under gust loads than under static 2.5g loads, showing the importance of the gust response for the design of aircraft wings. Furthermore, as can be seen, a different displacement shape along the span is observed for all cases.

In case of a long gust, the critical wing deformation is driven by the largest loads acting on the wing, which are obtained at the time instance of the maximum root

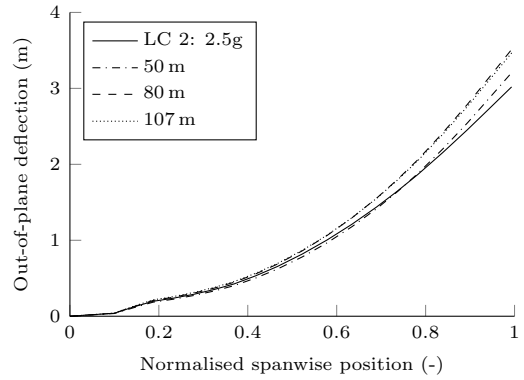


**(a)** Out-of-plane deflection.

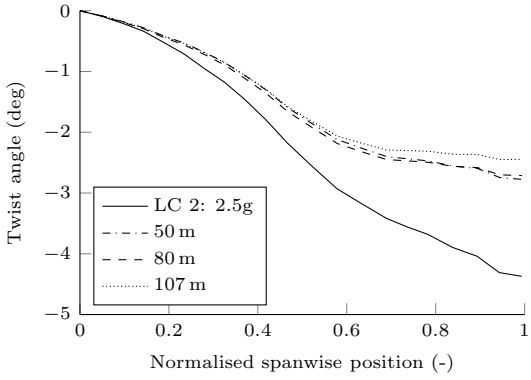


**(b)** Twist distribution.

**Figure 8.24:** Out-of-plane displacement and twist distribution for the statically optimised wing with unbalanced laminates with a free jig twist distribution for various gust lengths at 155.65 m/s at sea level.

bending moment. This results in the largest deformation of the wing root section, thereby making long gusts the critical gusts for the wing root region.

In case of a medium length gust, the critical wing deformation is driven by the largest wing displacement, which, because of phase lags introduced by inertial and unsteady aerodynamic effects, occurs slightly later than the maximum root bending moment. As can be seen, the aeroelastic response for the medium length gust shows a smaller displacement at the wing root than for the long gust, but a larger displacement at the wing tip. Consequently, a larger curvature is observed in the centre region of the wing, resulting in increased strains in the top and bottom skin, thereby making medium length gusts critical in the centre region of the wing.

Finally, in case of a short gust, as can be seen, the critical deformation is no longer driven by maximum displacement, but by maximum wing twist. A smaller displacement is observed along the entire wing span when comparing the short gust to the medium length gust or the long gust; however, when looking at the wing twist distribution, a larger twist angle is observed at the wing tip driving the critical gust response in the tip region and thereby making short gusts critical in the wing tip region.

In order to assess the importance of gust loads on the design of aeroelastically tailored wings in more detail, the strain factor distribution of the critical gust responses is compared to the static analysis results presented in Section 8.4. Figures 8.25a and 8.26a show the increase in strain factor of the critical gust responses over the static loadcases. As can be seen, similar trends can be observed for both wings, showing the largest increases in strain factor in the outboard half of the wing driven by inertial and unsteady aerodynamic effects in the dynamic response of the wing. The increased flexibility of the wing with unbalanced laminates makes it more susceptible to dynamic loads and, therefore, a significantly larger increase in strain factor is observed compared to the wing with predefined laminates.

More importantly, as can be concluded from Figures 8.25b and 8.26b showing the strain constraint violation due to the gust loads, both wing designs show failure under gust loads (6.0% in case of the wing with predefined laminates and 55.4% in case of the wing with unbalanced laminates), illustrating the importance of gust loads in the design of aircraft wings.



It should be noted however, that the present framework is limited to clamped wings only and, therefore, the effect of the flight dynamic response of the aircraft on the gust loads of the wing is not accounted for. Consequently, no definitive conclusions on the importance of gust loads in the design of aircraft wings can be drawn yet; however, the results do show that gust loads might become critical design loads and considering static loadcases only in preliminary design is no longer sufficient to guarantee a safe wing design, especially, as the flexibility of the wing increases.

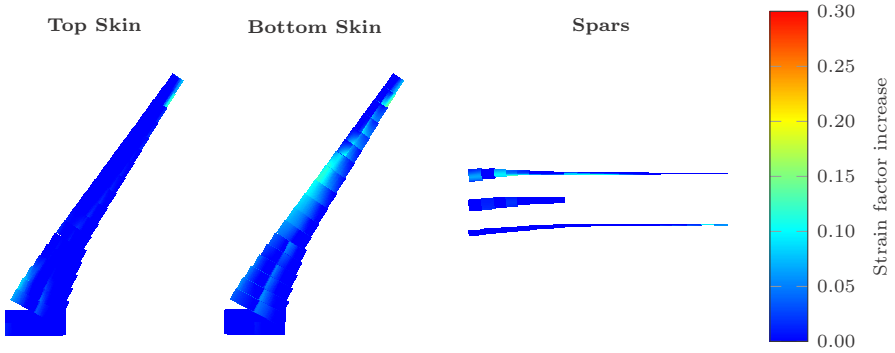


**(a)** Increase in strain factor with respect to static loads due to discrete gust loads.

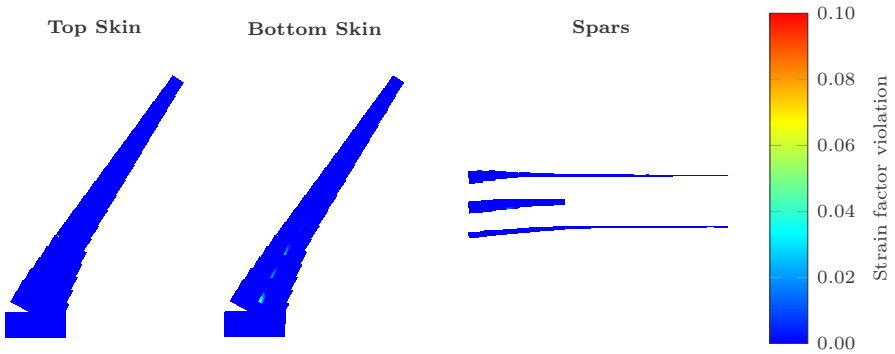


**(b)** Strain constraint violation under discrete gust loads.

**Figure 8.25:** Strain response of the statically optimised wing with predefined laminates with a free jig twist distribution under discrete gust loads. (The spars are displayed front to rear with the front spar at the top.)

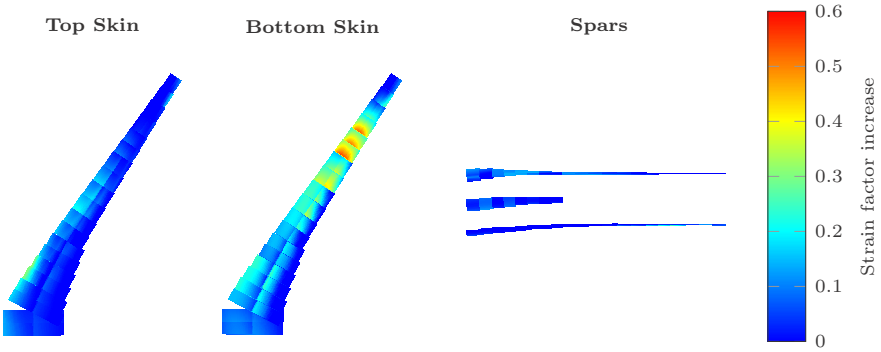


**(a)** Increase in strain factor with respect to static loads due to discrete gust loads.

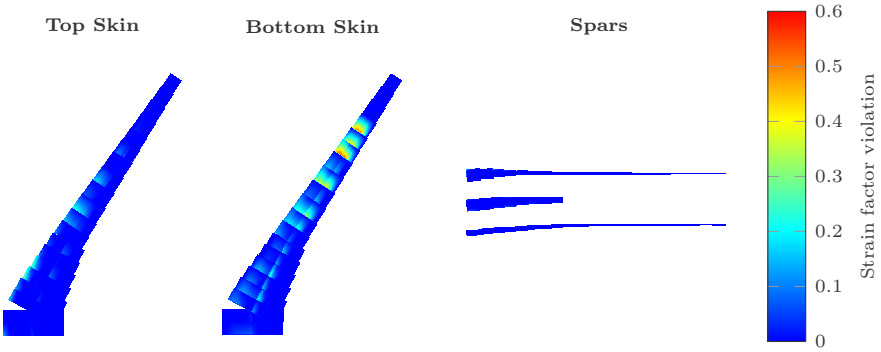


**(b)** Strain constraint violation under discrete gust loads.

**Figure 8.26:** Strain response of the statically optimised wing with unbalanced laminates with a free jig twist distribution under discrete gust loads. (The spars are displayed front to rear with the front spar at the top.)

**Table 8.17:** Loadcases for the dynamic optimisations.

| ID | Description | EAS | Altitude | Mach | $n_z$ | Fuel level (Tank 1-4) | | | |
|---|---|---|---|---|---|---|---|---|---|
| 1 | Cruise | 136 m/s | 11 000 m | 0.85 | 1.0 | 0.7 | 0.7 | 0.7 | 0.7 |
| 2 | Symm. pull up | 240 m/s | 3000 m | 0.85 | 2.5 | 0.8 | 0.8 | 0.8 | 0.8 |
| 3 | Symm. push down | 198 m/s | 0 m | 0.60 | −1.0 | 0.8 | 0.8 | 0.8 | 0.8 |
| 4 | Dynamic | 155.65 m/s | 0 m | 0.46 | 1.0 | 0.8 | 0.8 | 0.8 | 0.8 |

**Table 8.18:** Gust lengths for loadcase 4 included in the dynamic optimisations.

| Wing type | Gust length (m) |
|---|---|
| With predefined laminates | 70, 80, 90, and 100 |
| With unbalanced laminates | 50, 60, 70, 80, 90, 100, and 107 |

### 8.5.2 Optimisation setup

Based on the results of the loadcase selection, the optimisation setup discussed in Section 8.2 is expanded with a fourth loadcase, as given in Table 8.17. In order to reduce the computational time of the optimisation and reduce the total number of constraints, a subset of the total range of gust lengths is used in the dynamic optimisations based on the strain and buckling results obtained for the statically optimised wings, resulting in four critical gust lengths for the optimisation of the wing with predefined laminates and seven critical gust lengths for the wing with unbalanced laminates, as given in Table 8.18. For each critical gust length, the strain and buckling response of the wing are evaluated at three time instances: the time instance of (i) maximum root bending moment, (ii) maximum wing displacement, and (iii) maximum wing twist. This results in a total of 77 020 constraints for the optimisation of the wing with predefined laminates and 123 060 constraints for the optimisation of the wing with unbalanced laminates. The final optimisation setup is similar to the optimisation setup for the statically optimised wings, given in Table 8.14 on page 230, and has 596 design variables.

### 8.5.3 Dynamic optimisation results

Similar to the other optimisations, the dynamic aeroelastic stability constraints and local angle of attack constraints are not active and are, therefore, not included in the discussion of the results. However, by introducing a fourth loadcase and corresponding additional constraints, additional iterations were required to obtain the optimised wing designs, resulting in 60 to 80 iterations for the optimisations to converge. The wing structural mass, aileron effectiveness, and trim angles of attack of the dynamically optimised wing designs are given in Tables 8.11 to 8.13 on pages 216 to 217, respectively. The corresponding optimised stiffness and thickness distribution is shown in Figure 8.27a for the wing with predefined lamin-

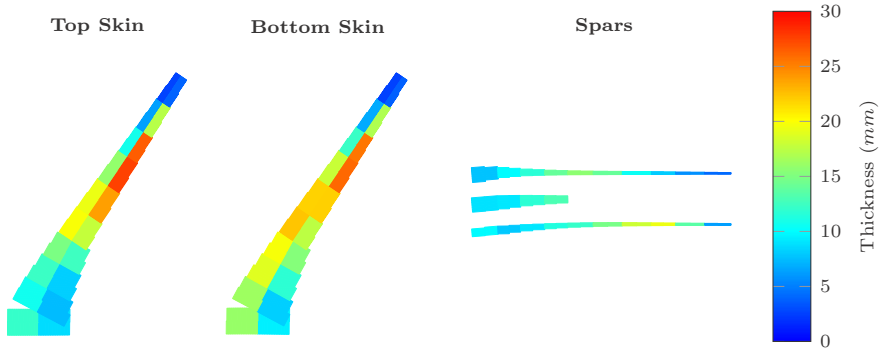


**(a)** Thickness distribution.

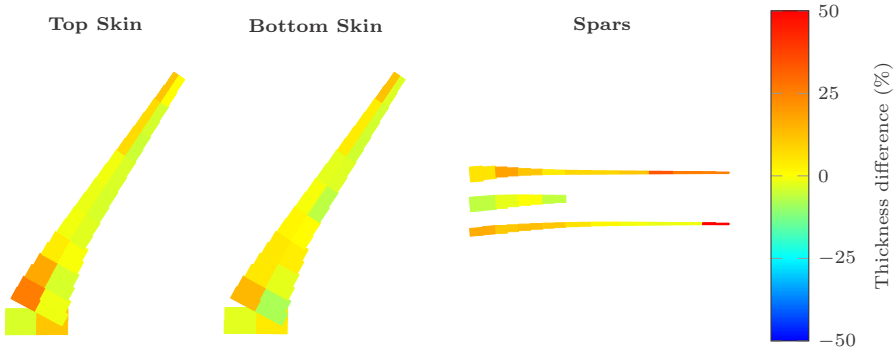


**(b)** Thickness comparison of the optimised CRM wing with predefined laminates including discrete gust responses to the wing excluding discrete gust responses.

**Figure 8.27:** Thickness distribution and thickness comparison for the optimised CRM wing with predefined laminates including discrete gust responses. (The spars are displayed front to rear with the front spar at the top.)

ates and in Figure 8.28 for the wing with unbalanced laminates. The differences in thickness between the dynamically optimised wings and statically optimised wings are shown in Figures 8.27b and 8.29, respectively.

First of all, as can be seen, the stiffness distribution of the dynamically optimised wing with unbalanced laminates is almost identical to the stiffness distribution of the statically optimised wing. Similarly the thickness distribution of both dynamically optimised wings shows the same thickness pattern as the statically optimised wings, indicating that the stiffness and thickness distribution of the dynamically optimised wings is also driven by aileron effectiveness. As is shown in Figures 8.27b and 8.29, the influence of the dynamic loads on the wing structural designs mainly results in an increase and redistribution of thickness, which results in a weight increase of 0.9% for the wing with predefined laminates and 7.4% for

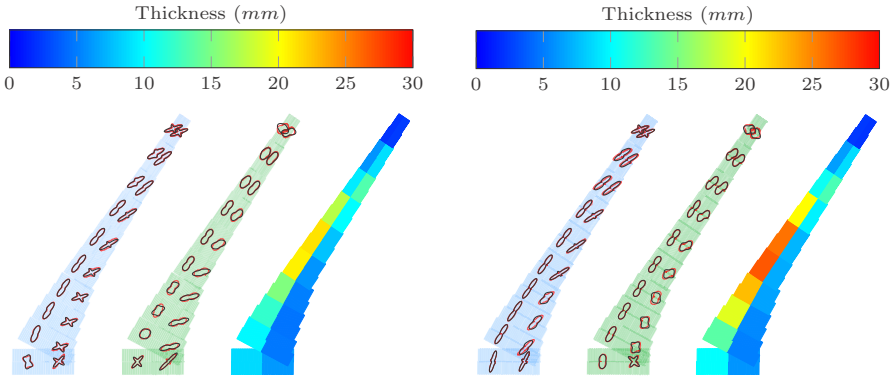


**(a)** Top skin. **(b)** Bottom skin.

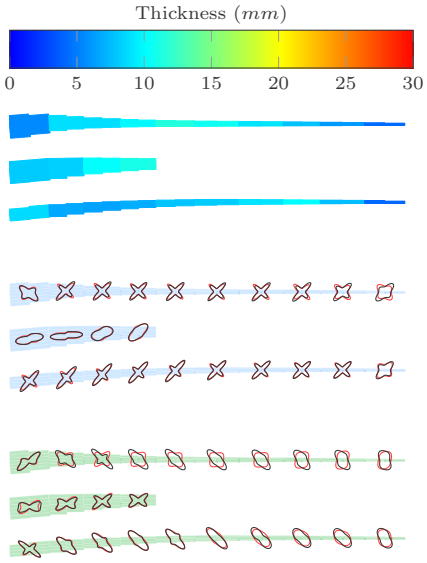


**(c)** Spars.

**Figure 8.28:** Stiffness and thickness distribution for the optimised CRM wing with unbalanced laminates including discrete gust responses. The stiffness distribution for the wing with unbalanced laminates excluding discrete gust responses is displayed in red for comparison. (In-plane stiffness: blue, out-of-plane stiffness: green. The spars are displayed front to rear with the front spar at the top.)

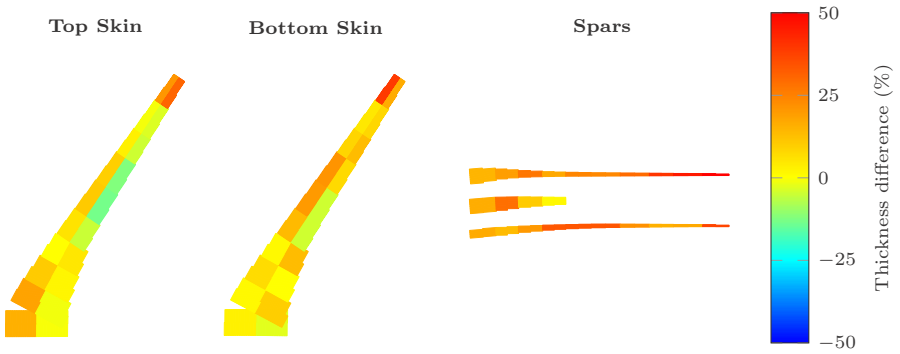


**Figure 8.29:** Thickness comparison of the optimised CRM wing with unbalanced laminates including discrete gust responses to the wing excluding discrete gust responses. (The spars are displayed front to rear with the front spar at the top.)

the wing with unbalanced laminates, resulting in a corresponding weight reduction by using unbalanced laminates of 28.5%.

In order to investigate the influence of the gust response on the design of both wings in more detail, Figures 8.30 and 8.31 show the critical loadcase for each wing laminate and the corresponding critical gust lengths for loadcase 4. Similar to what was observed for the statically optimised wings, a decreasing critical gust length is observed from the wing root to the wing tip. More importantly, both wing designs are driven by a combination of static and dynamic loadcases.

As can be expected, the design of the gust critical areas identified in the dynamic loadcase selection in Section 8.5.1 is indeed driven by the gust response of the wing, illustrating the importance of both static and dynamic loads for the design of aircraft wings. When looking at the corresponding strain factor distribution for the different loadcases, as is shown in Figure 8.32, it can be seen that the use of unbalanced laminates results in a more efficient and critical wing design and a wing that is optimised for a combination of static and dynamic loads across the entire wing span.

In conclusion, although care should be taken with drawing definitive conclusions on the importance of dynamic loads in the design of aircraft wings since the influence of the flight dynamic response of the aircraft on the dynamic loads acting on the aircraft has not been accounted for, the results clearly indicate that, since aeroelastic tailoring results in a more efficient and critical wing design, aeroelastically tailored wings become more susceptible to dynamic loads. Therefore, dynamic loads should be accounted for in the design of aeroelastically tailored aircraft wings.

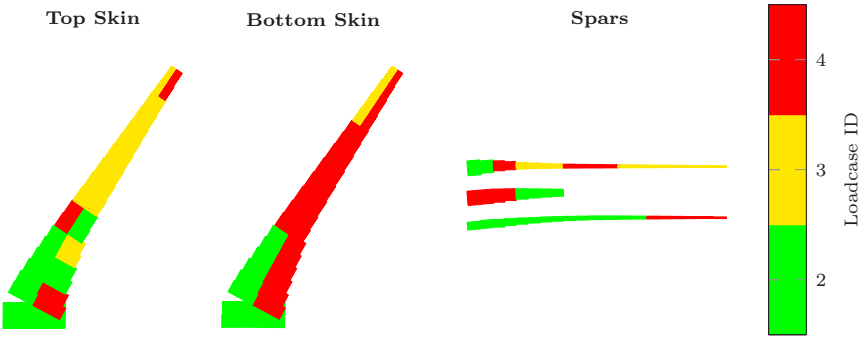


**(a)** Critical loadcases.

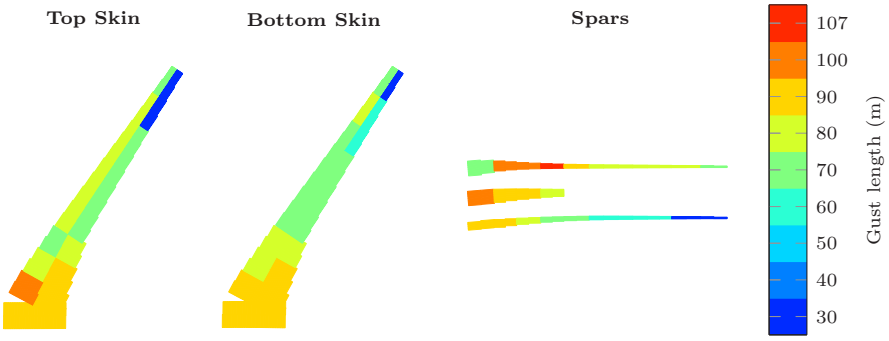


**(b)** Critical gust lengths for loadcase 4.

**Figure 8.30:** Critical gust lengths and corresponding gust lengths for the dynamically optimised CRM wing with predefined laminates. (The spars are displayed front to rear with the front spar at the top.)

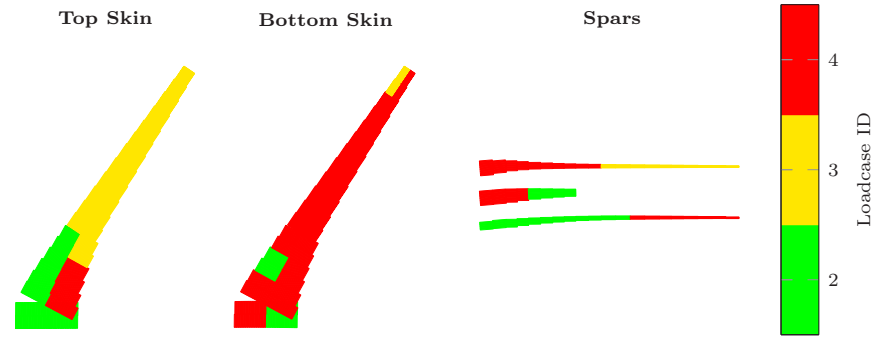


**(a)** Critical loadcases.

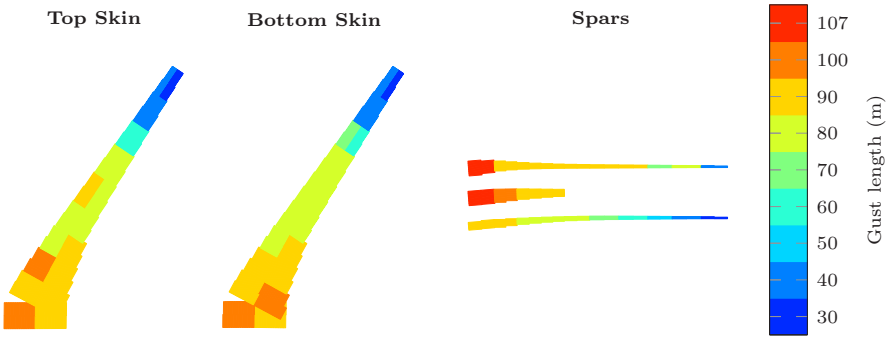


**(b)** Critical gust lengths for loadcase 4.

**Figure 8.31:** Critical loadcases and corresponding gust lengths for the dynamically optimised CRM wing with unbalanced laminates. (The spars are displayed front to rear with the front spar at the top.)

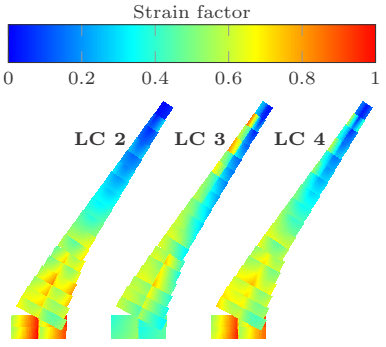


**(a)** Top skin. (Predefined laminates)

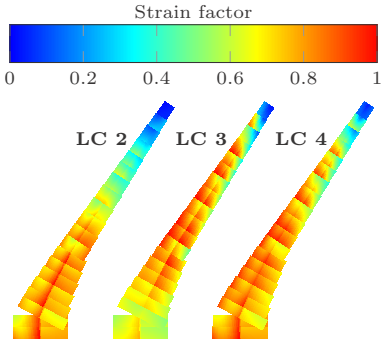


**(b)** Top skin. (Unbalanced laminates)

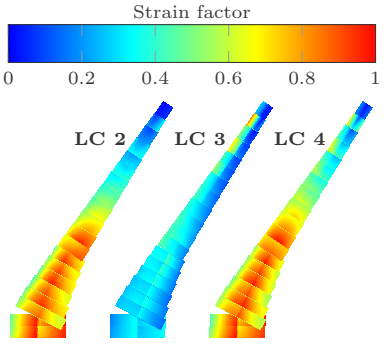


**(c)** Bottom skin. (Predefined laminates)

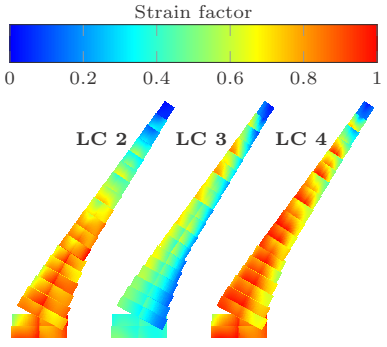


**(d)** Bottom skin. (Unbalanced laminates)

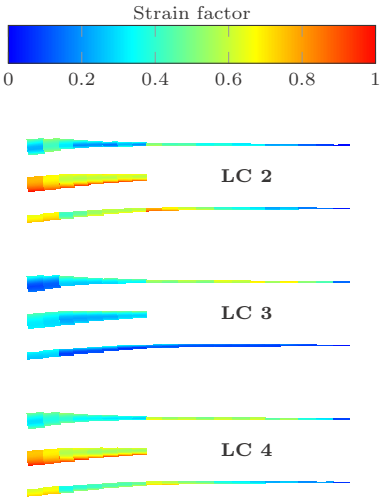


**(e)** Spars. (Predefined laminates)

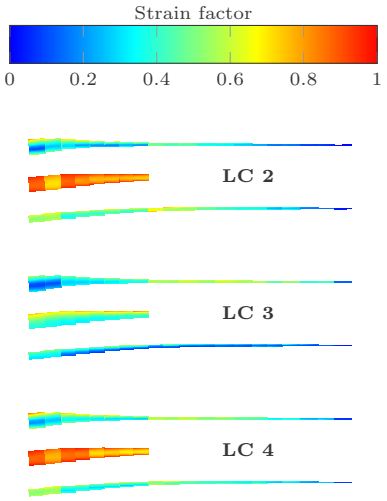


**(f)** Spars. (Unbalanced laminates)

**Figure 8.32:** Strain factor distribution of the dynamically optimised CRM wings for static loadcases 2 and 3 and dynamic loadcase 4. For clarity, only the maximum strain across the different gust lengths is displayed for loadcase 4. (The spars are displayed front to rear with the front spar at the top.)

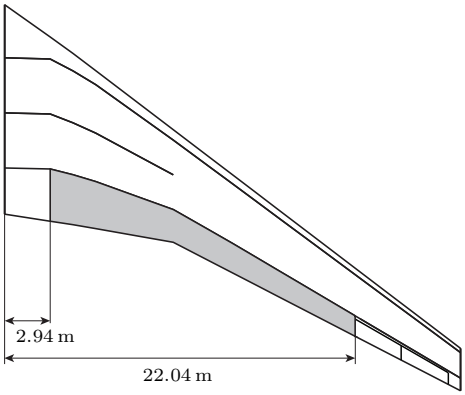


**Figure 8.33:** Wing planform highlighting the trailing edge camber morphing region.

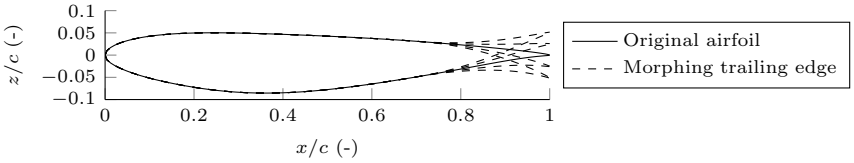


**Figure 8.34:** Camber morphing airfoils at 3.438 m span.

## 8.6 OPTIMAL WING STRUCTURAL DESIGN BY COMBINING AEROELASTIC TAILORING AND MORPHING

For the final design study, a range of trailing edge camber morphing mechanisms is installed on the NASA CRM wing. As discussed in Section 2.3, trailing edge morphing mechanisms provide great potential for combining the benefits of aeroelastic tailoring with morphing. The camber morphing mechanisms are mounted to the rear spar of the wingbox between the wing-fuselage connection at 2.94 m span and the ailerons at 22.04 m span, as shown in Figure 8.33. Each camber morphing mechanism can morph in a range of ±10 deg deflection modelled by means of a smooth deformation of the airfoil camber line based on a quadratic polynomial. The resulting camber morphing deformation for the first camber morphing location is, for example, shown in Figure 8.34.

The corresponding optimisation setup is presented in Section 8.6.1, followed by a discussion of the optimisation results in Section 8.6.2.

### 8.6.1 Optimisation setup

In order to investigate the influence of a combination of morphing and aeroelastic tailoring, the optimisation setup presented in Section 8.4 for the CRM wing, including a cruise twist constraints and given by Table 8.14 on page 230, is expanded with 14 camber morphing design variables, 7 for loadcase 2 and 7 for loadcase 3, resulting in a total of 610 design variables and 15 919 constraints. The original airfoil shape is maintained for loadcase 1 in order to maintain optimal aerodynamic performance in cruise conditions. Two sets of optimisations have been run both with and without aileron effectiveness: (i) a wing design with predefined laminates and (ii) a wing design with unbalanced laminates.

### 8.6.2 Optimisation results

Similar to the "conventional" weight minisations and the weight minimisations with a free jig twist distribution, the optimisation cases converged within 30 to 60 iterations and the dynamic aeroelastic stability constraints and local angle of attack constraints are not active and are, therefore, not included in the discussion of the results. The optimised trailing edge camber morphing distribution for loadcase 2 and loadcase 3 is shown in Figure 8.35. The corresponding wing structural mass, aileron effectiveness, and trim angles of attack of the optimised wing designs are given in Tables 8.11 to 8.13 on pages 216 to 217, respectively. The corresponding stiffness and thickness distributions are shown in Figures 8.36 and 8.37 for the optimised wings with aileron effectiveness constraints and in Appendix D.2 for the optimised wings without aileron effectiveness constraints.

When looking at the optimised camber morphing distribution in Figure 8.35, the expected camber morphing distribution is obtained for most wings, showing an increased camber inboard and a decreased camber outboard for loadcase 2, and vice versa for loadcase 3. This is to shift load inboard for manoeuvre load alleviation, as can, for example, be seen in Figure 8.39, which shows the lift distribution of the wing with unbalanced laminates including aileron effectiveness constraints. Similar trends have recently also been observed by Stanford et al. (2016), who investigated the use of a set of trailing edge flaps along the span of an aluminium wing for manoeuvre load alleviation.

However, in case of the wing with predefined laminates including aileron effectiveness constraints, a different trailing edge camber distribution is obtained for loadcase 2, showing increased camber at 60% wing span. In this case, the trailing edge camber distribution is not only driven by manoeuvre load alleviation, but also by aileron effectiveness. As a consequence, as can be seen in Figure 8.39a, the lift distribution is maintained close to the ailerons for aileron effectiveness and, consequently, less manoeuvre load alleviation is observed.

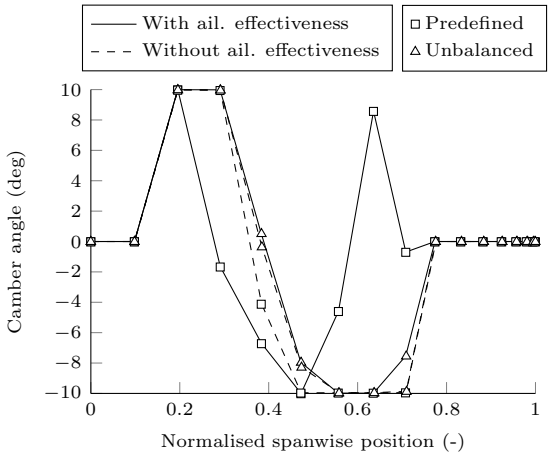


**(a)** Optimal trailing edge camber distribution for load-case 2.

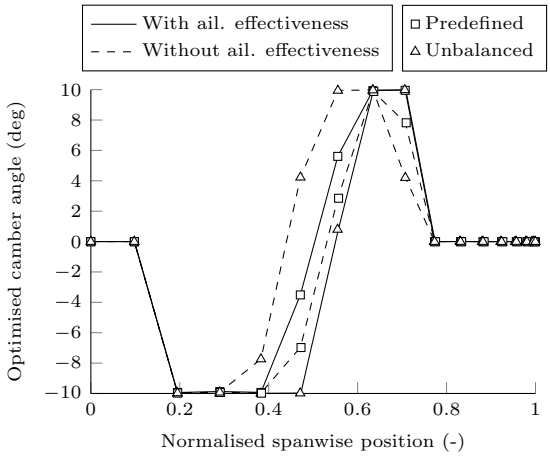


**(b)** Optimal trailing edge camber distribution for load-case 3.

**Figure 8.35:** Optimal trailing edge camber distribution for the optimised CRM wings including trailing edge camber morphing.

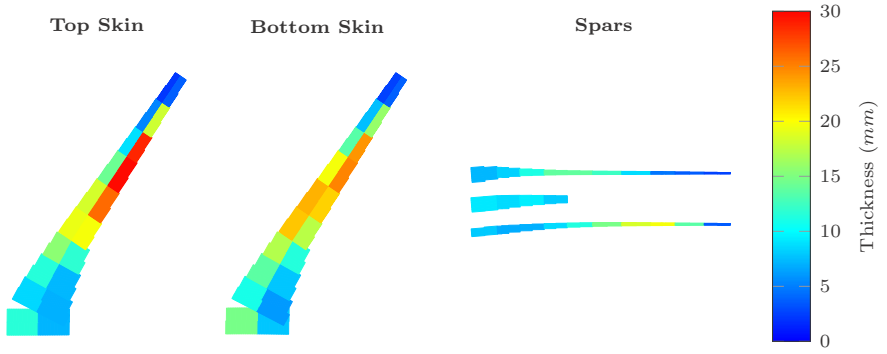


**(a)** Thickness distribution.

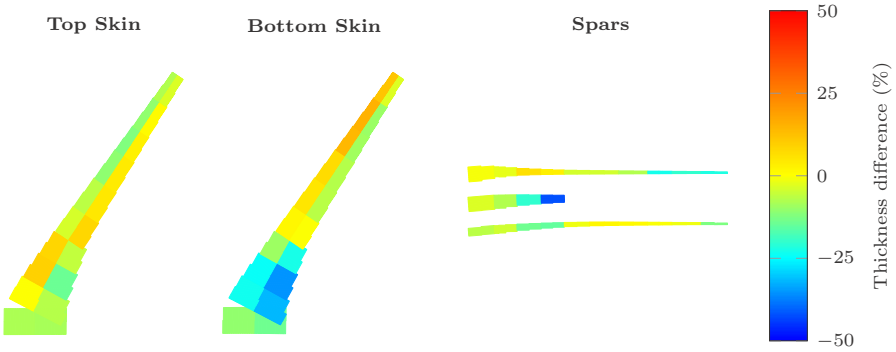


**(b)** Thickness comparison of the optimised CRM wing with predefined laminates including trailing edge camber morphing to the wing excluding trailing edge camber morphing.

**Figure 8.36:** Thickness distribution and thickness comparison for the optimised CRM wing with predefined laminates including trailing edge camber morphing. (The spars are displayed front to rear with the front spar at the top.)

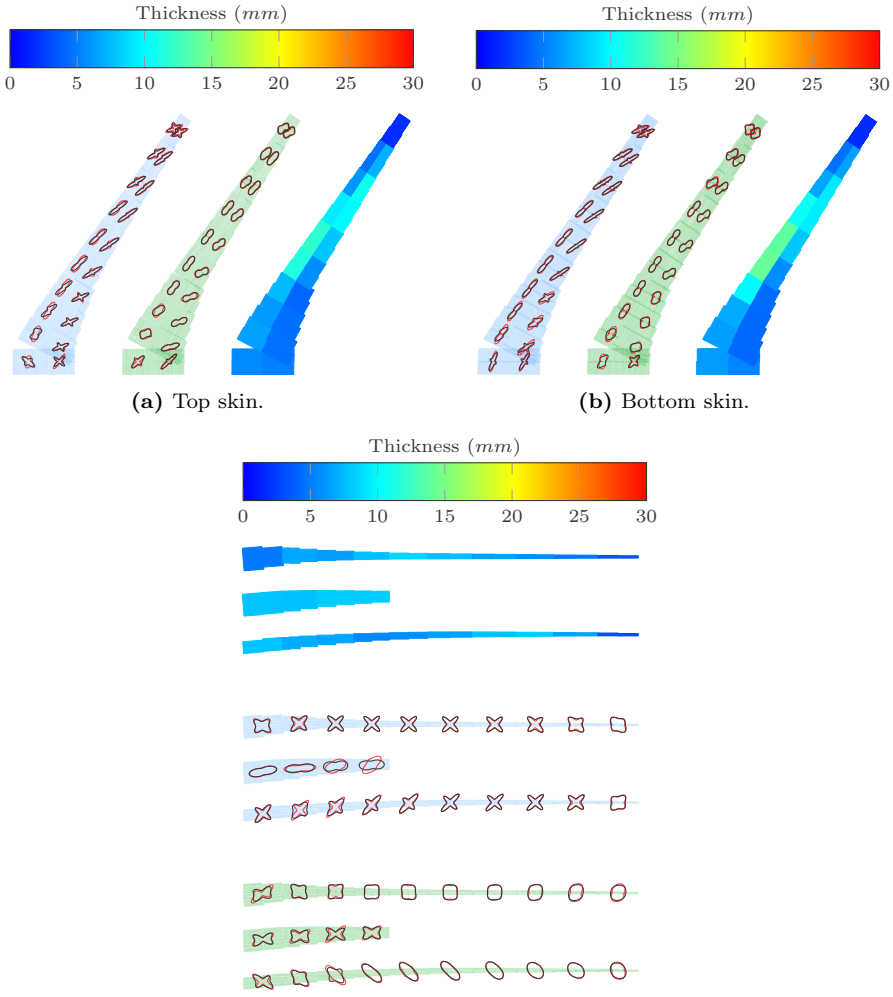


**(a)** Top skin.

**(b)** Bottom skin.

**(c)** Spars.

**Figure 8.37:** Stiffness and thickness distribution for the optimised CRM wing with unbalanced laminates including trailing edge camber morphing. The stiffness distribution for the wing with unbalanced laminates excluding trailing edge camber morphing is displayed in red for comparison. (In-plane stiffness: blue, out-of-plane stiffness: green. The spars are displayed front to rear with the front spar at the top.)

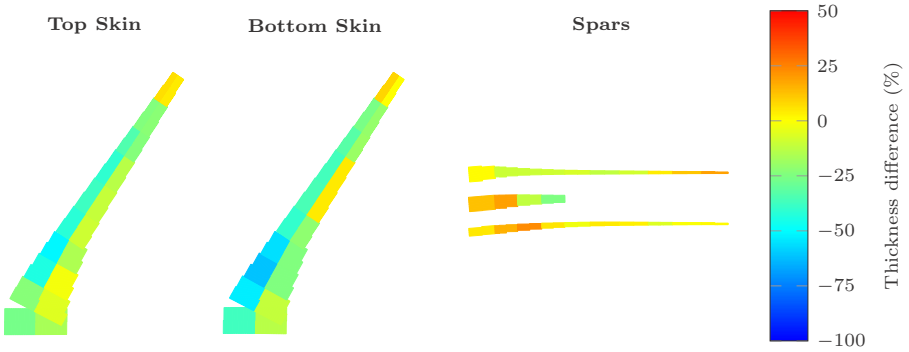


**Figure 8.38:** Thickness comparison of the weight optimised CRM wing with unbalanced laminates including trailing edge camber morphing to the wing excluding trailing edge camber morphing. (The spars are displayed front to rear with the front spar at the top.)

As a consequence of the manoeuvre load alleviation originating from camber morphing, both the wings with unbalanced laminates and the wings with predefined laminates show a significant reduction in weight, as can be seen in Table 8.11 on page 216 and can be concluded from Figures 8.36b and 8.38. In case of the wing with predefined laminates including aileron effectiveness constraints, the influence of the aileron effectiveness constraints can clearly be observed, resulting in a significantly smaller weight reduction of only 6.6% compared to around 30% for the other wings.

As can be seen in Figure 8.37, the primary stiffness direction of the top and bottom skin of the wing design with unbalanced laminates including trailing edge camber morphing is oriented further aft than the wing design excluding trailing edge camber morphing. This indicates reduced load carrying requirements on the wing skins, because of trailing edge camber morphing, such that aeroelastic tailoring can be used more effectively to satisfy the aileron effectiveness constraints and, consequently, reduce the wing weight.

Finally, as can be concluded from the strain and buckling response of the wing with unbalanced laminates shown in Figure 8.40, combining aeroelastic tailoring and morphing allows for wing designs that are optimal across all flight conditions over large areas of the wing, thereby improving the efficiency of the wing structure, resulting in a wing design that, in this case, is even critically designed under cruise conditions, showing the potential of combined aeroelastic tailoring and morphing for optimally designed wings across a range of flight conditions.

However, before drawing definitive conclusions on the potential benefits of combining aeroelastic tailoring and morphing, one remark needs to be made about the design and operation of wings with morphing mechanisms. When using morphing mechanisms for manoeuvre load alleviation, care should be taken to ensure

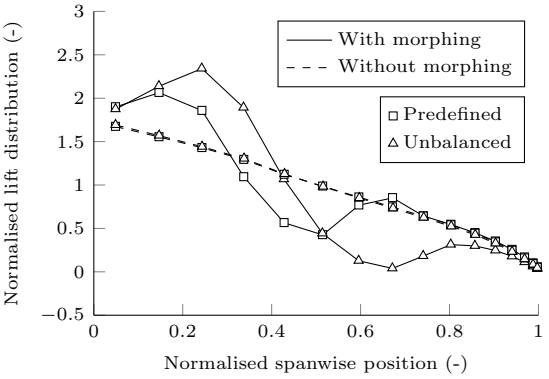


**(a)** Lift distribution for loadcase 2.

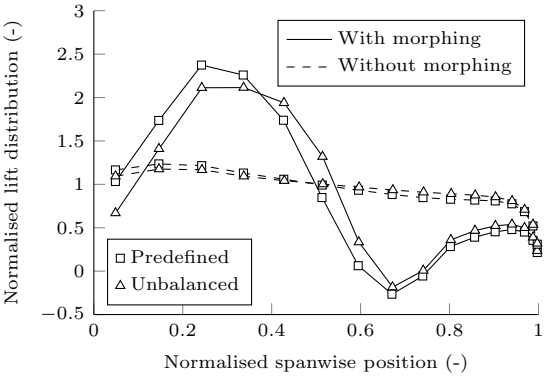


**(b)** Lift distribution for loadcase 3.

**Figure 8.39:** Comparison of the lift distribution for loadcase 2 and loadcase 3 between the optimised wings including trailing edge camber morphing and the wings excluding trailing edge camber morphing.

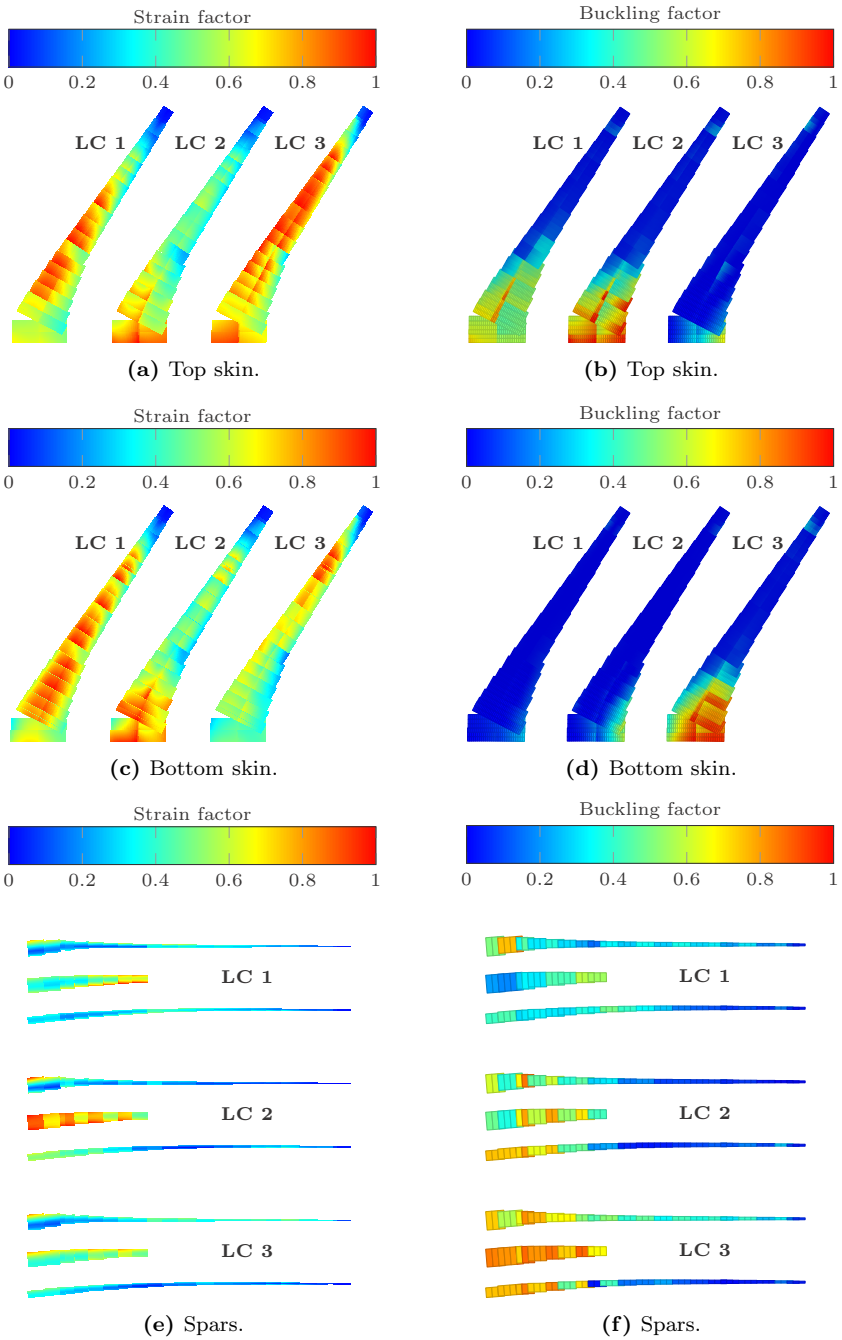


**(a)** Top skin. **(b)** Top skin.

**(c)** Bottom skin. **(d)** Bottom skin.

**(e)** Spars. **(f)** Spars.

**Figure 8.40:** Strain and buckling factor distribution of the optimised CRM wing with unbalanced laminates including trailing edge camber morphing. (The spars are displayed front to rear with the front spar at the top.)

aircraft safety in case the morphing mechanisms fail.

In conclusion, the optimisation results show clear benefits of combining aeroelastic tailoring and trailing edge camber morphing to increase the efficiency of aircraft structures across a range of flight conditions, resulting in significant weight savings. Mind that special attention should be given to aircraft safety.

## 8.7 IMPACT ON THE DESIGN OF WING STRUCTURES

As can be concluded from the CRM wing design studies presented in Sections 8.3 to 8.6, there are numerous aspects that influence the design of tailored wing structures. Based on the observations made in these design studies, this section highlights some general insights in the design of wing structures, addressing some of the assumptions made and their corresponding limitations.

First of all, all wing designs presented in this chapter are driven by the strain, buckling, and, if included, aileron effectiveness constraints, while aeroelastic stability is not critical for any of the wing designs. However, this does not imply that aeroelastic stability is not important in the design of wing structures and several remarks should be made about the presented wing designs before definitive conclusions can be drawn. Firstly, aeroelastic stability is not necessarily a wing only phenomenon, but might be driven by interactions with the fuselage or tail or with the flight dynamic response of the aircraft, which have not yet been accounted for in the present framework.

Another important aspect in the design of wing structures that not only affects aeroelastic stability, but the complete wing design, is the selection of design loadcases. This has already been discussed briefly in Section 8.5.1 when identifying the critical discrete gust flight condition(s) and corresponding gust lengths for the optimised wings. However, many other aspects are important in loadcase selection and should be investigated further to identify the critical design loadcases and improve the wing designs, such as: (i) the flight envelope, (ii) the fuel distribution, (iii) the aircraft configuration (e.g. take-off or cruise), or (iv) the flight manoeuvres (e.g. steady level flight, a roll manoeuvre or a control surface deflection). In this case, the static loadcases are based on the loadcases selected by NASA for the design of the CRM with a uniform fuel distribution; however, more loadcases should be accounted for before definitive conclusions can be drawn.

In selecting the critical loadcases, another important aspect is the analysis of the discrete gust response of the wing, as discussed in Section 8.5. The analysis results clearly show the importance of discrete gust loads in wing structural design, especially for aeroelastically tailored wings with increased flexibility. The present model, however, is limited to clamped wings only, and, therefore, further research including the effects of the flight dynamic response on the discrete gust response

is required before definitive conclusions can be drawn.

To identify the critical design loadcases, the critical design loads need to be identified. One of the key aspects in obtaining the correct design loads is the jig shape of the wing, as shown in Section 8.4. By changing the jig shape of the wing, optimal aircraft performance can be maintained at cruise conditions, while taking advantage of aeroelastic tailoring at off-cruise conditions. Furthermore, the jig twist distribution strongly affects the load distribution on the wing by modifying the local angle of attack. Therefore, it is of paramount importance to include the jig shape in the design of wing structures to obtain the correct design loads and select the critical design loadcases.

Another aspect that affects the design loads of the wing that has not been discussed yet is the influence of the fuselage. As a result of the fuselage, a loss of lift is observed at the wing root, which will change the load distribution on the wing. This is one of the effects that has not been accounted for in the present model and needs to be included in future developments of the framework in order to assess the influence of this effect on the structural design of the wing.

Besides identifying the correct critical loadcases and corresponding design loads, another aspect that is important in the design of wing structures is selecting the correct constraints. When investigating the influence of the different constraints on the wing design in more detail, two aspects stand out: (i) the limited influence of the buckling constraints in the present wing design and (ii) the significant influence of the aileron effectiveness constraints.

The main parameter driving the influence of the buckling constraints on the wing design is the stringer pitch. By selecting the stringer pitch used by NASA in one of their structural designs for the CRM, the present design studies resulted in strain and aileron effectiveness driven designs, as opposed to buckling driven designs. This indicates that potentially a larger stringer pitch could be used to obtain a more efficient wing structure, but further research is required before conclusions can be drawn.

In case of the aileron effectiveness constraints, two main questions arise that need to be addressed before definitive conclusions can be drawn on the importance of the aileron effectiveness constraints. Firstly, what control surfaces are active in which flight conditions? Spoilers or inboard ailerons might, for example, be more effective at high speeds, where outboard ailerons show reduced effectiveness or even reversal. And secondly, what control effectiveness is required in which flight conditions? Is the same control authority required in all flight conditions or can some control authority be sacrificed for improved wing structural efficiency?

When extending these observations on loadcase selection, design loads, and constraint selection to aeroelastically tailored wings, special care should be taken, since aeroelastic tailoring results in wing designs that are specifically tailored to the loadcases, design loads, and constraints that are included in the design,

making them more sensitive to failure in off-design conditions. When including trailing edge camber morphing, similar observations can be made; however, as already mentioned, when using morphing mechanisms for manoeuvre load alleviation, care should be taken in order to ensure aircraft safety, especially when the morphing mechanisms fail.

In conclusion, the design studies have clearly shown the potential use of aeroelastic tailoring and morphing to improve the efficiency of wing structures. Furthermore, some conclusions on the influence of loadcase selection, identifying the correct design loads, and constraint selection in the design of wing structures have been drawn. However, further research is required before definitive conclusions can be drawn.

## 8.8 SYNOPSIS

This chapter presented the application of the aeroelastic analysis and optimisation framework to the structural design of the Common Research Model (CRM) designed by NASA as a contemporary transonic supercritical wing with a semispan of 29.38 m.

- The wingbox consists of 64 laminates distributed over the top skin, bottom skin, and spars.
- Aileron effectiveness, aeroelastic stability, wing stall, panel buckling, and the Tsai-Wu failure criterion have been introduced as constraints in the optimisation.
- The design studies show the benefits of aeroelastical tailoring over conventional composite wing design approaches, resulting in significant weight reductions of up to 37% within the assumptions of the present framework. Care should be taken, however, before definitive conclusions are drawn. Although the results clearly show the benefits of aeroelastic tailoring, substantial further research is required to address some of the assumptions made in the presented framework and introduce additional factors and constraints that will most likely reduce the benefits of aeroelastic tailoring.
- All wing designs were driven by a combination of strain, buckling, and aileron effectiveness constraints.
- The jig shape of the wings has been identified as one of the key parameters in the design of wing structures to ensure optimal aircraft performance in cruise conditions and, more importantly, obtain the correct design loads. By constraining the cruise twist distribution and introducing the jig twist distribution as additional design variables, aerodynamic performance in cruise

is maintained, while taking advantage of aeroelastic tailoring in off-cruise conditions.

- Aeroelastic tailoring results in wing designs that are specifically tailored to the loadcases and constraints that are included in the design. As a consequence, aeroelastically tailored wing designs are more sensitive to failure in off-design conditions and, therefore, a correct selection of loadcases and constraints becomes increasingly important.
- The increased flexibility of aeroelastically tailored wings makes them more susceptible to dynamic loads, making discrete gust loads critical in some areas of the wing, showing the importance of dynamic loads in the design of wing structures.
- In order to investigate the benefits of combining aeroelastic tailoring and morphing, trailing edge camber morphing mechanisms have been installed on the CRM and combined optimisations have been carried out.
- The optimisation results show the potential benefits of combining aeroelastic tailoring with trailing edge camber morphing, resulting in a wing design that is optimally designed across of range of flight conditions, showing a corresponding weight reduction of 28.8% over the aeroelastically tailored wing without trailing edge camber morphing, although care should be taken, since substantial further research is required before definitive conclusions can be drawn. Furthermore, when using morphing mechanisms for manoeuvre load alleviation, care should be taken in order to ensure aircraft safety, especially when the morphing mechanisms fail, which might reduce the potential benefits of trailing edge camber morphing for wing weight reduction.

In conclusion, the design studies have shown the potential use of aeroelastic tailoring and morphing to improve the efficiency of wing structures. Furthermore, conclusions on the influence of loadcase selection, identifying the correct design loads, and constraint selection in the design of wing structures have been drawn. However, further research is required before definitive conclusions can be drawn.

*Prediction is very difficult, especially about the future*
**Niels Bohr**

# 9

# CONCLUSIONS AND RECOMMENDATIONS

As introduced in Chapter 1, the main research question that provides the basis for this dissertation is:

> *Can advanced composite and morphing technologies be used in the design of aircraft to minimise structural weight and improve aerodynamic performance, making use of the aeroelastic characteristics of the wing?*

This chapter presents a summary of the conclusions drawn throughout this dissertation in order to formulate an answer to this question, followed by recommendations for future research.

## 9.1 CONCLUSIONS

Substantial research has been carried out over the past decades in both morphing and aeroelastic tailoring. However, as was concluded in the presented literature overview, in both fields, there is a lack of models suitable for the design of aircraft wings that, on the one hand, are sufficiently efficient to explore the design space,

but, on the other hand, are sufficiently comprehensive to account for all factors relevant in the design of aircraft wings.

### AEROELASTIC ANALYSIS AND OPTIMISATION FRAMEWORK

In order to progress the state of the art, this dissertation introduced a novel dynamic aeroelastic analysis and optimisation framework suitable for the design of aeroelastically tailored and morphing wings. The wing is discretised in several spanwise sections, where each section has a number of laminates throughout the cross-section, each having their own stiffness and thickness. The laminates are described using lamination parameters to allow for the use of a gradient-based optimiser.

The geometrically nonlinear static aeroelastic solution is obtained by coupling a geometrically nonlinear Timoshenko beam model to a vortex lattice aerodynamic model. The dynamic aeroelastic response is obtained using a linear dynamic aeroelastic analysis around the geometrically nonlinear static equilibrium solution. The dynamic aeroelastic model couples a dynamic structural model based on Timoshenko beam elements to an unsteady aerodynamic model based on the unsteady vortex lattice method to obtain a monolithic system of continuous-time state-space equations describing the dynamic aeroelastic response of the wing.

By assuming small perturbations with respect to the steady solution and a fixed wake shape, a novel continuous-time state-space formulation of the unsteady vortex lattice method has been introduced. The presented results show the benefits of the present approach over conventional discrete-time models by varying the timestep independent of the spatial discretisation and introducing a non-constant wake discretisation. The approach allows for a straight-forward generalisation to any arbitrary wake shape and can easily be extended to higher-order panel methods. By introducing the Prandtl-Glauert transformation to account for compressibility, the model shows good agreement to the approximate closed-form solution of the Possio integral equation up to high subsonic Mach numbers for reduced frequencies up to 1.

Morphing has been introduced in the framework by a novel two-step approach for the modelling of morphing aircraft wings. The first step is concept-specific and is used to identify the different morphing mechanisms on the wing and their feasibility constraints. The second step is a generic morphing optimisation framework used to identify the optimal set of morphing parameters within the concept-specific bounds and assess whether a feasible morphing solution can be found. The main advantage of this approach is that the morphing optimisation framework is suitable for any morphing wing design, while concept-specific limitations can still be accounted for. In order to assess the feasibility of the final optimised morphing wing design, the required actuation forces and actuation energy are determined.

If necessary, the feasibility constraints derived in the first step are updated and a new optimisation is run until a feasible wing design has been found.

The optimised wing designs are obtained using a gradient-based optimiser for computational efficiency where the sensitivities of the aeroelastic responses with respect to the design variables are computed analytically. The framework has been extensively verified with both geometrically linear and nonlinear results in the literature showing good to excellent agreement.

### Experimental validation

A series of structural and wind tunnel tests have been carried out on a quasi-isotropic wing and an aeroelastically tailored wing to validate the framework. Comparison of the experimental data to the numerical results showed good agreement for both wings, both in terms of wing deformations and in terms of predicted aeroelastic loads. Only in case of the aeroelastically tailored wing some discrepancies were observed in wing deflection, probably caused by slight variations in material properties and wing geometry or some flexibility in the clamping mechanism.

### Morphing wing optimisation

The benefits of the two-step morphing approach have been illustrated by optimising a morphing wing designed for a 25 kg UAV over a flight mission consisting of four flight phases. In the first step, the wing is equipped with 7 morphing mechanisms, distributed over 4 types of morphing (camber, span, twist, and shear/sweep), thereby defining the feasibility constraints for the generic morphing optimisation problem.

The optimised morphing wing shows an increase in range in the high speed flight phase of 23% over an equivalent fixed wing design, while maintaining endurance in loiter, thereby illustrating the potential benefits of integrating morphing mechanisms on a UAV and showing the benefits of the presented two-step approach.

Based on the optimised morphing parameters for the different flight phases, two parameters that affect the corresponding actuation forces and moments have been investigated in more detail: (i) the sequence in which different morphing manoeuvres are carried out and (ii) the flight condition at which morphing is carried out. Varying both parameters resulted in changes of up to an order of magnitude in actuation forces and moments of the different morphing mechanisms. Furthermore, it was shown that the optimal morphing flight condition and sequence is dependent on the morphing mechanism and its location on the wing and is not necessarily the same for all morphing mechanisms. Therefore, a trade-off is required to obtain the optimal morphing flight condition and sequence on a systems

level.

In conclusion, the optimisation results of the morphing wing illustrate that the challenge of designing a morphing aircraft does not stop with designing morphing mechanisms, but requires a systems level approach where flight condition and morphing sequence are an integral part of the design process.

### AEROELASTIC TAILORING

The benefits of aeroelastic tailoring have been shown in a second design study by creating several optimised aeroelastically tailored wing designs for the NASA Common Research Model (CRM), a contemporary transonic supercritical wing with a semispan of 29.38 m. The wingbox consists of 64 laminates distributed over the top skin, bottom skin, and spars. Aileron effectiveness, aeroelastic stability, wing stall, panel buckling, and the Tsai-Wu failure criterion have been introduced as constraints in the optimisation. Furthermore, by constraining the cruise twist distribution and introducing the jig twist distribution as additional design variables, aerodynamic performance in cruise is maintained, while taking advantage of aeroelastic tailoring in off-cruise conditions. The optimised wing designs clearly show the benefits of aeroelastical tailoring over conventional composite wing design approaches, resulting in more efficient wing designs with significant structural weight reductions of up to 37% within the assumptions of the present framework. Care should be taken, however, before definitive conclusions are drawn. Although the results clearly show the benefits of aeroelastic tailoring, substantial further research is required to address some of the assumptions made in the presented framework and introduce additional factors and constraints that will most likely reduce the benefits of aeroelastic tailoring.

Furthermore, as a consequence of the significant reduction in weight, aeroelastically tailored wing designs are more sensitive to failure in off-design conditions and, therefore, a correct selection of loadcases and constraints becomes increasingly important. Although further research, including the effects of the flight dynamic response on the discrete gust loads acting on the wing, is required before definitive conclusions can be drawn, the results, for example, clearly show that the increased flexibility of aeroelastically tailored wings makes them more susceptible to dynamic loads.

Moreover, the jig shape of the wings has been identified as one of the key parameters in the design of wing structures, not only to ensure optimal aircraft performance in cruise conditions, but, more importantly, to obtain the correct design loads, making it paramount to integrate the jig shape in the design process of wing structures.

In conclusion, the optimised wing designs for the CRM show that aeroelastic tailoring provides significant benefits over conventional composite design approaches

making it one of the promising technologies to significantly improve future wing designs.

### Final conclusions

In order to further investigate the benefits of aeroelastic tailoring and morphing and formulate an answer to the main research question, trailing edge camber morphing mechanisms have been installed on the CRM and combined optimisations have been carried out. The resulting wing designs are optimally designed across a range of flight conditions, resulting in weight reductions of up to 34% over the wing designs without trailing edge camber morphing, thereby clearly illustrating the potential of combined aeroelastic tailoring and morphing for improved aircraft performance, although substantial further research is required before definitive conclusions can be drawn. Furthermore, when using morphing mechanisms for manoeuvre load alleviation, care should be taken in order to ensure aircraft safety, especially when the morphing mechanisms fail, which might reduce the potential benefits of trailing edge camber morphing for wing weight reduction.

In conclusion, both aeroelastic tailoring and morphing have been successfully applied to the structural design of aircraft wings, resulting in wing designs that take advantage of the aeroelastic response of the wing, ensuring optimal performance at cruise flight conditions, while showing significant improvements at off-cruise conditions.

## 9.2 Recommendations

The framework presented in this dissertation can be seen as the next step towards an aeroelastic analysis and optimisation framework for the design of aeroelastically tailored and morphing wings that incorporates all relevant factors and provides insights in the potential benefits of aeroelastic tailoring and morphing for the design of aircraft. However, several steps still need to be taken before definitive conclusions can be drawn. Hence, this section gives recommendations for future steps to improve the presented framework, provide additional experimental validation data, and improve the resulting wing designs, followed by a general outlook.



### Aeroelastic analysis and optimisation framework

Most aircraft operate in transonic flight conditions, where small disturbance potential flow theory looses accuracy and higher fidelity aerodynamic models are typically required. A possible approach to integrate transonic aerodynamic effects in the present framework is through a defect-correction approach as introduced

by Dillinger et al. (2015) and Jovanov and De Breuker (2015), thereby maintaining the efficiency of potential flow solutions when possible, while integrating the accuracy of high-fidelity CFD solutions when required.

The accuracy of the design loads acting on the wing can be further improved by modelling the complete aircraft in contrast to a wing-only approach. This should include the effects of the fuselage on the load distribution on the wing, the effects of the empennage on the trim equilibrium solution, and the effects of control surfaces and, especially for discrete gust loads, the effects of flight dynamics on the dynamic aeroelastic response of the wing. As a next step, a fully flexible aircraft, including the flexibility of the engine pylon, the fuselage, and the empennage, should be accounted for to improve the assessment of aeroelastic stability and investigate the influence of the interaction of different aircraft components on the aeroelastic stability of the aircraft.

A fully nonlinear dynamic aeroelastic model might be required, depending on the flexibility of the wing structure under investigation. This requires an extension of the framework with a fully nonlinear dynamic structural model and a free, non-flat wake in the unsteady aerodynamic model to account for the effect of large deformations on the dynamic aeroelastic solution.

Finally, a stacking sequence retrieval step should be included to convert the optimised lamination parameters to actual manufacturable stacking sequences. Several methods exist to convert lamination parameters to a stacking sequence (see, for example, IJsselmuiden (2011), van Campen et al. (2012), Irisarri et al. (2014), or Raju et al. (2015)). In order to improve the accuracy of the stacking sequence retrieval step, blending constraints can be introduced in the lamination parameter optimisation, limiting the change of lamination parameter between two neighbouring locations depending on the change in thickness, as introduced by Macquart et al. (2016).

### EXPERIMENTAL VALIDATION

In order to further assess the validity of the framework, several additional experimental validation steps are required. As a first step, the experimental wing models should be improved by replacing the foam core by regular spars and introducing wing sweep and wing taper to make the experimental wing models representative of actual wing structures.



As a second step, tests at additional load conditions are required. The wings should be tested at high subsonic to transonic Mach numbers to assess the range of validity of the aerodynamic model and under discrete gust loads to validate the dynamic aeroelastic response. Sufficient wing flexibility should be present under all test conditions of interest to obtain aeroelastic validation data.

### Application to wing structural design

Integrating morphing mechanisms in a wing introduces additional operational freedom for aircraft. In order to operate these mechanisms, a morphing controller is required, which not only determines the optimal morphing shape at a given flight condition, but also the flight condition(s) at which morphing is carried out and the corresponding morphing sequence. This has only received limited attention in the literature and further research is required to investigate the optimal morphing flight condition and morphing sequence for a given change in morphing shape and provide guidelines for the development of morphing controllers.

So far, all morphing manoeuvres have been assumed to be quasi-steady, neglecting any structural dynamic or unsteady aerodynamic effects, which is a valid assumption for slow morphing manoeuvres. However, when morphing mechanisms will be used for manoeuvre load alleviation or as control surfaces, this assumption might no longer be valid and the influence of morphing on the dynamic response of the aircraft should be investigated.

The morphing framework can also be used for shape optimisation, which has shown promising results when introducing a free jig shape in the aeroelastic optimisation, and should be explored further. As a result, a generic aerodynamic shape optimisation problem can be set up with a limited set of design variables. By integrating this approach with aeroelastic tailoring, the optimised wing designs can be further improved by a full aerostructural optimisation for, for example, minimum fuel burn.

Another important step to further improve the aeroelastically tailored wing designs is a full investigation of the critical design loadcases of the aircraft, accounting for both symmetric and anti-symmetric steady manoeuvres, dynamic loads, and different mass and fuel cases. Furthermore, additional design studies can be carried out investigating the influence of the structural layout (e.g. stringer or rib pitch), possible manufacturing constraints in both the lamination parameter domain and the stacking sequence retrieval step, the influence of maintenance holes in the bottom skin of the wing, or the influence of fatigue loads.

Finally, this dissertation has only investigated the effect of aeroelastic tailoring and morphing on the design of aircraft wings; however, the loads on the complete aircraft change by changing the aeroelastic response of the wing. As a consequence, further improvements can possibly be made to the overall aircraft design, which should be investigated further.



### Outlook

Although further research is still required before definitive conclusions can be drawn on the benefits of both aeroelastic tailoring and morphing, both have been

successfully applied to the structural design of aircraft wings, improving aircraft performance and, thus, paving the way to a bright future for aircraft.

# A

# ADDITIONAL LAMINATION PARAMETER CONSTRAINTS

As mentioned in Section 3.2.2, Raju et al. (2014) and Wu et al. (2015) used the Cauchy-Schwarz inequality to derive two closed-form expressions constraining a combination of in-plane and out-of-plane lamination parameters, resulting in:

$$
\begin{aligned}
&5\left(V_{1\mathbf{A}}-V_{1\mathbf{D}}\right)^2-2\left(1+V_{3\mathbf{A}}-2\left(V_{1\mathbf{A}}\right)^2\right)\leq 0 \qquad \text{(A.1)}\\
&-16+32V_{3\mathbf{A}}+40V_{2\mathbf{D}}^2+40V_{1\mathbf{D}}^2+16V_{4\mathbf{A}}^2-80V_{2\mathbf{A}}V_{2\mathbf{D}}+72V_{2\mathbf{A}}^2-80V_{1\mathbf{A}}V_{1\mathbf{D}}\\
&+72V_{1\mathbf{A}}^2-80V_{4\mathbf{A}}V_{1\mathbf{D}}V_{2\mathbf{D}}+80V_{2\mathbf{A}}V_{4\mathbf{A}}V_{1\mathbf{D}}-40V_{3\mathbf{A}}V_{2\mathbf{D}}^2-120V_{3\mathbf{A}}V_{1\mathbf{D}}^2\\
&-32V_{3\mathbf{A}}V_{4\mathbf{A}}^2+80V_{3\mathbf{A}}V_{2\mathbf{A}}V_{2\mathbf{D}}-72V_{3\mathbf{A}}V_{2\mathbf{A}}^2-32V_{3\mathbf{A}}^3+80V_{1\mathbf{A}}V_{4\mathbf{A}}V_{2\mathbf{D}}\\
&-144V_{1\mathbf{A}}V_{2\mathbf{A}}V_{4\mathbf{A}}+240V_{1\mathbf{A}}V_{3\mathbf{A}}V_{1\mathbf{D}}-216V_{1\mathbf{A}}^2V_{3\mathbf{A}}-25V_{1\mathbf{D}}^2V_{2\mathbf{D}}^2\\
&+50V_{2\mathbf{A}}V_{1\mathbf{D}}^2V_{2\mathbf{D}}-105V_{2\mathbf{A}}^2V_{1\mathbf{D}}^2+160V_{3\mathbf{A}}V_{4\mathbf{A}}V_{1\mathbf{D}}V_{2\mathbf{D}}-160V_{3\mathbf{A}}V_{2\mathbf{A}}V_{4\mathbf{A}}V_{1\mathbf{D}}\\
&-40V_{3\mathbf{A}}^2V_{2\mathbf{D}}^2+120V_{3\mathbf{A}}^2V_{1\mathbf{D}}^2+16V_{3\mathbf{A}}^2V_{4\mathbf{A}}^2+80V_{3\mathbf{A}}^2V_{2\mathbf{A}}V_{2\mathbf{D}}-72V_{3\mathbf{A}}^2V_{2\mathbf{A}}^2\\
&+16V_{3\mathbf{A}}^4+50V_{1\mathbf{A}}V_{1\mathbf{D}}V_{2\mathbf{D}}^2+20V_{1\mathbf{A}}V_{2\mathbf{A}}V_{1\mathbf{D}}V_{2\mathbf{D}}+90V_{1\mathbf{A}}V_{2\mathbf{A}}^2V_{1\mathbf{D}}\\
&-160V_{1\mathbf{A}}V_{3\mathbf{A}}V_{4\mathbf{A}}V_{2\mathbf{D}}+288V_{1\mathbf{A}}V_{3\mathbf{A}}V_{2\mathbf{A}}V_{4\mathbf{A}}-240V_{1\mathbf{A}}V_{3\mathbf{A}}^2V_{1\mathbf{D}}-105V_{1\mathbf{A}}^2V_{2\mathbf{D}}^2\\
&+90V_{1\mathbf{A}}^2V_{2\mathbf{A}}V_{2\mathbf{D}}-81V_{1\mathbf{A}}^2V_{2\mathbf{A}}^2+216V_{1\mathbf{A}}^2V_{3\mathbf{A}}^2+50V_{4\mathbf{A}}V_{1\mathbf{D}}V_{2\mathbf{D}}^3\\
&+...
\end{aligned}
$$

$$
\begin{aligned}
&- 150V_{2\mathbf{A}}V_{4\mathbf{A}}V_{1\mathbf{D}}V_{2\mathbf{D}}^2 + 190V_{2\mathbf{A}}^2V_{4\mathbf{A}}V_{1\mathbf{D}}V_{2\mathbf{D}} - 90V_{2\mathbf{A}}^3V_{4\mathbf{A}}V_{1\mathbf{D}} + 50V_{3\mathbf{A}}V_{1\mathbf{D}}^2V_{2\mathbf{D}}^2 \\
&- 100V_{3\mathbf{A}}V_{2\mathbf{A}}V_{1\mathbf{D}}^2V_{2\mathbf{D}} + 210V_{3\mathbf{A}}V_{2\mathbf{A}}^2V_{1\mathbf{D}}^2 - 80V_{3\mathbf{A}}^2V_{4\mathbf{A}}V_{1\mathbf{D}}V_{2\mathbf{D}} \\
&+ 80V_{3\mathbf{A}}^2V_{2\mathbf{A}}V_{4\mathbf{A}}V_{1\mathbf{D}} + 40V_{3\mathbf{A}}^3V_{2\mathbf{D}}^2 - 40V_{3\mathbf{A}}^3V_{1\mathbf{D}}^2 - 80V_{3\mathbf{A}}^3V_{2\mathbf{A}}V_{2\mathbf{D}} + 72V_{3\mathbf{A}}^3V_{2\mathbf{A}}^2 \\
&- 50V_{1\mathbf{A}}V_{4\mathbf{A}}V_{2\mathbf{D}}^3 + 190V_{1\mathbf{A}}V_{2\mathbf{A}}V_{4\mathbf{A}}V_{2\mathbf{D}}^2 - 270V_{1\mathbf{A}}V_{2\mathbf{A}}^2V_{4\mathbf{A}}V_{2\mathbf{D}} + 162V_{1\mathbf{A}}V_{2\mathbf{A}}^3V_{4\mathbf{A}} \\
&- 100V_{1\mathbf{A}}V_{3\mathbf{A}}V_{1\mathbf{D}}V_{2\mathbf{D}}^2 - 40V_{1\mathbf{A}}V_{3\mathbf{A}}V_{2\mathbf{A}}V_{1\mathbf{D}}V_{2\mathbf{D}} - 180V_{1\mathbf{A}}V_{3\mathbf{A}}V_{2\mathbf{A}}^2V_{1\mathbf{D}} \\
&+ 80V_{1\mathbf{A}}V_{3\mathbf{A}}^2V_{4\mathbf{A}}V_{2\mathbf{D}} - 144V_{1\mathbf{A}}V_{3\mathbf{A}}^2V_{2\mathbf{A}}V_{4\mathbf{A}} + 80V_{1\mathbf{A}}V_{3\mathbf{A}}^3V_{1\mathbf{D}} + 210V_{1\mathbf{A}}^2V_{3\mathbf{A}}V_{2\mathbf{D}}^2 \\
&- 180V_{1\mathbf{A}}^2V_{3\mathbf{A}}V_{2\mathbf{A}}V_{2\mathbf{D}} + 162V_{1\mathbf{A}}^2V_{3\mathbf{A}}V_{2\mathbf{A}}^2 - 72V_{1\mathbf{A}}^2V_{3\mathbf{A}}^3 - 25V_{4\mathbf{A}}^2V_{2\mathbf{D}}^4 \\
&+ 100V_{2\mathbf{A}}V_{4\mathbf{A}}^2V_{2\mathbf{D}}^3 - 190V_{2\mathbf{A}}^2V_{4\mathbf{A}}^2V_{2\mathbf{D}}^2 + 180V_{2\mathbf{A}}^3V_{4\mathbf{A}}^2V_{2\mathbf{D}} - 81V_{2\mathbf{A}}^4V_{4\mathbf{A}}^2 \\
&- 50V_{3\mathbf{A}}V_{4\mathbf{A}}V_{1\mathbf{D}}V_{2\mathbf{D}}^3 + 150V_{3\mathbf{A}}V_{2\mathbf{A}}V_{4\mathbf{A}}V_{1\mathbf{D}}V_{2\mathbf{D}}^2 - 190V_{3\mathbf{A}}V_{2\mathbf{A}}^2V_{4\mathbf{A}}V_{1\mathbf{D}}V_{2\mathbf{D}} \\
&+ 90V_{3\mathbf{A}}V_{2\mathbf{A}}^3V_{4\mathbf{A}}V_{1\mathbf{D}} - 25V_{3\mathbf{A}}^2V_{1\mathbf{D}}^2V_{2\mathbf{D}}^2 + 50V_{3\mathbf{A}}^2V_{2\mathbf{A}}V_{1\mathbf{D}}^2V_{2\mathbf{D}} - 105V_{3\mathbf{A}}^2V_{2\mathbf{A}}^2V_{1\mathbf{D}}^2 \\
&+ 50V_{1\mathbf{A}}V_{3\mathbf{A}}V_{4\mathbf{A}}V_{2\mathbf{D}}^3 - 190V_{1\mathbf{A}}V_{3\mathbf{A}}V_{2\mathbf{A}}V_{4\mathbf{A}}V_{2\mathbf{D}}^2 + 270V_{1\mathbf{A}}V_{3\mathbf{A}}V_{2\mathbf{A}}^2V_{4\mathbf{A}}V_{2\mathbf{D}} \\
&- 162V_{1\mathbf{A}}V_{3\mathbf{A}}V_{2\mathbf{A}}^3V_{4\mathbf{A}} + 50V_{1\mathbf{A}}V_{3\mathbf{A}}^2V_{1\mathbf{D}}V_{2\mathbf{D}}^2 + 20V_{1\mathbf{A}}V_{3\mathbf{A}}^2V_{2\mathbf{A}}V_{1\mathbf{D}}V_{2\mathbf{D}} \\
&+ 90V_{1\mathbf{A}}V_{3\mathbf{A}}^2V_{2\mathbf{A}}^2V_{1\mathbf{D}} - 105V_{1\mathbf{A}}^2V_{3\mathbf{A}}^2V_{2\mathbf{D}}^2 + 90V_{1\mathbf{A}}^2V_{3\mathbf{A}}^2V_{2\mathbf{A}}V_{2\mathbf{D}} \\
&- 81V_{1\mathbf{A}}^2V_{3\mathbf{A}}^2V_{2\mathbf{A}}^2 \leq 0
\end{aligned}
\tag{A.2}
$$

# B

# STIFFNESS MATRIX CONTRIBUTION OF ECCENTRIC FORCES AND MOMENTS

This appendix presents the stiffness contribution originating from applied eccentric forces and moments, as introduced in Section 3.4.2. Starting from equation (3.61):

$$\mathbf{F_e} = \mathbf{H^T B_{ex}^T F_{ec}}$$

the corresponding stiffness matrix is defined by equation (3.62):

$$\boldsymbol{\delta} \mathbf{F_e} = \mathbf{K_e} \boldsymbol{\delta} \mathbf{p}$$

Taking the variation of equation (3.61), three contributions to the stiffness matrix can be identified:

$$\boldsymbol{\delta} \mathbf{F_e} = \boldsymbol{\delta} \mathbf{H^T B_{ex}^T F_{ec}} + \mathbf{H^T} \boldsymbol{\delta} \mathbf{B_{ex}^T F_{ec}} + \mathbf{H^T B_{ex}^T} \boldsymbol{\delta} \mathbf{F_{ec}} \tag{B.1}$$

where the first contribution (i.e. the variation of $\mathbf{H}$) is commonly called the geometric moment stiffness, the second contribution (i.e. the variation of $\mathbf{B_{ex}}$) is commonly called the geometric rotation stiffness, and the final contribution (i.e. the variation of the external force vector, $\mathbf{F_{ec}}$) is commonly called the material

stiffness. Note that the final contribution will only be non-zero in case of follower forces and moments.

First of all, the geometric moment stiffness matrix, $\mathbf{K_h}$, can be derived by inserting equation (3.60) in the first term of equation (B.1) and introducing $\mathbf{a} = \mathbf{B_{ex}^T F_{ec}}$ for brevity, resulting in:



$$\boldsymbol{\delta}\mathbf{H}^{\mathbf{T}}\mathbf{B}_{\mathbf{ex}}^{\mathbf{T}}\mathbf{F}_{\mathbf{ec}} = \begin{bmatrix} \mathbf{0} & & & \mathbf{0} \\ & \boldsymbol{\delta}\mathbf{T_s}\left(\boldsymbol{\theta_1}\right)\mathbf{a} & & \\ & & \mathbf{0} & \\ \mathbf{0} & & & \boldsymbol{\delta}\mathbf{T_s}\left(\boldsymbol{\theta_2}\right)\mathbf{a} \end{bmatrix} \tag{B.2}$$

$$= \underbrace{\begin{bmatrix} \mathbf{0} & & & \mathbf{0} \\ & \frac{\partial}{\partial \boldsymbol{\theta_1}}\left[\mathbf{T_s}\left(\boldsymbol{\theta_1}\right)\mathbf{a}\right] & & \\ & & \mathbf{0} & \\ \mathbf{0} & & & \frac{\partial}{\partial \boldsymbol{\theta_1}}\left[\mathbf{T_s}\left(\boldsymbol{\theta_2}\right)\mathbf{a}\right] \end{bmatrix}}_{\mathbf{K_h}} \boldsymbol{\delta}\mathbf{p} \tag{B.3}$$

where $\mathbf{a}$ is a constant vector under differentiation and $\frac{\partial}{\partial \boldsymbol{\theta}}\left[\mathbf{T_s a}\right]$ has been derived by Battini and Pacoste (2002).

Secondly, the geometric rotation stiffness, $\mathbf{K_g}$, can be derived by first taking the variation of $\mathbf{B_{ex}}$, as defined by equation (3.57), resulting in:

$$\boldsymbol{\delta}\mathbf{B}_{\mathbf{ex}} = \begin{bmatrix} \mathbf{0} & -\left(1-\xi\right)\boldsymbol{\delta}\tilde{\mathbf{r}} & \mathbf{0} & -\xi\boldsymbol{\delta}\tilde{\mathbf{r}} \\ \mathbf{0} & \mathbf{0} & \mathbf{0} & \mathbf{0} \end{bmatrix} \tag{B.4}$$

where $\boldsymbol{\delta}\mathbf{r}$ can be derived through equations (3.47) and (3.54), resulting in:

$$\boldsymbol{\delta}\mathbf{r} = -\tilde{\mathbf{r}}\boldsymbol{\delta}\boldsymbol{\vartheta}_{\mathbf{a}} \tag{B.5}$$

Next, by inserting equations (B.4) and (B.5) in the second term of equation (B.1) and introducing a linear interpolation similar to equation (3.57) to link the degrees of freedom of location $a$ to the degrees of freedom of corresponding nodes 1 and 2, the final expression for $\mathbf{K_g}$ can be derived, resulting in:

$$\mathbf{H^T}\boldsymbol{\delta}\mathbf{B_{ex}^T}\mathbf{F_{ec}} = \mathbf{H^T}\underbrace{\begin{bmatrix}\mathbf{0} & \mathbf{0} & \mathbf{0} & \mathbf{0}\\ \mathbf{0} & (1-\xi)^2\,\tilde{\mathbf{N}}_{\mathbf{ec}}\tilde{\mathbf{r}} & \mathbf{0} & \xi\,(1-\xi)\,\tilde{\mathbf{N}}_{\mathbf{ec}}\tilde{\mathbf{r}}\\ \mathbf{0} & \mathbf{0} & \mathbf{0} & \mathbf{0}\\ \mathbf{0} & \xi\,(1-\xi)\,\tilde{\mathbf{N}}_{\mathbf{ec}}\tilde{\mathbf{r}} & \mathbf{0} & \xi^2\tilde{\mathbf{N}}_{\mathbf{ec}}\tilde{\mathbf{r}}\end{bmatrix}}_{\mathbf{L_g}}\boldsymbol{\delta}\mathbf{p_g} \tag{B.6}$$

$$= \underbrace{\mathbf{H^T}\mathbf{L_g}\mathbf{H}}_{\mathbf{K_g}}\boldsymbol{\delta}\mathbf{p} \tag{B.7}$$



where the eccentric forces and moments, $\mathbf{F_{ec}}$, have been split in separate forces, $\mathbf{N_{ec}}$, and moments, $\mathbf{M_{ec}}$. As can be seen, only applied eccentric forces results in additional geometric rotation stiffness.

Thirdly, the material stiffness matrix, $\mathbf{K_m}$, can be obtained by recognizing that, in case of follower forces and moments, the eccentric forces and moments follow the rotation of location $a$:

$$\mathbf{F_{ec}} = \begin{pmatrix}\mathbf{N_{ec}}\\ \mathbf{M_{ec}}\end{pmatrix} = \begin{pmatrix}\mathbf{R_a}\mathbf{N_0}\\ \mathbf{R_a}\mathbf{M_0}\end{pmatrix} \tag{B.8}$$

where $\mathbf{N_0}$ and $\mathbf{M_0}$ represent the original eccentric forces and moments, respectively, applied on the undeformed structure. Taking the variation of equation (B.8), introducing equation (3.54) for the variation of a rotation matrix and using $\mathbf{a\tilde{b}} = -\mathbf{b\tilde{a}}$, the following relation is obtained:

$$\boldsymbol{\delta}\mathbf{F_{ec}} = \begin{pmatrix}\boldsymbol{\delta}\mathbf{R_a}\mathbf{N_0}\\ \boldsymbol{\delta}\mathbf{R_a}\mathbf{M_0}\end{pmatrix} = \begin{pmatrix}\boldsymbol{\delta}\tilde{\boldsymbol{\vartheta}}_\mathbf{a}\mathbf{R_a}\mathbf{N_0}\\ \boldsymbol{\delta}\tilde{\boldsymbol{\vartheta}}_\mathbf{a}\mathbf{R_a}\mathbf{M_0}\end{pmatrix} = -\begin{pmatrix}\tilde{\mathbf{N}}_{\mathbf{ec}}\boldsymbol{\delta}\boldsymbol{\vartheta}_\mathbf{a}\\ \tilde{\mathbf{M}}_{\mathbf{ec}}\boldsymbol{\delta}\boldsymbol{\vartheta}_\mathbf{a}\end{pmatrix} \tag{B.9}$$

Next, by inserting equation (B.9) in the third term of equation (B.1) and introducing a linear interpolation to link the degrees of freedom of location $a$ to the degrees of freedom of corresponding nodes 1 and 2, the final expression of $\mathbf{K_m}$ can be derived, resulting in:

$$\mathbf{H^T}\mathbf{B_{ex}^T}\boldsymbol{\delta}\mathbf{F_{ec}} = \underbrace{\mathbf{H^T}\mathbf{B_{ex}^T}\begin{bmatrix}\tilde{\mathbf{N}}_{\mathbf{ec}}\\ \tilde{\mathbf{M}}_{\mathbf{ec}}\end{bmatrix}\begin{bmatrix}\mathbf{0} & (1-\xi)\mathbf{I} & \mathbf{0} & \xi\mathbf{I}\end{bmatrix}\mathbf{H}}_{\mathbf{K_m}}\boldsymbol{\delta}\mathbf{p} \tag{B.10}$$

Finally, introducing equations (B.2), (B.6), and (B.10) in equation (3.62), the stiffness matrix contribution originating from applied eccentric forces and moments becomes:

$$\mathbf{K_e} = \mathbf{K_h} + \mathbf{K_g} + \mathbf{K_m} \tag{B.11}$$

# C

# DERIVATION OF THE CONTINUOUS-TIME STATE-SPACE SYSTEM

This appendix presents the derivation of the continuous-time state-space system of the unsteady aerodynamics around an aircraft wing, as presented in Section 4.5.

## C.1 DERIVATION OF THE STATE EQUATION

As derived in Sections 4.3 and 4.5.1, the system of equations governing the potential flow solution around a wing is given by equations (4.19), (4.22), and (4.35):

$$\begin{aligned} \mathbf{K_1\Gamma_b} + \mathbf{K_2\Gamma_{w_0}} + \mathbf{K_3\Gamma_w} &= -\mathbf{V}\cdot\mathbf{n} \\ \mathbf{K_4\Gamma_b} + \mathbf{K_5\Gamma_{w_0}} &= \mathbf{0} \\ \mathbf{K_6\Gamma_w} + \mathbf{K_7\Gamma_{w_0}} &= \dot{\mathbf{\Gamma}}_\mathbf{w} \end{aligned}$$

with $-\mathbf{V} \cdot \mathbf{n}$ for a panel $p$ defined by equation (4.21):

$$-\mathbf{V_p} \cdot \mathbf{n_p} = \underbrace{-\mathbf{V_\infty} \cdot \mathbf{n_p}}_{\text{mean steady flow}} \quad \underbrace{-V_\infty n_{z_p} \alpha}_{\text{free-stream perturbation}} \quad \underbrace{-\mathbf{V_\infty} \cdot \Delta\mathbf{n_p} + \mathbf{V_b} \cdot \mathbf{n_p}}_{\text{motion of the wing surface}}$$

Focusing on the unsteady aerodynamic solution around the mean steady flow, equation (4.19) can be written as:

$$\mathbf{K_1 \Gamma_b} + \mathbf{K_2 \Gamma_{w_0}} + \mathbf{K_3 \Gamma_w} = \mathbf{B_1} \boldsymbol{\alpha} + \mathbf{B_2} \tag{C.1}$$

C

where $\mathbf{B_1}$ represents the contribution of the free-stream perturbation and $\mathbf{B_2}$ the contribution of the motion of the wing surface.

Using equation (4.19), $\mathbf{\Gamma_b}$ can be written as function of $\mathbf{\Gamma_{w_0}}$, $\mathbf{\Gamma_w}$, the free-stream perturbation, and the motion of the wing surface:

$$\mathbf{\Gamma_b} = \mathbf{K_1}^{-1} \left( -\mathbf{K_2 \Gamma_{w_0}} - \mathbf{K_3 \Gamma_w} + \mathbf{B_1} \boldsymbol{\alpha} + \mathbf{B_2} \right) \tag{C.2}$$

When this is inserted in equation (4.22), $\mathbf{\Gamma_{w_0}}$ can be written as function of $\mathbf{\Gamma_w}$, the free-stream perturbation, and the motion of the wing surface:

$$\mathbf{\Gamma_{w_0}} = \left( \mathbf{K_5} - \mathbf{K_4 K_1^{-1} K_2} \right)^{-1} \mathbf{K_4 K_1^{-1}} \left( \mathbf{K_3 \Gamma_w} - \mathbf{B_1} \boldsymbol{\alpha} - \mathbf{B_2} \right) \tag{C.3}$$

Substituting this relation in the wake transport equation, the state equation of the state-space system can be derived and the unsteady aerodynamic solution can be obtained:

$$\dot{\mathbf{\Gamma}}_\mathbf{w} = \mathbf{K_8 \Gamma_w} + \mathbf{K_9} \boldsymbol{\alpha} + \mathbf{K_{10}}$$

where

$$\begin{aligned}
\mathbf{K_8} &= \mathbf{K_6} + \mathbf{K_7} \left( \mathbf{K_5} - \mathbf{K_4 K_1^{-1} K_2} \right)^{-1} \mathbf{K_4 K_1^{-1} K_3} \\
\mathbf{K_9} &= -\mathbf{K_7} \left( \mathbf{K_5} - \mathbf{K_4 K_1^{-1} K_2} \right)^{-1} \mathbf{K_4 K_1^{-1} B_1} \\
\mathbf{K_{10}} &= -\mathbf{K_7} \left( \mathbf{K_5} - \mathbf{K_4 K_1^{-1} K_2} \right)^{-1} \mathbf{K_4 K_1^{-1} B_2}
\end{aligned}$$

## C.2 Derivation of the output equation

Starting from equation (4.22) to write $\mathbf{\Gamma_{w_0}}$ as a function of $\mathbf{\Gamma_b}$:

$$\mathbf{\Gamma_{w_0}} = -\mathbf{K_5}^{-1}\mathbf{K_4}\mathbf{\Gamma_b} \tag{C.4}$$

and introducing this in equation (4.19), the vortex strength of the body panels can be related to the vortex strength of the free wake panels, $\mathbf{\Gamma_w}$, the free-stream perturbation, and the motion of the wing surface, resulting in:

$$\mathbf{\Gamma_b} = -\mathbf{L_3}^{-1}\mathbf{K_1}^{-1}\mathbf{K_3}\mathbf{\Gamma_w} + \mathbf{L_3}^{-1}\mathbf{K_1}^{-1}\mathbf{B_1}\boldsymbol{\alpha} + \mathbf{L_3}^{-1}\mathbf{K_1}^{-1}\mathbf{B_2} \tag{C.5}$$



where $\mathbf{L_3} = \mathbf{I} - \mathbf{K_1}^{-1}\mathbf{K_2}\mathbf{K_5}^{-1}\mathbf{K_4}$ with $\mathbf{I}$ the identity matrix and $\mathbf{B_1}$ represents the contribution of the free-stream perturbation and $\mathbf{B_2}$ the contribution of the motion of the wing surface, similar to Section C.1. Taking the time derivative of this equation, grouping all terms related to the motion of the wing surface, and substituting this in equation (4.26), the following equation for the aerodynamic forces and moments is found:

$$\begin{pmatrix}\mathbf{F}\\ \mathbf{M}\end{pmatrix} = \mathbf{L_4}\mathbf{\Gamma_w} + \mathbf{L_5}\boldsymbol{\alpha} + \mathbf{L_6}\dot{\mathbf{\Gamma}}_\mathbf{w} + \mathbf{L_7}\dot{\boldsymbol{\alpha}} + \mathbf{L_8} \tag{C.6}$$

where

$$\mathbf{L_4} = -\mathbf{L_1}\mathbf{L_3}^{-1}\mathbf{K_1}^{-1}\mathbf{K_3} \tag{C.7}$$
$$\mathbf{L_5} = \mathbf{L_1}\mathbf{L_3}^{-1}\mathbf{K_1}^{-1}\mathbf{B_1} \tag{C.8}$$
$$\mathbf{L_6} = -\mathbf{L_2}\mathbf{L_3}^{-1}\mathbf{K_1}^{-1}\mathbf{K_3} \tag{C.9}$$
$$\mathbf{L_7} = \mathbf{L_2}\mathbf{L_3}^{-1}\mathbf{K_1}^{-1}\mathbf{B_1} \tag{C.10}$$
$$\mathbf{L_8} = \mathbf{L_1}\mathbf{L_3}^{-1}\mathbf{K_1}^{-1}\mathbf{B_2} + \mathbf{L_2}\mathbf{L_3}^{-1}\mathbf{K_1}^{-1}\dot{\mathbf{B}}_\mathbf{2} \tag{C.11}$$

Finally, using equation (4.36), equation (C.6) can be reduced to:

$$\begin{pmatrix}\mathbf{F}\\ \mathbf{M}\end{pmatrix} = \mathbf{L_9}\mathbf{\Gamma_w} + \mathbf{L_{10}}\boldsymbol{\alpha} + \mathbf{L_7}\dot{\boldsymbol{\alpha}} + \mathbf{L_{11}}$$

with

$$\mathbf{L_9} = \mathbf{L_4} + \mathbf{L_6}\mathbf{K_8}$$
$$\mathbf{L_{10}} = \mathbf{L_5} + \mathbf{L_6}\mathbf{K_9}$$
$$\mathbf{L_{11}} = \mathbf{L_8} + \mathbf{L_6}\mathbf{K_{10}}$$

# D

# OPTIMISATION RESULTS WITHOUT AILERON EFFECTIVENESS CONSTRAINTS

This appendix shows the additional optimisation results of the optimised wing designs without aileron effectiveness constraints for the wings with a free jig twist distribution with and without trailing edge camber morphing. These results accompany the results discussed in Sections 8.4 and 8.6.

# D.1 WING DESIGNS WITH A FREE JIG TWIST DISTRIBUTION

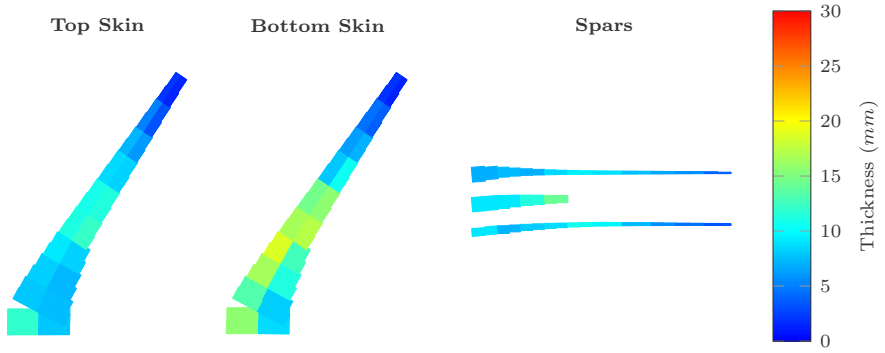


**(a)** Thickness distribution.



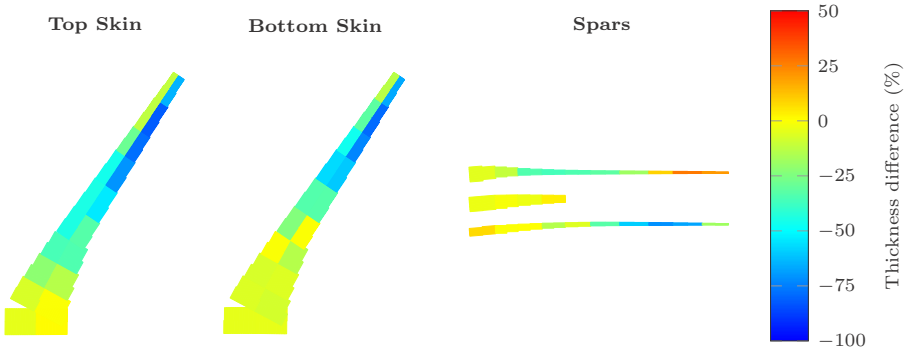


**(b)** Thickness comparison of the optimised CRM wing with predefined laminates with a free jig twist distribution and a cruise twist constraint without aileron effectiveness constraints to the wing with a free jig twist distribution and a cruise twist constraint with aileron effectiveness constraints.

**Figure D.1:** Thickness distribution and thickness comparison for the optimised CRM wing with predefined laminates with a free jig twist distribution and a cruise twist constraint without aileron effectiveness constraints. (The spars are displayed front to rear with the front spar at the top.)

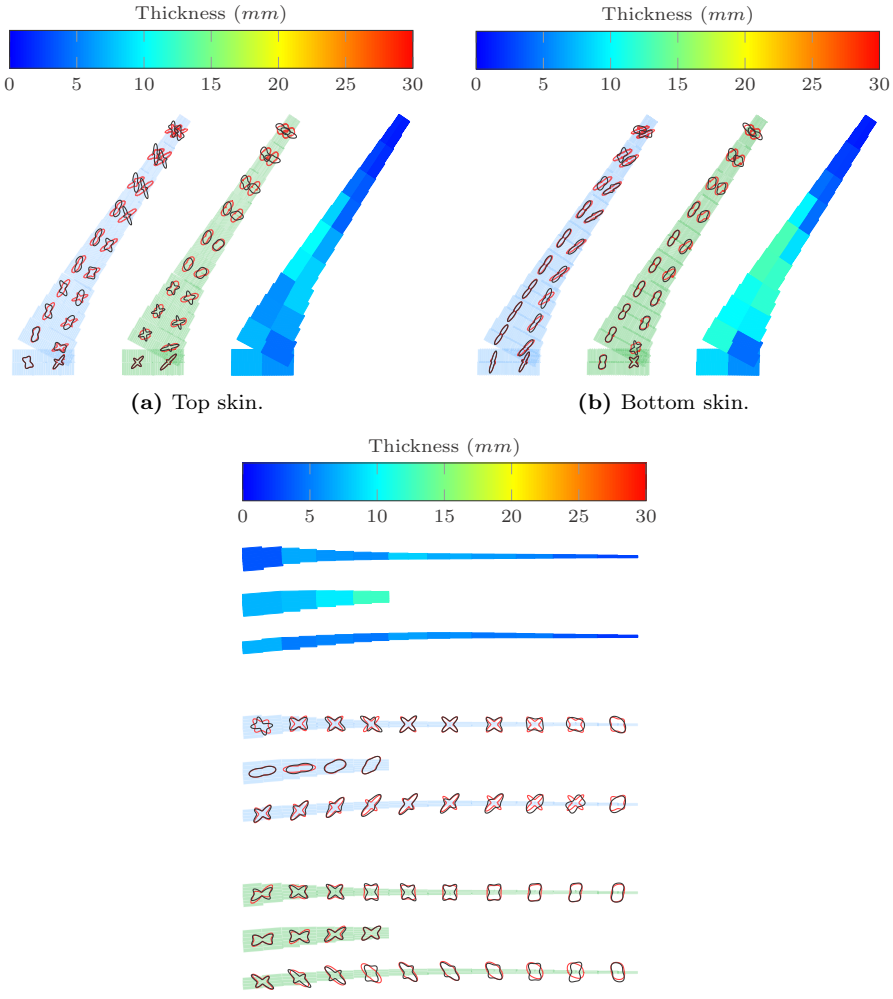


**(a)** Top skin. **(b)** Bottom skin.

**(c)** Spars.

**Figure D.2:** Stiffness and thickness distribution for the optimised CRM wing with unbalanced laminates with a free jig twist distribution and a cruise twist constraint without aileron effectiveness constraints. The stiffness distribution for the wing with unbalanced laminates with a free jig twist distribution and a cruise twist constraint with aileron effectiveness constraints is displayed in red for comparison.(In-plane stiffness: blue, out-of-plane stiffness: green. The spars are displayed front to rear with the front spar at the top.)

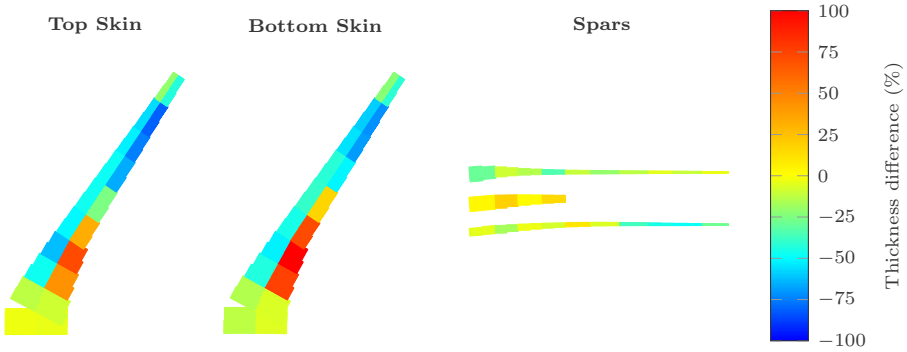


**Figure D.3:** Thickness comparison of the optimised CRM wing with unbalanced laminates with a free jig twist distribution and a cruise twist constraint without aileron effectiveness constraints to the wing with a free jig twist distribution and a cruise twist constraint with aileron effectiveness constraints. (The spars are displayed front to rear with the front spar at the top.)

## D.2 WING DESIGNS INCLUDING TRAILING EDGE CAMBER MORPHING

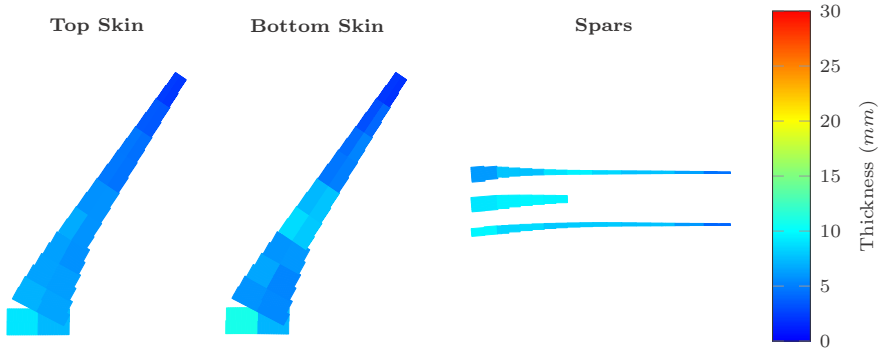


**(a)** Thickness distribution.

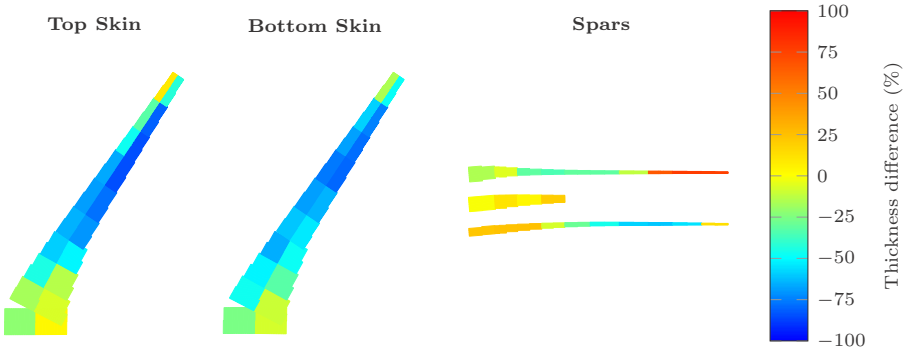


**(b)** Thickness comparison of the optimised CRM wing with predefined laminates including trailing edge camber morphing without aileron effectiveness constraints to the wing including trailing edge camber morphing with aileron effectiveness constraints.

**Figure D.4:** Thickness distribution and thickness comparison for the optimised CRM wing with predefined laminates including trailing edge camber morphing without aileron effectiveness constraints. (The spars are displayed front to rear with the front spar at the top.)

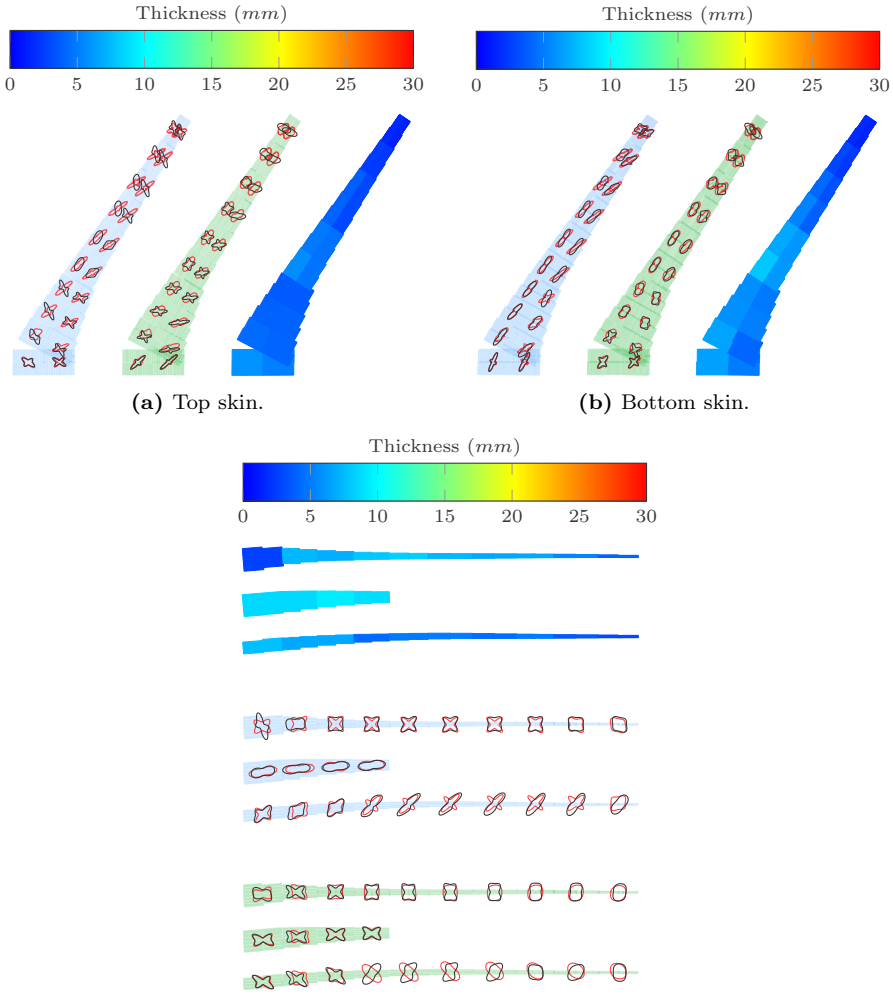


**(a)** Top skin.

**(b)** Bottom skin.

**(c)** Spars.

**Figure D.5:** Stiffness and thickness distribution for the optimised CRM wing with unbalanced laminates including trailing edge camber morphing without aileron effectiveness constraints. The stiffness distribution for the wing with unbalanced laminates including trailing edge camber morphing with aileron effectiveness constraints is displayed in red for comparison.(In-plane stiffness: blue, out-of-plane stiffness: green. The spars are displayed front to rear with the front spar at the top.)

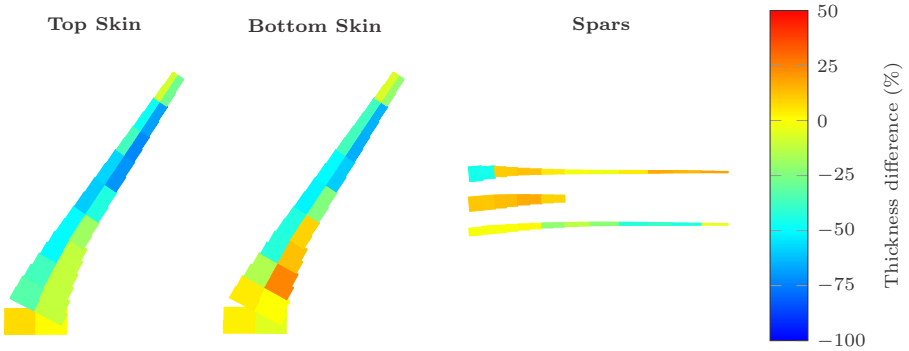


**Figure D.6:** Thickness comparison of the optimised CRM wing with unbalanced laminates including trailing edge camber morphing without aileron effectiveness constraints to the wing including trailing edge camber morphing with aileron effectiveness constraints. (The spars are displayed front to rear with the front spar at the top.)

# BIBLIOGRAPHY


Afonso, F., Vale, J., Lau, F., and Suleman, A. (2014). "Multidisciplinary performance based optimization of morphing aircraft". In *Proceedings of the 22nd AIAA/ASME/AHS Adaptive Structures Conference*. doi:10.2514/6.2014-0761.

Albano, E. and Rodden, W. P. (1969). "A doublet-lattice method for calculating lift distributions on oscillating surfaces in subsonic flows." *AIAA Journal*, vol. 7, no. 2, pp. 279–285. doi:10.2514/3.5086.

Bach, C., Jebari, R., Viti, A., and Hewson, R. (2017). "Composite stacking sequence optimization for aeroelastically tailored forward-swept wings". *Structural and Multidisciplinary Optimization*, vol. 55, no. 1, pp. 105–119. doi:10.1007/s00158-016-1477-3.

Barbarino, S., Bilgen, O., Ajaj, R. M., Friswell, M. I., and Inman, D. J. (2011). "A review of morphing aircraft". *Journal of Intelligent Material Systems and Structures*, vol. 22, no. 9, pp. 823–877. doi:10.1177/1045389X11414084.

Barbarino, S., Flores, E. I. S., Ajaj, R. M., Dayyani, I., and Friswell, M. I. (2014). "A review on shape memory alloys with applications to morphing aircraft". *Smart Materials and Structures*, vol. 23, no. 6, p. 063001. doi:10.1088/0964-1726/23/6/063001.

Bathe, K.-J. and Bolourchi, S. (1979). "Large displacement analysis of three-dimensional beam structures". *International Journal for Numerical Methods in Engineering*, vol. 14, no. 7, pp. 961–986. doi:10.1002/nme.1620140703.

Battini, J.-M. and Pacoste, C. (2002). "Co-rotational beam elements with warping effects in instability problems". *Computer Methods in Applied Mechanics and Engineering*, vol. 191, no. 1718, pp. 1755–1789. doi:10.1016/S0045-7825(01)00352-8.

Beaverstock, C. S., Fincham, J., Friswell, M. I., Ajaj, R. M., De Breuker, R., and Werter, N. P. M. (2014). "Effect of symmetric & asymmetric span morphing on flight dynamics". In *Proceedings of the AIAA Atmospheric Flight Mechanics Conference*. doi:10.2514/6.2014-0545.

Beran, P. S., Khot, N. S., Eastep, F. E., Snyder, R. D., and Zweber, J. V. (2004). "Numerical analysis of store-induced limit-cycle oscillation". *Journal of Aircraft*, vol. 41, no. 6, pp. 1315–1326. doi:10.2514/1.404.

Bertin, J. J. and Cummings, R. M. (2009). *Aerodynamics for Engineers*. Pearson Education, Inc., Upper Saddle River, NJ, USA.

Blair, M. (1992). "A compilation of the mathematics leading to the doublet lattice method". Tech. Rep. WL-TR-92-3028, DTIC.

Blair, M. and Weisshaar, T. A. (1982). "Swept composite wing aeroelastic divergence experiments". *Journal of Aircraft*, vol. 19, no. 11, pp. 1019–1024. doi:10.2514/3.44806.

Bloomfield, M. W., Diaconu, C. G., and Weaver, P. M. (2009). "On feasible regions of lamination parameters for lay-up optimization of laminated composites". *Proceedings of the Royal Society of London A: Mathematical, Physical and Engineering Sciences*, vol. 465, no. 2104, pp. 1123–1143. doi: 10.1098/rspa.2008.0380.

Bolonkin, A. and Gilyard, G. B. (1999). "Estimated benefits of variable-geometry wing camber control for transport aircraft". Tech. Rep. TM-1999-206586, NASA.

Bonnema, K. L. and Lokos, W. A. (1989). "AFTI/F-111 mission adaptive wing flight test instrumentation overview". In *Proceedings of the International Instrumentation Symposium*.

Bowman, J., Reich, G., Sanders, B., and Frank, G. (2006). "Simulation tool for analyzing complex shape-changing mechanisms in aircraft". In *Proceedings of the AIAA Modeling and Simulation Technologies Conference and Exhibit*. doi:10.2514/6.2006-6727.

Bowman, J., Sanders, B., Cannon, B., Kudva, J., Joshi, S., and Weisshaar, T. (2007). "Development of next generation morphing aircraft structures". In *Proceedings of the 48th AIAA/ASME/ASCE/AHS/ASC Structures, Structural Dynamics, and Materials Conference*. doi:10.2514/6.2007-1730.

Brooks, T. R., Kennedy, G., and Martins, J. R. R. A. (2016). "High-fidelity aerostructural optimization of a high aspect ratio tow-steered wing". In *Proceedings of the 57th AIAA/ASCE/AHS/ASC Structures, Structural Dynamics, and Materials Conference*. doi:10.2514/6.2016-1179.

Burdette, D. A., Kenway, G. K., Lyu, Z., and Martins, J. R. R. A. (2015). "Aerostructural design optimization of an adaptive morphing trailing edge wing". In *Proceedings of the 56th AIAA/ASCE/AHS/ASC Structures, Structural Dynamics, and Materials Conference*. doi:10.2514/6.2015-1129.

Burdette, D. A., Kenway, G. K., and Martins, J. R. R. A. (2016a). "Aerostructural design optimization of a continuous morphing trailing edge aircraft for improved mission performance". In *Proceedings of the 17th AIAA/ISSMO Multidisciplinary Analysis and Optimization Conference*. doi:10.2514/6.2016-3209.

Burdette, D. A., Kenway, G. K., and Martins, J. R. R. A. (2016b). "Performance evaluation of a morphing trailing edge using multipoint aerostructural design optimization". In *Proceedings of the 57th AIAA/ASCE/AHS/ASC Structures, Structural Dynamics, and Materials Conference*. doi:10.2514/6.2016-0159.

van Campen, J. M. J. F., Kassapoglou, C., and Gürdal, Z. (2012). "Generating realistic laminate fiber angle distributions for optimal variable stiffness laminates". *Composites Part B: Engineering*, vol. 43, no. 2, pp. 354–360. doi:10.1016/j.compositesb.2011.10.014.

Capuzzi, M., Pirrera, A., and Weaver, P. M. (2015). "Structural design of a novel aeroelastically tailored wind turbine blade". *Thin-Walled Structures*, vol. 95, pp. 7–15. doi:10.1016/j.tws.2015.06.006.

Cardoso, J., Suleman, A., and Cooper, J. E. (2013). "Performance evaluation of a morphing joined wing aircraft configuration". In *Proceedings of the 54th AIAA/ASME/ASCE/AHS/ASC Structures, Structural Dynamics, and Materials Conference*. doi:10.2514/6.2013-1450.

Carossa, G. M., Ricci, S., De Gaspari, A., Liauzun, C., Dumont, A., and Steinbuch, M. (2016). "Adaptive trailing edge: Specifications, aerodynamics, and exploitation". In Wölcken, P. C. and Papadopoulos, M., eds., *Smart Intelligent Aircraft Structures (SARISTU)*, pp. 143–158. Springer International Publishing. doi:10.1007/978-3-319-22413-8_7.

Cavagna, L., De Gaspari, A., and Ricci, S. (2013). "NeoCASS+, A conceptual design and simulation framework for morphing aircraft". *Journal of Aerospace Science, Technologies & Systems*, vol. 92, no. 1-2, pp. 52–60. doi:10.19249/ams.v92i1-2.91.

Cesnik, C. E. S. and Hodges, D. H. (1997). "VABS: A new concept for composite rotor blade crosssectional modeling". *Journal of the American Helicopter Society*, vol. 42, no. 1, pp. 27–38. doi:10.4050/JAHS.42.27.

Cesnik, C. E. S., Hodges, D. H., and Patil, M. J. (1996). "Aeroelastic analysis of composite wings". In *Proceedings of the 37th Structures, Structural Dynamics and Materials Conference*. doi:10.2514/6.1996-1444.

Chandra, R., Stemple, A. D., and Chopra, I. (1990). "Thin-walled composite beams under bending, torsional, and extensional loads". *Journal of Aircraft*, vol. 27, no. 7, pp. 619–626. doi:10.2514/3.25331.

Chen, G.-S. and Dugundji, J. (1987). "Experimental aeroelastic behavior of forward-swept graphite/epoxy wings with rigid-body freedom". *Journal of Aircraft*, vol. 24, no. 7, pp. 454–462. doi:10.2514/3.45501.

Ciarella, A., Tsotskas, C., Hahn, M., Werter, N. P. M., De Breuker, R., Beaverstock, C. S., Friswell, M. I., Yang, Y., Özgen, S., Antoniadis, A., Drikakis, D., and Tsoutsanis, P. (2015). "A multi-fidelity, multi-disciplinary analysis and optimization framework for the design of morphing UAV wing". In *Proceedings of the 16th AIAA/ISSMO Multidisciplinary Analysis and Optimization Conference*. doi:10.2514/6.2015-2326.

Correlated Solutions, Inc. (2015). "VIC-3D$^{TM}$ measurement system".

Crisfield, M. A. (1990). "A consistent co-rotational formulation for non-linear, three-dimensional, beam-elements". *Computer Methods in Applied Mechanics and Engineering*, vol. 81, no. 2, pp. 131–150. doi:10.1016/0045-7825(90)90106-V.

Crossley, W. A., Skillen, M. D., Frommer, J. B., and Roth, B. D. (2011). "Morphing aircraft sizing using design optimization". *Journal of Aircraft*, vol. 48, no. 2, pp. 612–622. doi:10.2514/1.C031180.

Cuji, E. and Garcia, E. (2008). "Prediction of aircraft dynamics with shape changing wings". In *Proceedings of the SPIE Conference on Active and Passive Smart Structures and Integrated Systems*, vol. 6928. doi:10.1117/12.776351.

Daniel, I. M. and Ishai, O. (2006). *Engineering Mechanics of Composite Materials*. Oxford University Press, New York, NY, USA.

Dayyani, I., Khodaparast, H. H., Woods, B. K. S., and Friswell, M. I. (2015). "The design of a coated composite corrugated skin for the camber morphing airfoil". *Journal of Intelligent Material Systems and Structures*, vol. 26, no. 13, pp. 1592–1608. doi:10.1177/1045389X14544151.

De Breuker, R. (2011). *Energy-based Aeroelastic Analysis and Optimisation of Morphing Wings*. Ph.D. thesis, Delft University of Technology, Delft, The Netherlands.

De Breuker, R., Abdalla, M. M., and Gürdal, Z. (2011). "A generic morphing wing analysis and design framework". *Journal of Intelligent Material Systems and Structures*, vol. 22, no. 10, pp. 1025–1039. doi:10.1177/1045389x11414958.

De Breuker, R. and Werter, N. P. M. (2016). "On the importance of morphing deformation scheduling for actuation force and energy". *Aerospace*, vol. 3, no. 4, p. 41. doi:10.3390/aerospace3040041.

De Gaspari, A. and Ricci, S. (2011). "A two-level approach for the optimal design of morphing wings based on compliant structures". *Journal of Intelligent Material Systems and Structures*, vol. 22, no. 10, pp. 1091–1111. doi:10.1177/1045389X11409081.

De Gaspari, A. and Ricci, S. (2014). "Application of the active camber morphing concept based on compliant structures to a regional aircraft". In *Proceedings of the SPIE Conference on Industrial and Commercial Applications of Smart Structures*, vol. 9059. doi:10.1117/12.2045225.

De Gaspari, A. and Ricci, S. (2015). "Knowledge-based shape optimization of morphing wing for more efficient aircraft". *International Journal of Aerospace Engineering*, vol. 2015. doi:10.1155/2015/325724.

De Gaspari, A., Ricci, S., Antunes, A., Odaguil, F., and Lima, G. (2014). "Application of active camber morphing concept to a regional aircraft". In *Proceedings of the 22nd AIAA/ASME/AHS Adaptive Structures Conference*. doi:10.2514/6.2014-1259.

De Gaspari, A., Ricci, S., Travaglini, L., Cavagna, L., Antunes, A., Odaguil, F., and Lima, G. (2015). "Active camber morphing wings based on compliant structures: an aeroelastic assessment". In *Proceedings of the 23rd AIAA/AHS Adaptive Structures Conference*. doi:10.2514/6.2015-1054.

De Leon, D. M., de Souza, C. E., Fonseca, J. S. O., and da Silva, R. G. A. (2012). "Aeroelastic tailoring using fiber orientation and topology optimization". *Structural and Multidisciplinary Optimization*, vol. 46, no. 5, pp. 663–677. doi:10.1007/s00158-012-0790-8.

Dillinger, J. K. S., Abdalla, M. M., Meddaikar, Y. M., and Klimmek, T. (2015). "Static aeroelastic stiffness optimization of a forward swept composite wing with CFD corrected aero loads". In *Proceedings of the International Forum on Aeroelasticity and Structural Dynamics 2015*.

Dillinger, J. K. S., Klimmek, T., Abdalla, M. M., and Gürdal, Z. (2013). "Stiffness optimization of composite wings with aeroelastic constraints". *Journal of Aircraft*, vol. 50, no. 4, pp. 1159–1168. doi:10.2514/1.C032084.

Dimino, I., Ciminello, M., Concilio, A., Pecora, R., Amoroso, F., Magnifico, M., Schueller, M., Gratias, A., Volovick, A., and Zivan, L. (2016). "Distributed actuation and control of a morphing wing trailing edge". In Wölcken, P. C. and Papadopoulos, M., eds., *Smart Intelligent Aircraft Structures (SARISTU)*, pp. 171–186. Springer International Publishing. doi:10.1007/978-3-319-22413-8_9.

Diodati, G., Concilio, A., Ricci, S., De Gaspari, A., Huvelin, F., Dumont, A., and Godard, J.-L. (2013). "Estimated performance of an adaptive trailing-edge device aimed at reducing fuel consumption on a medium-size aircraft". In

*Proceedings of the SPIE Conference on Industrial and Commercial Applications of Smart Structures*, vol. 8690. doi:10.1117/12.2013685.

Drela, M. (1999). "Integrated simulation model for preliminary aerodynamic, structural, and control-law design of aircraft". In *Proceedings of the 40th Structures, Structural Dynamics, and Materials Conference and Exhibit*. doi:10.2514/6.1999-1394.

EASA (2016). "Certification specifications and acceptable means of compliance for large aeroplanes CS-25". Tech. Rep., EASA.

Eastep, F. E., Tischler, V. A., Venkayya, V. B., and Khot, N. S. (1999). "Aeroelastic tailoring of composite structures". *Journal of Aircraft*, vol. 36, no. 6, pp. 1041–1047. doi:10.2514/2.2546.

Engø, K. (2001). "On the BCH-formula in so(3)". *BIT Numerical Mathematics*, vol. 41, no. 3, pp. 629–632. doi:10.1023/A:1021979515229.

Essa, Y., Cutillas, F. M. d. l. E., Dimino, I., Ciminello, M., and Concilio, A. (2016). "Manufacturing and testing of smart morphing SARISTU trailing edge". In Wölcken, P. C. and Papadopoulos, M., eds., *Smart Intelligent Aircraft Structures (SARISTU)*, pp. 199–215. Springer International Publishing. doi:10.1007/978-3-319-22413-8_11.

European Commission (2011). "Flightpath 2050 Europes vision for aviation". Tech. Rep., European Union.

FAA (2016). "Federal aviation regulations Part 25 - Airworthiness standards: Transport category airplanes". Tech. Rep., FAA.

Farhat, C. (2004). "CFD-based nonlinear computational aeroelasticity". In *Encyclopedia of Computational Mechanics*. John Wiley & Sons, Ltd. doi:10.1002/0470091355.ecm063.

Fazelzadeh, S. A., Mazidi, A., and Kalantari, H. (2009). "Bending-torsional flutter of wings with an attached mass subjected to a follower force". *Journal of Sound and Vibration*, vol. 323, no. 12, pp. 148–162. doi:10.1016/j.jsv.2009.01.002.

Ferede, E. and Abdalla, M. M. (2014). "Cross-sectional modelling of thin-walled composite beams". In *Proceedings of the 55th AIAA/ASME/ASCE/AHS/SC Structures, Structural Dynamics, and Materials Conference*. doi:10.2514/6.2014-0163.

Ferrier, Y., Nguyen, N. T., and Ting, E. (2016). "Real-time adaptive least-squares drag minimization for performance adaptive aeroelastic wing". In *Proceedings of the 34th AIAA Applied Aerodynamics Conference*. doi:10.2514/6.2016-3567.

Frommer, J. and Crossley, W. A. (2005). "Enabling continuous optimization for sizing morphing aircraft concepts". In *Proceedings of the 43rd AIAA Aerospace Sciences Meeting and Exhibit*. doi:10.2514/6.2005-816.

Frommer, J. and Crossley, W. A. (2006). "Building surrogate models for capability-based evaluation: Comparing morphing and fixed geometry aircraft in a fleet context". In *Proceedings of the 6th AIAA Aviation Technology, Integration and Operations Conference (ATIO)*. doi:10.2514/6.2006-7700.

Gamboa, P., Vale, J., Lau, F. J. P., and Suleman, A. (2009). "Optimization of a morphing wing based on coupled aerodynamic and structural constraints". *AIAA Journal*, vol. 47, no. 9, pp. 2087–2104. doi:10.2514/1.39016.

Georgiou, G., Vio, G. A., and Cooper, J. E. (2014). "Aeroelastic tailoring and scaling using bacterial foraging optimisation". *Structural and Multidisciplinary Optimization*, vol. 50, no. 1, pp. 81–99. doi:10.1007/s00158-013-1033-3.

Gern, F. H., Inman, D. J., and Kapania, R. K. (2002). "Structural and aeroelastic modeling of general planform wings with morphing airfoils". *AIAA Journal*, vol. 40, no. 4, pp. 628–637. doi:10.2514/2.1719.

Gern, F. H. and Librescu, L. (2000). "Aeroelastic tailoring of composite wings exhibiting nonclassical effects and carrying external stores". *Journal of Aircraft*, vol. 37, no. 6, pp. 1097–1104. doi:10.2514/2.2718.

Geuzaine, P., Brown, G., Harris, C., and Farhat, C. (2003). "Aeroelastic dynamic analysis of a full F-16 configuration for various flight conditions". *AIAA Journal*, vol. 41, no. 3, pp. 363–371. doi:10.2514/2.1975.

Giesing, J. P., Kalman, T. P., and Rodden, W. P. (1971). "Subsonic unsteady aerodynamic for general configurations Part I,Vol I - Direct application of the nonplanar doublet-lattice method". Tech. Rep. TR-71-5, AFFDL.

Gimmestad, D. (1979). "An aeroelastic optimization procedure for composite high aspect ratio wings". In *Proceedings of the 20th Structures, Structural Dynamics, and Materials Conference*. doi:10.2514/6.1979-726.

Goland, M. (1945). "The flutter of a uniform cantilever wing". *Journal of Applied Mechanics*, vol. 12, no. 4, pp. A197–A208.

Gomez, J. C. and Garcia, E. (2011). "Morphing unmanned aerial vehicles". *Smart Materials and Structures*, vol. 20, no. 10. doi:10.1088/0964-1726/20/10/103001.

Guo, S. J. (2007). "Aeroelastic optimization of an aerobatic aircraft wing structure". *Aerospace Science and Technology*, vol. 11, no. 5, pp. 396–404. doi:10.1016/J.Ast.2007.01.003.

Guo, S. J., Bannerjee, J. R., and Cheung, C. W. (2003). "The effect of laminate lay-up on the flutter speed of composite wings". *Proceedings of the Institution of Mechanical Engineers Part G: Journal of Aerospace Engineering*, vol. 217, no. 3, pp. 115–122. doi:10.1243/095441003322297225.

Guo, S. J., Cheng, W. Y., and Cui, D. G. (2006). "Aeroelastic tailoring of composite wing structures by laminate layup optimization". *AIAA Journal*, vol. 44, no. 12, pp. 3146–3150. doi:10.2514/1.20166.

Gürdal, Z., Haftka, R., and Hajela, P. (1999). *Design and Optimization of Laminated Composite Materials*. John Wiley & Sons, Inc., New York, NY, USA.

Guyan, R. J. (1965). "Reduction of stiffness and mass matrices". *AIAA Journal*, vol. 3, no. 2, p. 380. doi:10.2514/3.2874.

Haddadpour, H. and Zamani, Z. (2012). "Curvilinear fiber optimization tools for aeroelastic design of composite wings". *Journal of Fluids and Structures*, vol. 33, pp. 180–190. doi:10.1016/j.jfluidstructs.2012.05.008.

Hall, K. C. (1994). "Eigenanalysis of unsteady flows about airfoils, cascades, and wings". *AIAA Journal*, vol. 32, no. 12, pp. 2426–2432. doi:10.2514/3.12309.

Hammer, V. B., Bendsøe, M. P., Lipton, R., and Pedersen, P. (1997). "Parametrization in laminate design for optimal compliance". *International Journal of Solids and Structures*, vol. 34, no. 4, pp. 415–434. doi:10.1016/S0020-7683(96)00023-6.

Hayat, K. and Ha, S. K. (2015). "Load mitigation of wind turbine blade by aeroelastic tailoring via unbalanced laminates composites". *Composite Structures*, vol. 128, pp. 122–133. doi:10.1016/j.compstruct.2015.03.042.

Hertz, T. J., Shirk, M. H., Ricketts, R. H., and Weisshaar, T. A. (1981). "Aeroelastic tailoring with composites applied to forward swept wings". Tech. Rep. AFWAL-TR-81-3043, DTIC.

Hesse, H. and Palacios, R. (2014). "Reduced-order aeroelastic models for dynamics of maneuvering flexible aircraft". *AIAA Journal*, vol. 52, no. 8, pp. 1717–1732. doi:10.2514/1.J052684.

Hollowell, S. J. and Dugundji, J. (1984). "Aeroelastic flutter and divergence of stiffness coupled, graphite/epoxy cantilevered plates". *Journal of Aircraft*, vol. 21, no. 1, pp. 69–76. doi:10.2514/3.48224.

Ibrahimbegovic, A. (1997). "On the choice of finite rotation parameters". *Computer Methods in Applied Mechanics and Engineering*, vol. 149, no. 14, pp. 49–71. doi:10.1016/S0045-7825(97)00059-5.

IJsselmuiden, S. T. (2011). *Optimal Design of Variable Stiffness Composite Structures Using Lamination Parameters*. Ph.D. thesis, Delft University of Technology, Delft, The Netherlands.

IJsselmuiden, S. T., Abdalla, M. M., and Gürdal, Z. (2008). "Implementation of strength-based failure criteria in the lamination parameter design space". *AIAA Journal*, vol. 46, no. 7, pp. 1826–1834. doi:10.2514/1.35565.

Iovnovich, M. and Raveh, D. E. (2012). "Reynolds-averaged navier-stokes study of the shock-buffet instability mechanism". *AIAA Journal*, vol. 50, no. 4, pp. 880–890. doi:10.2514/1.J051329.

Irisarri, F. X., Lasseigne, A., Leroy, F. H., and Le Riche, R. (2014). "Optimal design of laminated composite structures with ply drops using stacking sequence tables". *Composite Structures*, vol. 107, pp. 559–569. doi:10.1016/j.compstruct.2013.08.030.

Jin, P., Song, B., Zhong, X., Yu, T., and Xu, F. (2016). "Aeroelastic tailoring of composite sandwich panel with lamination parameters". *Proceedings of the Institution of Mechanical Engineers, Part G: Journal of Aerospace Engineering*, vol. 230, no. 1. doi:10.1177/0954410015587724.

Jones, W. P. (1945). "Aerodynamic forces on wings in non-uniform motion". Tech. Rep. ARC-2117, H.M. Stationery Office.

Jovanov, K. and De Breuker, R. (2015). "Accelerated convergence of static aeroelasticity using low-fidelity aerodynamics". In *Proceedings of the 56th AIAA/ASCE/AHS/ASC Structures, Structural Dynamics, and Materials Conference*. doi:10.2514/6.2015-0175.

Jutte, C. and Stanford, B. K. (2014). "Aeroelastic tailoring of transport aircraft wings: State-of-the-art and potential enabling technologies". Tech. Rep. TM-2014-218252, NASA.

Jutte, C. V., Stanford, B., Wieseman, C. D., and Moore, J. B. (2014). "Aeroelastic tailoring of the NASA Common Research Model via novel material and structural configurations". In *Proceedings of the 52nd Aerospace Sciences Meeting*. doi:10.2514/6.2014-0598.

Kalman, T. P., Rodden, W. P., and Giesing, J. P. (1971). "Application of the doublet-lattice method to nonplanar configurations in subsonic flow". *Journal of Aircraft*, vol. 8, no. 6, pp. 406–413. doi:10.2514/3.59117.

Kameyama, M. and Fukunaga, H. (2007). "Optimum design of composite plate wings for aeroelastic characteristics using lamination parameters". *Computers & Structures*, vol. 85, no. 3-4, pp. 213–224. doi:10.1016/J.Compstruc.2006.08.051.

Karpel, M. (1982). "Design for active flutter suppression and gust alleviation using state-space aeroelastic modeling". *Journal of Aircraft*, vol. 19, no. 3, pp. 221–227. doi:10.2514/3.57379.

Karpel, M., Moulin, B., and Chen, P. C. (2005). "Dynamic response of aeroservoelastic systems to gust excitation". *Journal of Aircraft*, vol. 42, no. 5, pp. 1264–1272. doi:10.2514/1.6678.

Kassapoglou, C. (2013). *Design and Analysis of Composite Structures: With Applications to Aerospace Structures*. Aerospace Series. John Wiley & Sons, Ltd, West Sussex, United Kingdom. doi:10.1002/9781118536933.

Katz, J. (1985). "Calculation of the aerodynamic forces on automotive lifting surfaces". *Journal of Fluids Engineering*, vol. 107, no. 4, pp. 438–443. doi:10.1115/1.3242507.

Katz, J. and Plotkin, A. (2001). *Low-Speed Aerodynamics*. Cambridge University Press, Cambridge, United Kingdom.

Kaul, U. K. and Nguyen, N. T. (2014). "Drag optimization study of variable camber continuous trailing edge flap (VCCTEF) using OVERFLOW". In *Proceedings of the 32nd AIAA Applied Aerodynamics Conference*. doi:10.2514/6.2014-2444.

Kennedy, G. J. and Martins, J. R. R. A. (2014). "A parallel aerostructural optimization framework for aircraft design studies". *Structural and Multidisciplinary Optimization*, vol. 50, no. 6, pp. 1079–1101. doi:10.1007/s00158-014-1108-9.

Kenway, G., Kennedy, G., and Martins, J. R. R. A. (2014). "Aerostructural optimization of the Common Research Model configuration". In *Proceedings of the 15th AIAA/ISSMO Multidisciplinary Analysis and Optimization Conference*. doi:10.2514/6.2014-3274.

Kenway, G. K. W. and Martins, J. R. R. A. (2014). "Multipoint high-fidelity aerostructural optimization of a transport aircraft configuration". *Journal of Aircraft*, vol. 51, no. 1, pp. 144–160. doi:10.2514/1.C032150.

Khani, A., IJsselmuiden, S. T., Abdalla, M. M., and Gürdal, Z. (2011). "Design of variable stiffness panels for maximum strength using lamination parameters". *Composites Part B: Engineering*, vol. 42, no. 3, pp. 546–552. doi:10.1016/j.compositesb.2010.11.005.

Kholodar, D. B., Dowell, E. H., Thomas, J. P., and Hall, K. C. (2004). "Limit cycle oscillation of a typical airfoil in transonic flow". *Journal of Aircraft*, vol. 41, no. 5, pp. 1067–1072. doi:10.2514/1.618.

Kier, T. M. and Looye, G.-J. H. N. (2009). "Unifying manoeuvre and gust loads analysis models". In *Proceedings of the International Forum on Aeroelasticity and Structural Dynamics 2009*.

Kim, T. U. and Hwang, I. H. (2005). "Optimal design of composite wing subjected to gust loads". *Computers & Structures*, vol. 83, no. 19-20, pp. 1546–1554. doi: 10.1016/J.Compstruc.2005.02.002.

Klimmek, T. (2014). "Parametric set-up of a structural model for FERMAT configuration aeroelastic and loads analysis". *Journal of Aeroelasticity and Structural Dynamics*, vol. 3, no. 2. doi:10.3293/asdj.v3i2.27.

Körpe, D. S. and Özgen, S. (in press 2016). "Morphing wing optimization for steady level flight". *Proceedings of the Institution of Mechanical Engineers, Part G: Journal of Aerospace Engineering*. doi:10.1177/0954410016662063.

Kota, S. (1999). "System for varying a surface contour". US Patent US5971328 A.

Kota, S. (2002). "System for varying a surface contour". US Patent US6491262 B1.

Kota, S. and Hetrick, J. A. (2008). "Adaptive compliant wing and rotor system". US Patent US7384016 B2.

Kuder, I. K., Arrieta, A. F., Raither, W. E., and Ermanni, P. (2013). "Variable stiffness material and structural concepts for morphing applications". *Progress in Aerospace Sciences*, vol. 63, pp. 33–55. doi:10.1016/j.paerosci.2013.07.001.

Lambe, A. B. and Martins, J. R. R. A. (2015). "Matrix-free aerostructural optimization of aircraft wings". *Structural and Multidisciplinary Optimization*, vol. 53, no. 3, pp. 589–603. doi:10.1007/s00158-015-1349-2.

Landsberger, B. J. and Dugundji, J. (1985). "Experimental aeroelastic behavior of unswept and forward-swept cantilever graphite/epoxy wings". *Journal of Aircraft*, vol. 22, no. 8, pp. 679–686. doi:10.2514/3.45186.

Le, T.-N., Battini, J.-M., and Hjiaj, M. (2014). "A consistent 3D corotational beam element for nonlinear dynamic analysis of flexible structures". *Computer Methods in Applied Mechanics and Engineering*, vol. 269, pp. 538–565. doi: 10.1016/j.cma.2013.11.007.

Lebofsky, S., Ting, E., Trinh, K. V., and Nguyen, N. T. (2015). "Optimization for load alleviation of truss-braced wing aircraft with variable camber continuous trailing edge flap". In *Proceedings of the 33rd AIAA Applied Aerodynamics Conference*. doi:10.2514/6.2015-2723.

Leishman, J. G. and Nguyen, K. Q. (1990). "State-space representation of unsteady airfoil behavior". *AIAA Journal*, vol. 28, no. 5, pp. 836–844. doi: 10.2514/3.25127.

Li, B. Q. (2006). *Discontinuous Finite Elements in Fluid Dynamics and Heat Transfer*. Computational Fluid and Solid Mechanics. Springer London, London, United Kingdom. doi:10.1007/1-84628-205-5.

Librescu, L. and Khdeir, A. (1988). "Aeroelastic divergence of swept-forward composite wings including warping restraint effect". *AIAA Journal*, vol. 26, no. 11, pp. 1373–1377. doi:10.2514/3.10050.

Librescu, L. and Simovich, J. (1988). "General formulation for the aeroelastic divergence of composite swept-forward wing structures". *Journal of Aircraft*, vol. 25, no. 4, pp. 364–371. doi:10.2514/3.45572.

Librescu, L. and Song, O. (1992). "On the static aeroelastic tailoring of composite aircraft swept wings modelled as thin-walled beam structures". *Composite Engineering*, vol. 2, no. 5-7, pp. 497–512. doi:10.1016/0961-9526(92)90039-9.

Librescu, L. V. and Thangjitham, S. (1991). "Analytical studies on static aeroelastic behavior of forward-swept composite wing structures". *Journal of Aircraft*, vol. 28, no. 2, pp. 151–157. doi:10.2514/3.46004.

Liem, R. P., Kenway, G. K. W., and Martins, J. R. R. A. (2015). "Multimission aircraft fuel-burn minimization via multipoint aerostructural optimization". *AIAA Journal*, vol. 53, no. 1, pp. 104–122. doi:10.2514/1.J052940.

Lin, J. and Iliff, K. W. (2000). "Aerodynamic lift and moment calculations using a closed-form solution of the Possio equation". Tech. Rep. TM-2000-209019, NASA.

Lyu, Z. and Martins, J. R. R. A. (2015). "Aerodynamic shape optimization of an adaptive morphing trailing-edge wing". *Journal of Aircraft*, vol. 52, no. 6, pp. 1951–1970. doi:10.2514/1.C033116.

Macquart, T., Bordogna, M. T., Lancelot, P., and De Breuker, R. (2016). "Derivation and application of blending constraints in lamination parameter space for composite optimisation". *Composite Structures*, vol. 135, pp. 224–235. doi:10.1016/j.compstruct.2015.09.016.

Macquart, T., Werter, N. P. M., and De Breuker, R. (2017). "Aeroelastic design of blended composite structures using lamination parameters". *Journal of Aircraft*, vol. 54, no. 2, pp. 561–571. doi:10.2514/1.C033859.

Manan, A., Vio, G. A., Harmin, M. Y., and Cooper, J. E. (2010). "Optimization of aeroelastic composite structures using evolutionary algorithms". *Engineering Optimization*, vol. 42, no. 2, pp. 171–184. doi:10.1080/03052150903104358.

Martin, E. and Crossley, W. A. (2002). "Multiobjective aircraft design to investigate potential geometric morphing features". In *Proceedings of AIAA's Aircraft Technology, Integration, and Operations (ATIO) 2002 Technical Forum*. doi:10.2514/6.2002-5859.

McGowan, A.-M. R., Washburn, A. E., Horta, L. G., Bryant, R. G., Cox, D. E., Siochi, E. J., Padula, S. L., and Holloway, N. M. (2002). "Recent results from NASA's morphing project". In *Proceedings of the SPIE Conference on Smart Structures and Materials*, vol. 4698, pp. 97–111. doi:10.1117/12.475056.

Micro Epsilon (2015). "optoNCDT 1302 compact laser sensor".

Miller, S., Vio, G., Cooper, J., Vale, J., Gomes, A., Lau, F., Suleman, A., Cavagna, L., De Gaspari, A., Ricci, S., da Luz, L., Riccobene, L., Scotti, A., and Terraneo, M. (2010). "SMorph - Smart aircraft morphing technologies project". In *Proceedings of the 51st AIAA/ASME/ASCE/AHS/ASC Structures, Structural Dynamics, and Materials Conference*. doi:10.2514/6.2010-2742.

Mohammadi-Amin, M., Ghadiri, B., Abdalla, M. M., Haddadpour, H., and De Breuker, R. (2012). "Continuous-time state-space unsteady aerodynamic modeling based on boundary element method". *Engineering Analysis with Boundary Elements*, vol. 36, no. 5, pp. 789–798. doi:10.1016/j.enganabound.2011.12.007.

Molinari, G., Quack, M., Dmitriev, V., Morari, M., Jenny, P., and Ermanni, P. (2011). "Aero-structural optimization of morphing airfoils for adaptive wings". *Journal of Intelligent Material Systems and Structures*, vol. 22, no. 10, pp. 1075–1089. doi:10.1177/1045389X11414089.

Morino, L. (1993). "Boundary integral equations in aerodynamics". *Applied Mechanics Reviews*, vol. 46, no. 8, pp. 445–466. doi:10.1115/1.3120373.

Munk, M. M. (1949). "Propeller containing diagonally disposed fibrous material". US Patent US2484308 A.

Murua, J., Palacios, R., and Graham, J. M. R. (2012a). "Applications of the unsteady vortex-lattice method in aircraft aeroelasticity and flight dynamics". *Progress in Aerospace Sciences*, vol. 55, pp. 46–72. doi:10.1016/j.paerosci.2012.06.001.

Murua, J., Palacios, R., and R. Graham, J. M. (2012b). "Assessment of wake-tail interference effects on the dynamics of flexible aircraft". *AIAA Journal*, vol. 50, no. 7, pp. 1575–1585. doi:10.2514/1.J051543.

Namgoong, H., Crossley, W. A., and Lyrintzis, A. S. (2007). "Aerodynamic optimization of a morphing airfoil using energy as an objective". *AIAA Journal*, vol. 45, no. 9, pp. 2113–2124. doi:10.2514/1.24355.

Namgoong, H., Crossley, W. A., and Lyrintzis, A. S. (2012). "Morphing airfoil design for minimum drag and actuation energy including aerodynamic work". *Journal of Aircraft*, vol. 49, no. 4, pp. 981–990. doi:10.2514/1.C031395.

Ng, B. F., Hesse, H., Palacios, R., Graham, J. R., and Kerrigan, E. C. (2015). "Aeroservoelastic state-space vortex lattice modeling and load alleviation of wind turbine blades". *Wind Energy*, vol. 18, no. 7, pp. 1317–1331. doi:10.1002/we.1752.

Niksch, A., Valasek, J., Strganac, T., and Carlson, L. (2009). "Six degree-of-freedom dynamical model of a morphing aircraft". In *Proceedings of the AIAA Atmospheric Flight Mechanics Conference*. doi:10.2514/6.2009-5849.

Obradovic, B. and Subbarao, K. (2011a). "Design and simulation of a morphing-wing controller with actuator loading penalization". In *Proceedings of the AIAA Atmospheric Flight Mechanics Conference*. doi:10.2514/6.2011-6390.

Obradovic, B. and Subbarao, K. (2011b). "Modeling of dynamic loading of morphing-wing aircraft". *Journal of Aircraft*, vol. 48, no. 2, pp. 424–435. doi:10.2514/1.C000313.

Obradovic, B. and Subbarao, K. (2011c). "Modeling of flight dynamics of morphing wing aircraft". *Journal of Aircraft*, vol. 48, no. 2, pp. 391–402. doi:10.2514/1.C000269.

Patil, M. J., Cesnik, C. E. S., and Hodges, D. H. (1999). "Nonlinear aeroelasticity and flight dynamics of high-altitude long-endurance aircraft". In *Proceedings of the 40th Structures, Structural Dynamics, and Materials Conference and Exhibit*. doi:10.2514/6.1999-1470.

Patil, M. J. and Hodges, D. H. (2004). "On the importance of aerodynamic and structural geometrical nonlinearities in aeroelastic behavior of high-aspect-ratio wings". *Journal of Fluids and Structures*, vol. 19, no. 7, pp. 905–915. doi:10.1016/j.jfluidstructs.2004.04.012.

Patil, M. J., Hodges, D. H., and Cesnik, C. E. S. (2000). "Nonlinear aeroelastic analysis of complete aircraft in subsonic flow". *Journal of Aircraft*, vol. 37, no. 5, pp. 753–760. doi:10.2514/2.2685.

Patil, M. J., Hodges, D. H., and Cesnik, C. E. S. (2001a). "Limit-cycle oscillations in high-aspect-ratio wings". *Journal of Fluids and Structures*, vol. 15, no. 1, pp. 107–132. doi:10.1006/jfls.2000.0329.

Patil, M. J., Hodges, D. H., and Cesnik, C. E. S. (2001b). "Nonlinear aeroelasticity and flight dynamics of high-altitude long-endurance aircraft". *Journal of Aircraft*, vol. 38, no. 1, pp. 88–94. doi:10.2514/2.2738.

Pecora, R., Magnifico, M., Amoroso, F., Lecce, L., Bellucci, M., Dimino, I., Concilio, A., and Ciminello, M. (2016). "Structural design of an adaptive wing trailing edge for large aeroplanes". In Wölcken, P. C. and Papadopoulos, M., eds., *Smart Intelligent Aircraft Structures (SARISTU)*, pp. 159–170. Springer International Publishing. doi:10.1007/978-3-319-22413-8_8.

Pendleton, E. W., Bessette, D., Field, P. B., Miller, G. D., and Griffin, K. E. (2000). "Active aeroelastic wing flight research program: Technical program and model analytical development". *Journal of Aircraft*, vol. 37, no. 4, pp. 554–561. doi:10.2514/2.2654.

Perry, B., Cole, S. R., and Miller, G. D. (1995). "Summary of an active flexible wing program". *Journal of Aircraft*, vol. 32, no. 1, pp. 10–15. doi:10.2514/3.46677.

Peters, D. A., Karunamoorthy, S., and Cao, W.-M. (1995). "Finite state induced flow models. I - Two-dimensional thin airfoil". *Journal of Aircraft*, vol. 32, no. 2, pp. 313–322. doi:10.2514/3.46718.

Phillips, W. F. (2004). "Lifting-line analysis for twisted wings and washout-optimized wings". *Journal of Aircraft*, vol. 41, no. 1, pp. 128–136. doi:10.2514/1.262.

Qin, Z., Marzocca, P., and Librescu, L. (2002). "Aeroelastic instability and response of advanced aircraft wings at subsonic flight speeds". *Aerospace Science and Technology*, vol. 6, pp. 195–208. doi:10.1016/S1270-9638(02)01158-6.

Raju, G., White, S., Wu, Z., and Weaver, P. (2015). "Optimal postbuckling design of variable angle tow composites using lamination parameters". In *Proceedings of the 56th AIAA/ASCE/AHS/ASC Structures, Structural Dynamics, and Materials Conference*. doi:10.2514/6.2015-0451.

Raju, G., Wu, Z., and Weaver, P. (2014). "On further developments of feasible region of lamination parameters for symmetric composite laminates". In *Proceedings of the 55th AIAA/ASME/ASCE/AHS/SC Structures, Structural Dynamics, and Materials Conference*. doi:10.2514/6.2014-1374.

Raveh, D. E. (2007). "CFD-based models of aerodynamic gust response". *Journal of Aircraft*, vol. 44, no. 3, pp. 888–897. doi:10.2514/1.25498.

Raveh, D. E. (2011). "Gust-response analysis of free elastic aircraft in the transonic flight regime". *Journal of Aircraft*, vol. 48, no. 4, pp. 1204–1211. doi:10.2514/1.C031224.

Raveh, D. E. and Dowell, E. H. (2014). "Aeroelastic responses of elastically suspended airfoil systems in transonic buffeting flows". *AIAA Journal*, vol. 52, no. 5, pp. 926–934. doi:10.2514/1.J052185.

Raveh, D. E., Levy, Y., and Karpel, M. (2001). "Efficient aeroelastic analysis using computational unsteady aerodynamics". *Journal of Aircraft*, vol. 38, no. 3, pp. 547–556. doi:10.2514/2.2795.

Reckzeh, D. (2014). "Multifunctional wing moveables: Design of the A350XWB and the way to future concepts". In *Proceedings of the 29th Congress of the International Council of the Aeronautical Sciences*.

Reed, W. H. and Hill, T. R. (1973). "Triangular mesh methods for the neutron transport equation". Tech. Rep. LA-UR–73-479; CONF-730414–2, Los Alamos Scientific Lab., NM, USA.

Reich, G., Bowman, J., Sanders, B., and Frank, G. (2006). "Development of an integrated aeroelastic multi-body morphing simulation tool". In *Proceedings of the 47th AIAA/ASME/ASCE/AHS/ASC Structures, Structural Dynamics, and Materials Conference*. doi:10.2514/6.2006-1892.

Reimer, L., Ritter, M., Heinrich, R., and Krüger, W. (2015). "CFD-based gust load analysis for a free-flying flexible passenger aircraft in comparison to a DLM-based approach". In *Proceedings of the 22nd AIAA Computational Fluid Dynamics Conference*. doi:10.2514/6.2015-2455.

Rodriguez, D. L., Aftosmis, M. J., Nemec, M., and Anderson, G. R. (2016). "Optimization of flexible wings with distributed flaps at off-design conditions". *Journal of Aircraft*, vol. 53, no. 6, pp. 1731–1745. doi:10.2514/1.C033535.

Roger, K. (1977). "Airplane math modelling and active aeroelastic control design". Tech. Rep. CP-228, AGARD.

Roth, B. and Crossley, W. A. (2003). "Application of optimization techniques in the conceptual design of morphing aircraft". In *Proceedings of AIAA's 3rd Annual Aviation Technology, Integration, and Operations (ATIO) Forum*. doi: 10.2514/6.2010-9312.

Runyan, H. L. and Sewall, J. L. (1948). "Experimental investigation of the effects of concentrated weights on flutter characteristics of a straight cantilever wing". Tech. Rep. TN-1594, NACA.

Samareh, J. A., Chwalowski, P., Horta, L. G., Piatak, D. J., and McGowan, A. R. (2007). "Integrated aerodynamic/structural/dynamic analyses of aircraft with large shape changes". In *Proceedings of the 48th AIAA/ASME/ASCE/AHS/ASC Structures, Structural Dynamics, and Materials Conference*. doi:10.2514/6.2007-2346.

Sanders, B., Crowe, R., and Garcia, E. (2004). "Defense advanced research projects agency smart materials and structures demonstration program overview". *Journal of Intelligent Material Systems and Structures*, vol. 15, no. 4, pp. 227–233. doi:10.1177/1045389X04042793.

Sanders, B., Eastep, F. E., and Forster, E. (2003). "Aerodynamic and aeroelastic characteristics of wings with conformal control surfaces for morphing aircraft". *Journal of Aircraft*, vol. 40, no. 1, pp. 94–99. doi:10.2514/2.3062.

Schweiger, J., Suleman, A., Kuzmina, S., and Chedrik, V. (2002). "MDO concepts for an european research project on active aeroelastic aircraft". In *Proceedings*

*of the 9th AIAA/ISSMO Symposium on Multidisciplinary Analysis and Optimization*. doi:10.2514/6.2002-5403.

Scott, S., Capuzzi, M., Langston, D., Bossanyi, E., McCann, G., Weaver, P. M., and Pirrera, A. (2016). "Gust response of aeroelastically tailored wind turbines". *Journal of Physics: Conference Series*, vol. 753, no. 4. doi: 10.1088/1742-6596/753/4/042006.

Seigler, T. M., Neal, D. A., Bae, J. S., and Inman, D. J. (2007). "Modeling and flight control of large-scale morphing aircraft". *Journal of Aircraft*, vol. 44, no. 4, pp. 1077–1087. doi:10.2514/1.21439.

Selitrennik, E., Karpel, M., and Levy, Y. (2012). "Computational aeroelastic simulation of rapidly morphing air vehicles". *Journal of Aircraft*, vol. 49, no. 6, pp. 1675–1686. doi:10.2514/1.C031041.

Setoodeh, S., Abdalla, M. M., and Gürdal, Z. (2006). "Approximate feasible regions for lamination parameters". In *Proceedings of the 11th AIAA/ISSMO Multidisciplinary Analysis and Optimization Conference*. doi:10.2514/6.2006-6973.

Sherrer, V. C., Hertz, T. J., and Shirk, M. H. (1981). "Wind tunnel demonstration of aeroelastic tailoring applied to forward swept wings". *Journal of Aircraft*, vol. 18, no. 11, pp. 976–983. doi:10.2514/3.57589.

Shevell, R. (1989). *Fundamentals of Flight*. Prentice Hall, Englewood Cliffs, NJ, USA.

Shi, R. and Peng, J. (2015). "Morphing strategy design for variable-wing aircraft". In *Proceedings of the 15th AIAA Aviation Technology, Integration, and Operations Conference*. doi:10.2514/6.2015-3002.

Shirk, M. H., Hertz, T. J., and Weisshaar, T. A. (1986). "Aeroelastic tailoring theory, practice, and promise". *Journal of Aircraft*, vol. 23, no. 1, pp. 6–18. doi:10.2514/3.45260.

Simpson, R. J. S., Palacios, R., and Murua, J. (2013). "Induced-drag calculations in the unsteady vortex lattice method". *AIAA Journal*, vol. 51, no. 7, pp. 1775–1779. doi:10.2514/1.J052136.

Skillen, M. D. and Crossley, W. A. (2007). "Modeling and optimization for morphing wing concept generation". Tech. Rep. CR-2007-214860, NASA.

Skillen, M. D. and Crossley, W. A. (2008). "Modeling and optimization for morphing wing concept generation II Part I- Morphing wing modeling and structural sizing techniques". Tech. Rep. CR-2008-214902, NASA.

Stanford, B. and Jutte, C. (2016). "Comparison of curvilinear stiffeners and tow steered composites for aeroelastic tailoring of transports". In *Proceedings of the 34th AIAA Applied Aerodynamics Conference*. doi:10.2514/6.2016-3415.

Stanford, B. K., Jutte, C. V., and Chauncey Wu, K. (2014). "Aeroelastic benefits of tow steering for composite plates". *Composite Structures*, vol. 118, pp. 416–422. doi:10.1016/j.compstruct.2014.08.007.

Stanford, B. K., Jutte, C. V., and Wieseman, C. D. (2016). "Trim and structural optimization of subsonic transport wings using nonconventional aeroelastic tailoring". *AIAA Journal*, vol. 54, no. 1, pp. 293–309. doi:10.2514/1.J054244.

Stewart, E. C., Patil, M. J., Canfield, R. A., and Snyder, R. D. (2016). "Aeroelastic shape optimization of a flapping wing". *Journal of Aircraft*, vol. 53, no. 3, pp. 636–650. doi:10.2514/1.C033278.

Stodieck, O., Cooper, J. E., Weaver, P. M., and Kealy, P. (2013). "Improved aeroelastic tailoring using tow-steered composites". *Composite Structures*, vol. 106, pp. 703–715. doi:10.1016/J.Compstruct.2013.07.023.

Stodieck, O., Cooper, J. E., Weaver, P. M., and Kealy, P. (2017). "Aeroelastic tailoring of a representative wing box using tow-steered composites". *AIAA Journal*, vol. 55, no. 4, pp. 1425–1439. doi:10.2514/1.J055364.

Su, W. and Cesnik, C. E. S. (2010). "Nonlinear aeroelasticity of a very flexible blended-wing-body aircraft". *Journal of Aircraft*, vol. 47, no. 5, pp. 1539–1553. doi:10.2514/1.47317.

Sun, J., Guan, Q., Liu, Y., and Leng, J. (2016). "Morphing aircraft based on smart materials and structures: A state-of-the-art review". *Journal of Intelligent Material Systems and Structures*, vol. 27, no. 17, pp. 2289–2312. doi:10.1177/1045389X16629569.

Svanberg, K. (2002). "A class of globally convergent optimization methods based on conservative convex separable approximations". *SIAM Journal on Optimization*, vol. 12, no. 2, pp. 555–573. doi:10.1137/S1052623499362822.

Szodruch, J. and Hilbig, R. (1988). "Variable wing camber for transport aircraft". *Progress in Aerospace Sciences*, vol. 25, no. 3, pp. 297–328. doi:10.1016/0376-0421(88)90003-6.

Tang, D. M. and Dowell, E. H. (2001). "Experimental and theoretical study on aeroelastic response of high-aspect-ratio wings". *AIAA Journal*, vol. 39, no. 8, pp. 1430–1441. doi:10.2514/2.1484.

Tang, D. M. and Dowell, E. H. (2002a). "Experimental and theoretical study of gust response for high-aspect-ratio wing". *AIAA Journal*, vol. 40, no. 3, pp. 419–429. doi:10.2514/2.1691.

Tang, D. M. and Dowell, E. H. (2002b). "Limit-cycle hysteresis response for a high-aspect-ratio wing model". *Journal of Aircraft*, vol. 39, no. 5, pp. 885–888. doi:10.2514/2.3009.

Tang, D. M. and Dowell, E. H. (2004). "Effects of geometric structural nonlinearity on flutter and limit cycle oscillations of high-aspect-ratio wings". *Journal of Fluids and Structures*, vol. 19, no. 3, pp. 291–306. doi:10.1016/j.jfluidstructs.2003.10.007.

Tang, D. M., Grasch, A., and Dowell, E. H. (2010). "Gust response for flexibly suspended high-aspect ratio wings". *AIAA Journal*, vol. 48, no. 10, pp. 2430–2444. doi:10.2514/1.J050309.

Theodorsen, T. (1935). "General theory of aerodynamic instability and the mechanism of flutter". Tech. Rep. TR-496, NACA.

Thomas, J. P., Dowell, E. H., and Hall, K. C. (2002). "Nonlinear inviscid aerodynamic effects on transonic divergence, flutter, and limit-cycle oscillations". *AIAA Journal*, vol. 40, no. 4, pp. 638–646. doi:10.2514/2.1720.

Thomas, J. P., Dowell, E. H., and Hall, K. C. (2004). "Modeling viscous transonic limit cycle oscillation behavior using a harmonic balance approach". *Journal of Aircraft*, vol. 41, no. 6, pp. 1266–1274. doi:10.2514/1.9839.

Thuwis, G. A. A., De Breuker, R., Abdalla, M. M., and Gürdal, Z. (2009). "Aeroelastic tailoring using lamination parameters". *Structural and Multidisciplinary Optimization*, vol. 41, no. 4, pp. 637–646. doi:10.1007/s00158-009-0437-6.

Tian, W., Yang, Z., Gu, Y., and Ouyang, Y. (2016). "Aeroelastic tailoring of a composite forward-swept wing using a novel hybrid pattern search method". *Journal of Aerospace Engineering*, vol. 29, no. 6. doi:10.1061/(ASCE)AS.1943-5525.0000652.

Traub, L. W. (2011). "Range and endurance estimates for battery-powered aircraft". *Journal of Aircraft*, vol. 48, no. 2, pp. 703–707. doi:10.2514/1.C031027.

Tsai, S. W. and Pagano, N. J. (1968). "Invariant properties of composite materials". In *Composite Materials Workshop*, pp. 233–253. Technomic Publishing Co., Westport, CT, USA.

Urnes, J., Nguyen, N., Ippolito, C., Totah, J., Trinh, K. V., and Ting, E. (2013). "A mission adaptive variable camber flap control system to optimize high lift and cruise lift to drag ratios of future N+3 transport aircraft". In *Proceedings of the 51st AIAA Aerospace Sciences Meeting including the New Horizons Forum and Aerospace Exposition*. doi:10.2514/6.2013-214.

Vale, J., Leite, A., Lau, F., and Suleman, A. (2011). "Aero-structural optimization and performance evaluation of a morphing wing with variable span and camber". *Journal of Intelligent Material Systems and Structures*, vol. 22, no. 10, pp. 1057–1073. doi:10.1177/1045389X11416031.

Vassberg, J., Dehaan, M., Rivers, M., and Wahls, R. (2008). "Development of a Common Research Model for applied CFD validation studies". In *Proceedings of the 26th AIAA Applied Aerodynamics Conference*. doi:10.2514/6.2008-6919.

Volovoi, V. V. and Hodges, D. H. (2000). "Theory of anisotropic thin-walled beams". *Journal of Applied Mechanics*, vol. 67, no. 3, pp. 453–459. doi:10.1115/1.1312806.

Wakayama, S. R. and White, E. V. (2015). "Evaluation of adaptive compliant trailing edge technology". In *Proceedings of the 33rd AIAA Applied Aerodynamics Conference*. doi:10.2514/6.2015-3289.

Wang, Z., Chen, P. C., Liu, D. D., and Mook, D. T. (2010). "Nonlinear-aerodynamics/nonlinear-structure interaction methodology for a high-altitude long-endurance wing". *Journal of Aircraft*, vol. 47, no. 2, pp. 556–566. doi:10.2514/1.45694.

Wang, Z., Chen, P. C., Liu, D. D., Mook, D. T., and Patil, M. J. (2006). "Time domain nonlinear aeroelastic analysis for HALE wings". In *Proceedings of the 47th AIAA/ASME/ASCE/AHS/ASC Structures, Structural Dynamics, and Materials Conference*. doi:10.2514/6.2006-1640.

Weatherill, N., Soni, B., and Thompson, J., eds. (1998). *Handbook of Grid Generation*. CRC Press, Boca Raton, FL, USA.

Webb, M. and Subbarao, K. (2006). "On the dynamic aeroelastic stability of morphable wing structures". In *Proceedings of the 47th AIAA/ASME/ASCE/AHS/ASC Structures, Structural Dynamics, and Materials Conference*. doi:10.2514/6.2006-2133.

Weisshaar, T. (1987). "Aeroelastic tailoring - Creative uses of unusual materials". In *Proceedings of 28th Structures, Structural Dynamics and Materials Conference*. doi:10.2514/6.1987-976.

Weisshaar, T. A. (2006). "Morphing aircraft technology - New shapes for aircraft design". Tech. Rep. RTO-MP-AVT-141, NATO.

Werter, N. P. M., De Breuker, R., Friswell, M. I., Dettmer, W., and Beaverstock, C. S. (2013). "Two-level conceptual design of morphing wings". In *Proceedings of the 54th AIAA/ASCE/AHS/ASC Structures, Structural Dynamics, and Materials Conference*. doi:10.2514/6.2013-1720.

Wölcken, P. C. and Papadopoulos, M., eds. (2016). *Smart Intelligent Aircraft Structures (SARISTU)*. Springer International Publishing. doi:10.1007/978-3-319-22413-8.

Wu, Z., Raju, G., and Weaver, P. M. (2015). "Framework for the buckling optimization of variable-angle tow composite plates". *AIAA Journal*, vol. 53, no. 12, pp. 3788–3804. doi:10.2514/1.J054029.

# LIST OF PUBLICATIONS

## JOURNAL PUBLICATIONS

10. Werter, N.P.M. and De Breuker, R. "An optimisation framework for aeroelastic tailoring and morphing of wings under manoeuvre and gust loads". *Composite Structures*, to be submitted.

9. Werter, N.P.M. and De Breuker, R. "A two-step approach for the aeroelastic analysis and design of generic morphing wings". *Journal of Intelligent Material Systems and Structures*, to be submitted.

8. Sodja, J., Werter, N.P.M., Dillinger, J.K.S., and De Breuker, R. "Dynamic response of aeroelastically tailored composite wings: analysis and experiment", to be submitted.

7. Werter, N.P.M., De Breuker, R., and Abdalla, M.M. "Continuous-time state-space unsteady aerodynamic modelling for efficient loads analysis". *AIAA Journal*, revision under review.

6. Werter, N.P.M., Sodja, J., Spirlet, G., and De Breuker, R. "Design and experiments of a camber-twist morphing leading and trailing edge device". *Journal of Aircraft*, revision under review.

5. Werter, N.P.M., Sodja, J., and De Breuker, R. (2017). "Design and testing of aeroelastically tailored wings under maneuver loading". *AIAA Journal*, vol. 55, no. 3, pp. 1012-1025.

4. Macquart, T., Werter, N.P.M., and De Breuker, R. (2017). "Aeroelastic design of blended composite structures using lamination parameters" *Journal of Aircraft*, vol. 54, no. 2, pp. 561-571.

3. Lancelot P.M.G.J., Sodja, J., Werter, N.P.M., and De Breuker, R. (2017). "Design and testing of a low subsonic wind tunnel gust generator". *Advances in Aircraft and Spacecraft Science*, vol. 4, no. 2, pp. 125-144.

2. De Breuker, R. and Werter, N.P.M. (2016). "On the importance of morphing deformation scheduling for actuation force and energy". *Aerospace*, vol. 3, no. 4, 41, pp. 1-9.

1. Werter, N.P.M. and De Breuker, R. (2016). "A novel dynamic aeroelastic framework for aeroelastic tailoring and structural optimisation". *Composite Structures*, vol. 158, pp. 369-386.

## PATENTS

1. Werter N.P.M., De Breuker, R., Sodja, J., Spirlet, G., and Senkal B. (2016). "Air guiding structure". National Patent, no. 2013594, the Netherlands.

## CONFERENCE PUBLICATIONS

18. Radestock, M., Riemenschneider, J., Monner, H.P., Huxdorf, O., Werter, N.P.M., and De Breuker, R. (2016). "Deformation measurement in the wind tunnel for an UAV leading edge with a morphing mechanism". In *Proceedings of the 30th Congress of International Council of the Aeronautical Sciences*, pp. 1-9. Daejeon, Republic of Korea.

17. Werter, N.P.M., Sodja, J., Spirlet, G., and De Breuker, R. (2016). "Design and experiments of a warp induced camber and twist morphing leading and trailing edge device". In *Proceedings of the 24th AIAA/AHS Adaptive Structures Conference*, pp. 1-20. San Diego, CA, USA.

16. Sodja, J., Werter, N.P.M., Dillinger, J.K.S., and De Breuker, R. (2016). "Dynamic response of aeroelastically tailored composite wing: Analysis and experiment". In *Proceedings of the 57th AIAA/ASCE/AHS/ASC Structures, Structural Dynamics, and Materials Conference*, pp. 1-20. San Diego, CA, USA.

15. Macquart, T.B.M.J., Werter, N.P.M., and De Breuker, R. (2016). "Aeroelastic tailoring of blended composite structures using lamination parameters". In *Proceedings of the 57th AIAA/ASCE/AHS/ASC Structures, Structural Dynamics, and Materials Conference*, pp. 1-13. San Diego, CA, USA.

14. Keidel, D., Sodja, J., Werter, N., De Breuker, R., and Ermanni, P. 2015. "Development and testing of an unconventional morphing wing concept with variable chord and camber". In *Proceedings of the 26th International Conference on Adaptive Structures and Technologies*, pp. 1-12. Kobe, Japan.

13. Ciarella, A., Tsotskas, C., Hahn, M., Werter, N.P.M., De Breuker, R., Beaverstock, C.S., Friswell, M.I., Yang, Y., Özgen, S., Antoniadis, A., Tsoutsanis, P., and Drikakis, D. (2015). "A multi-fidelity, multi-disciplinary analysis and optimization framework for the design of morphing UAV wing".

In *Proceedings of the 16th AIAA/ISSMO Multidisciplinary Analysis and Optimization Conference*, pp. 1-21. Dallas, TX, USA.

12. Werter, N.P.M. and De Breuker, R. (2015). "Aeroelastic tailoring and structural optimisation using an advanced dynamic aeroelastic framework". In *Proceedings of the International Forum on Aeroelasticity and Structural Dynamics 2015*, pp. 1-20. St. Petersburg, Russia.

11. Werter, N.P.M., De Breuker, R., and Abdalla, M.M. (2015). "Continuous-time state-space unsteady aerodynamic modelling for efficient aeroelastic load analysis". In *Proceedings of the International Forum on Aeroelasticity and Structural Dynamics 2015*, pp. 1-18. St. Petersburg, Russia.

10. Werter, N.P.M., Sodja, J., and De Breuker, R. (2015). "Design and testing of an aeroelastically tailored wing under manoeuvre loading". In *Proceedings of the International Forum on Aeroelasticity and Structural Dynamics 2015*, pp. 1-16. St. Petersburg, Russia.

9. Lancelot, P.M.G.J., Sodja, J., Werter, N.P.M., and De Breuker, R. (2015). "Design and testing of a low subsonic wind tunnel gust generator". In *Proceedings of the International Forum on Aeroelasticity and Structural Dynamics 2015*, pp. 1-18. St. Petersburg, Russia.

8. Werter, N.P.M. and De Breuker, R. (2015). "A framework for the aeroelastic analysis and design of generic morphing wings". In *Proceedings of the 23rd AIAA/AHS Adaptive Structures Conference*, pp. 1-15. Kissimmee, FL, USA.

7. Werter, N.P.M., De Breuker, R., Beaverstock, C.S., and Friswell, M.I. (2014). "Feasible conceptual design of morphing structures". In *Proceedings of the 22nd AIAA/ASME/AHS Adaptive Structures Conference*, pp. 1-14. National Harbor, MD, USA.

6. Beaverstock, C. S., Fincham, J. H. S., Friswell, M. I., Ajaj, R. M., De Breuker, R., and Werter, N. P. M. 2014. "Effect of symmetric & asymmetric span morphing on flight dynamics". In *Proceedings of the AIAA Atmospheric Flight Mechanics Conference*, p. 1-15. National Harbor, MD, USA.

5. De Breuker, R., Abdalla, M.M., Werter, N.P.M., Vandewaeter, L., Ferede, E.A., Dillinger, J.K.S., and Kruger, W. (2013). "An aeroelastic multi-fidelity approach for aeroelastic tailoring". In *Proceedings of the International forum on Aeroelasticity and Structural Dynamics 2013*, pp. 1-19. Bristol, United Kingdom.

4. Beaverstock, C.S., Ajaj, R.M., Friswell, M.I., Dettmer, W.G., De Breuker, R., and Werter, N.P.M. (2013). "Effect of span-morphing on the longitudinal flight stability and control". In *Proceedings of the AIAA Guidance, Navigation and Control Conference* pp. 1-24. Boston, MA, USA.

3. Beaverstock, C.S., Ajaj, R.M., Friswell, M.I., De Breuker, R., and Werter, N.P.M. (2013). "Optimising mission performance for a morphing MAV". In *Proceedings of the 7th Ankara International Aerospace Conference*, pp. 1-13. Ankara, Turkey.

2. Werter, N.P.M., De Breuker, R., Beaverstock, C.S., Friswell, M.I., and Dettmer, W.G. (2013). "Two-level conceptual design of morphing wings". In *Proceedings of the 54th AIAA/ASME/ASCE/AHS/ASC Structures, Structural Dynamics, and Materials Conference*, pp 1-13. Boston, MA, USA.

1. Werter, N.P.M. and De Breuker, R. (2012). "Design of a composite forward swept wing using advanced aeroelastic tailoring optimisation methods". In *Proceedings of RAeS 3rd Aircraft Structural Design Conference*, pp. 1-12. Delft, the Netherlands.

# BIOGRAPHICAL NOTE

Noud Philip Maria Werter was born on April 11, 1989 in Hengelo (O), the Netherlands. After finishing the gymnasium at SG De Grundel in 2006, he decided to move to Delft and pursue a degree in Aerospace Engineering at the Delft University of Technology, where he obtained a Bachelor of Science degree with distinction in 2009.

After obtaining his Bachelor's degree, he obtained his Master of Science with distinction in 2012, specialising in aerospace structures combined with an honours track in aerodynamics. During his Master's degree he left the university for two periods of three months: an internship at Intespring B.V. working on a composite spring mechanism for a back support for caretakers and a short training program at the Von Karman Institute working on a prototype for an airborne laser interferometric droplet sizing instrument. Noud graduated on *An advanced aeroelastic tailoring tool for wing optimisation, preliminary design of composite wings* under the supervision of dr. Roeland De Breuker.

Following his Master's degree, in 2012, Noud was given the opportunity to continue working in the field of aeroelasticity and start his PhD under the supervision of dr. Roeland De Breuker resulting in this dissertation. During his PhD, he was active in the EU FP7 project CHANGE, collaborating with nine partners from industry, research institutes, and academy on morphing analysis software and the development of a prototype morphing aircraft.